Sea ice and the ocean mixed layer over the Antarctic continental shelf

Alek Petty

UCL

A dissertation submitted to University College London for the degree of Doctor of Philosophy.

November 2013

I, Alek Petty confirm that the work presented in this thesis is my own. Where information has been derived from other sources, I confirm that this has been indicated in the thesis.

Abstract

In this thesis, a modelling approach is taken to investigate the sea ice and ocean mixed layer over the Antarctic continental shelf. A primary motivation is to understand why the Amundsen and Bellingshausen (AB) shelf seas are flooded by Circumpolar Deep Water that is several degrees Celsius warmer than the cold shelf waters prevalent in the Weddell and Ross (WR) seas. An idealised sea ice-mixed layer model is used to investigate this apparent bimodal distribution. The formation of shelf waters (fully mixed water column) is shown to be driven primarily by the 'cold' WR atmospheric forcing, independent of the ocean profile, suggesting that the regional difference in atmospheric forcing alone is sufficient and perhaps necessary to account for the bimodal distribution in shelf sea temperature.

Coupling the mixed layer model to the sea ice model CICE extends the study to the entire Southern Ocean, and provides a more accurate representation of the sea ice and the processes controlling mixed layer deepening within the shelf seas. The model captures well the expected sea ice thickness distribution, and produces deep (>500 m) mixed layers in the WR shelf seas each winter. Shallower wintertime mixed layers are produced in the AB seas. Deconstructing the surface mechanical power input to the mixed layer, shows that the salt flux from sea ice growth/melt dominates the evolution of the mixed layer in all four shelf seas. An analysis of the sea ice mass balance demonstrates the contrasting mean annual ice growth, melt and export within each of the four shelf seas.

The CICE-mixed layer model is also used to investigate recent and future trends in the sea ice and mixed layer. The recent ERA-Interim forced simulation compares well with the observed regional trends in ice concentration, but shows mainly insignificant trends in the sea ice, the surface inputs of salt and heat, and the mixed layer depth over the shelf seas. The future HadGEM2-ES forced simulation shows, in-contrast, significant declines in the sea ice, the surface inputs of salt and heat and the mixed layer depth over the shelf seas. This simulation, however, shows poor agreement with recently observed sea ice trends; highlighting the on-going inability of climate models to accurately simulate Antarctic climate trends.

Acknowledgements

I jumped into this PhD without really knowing anything about the topic I was set to spend the next three years studying. Somehow, I bagged myself an interesting and topical PhD, along with two knowledgeable and personable supervisors in Danny and Paul. My thanks are mainly reserved for the top-notch supervision they gave me over the past three years. My weekly(ish!) meetings were always extremely useful and kept my PhD well on track. I think it's about time they had a break (temporarily...) from correcting my overly long draft manuscripts.

The loss of Seymour and Katharine made my last year at UCL a tragic one. They were both extremely well respected scientists who offered great advice and inspiration during my PhD. I am confident that through the enthusiasm and abilities of the current PhD crop (Tom, Sam and Rachel), the pioneering work of CPOM at UCL will continue in their absence. I would also like to thank the former members of CPOM-UCL (Harry, Rosie, Nikhil and Alex) and the current CPOM-Reading team (Michel, David and Daniela) for their help and encouragement throughout my PhD.

I am pretty sure that a key element of my PhD success was the good times I enjoyed outside of the office. For this I reserve special thanks to my housemates past (The Darty Boys) and present (Jez). While my efforts to teach them all about Antarctic sea ice may well have fallen on deaf ears, they did offer nods and smiles when appropriate.

Finally, my thanks go out to the Petty family. Hearing each family members' differing explanation of my PhD always brought a smile to my face!

This PhD was funded by the Natural Environment Research Council, with case sponsorship provided by the British Antarctic Survey.

Contents

List of Figures

List of Tables

List of Symbols and Abbreviations

Physical Constants

α	thermal expansion coefficient, K^{-1}
β	saline contraction coefficient,
c_0	specific heat capacity of fresh ice, J kg^{-1} K^{-1}
c_a	specific heat capacity of air, J kg^{-1} K^{-1}
c_w	specific heat capacity of water, J kg^{-1} K^{-1}
ϵ_s	longwave emissivity of snow
ϵ_o	longwave emissivity of open water
g	acceleration due to gravity, m s^{-2}
k_i	thermal conductivity of (fresh) ice, W m^{-1} K^{-1}
k_s	thermal conductivity of snow, W m^{-1} K^{-1}
L_f	latent heat of fusion, J kg^{-1}
L_s	latent heat of sublimation, J kg^{-1}
L_v	latent heat of vaporisation, J kg^{-1}
μ	liquidus relation coefficient, °C
ρ_a	density of air, kg m^{-3}
ρ_i	density of ice, kg m^{-3}
ρ_s	density of snow, kg m^{-3}
ρ_w	density of seawater, kg m^{-3}
σ	Stefan-Boltzmann constant, 5.67×10^{-8} W m^{-2} K^{-4}

Model Variables

All Chapters

A	Ice concentration
F_{ai}	net incoming heat flux from the atmosphere over the sea ice fraction, W m^{-2}
F_{lw}	incoming longwave radiative heat flux, W m^{-2}
F_{sw}	incoming shortwave radiative heat flux, W m^{-2}
F^o_{sw}	shortwave radiation absorbed by the open ocean fraction of the mixed layer, W m^{-2}
h_i	ice thickness, m
h_{mix}	mixed layer depth, m
h_s	snow thickness, m
P_{wind}	power input to the mixed layer from wind stirring, m^3 s^{-3}
q_a	2 m specific air humidity, g g^{-1}

S_b	salinity directly below the mixed layer
T_a	2 m air temperature, °C
T_b	temperature directly below the mixed layer, °C
T_f	freezing temperature of sea water, °C
T_{mix}	mixed layer temperature, °C
T_S^i	ice surface temperature, °C
U_a	10 m wind speed, m s^{-1}
$u_\star$	effective friction velocity at the upper surface of the mixed layer, m s^{-1}
w	entrainment rate, m s^{-1}
Δb	buoyancy difference across the mixed layer base
	Chapter 2
F_{ao}	net incoming heat flux from the atmosphere over the open water fraction, W m^{-2}
F_c	conductive heat flux through the ice (0-layer), W m^{-2}
F_{mi}	heat flux into the base of the sea ice at the mixed layer-sea ice boundary, W m^{-2}
F_{mo}	heat flux from the mixed layer to the open water surface layer, W m^{-2}
F_S	heat flux out of the mixed layer, K m s^{-1}
F_{sb}	basal heat flux from surface heat partitioning, W m^{-2}
F_T	salt flux out of the mixed layer, m s^{-1}
H_E	annual change in heat content of ice-ocean column from ice export, J m^{-2}
H_{fr}	ocean surface heat potential, W m^{-2}
H_R	annual change in heat content of ice-ocean column from ocean relaxation, J m^{-2}
H_S	annual change in heat content of ice-ocean column from atmospheric fluxes, J m^{-2}
P_B	power input to the mixed layer from surface buoyancy fluxes, m^3 s^{-3}
P_E	power required to entrain deep water into the mixed layer, m^3 s^{-3}
q_{sat}	saturation specific humidity, g g^{-1}
S_p	idealised 1D salinity profile, °C
S_E	annual change in salt content of ice-ocean column from ice export, kg m^{-2}
S_R	annual change in salt content of ice-ocean column from ocean relaxation, kg m^{-2}
S_P	annual change in salt content of ice-ocean column from net precipitation, kg m^{-2}
T_p	idealised 1D temperature profile, °C
T_S^o	open water surface temperature, °C
$u_\star^i$	friction velocity between the ice and the mixed layer, m s^{-1}
$u_\star^o$	friction velocity between the open water surface layer and mixed layer, m s^{-1}
$\mathbf{v}$	sea ice velocity, m s^{-1}
σ_θ	density anomaly, kg m^{-3}
Φ_A	rate of change of ice concentration, s^{-1}
Φ_h	basal ice growth, m s^{-1}
Φ_R	vertical redistribution of the sea ice through pressure ridging, m s^{-1}
ξ	ice divergence rate, s^{-1}

Chapters 3 and 4

c_B	fraction of energy remaining after convective dissipation
c_i	specific heat capacity of sea ice, J kg^{-1} K^{-1}
E_i	annual shelf sea ice export, km^3 yr^{-1}
F^i_{bot}	heat flux into the base of the sea ice, W m^{-2}
F^i_{fresh}	direct fresh-water flux from ice/snow growth/melt, kg m^{-2}s^{-1}
F^{pe}_{fresh}	direct fresh-water flux from net precipitation, kg m^{-2}s^{-1}
F_{ms}	mixed layer to ocean surface layer heat flux, W m^{-2}
F^i_S	salinity flux from ice/snow growth/melt, m s^{-1}
F^{pe}_S	salinity flux from net precipitation, m s^{-1}
F^i_{salt}	direct salt flux from ice/snow growth/melt, kg m^{-2}s^{-1}
$\widehat{F}^i_{salt}$	effective salt flux from ice/snow growth/melt, kg m^{-2}s^{-1}
$\widehat{F}^{pe}_{salt}$	effective salt flux from net precipitation, kg m^{-2}s^{-1}
F^i_{side}	lateral ice heat flux, W m^{-2}
F^i_{swabs}	shortwave radiation absorbed at the upper ice/snow surface, W m^{-2}
$F_{surface}$	heat flux into the ocean surface layer from the ice and open ocean, W m^{-2}
G_i	annual shelf sea ice growth, km^3 yr^{-1}
H_S	annual surface to mixed layer heat input, J m^{-2}
H_{frzmlt}	net heat potential for ice growth/melt, W m^{-2}
H^S_{frzmlt}	heat potential for ice growth/melt from the ocean surface layer, W m^{-2}
H^{mix}_{frzmlt}	heat potential for ice growth from the mixed layer, W m^{-2}
M_i	annual shelf sea ice melt, km^3 yr^{-1}
P_{heat}	mixed layer (mechanical) power input from surface heat flux, m^3 s^{-3}
P_{net}	net mixed layer (mechanical) power input, m^3 s^{-3}
P_{pe}	mixed layer (mechanical) power input from net precipitation, m^3 s^{-3}
P_{salt}	mixed layer (mechanical) power input from ice/snow salt/freshwater flux, m^3 s^{-3}
q_i	sea ice enthalpy, J m^{-3}
q_s	snow enthalpy, J m^{-3}
R_{side}	lateral melt fraction
$\widehat{S}$	inferred annual shelf sea salinity change
S_i	sea ice salinity
S_{ice}	annual effective salt input from ice/snow growth/melt, kg m^{-2}
S_{net}	annual net effective salt input, kg m^{-2}
S_{pe}	annual effective salt input from net precipitation, kg m^{-2}
S_{ocean}	Southern Ocean 3D salinity grid
$\widehat{T}$	inferred annual shelf sea temperature change, °C
T^i_b	ice bottom temperature, °C
T_i	internal sea ice temperature, °C
T_m	melting temperature of sea ice, °C

T_{ocean}	Southern Ocean 3D temperature grid, °C
T_S	ocean surface temperature, °C
U	10 m zonal wind speed, m s^{-1}
V	10 m meridional wind speed, m s^{-1}
V_i	volume of ice (per unit area), m
V_i^{new}	volume of new ice grown (per unit area), m
W_{heat}	annual mixed layer (mechanical) energy input from surface heat, J m^{-2}
W_{net}	net annual mixed layer (mechanical) energy input, J m^{-2}
W_{pe}	annual mixed layer (mechanical) energy input from net precipitation, J m^{-2}
W_{salt}	annual (mechanical) energy input from ice/snow fluxes, J m^{-2}

Model Parameters

All Chapters

c_m	unsteadiness coefficient, m s^{-1}
d_w	scale depth of dissipation from wind mixing, m^{-1}

Chapter 2

A_{max}	prescribed maximum ice concentration
α_s	albedo of snow
α_w	albedo of water
c_1	maximum magnitude of wind stirring in the mixed layer
c_2	mixed layer energy dissipation coefficient
C_D^i	turbulent transfer coefficient over ice fraction
C_D^o	turbulent transfer coefficient over lead fraction
c_h	Stanton number for mixed layer to sea ice heat transfer
h_{min}	minimum sea ice thickness, m
$I_o(0)$	fraction of shortwave radiation that penetrates the ocean surface
κ_w	extinction coefficient of shortwave radiation in ocean waters, m^{-1}
R_b	lateral melt partition
S_i	average bulk salinity of sea ice
S_{init}	initial idealised summertime salinity profile
T_{init}	initial idealised summertime temperature profile, °C
Δz	ocean profile vertical resolution, m

Chapters 3 and 4

c_d	ice-ocean drag coefficient
d_B	scale depth of dissipation from buoyancy driven mixing, m^{-1}
h_{min}	minimum mixed layer depth, m
h_S	fixed surface (temperature) layer thickness, m

Abbreviations

AABW	Antarctic Bottom Water
AB	Amundsen and Bellingshausen
ACC	Antarctic Circumpolar Current
AP	Antarctic Peninsular
AASW	Antarctic Surface Water
BB	Berkner Bank
BIS	Brunt Ice Shelf
CDW	Circumpolar Deep Water
EB	Eltanin Bay
ENSO	El Niño Southern Oscillation
FD	Filchner Depression
FIS	Filchner Ice Shelf
FRIS	Filchner-Ronne Ice Shelf
HSSW	High Salinity Shelf Water
IDW	Indian Deep Water
ISW	Ice Shelf Water
LC	Luitpold Coast
LCDW	Lower Circumpolar Deep Water
MB	Marguerite Bay
MCDW	Modified Circumpolar Deep Water
MMLD	Maximum Mixed Layer Depth
MS	McMurdo Sound
MWDW	Modified Warm Deep Water
PIG	Pine Island Glacier
PDW	Pacific Deep Water
RI	Ross Island
RIS	Ross Ice Shelf
RSBW	Ross Sea Bottom Water
SAM	Southern Annular Mode
SW	Shelf Water
TNB	Terra Nova Bay
UCDW	Upper Circumpolar Deep Water
WDW	Warm Deep Water
WR	Weddell and Ross
WSBW	Weddell Sea Bottom Water
WSDW	Weddell Sea Deep Water
WW	Winter Water

Overview

The Antarctic shelf seas are a crucial component of the Earth's climate system. The Amundsen and Bellingshausen shelf seas are implicit in the recent ocean-driven erosion of the Antarctic Ice Sheet (*Shepherd et al.*, 2004; *Holland et al.*, 2010; *Jacobs et al.*, 2011; *Pritchard et al.*, 2012; *Rignot et al.*, 2013); while the Weddell and Ross shelf seas cool and ventilate the deep ocean (*Orsi et al.*, 2001), and feed the global thermohaline circulation through AABW formation (*Orsi et al.*, 1999; *Jacobs*, 2004). The overall aim of this thesis is to increase our understanding of these important, yet poorly understood, climatic regions.

To place this work in context, Chapter 1 provides an overview of the Antarctic shelf seas, the wider Southern Ocean including the Antarctic sea ice cover, and Antarctic climate variability.

In Chapter 2, an idealised sea ice-mixed layer model is presented, before results from the model are discussed and summarised. The principal objective of this chapter is to test whether the bimodal distribution in the Antarctic shelf sea temperature can be explained directly by differing surface (atmospheric) fluxes between the warm and cold regions. The chapter starts with a detailed description of the model, including the atmospheric forcing and idealised ocean profiles used by the model. Results from the model are then presented and discussed, including reference simulations and switched forcing simulations, where the impact of regional atmospheric forcing differences on potential shelf water formation is tested. The impact of the idealised temperature and salinity ocean profiles on mixed layer deepening is also investigated to understand, simplistically, the role of the ocean in controlling the mixed layer evolution. Sensitivity studies are carried out to explore the impact of each atmospheric forcing variable and various model parameters on mixed layer deepening. The majority of the work presented in this chapter comes from the following recent publication:

Petty, A. A., D. L. Feltham, and P. R. Holland (2012), Impact of atmospheric forcing on Antarctic continental shelf water masses, *Journal of Physical Oceanography*, 43(5), 920-940.

In Chapter 3, the CICE-mixed layer model is presented, before results from the model are discussed and summarised. The principal objective of this chapter is to accurately quantify the cause of regional variations in the surface-driven formation of Antarctic shelf sea waters. The chapter starts with a summary of the main thermodynamic/dynamic processes included in the CICE sea ice model, before describing the inclusion of a variable mixed layer model into CICE. Results from this model then follow, including comparisons to observations where possible. The regional variation in the sea ice mass balance and surface driven deepening of the mixed layer is investigated, to understand the key processes controlling the mixed layer evolution across the four Antarctic shelf seas. A linear regression analysis is carried out to link both spatial and temporal mixed layer variability to atmospheric variability. The majority of the work presented in this chapter comes from the following manuscript recently submitted for publication:

Petty, A.A, P.R. Holland, D.L. Feltham (2013), Sea ice and the ocean mixed layer over the Antarctic shelf seas, *The Cryosphere Discussions*, 7(4), 4321-4377.

In Chapter 4, the CICE-mixed layer model is used to investigate recent and future trends in the Antarctic sea ice and mixed layer. The principal objective of this chapter is to understand the potential impact of atmospheric/surface trends on the mixed layer and thus shelf seas below. This analysis is carried out over recent decades using relatively accurate reanalysis forcing and for the coming century using the output of a general circulation model (GCM) under a moderate climate warming scenario. The chapter starts by introducing the GCM atmospheric forcing data and compares the forcing and model results to the potentially more accurate reanalysis simulation. An extended linear regression analysis is carried out to test the conclusions made in the previous chapter using the long-term forcing. Recent and future trends in the atmospheric forcing data are presented and discussed, before a qualitative analysis of the sea ice trends (ice concentration, motion and thickness) are presented for each simulation. A quantitive analysis of trends in the sea ice mass balance, the surface input of salt, freshwater and heat, and the mixed layer depth are then presented and discussed. The estimated freshening due to these surface-

driven trends are placed in context with the recent increase in fresh glacial meltwater from the recent thinning and accelerating of the West Antarctic ice shelves.

In Chapter 5, the main conclusions from each chapter are summarised including a brief discussion of the questions left unanswered and possible follow-on work resulting from this thesis.

A key theme throughout the thesis is the focus on surface processes in preference to variable ocean dynamics. This approach was taken to simplify the analysis of model results and to provide a clearer understanding of the direct impact of surface processes on the regional variations and potential trends in the Antarctic sea ice and shelf seas.

Chapter 1

Introduction

"...a dark / Illimitable ocean without bound, / Without dimension; where length, breadth, and highth, / And time and place are lost."

— John Milton; *Paradise Lost*

This chapter presents background information and introduces the themes investigated in this thesis. A description of the Southern Ocean and the Antarctic shelf seas is presented in Sect. 1.1, sea ice growth and the Antarctic sea ice cover are discussed in Sect. 1.2, and Antarctic climate trends are discussed in Sect. 1.3. The objectives of this thesis are presented in Sect. 1.4.

1.1 The Southern Ocean

Surrounding Antarctica is the Southern Ocean; the central hub of the Earth's oceans, which connects the three great ocean basins (Pacific, Atlantic and Indian). The signature feature of the Southern Ocean is the Antarctic Circumpolar Current (ACC), where the absence of land barriers within the latitudinal band of Drake Passage (∼56–62°S) allows strong westerly winds to drive a deep-reaching eastward circumpolar current (*Orsi et al.*, 1995). The ACC transports around 130–140 Sv (1 Sv = 10^6 m^3 s^{-1}) of water around the continent (*Whitworth et al.*, 1982; *Cunningham et al.*, 2003), making it the Earth's largest ocean current (shown in Fig. 1.1). The

strong zonal flow of the ACC acts as an isolating ring around Antarctica, protecting it from warmer waters further north (*Rintoul et al.*, 2001).

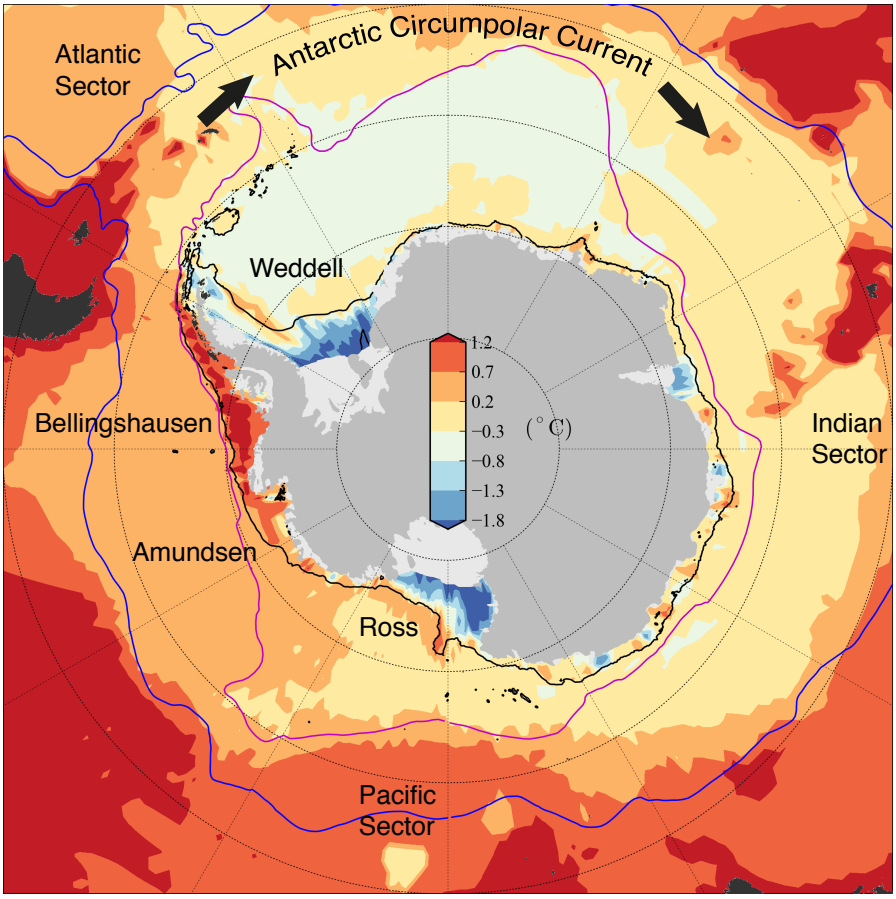

Figure 1.1: Map of the Southern Ocean bottom temperature. *In situ* ocean temperature data are taken from the WOA09 climatology (*Locarnini et al.*, 2010). The 1000 m isobath contour (black line) and the Antarctic landmask are taken from the RTOPO dataset (*Timmermann et al.*, 2010). The ACC is bound by the Subantarctic Front (blue line) and the southern boundary of UCDW (magenta line), which are taken from *Orsi et al.* (1995).

The ACC is mostly composed of Circumpolar Deep Water (CDW) (*Deacon*, 1937), which is a mixture of warm deep waters formed in all three ocean basins (*Orsi et al.*, 1999). *Gordon* (1971) distinguishes between Upper and Lower CDW, characterised by either a temperature (∼1.6–2.0°C, UCDW) or salinity (∼34.74, LCDW) maximum, with the southern boundary of UCDW used by *Orsi et al.* (1995) to define the southern boundary of the ACC, as depicted in Fig. 1.1.

Much of the LCDW that is present around Antarctica is a result of wind-driven (adiabatic) upwelling of North Atlantic Deep Water (NADW), formed predominantly in the marginal seas of the North Atlantic, modified through diapycnal mixing with deep waters (described in more detail by *Marshall and Speer*, 2012; *Talley*, 2013). UCDW, in contrast, is thought to form predominantly through wind-driven upwelling of Indian Deep Water (IDW) and Pacific Deep Water (PDW), which are formed through diapycnal upwelling of Antarctic Bottom Water (AABW) (the formation of which is described in more detail in later sections) in the Indian and Pacific oceans (e.g. *Schmitz*, 1995). A significant fraction of this UCDW freshens and warms at the surface and is returned north through Ekman transport (driven by the strong westerly winds) as Subantarctic Mode Water (SAMW) (e.g. *Rintoul et al.*, 2001). The upwelling of AABW ventilates deep ocean waters with high carbon dioxide (CO_2) concentrations (e.g. *Orsi et al.*, 2002), providing a crucial control on the atmospheric concentration of CO_2 over glacial-interglacial time-scales (e.g. *Skinner et al.*, 2010). The central role of the Southern Ocean in the global overturning circulation (GOC) is shown schematically in Fig. 1.2.

At the southern periphery of the Southern Ocean reside the relatively shallow Antarctic shelf seas (defined throughout this thesis by the 1000 m isobath contour). The Antarctic continental shelf is deep compared to continental shelves found elsewhere on Earth; a result of the considerable weight of the thick (several kilometres) Antarctic Ice Sheet (AIS), and its northward extension during previous glacial maxima. While most of East Antarctica shows no pronounced continental shelf, the Weddell, Ross, Amundsen and Bellingshausen shelf seas of West Antarctica extend by several hundred kilometres from the Antarctic coastline (the bathymetry, bottom temperature and bottom salinity of each of the shelf seas is shown in Fig. 1.3).

All four shelf seas are crucial components of the Earth's climate system. The Amundsen and Bellingshausen (AB) shelf seas are unique for their close proximity to the ACC (see Fig. 1.1) and are implicit in the recent rapid ocean-driven melting of the West Antarctic Ice Sheet (WAIS) (*Shepherd et al.*, 2004; *Holland et al.*, 2010; *Jacobs et al.*, 2011; *Pritchard et al.*, 2012; *Rignot et al.*, 2013). The Weddell and Ross (WR) shelf seas, in contrast, cool and ventilate the deep ocean (*Orsi et al.*, 2001, 2002), and feed the global thermohaline circulation through AABW formation (*Orsi et al.*, 1999; *Jacobs*, 2004). These ideas will be discussed more in later sections,

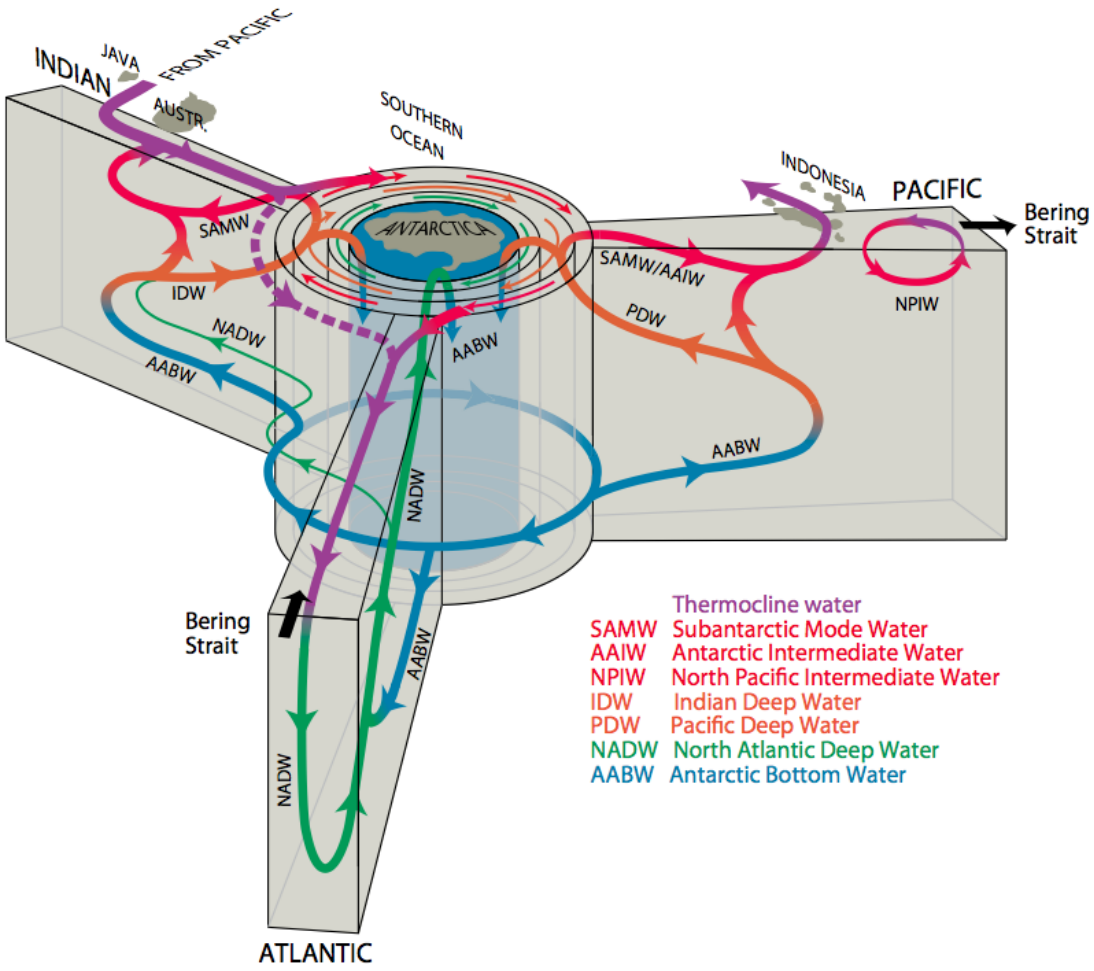

Figure 1.2: The global overturning circulation from a Southern Ocean perspective; a recent update to several other overturning circulation schematics (e.g. *Schmitz*, 1995; *Lumpkin and Speer*, 2007). Taken from *Talley* (2013).

but first a brief overview is provided of these four seas (while focussing on the processes taking place over the continental shelf).

1.1.1 The Weddell Sea

In the Weddell Sea, brine rejection during winter sea ice growth (described in more detail in Sect. 1.2) results in the formation of High Salinity Shelf Water (HSSW). Interaction with the atmosphere progressively cools and salinates the sea surface until the negative buoyancy flux

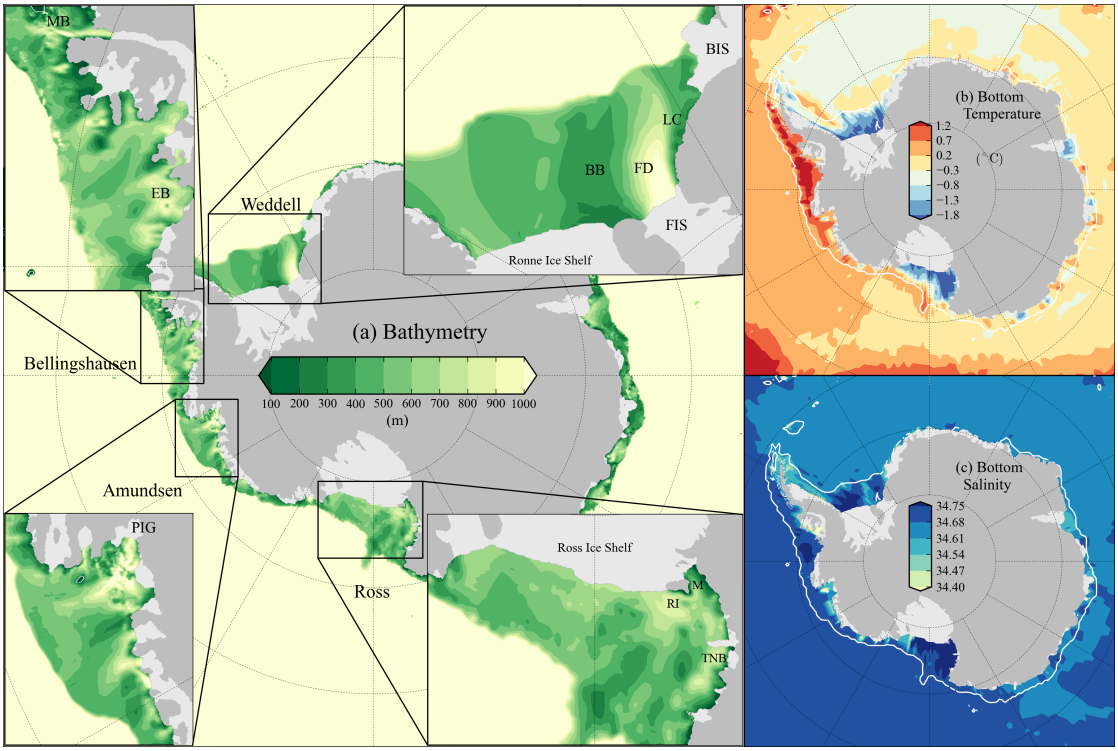

Figure 1.3: (a) Bathymetry, (b) bottom temperature and (c) bottom salinity of the Southern Ocean. The bathymetry (a) and landmask are taken from the RTOPO dataset (*Timmermann et al.*, 2010). Ocean data are taken from the World Ocean Atlas (2009) temperature (*Antonov et al.*, 2010) and salinity (*Locarnini et al.*, 2010) datasets. The white line in (b) and (c) is the 1000 m isobath contour. BB: Berkner Bank, FD: Filchner Depression, FIS: Filchner Ice Shelf, BIS: Brunt Ice Shelf, LC: Luitpold Coast, MB: Marguerite Bay, EB: Eltanin Bay, PIG: Pine Island Glacier, RI: Ross Island, M: McMurdo Sound, TNB: Terra Nova Bay.

mixes the entire water column (destratification), and the surface mixed layer can be regarded as extending to the shelf seabed. This process is strongest in the coastal polynya in the southwestern corner of the Weddell Sea, however the winter heat loss through the polynya provides only a small fraction (around 10%) of the heat loss needed to convert the summertime shelf waters into HSSW (*Renfrew et al.*, 2002; *Nicholls et al.*, 2009). The gradual brine flux from the more extensive pack ice is therefore thought to be the principal mechanism for creating shelf water in the Weddell Sea. HSSW resides on the shelf for several years (*Gill*, 1973), before either crossing the shelf break to the north or entering the Ronne Ice Shelf (RIS) cavity to the south, producing Ice Shelf Water (ISW) as the HSSW melts the base of the Filchner-Ronne Ice Shelf (FRIS). Most of this ISW is thought to be transported off the continental shelf via the Filchner Depression (*Foldvik*

et al., 2004; *Wilchinsky and Feltham*, 2009), along with a smaller fraction emerging at various locations along the Ronne ice front. δ_{18}O data from *Nicholls et al.* (2003) show that none of the HSSW entering the cavity is reconverted ISW. It is therefore expected that ISW does not contribute much to the properties of the waters within the Weddell shelf sea.

North of the continental shelf, warm CDW enters at the the north-eastern corner of the Weddell Gyre and mixes with cold Antarctic Surface Water (AASW) to produce Warm Deep Water (WDW) (*Whitworth and Nowlin*, 1987; *Fahrbach et al.*, 1994b). Below the WDW is Weddell Sea Deep Water (WSDW), an intermediate water mass which can be regarded as the Weddell Sea component of AABW (*Foldvik et al.*, 1985), the densest water mass of the global thermohaline circulation (*Orsi et al.*, 1999; *Jacobs*, 2004). At the shelf break, interaction between the cold mixed layer waters and WDW produces Modified Warm Deep Water (MWDW), which is thought to be the principal source water-mass over the continental shelf, forming a significant proportion of the source waters for the formation of HSSW during winter (*Nicholls et al.*, 2009). A signature feature over the Antarctic continental shelf break is the Antarctic Slope Front (ASF), which separates the cold/fresh shelf waters from the warm/saline waters further north (e.g. *Jacobs*, 1991). The prevailing westward winds near the Antarctic coastline generate an Ekman transport of surface waters towards the shelf, and induce a westward flowing geostrophic current, that extends virtually circumpolar Antarctica (*Heywood et al.*, 2004). The competing off-shelf flow of HSSW in the Weddell Sea then generates a characteristic V shaped ASF (*Gill*, 1973), as highlighted schematically in Fig. 1.6. As the HSSW flows off the shelf, it mixes with WDW around the shelf break to form Weddell Sea Bottom Water (WSBW) (*Gill*, 1973; *Foster and Carmack*, 1976), which resides in the Weddell basin until it mixes up with the overlying WSDW. As a result of the various mixing processes north of the shelf break and the conversion of MWDW to HSSW on the wide continental shelf, the FRIS in the southern Weddell Sea is well protected from the relatively warm CDW residing in the ACC.

1.1.2 The Ross Sea

The brine rejection from sea ice growth in the Ross shelf seas also causes a salination and deepening of the surface mixed layer, resulting in the formation of HSSW through mixing of the entire water column. In the Ross Sea, the coastal polynyas are thought to produce significantly more sea ice, both in volume and as a fraction of the ice exported out of the shelf (*Drucker et al.*, 2011), although it is expected the remaining sea ice growth plays a similar role to that in the Weddell Sea. The HSSW is either transported directly northwards past the Ross continental shelf break (*Jacobs et al.*, 1970; *Orsi et al.*, 1999) or is transported southwards into the Ross Ice Shelf (RIS) cavity, with the resulting ISW flowing northwards through the eastern shelf sea (*Jacobs et al.*, 1970, 1985). Similar to the Weddell Sea, north of the shelf break, interaction between cold surface waters and CDW produces Modified Circumpolar Deep Water (MCDW), which forms a significant proportion of the source waters for the formation of HSSW during winter. The westward-flowing geostrophic slope current and the formation of HSSW, also results in a V shaped ASF around the shelf break (*Ainley and Jacobs*, 1981). The mixing of HSSW with MCDW around the shelf break results in the formation of Ross Sea Bottom Water (RSBW) (*Orsi et al.*, 1999; *Jacobs*, 2004; *Orsi and Wiederwohl*, 2009); the Ross Sea component of AABW. As a result of these mixing processes, the RIS in the southern Ross Sea is also relatively well protected from the warm waters residing offshore in the ACC.

The WR seas experience the coldest ($\sim$-25°C) near-surface air temperatures over the Antarctic continental shelf in winter, due to strong and persistent katabatic winds carrying cold air to the WR coastlines from the centre of Antarctica (Fig. 1.4 taken from *van Lipzig et al.*, 2004). The location of the pressure lows surrounding Antarctica also generate strong southerly (prevailing) winds over the Ross Sea, and weaker southeasterly winds over the Weddell Sea (see Fig. 3.2f). The southerly winds result in a divergent wind stress applied to the ice along the coastline due to the fixed coastal boundary perpendicular to the wind flow, which is also thought to play a key role in sea ice production and the resultant shelf water formation. The relative size and impact of the coastal polynyas in the WR shelf seas is likely driven by the difference in the prevailing winds, whereby the stronger and more southerly wind flow in the Ross Sea generates

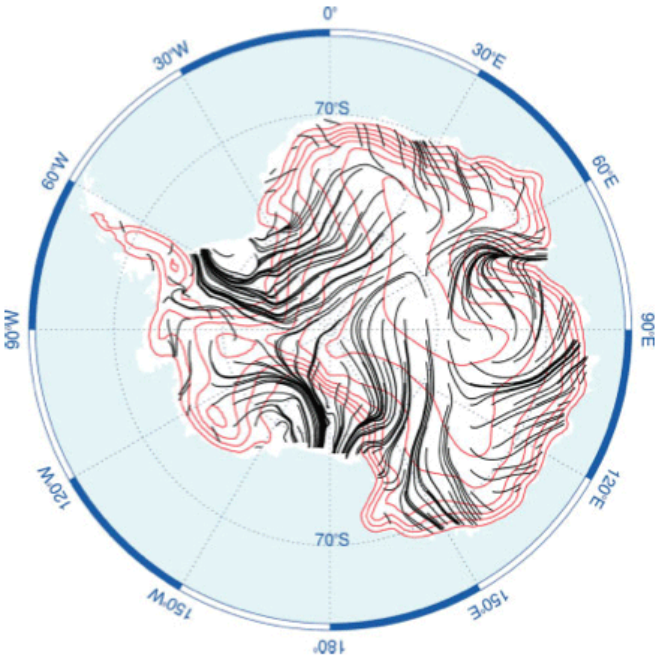

Figure 1.4: Mean (1980-1993) winter (JJA) 7 m wind stream lines over Antarctica, based on the output of the high-resolution Regional Atmospheric Climate Model (RACMO). Stream lines are plotted using every fifth grid point (from a 55 km grid spacing). The surface elevation contours (red lines) are plotted every 0.5 km. Taken from *van Lipzig et al.* (2004)

a greater ice divergence along the coast.

RSBW and WSBW, together with Adélie Land Bottom Water (ALBW) (*Williams et al.*, 2010) and the more recently discovered Cape Darnley Bottom Water (CDBW) (*Ohshima et al.*, 2013), form the total AABW; the southern limb of the global thermohaline circulation, that accounts for around a third of the total ocean volume (*Johnson*, 2008). The relative contribution of each source to the total AABW volume is an on-going area of investigation, as demonstrated by Fig. 1.5.

1.1.3 The Bellingshausen Sea

The Bellingshausen shelf sea is flooded by virtually unmodified CDW, overlain by its mixtures with Winter Water (WW), the remnant of mixed layer deepening in winter, and Antarctic Surface Water (AASW) (*Talbot*, 1988; *Jenkins and Jacobs*, 2008). Importantly, wintertime sea ice growth

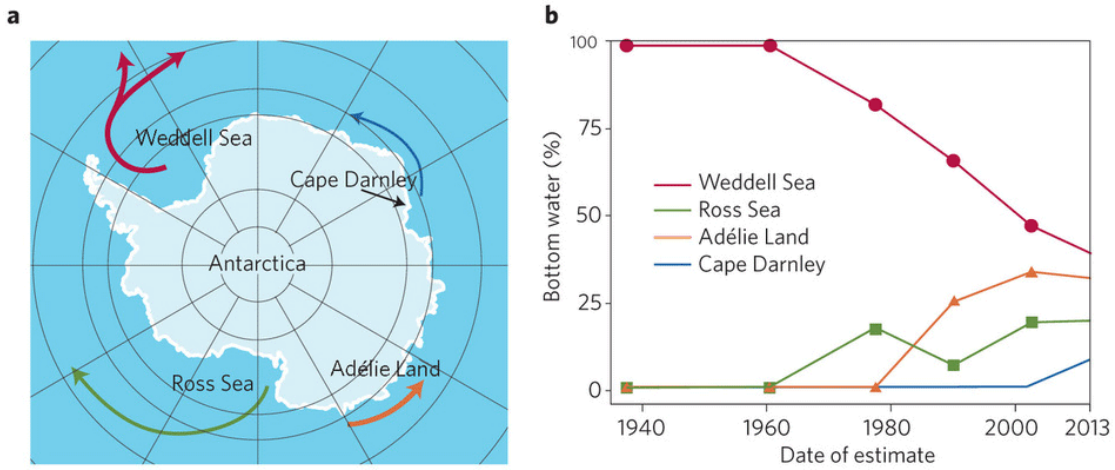

Figure 1.5: Main contributions to Antarctic Bottom Water formation. (a) shows the main sites for the production and export of dense waters, while (b) shows the time-evolving estimates of each contribution to the total bottom water formation, updated from *Jacobs* (2004). Taken from *Meredith* (2013).

does not deepen the mixed layer sufficiently to convert all of this CDW into colder shelf waters, and it therefore persists at depth throughout the shelf. Directly north of the shelf break, the ACC flows northeastward along the shelf break, composed of UCDW, underlain by LCDW present at a depth just below the shelf break. Due to the ready access of CDW, the ASF is not thought to be a prominent feature of the Bellingshausen Sea (*Whitworth et al.*, 1998).

The eastern Bellingshausen shelf sea (around Marguerite Bay, see Fig. 1.3) has been well observed due to the location of research stations nearby and interest in the rapid warming observed over the Antarctic Peninsula in recent decades (*Vaughan et al.*, 2003). UCDW is thought to dominate the presence of CDW over the shelf in this region (*Klinck et al.*, 2004; *Moffat et al.*, 2009), although the mechanism by which the waters access the shelf is still an active area of investigation. Proposed mechanisms are discussed by *Martinson and McKee* (2012) and include: eddy-shedding from the ACC (e.g. *Moffat et al.*, 2009; *Klinck and Dinniman*, 2010), entry through bathymetric troughs in the shelf seabed (e.g. *Klinck et al.*, 2004), upwelling of waters onto the shelf (e.g. *Martinson et al.*, 2008), or episodic advective processes (e.g. *Dinniman and Klinck*, 2004). It is thought that eddy-shedding dominates UCDW transport on to the shelf, with smaller amounts of LCDW transported through bathymetric troughs (*Martinson and McKee*, 2012). The

potential for upwelling of CDW onto the shelf is still uncertain. Understanding the processes by which CDW is transported onto the western Bellingshausen shelf is hindered by the lack of published research in this region. The lower temperature maximum observed here using recent seal-tagged observations (*Hofmann et al.*, 2009) suggests a different mechanism (from those listed previously) could be dominating the transport, although more research is needed to investigate this. In the modelling study of *Holland et al.* (2010), variability in the thickness of the CDW layer was shown to be strongly linked to surface (e.g. sea ice) conditions, through variability in the mixing of warm CDW into the surface layer.

1.1.4 The Amundsen Sea

The Amundsen shelf sea is also flooded by CDW, predominantly in a modified form from its source offshore in the ACC (through mixing with WW and AASW) (*Hellmer et al.*, 1998; *Jacobs et al.*, 2011). Unlike the Bellingshausen Sea, seasonal wind pulses of LCDW into glacially-carved troughs in the continental shelf appear to be the primary mechanism of CDW transport onto the shelf (*Walker et al.*, 2007; *Thoma et al.*, 2008; *Wåhlin et al.*, 2010; *Arneborg et al.*, 2012). The Amundsen Sea ASF is a more prominent feature compared to the Bellingshausen Sea, however the Ekman transport only causes a slight deepening of the pycnoclines, which is not sufficient to deepen the surface waters down to the shelf break (*Jacobs et al.*, 2012), as shown schematically in Fig. 1.6. Modelling studies have shown the transport to be driven by eastward winds at the shelf break, resulting in a northward Ekman transport in the surface layer, and a compensating southward return flow below the surface layer (*Thoma et al.*, 2008; *Steig et al.*, 2012; *Schodlok et al.*, 2012). There are no observations of warmer UCDW on the Amundsen shelf, meaning the Amundsen Sea appears to be successfully shielding ice shelves against the warmest class of CDW. Variability in the thickness of the Amundsen CDW layer is likely driven by variable upwelling at the shelf break (*Thoma et al.*, 2008; *Steig et al.*, 2012), although the potential contribution of variable mixing of cold waters from above, as has been suggested in the Bellingshausen Sea (*Holland et al.*, 2010), is still uncertain.

The variability of the warm CDW layer on the shelf has been implicated in the recent

rapid thinning of the ice shelves in the AB seas (*Shepherd et al.*, 2004; *Holland et al.*, 2010; *Jacobs et al.*, 2011; *Fricker and Padman*, 2012; *Pritchard et al.*, 2012; *Rignot et al.*, 2013) as discussed in more detail in Sect. 1.1.7.

1.1.5 The Antarctic shelf seas - a bimodal distribution

The contrast in the behaviour of the shelf seas is most apparent in the clear bimodal distribution in the ocean temperature at the shelf seabed (Fig. 1.1). The temperature of the shelf seabed water masses is thought to result from a balance between the transport of warm water onto the shelf and the cooling on-shelf that arises from mixed layer deepening, as demonstrated schematically in Fig. 1.6.

The basic geometry of the continental shelf regions is similar, so the remaining physical explanations for the observed temperature distribution can be divided into external forcings and internal feedback mechanisms. Candidate external mechanisms are: (i) differing surface fluxes between the warm and cold regions, leading to a difference in sea ice production and thus the destratifying potential from brine release (*Talbot*, 1988); and (ii) a difference in the rate and/or temperature of warm-water transport onto the shelf (*Dinniman et al.*, 2011). Candidate internal mechanisms are: (iii) Warm water on-shelf reduces sea-ice formation because mixed-layer deepening entrains heat into the mixed layer that must be removed before further ice growth can occur (*Martinson*, 1990); (iv) the presence of dense cold water on-shelf reduces the import of less-dense warm waters (*Talbot*, 1988); and (v) warmer waters induce a greater flux of ice-shelf meltwater, stratifying the water column and suppressing mixed layer deepening (*Jenkins and Jacobs*, 2008).

Through the focus on surface processes over the Antarctic shelf seas, this thesis seeks to understand the direct mechanisms that could explain the distribution, with a specific focus on testing hypothesis (i).

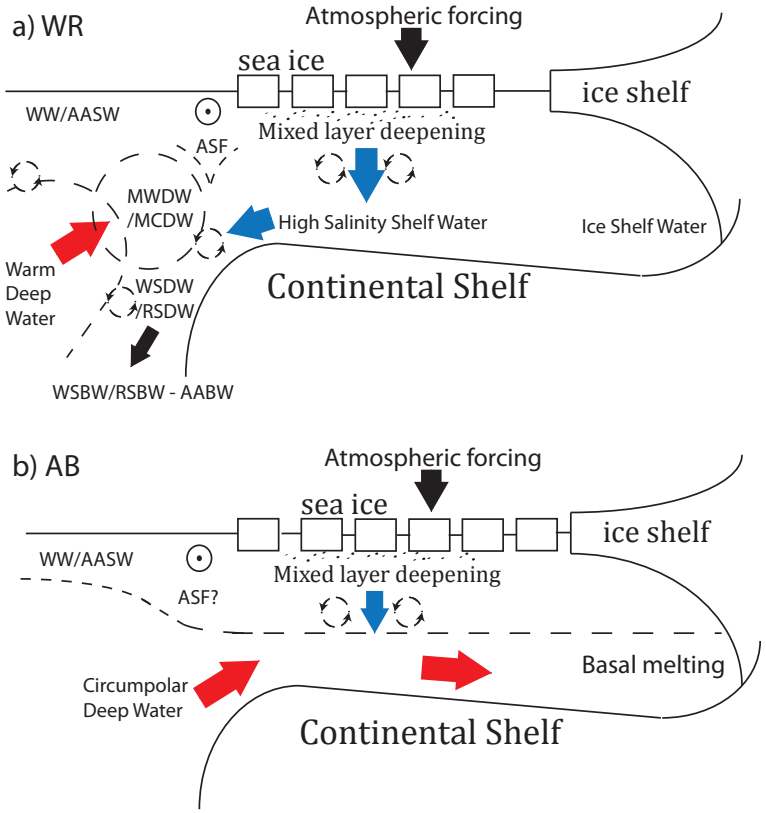

Figure 1.6: Schematic of main processes in the (a) Weddell/Ross and (b) Amundsen/Bellingshausen shelf seas. AASW-Antarctic Surface Waters, ASF-Antarctic Slope Front, CDW-Circumpolar Deep Water, MCDW-Modified Circumpolar Deep Water, MWDW-Modified Warm Deep Water, RSBW-Ross Sea Bottom Water, RSDW-Ross Sea Deep Water, WDW -Warm Deep Water,WSBW-Weddell Sea Bottom Water, WSDW-Weddell Sea Deep Water, WW-Winter Water. The dotted circle indicates a westward flowing (out of the page) slope current.

1.1.6 Antarctic shelf sea trends

Understanding recent trends in the Antarctic shelf seas suffers from a lack of both spatial and temporal data coverage. Perhaps the best-sampled of the Antarctic shelf seas is the Ross shelf sea, for which a freshening of 0.03 dec^{-1} has been observed since the 1950s within the southwestern corner of the shelf (the HSSW forming region) (*Jacobs and Giulivi*, 1998; *Jacobs et al.*, 2002; *Jacobs and Giulivi*, 2010). Note that throughout this thesis, salinity is reported using the 1978 Practical Salinity Scale (PSS-78), a dimensionless unit derived from the seawater conductivity. Concurrently, a freshening of 0.08 $decade^{-1}$ has been observed in the upper 200 m of the westward

flowing coastal and slope front currents (consisting mainly of AASW), which originate in the Amundsen Sea before flowing through the eastern Ross Sea (shown schematically in Fig. 1.7, taken from *Smith et al.*, 2012b).

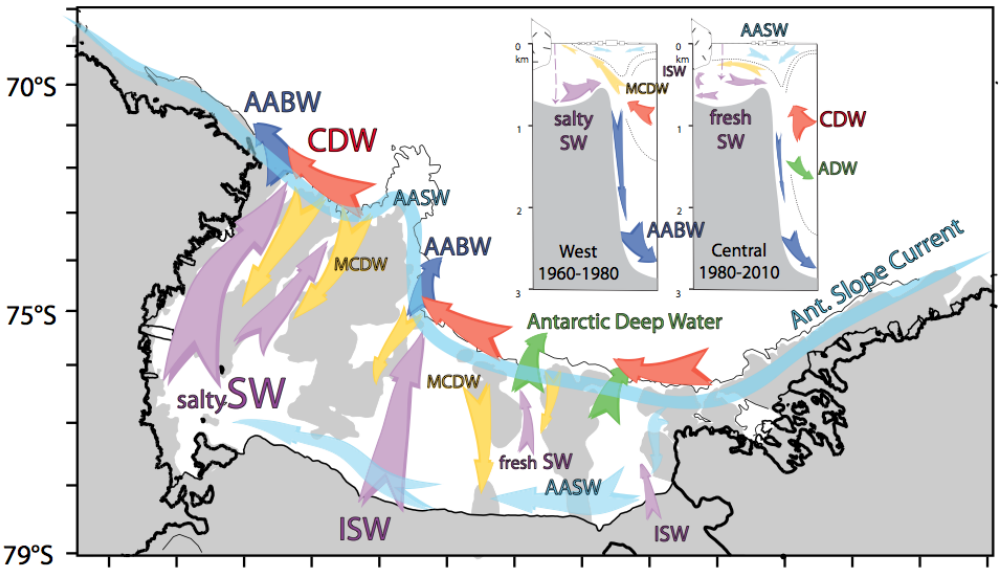

Figure 1.7: Schematic of the Ross shelf sea oceanography. AABW-Antarctic Bottom Water, AASW-Antarctic Surface Waters, CDW-Circumpolar Deep Water, ISW - Ice Shelf Water, MCDW-Modified Circumpolar Deep Water, SW - Shelf Water. Taken from *Smith et al.* (2012b)

Modelling studies have demonstrated that the variability in Ross shelf water properties are probably dominated by changes occurring upstream in the Amundsen Sea (*Assmann et al.*, 2005; *Assmann and Timmermann*, 2005). The increased input of freshwater from the accelerating and thinning ice shelves fringing the Amundsen Sea (*Rignot et al.*, 2008; *Shepherd et al.*, 2012; *Pritchard et al.*, 2012; *Depoorter et al.*, 2013; *Rignot et al.*, 2013) is strongly implicated in this freshening, as discussed in more detail in the following section (Sect. 1.1.7). The potential contribution from changes in sea ice and net precipitation is still relatively unknown, however (*Jacobs and Giulivi*, 2010). Sea ice driven changes in shelf water properties are thought to provide only a negligible direct impact on the salinity of AABW (*Toggweiler and Samuels*, 1995). However, changes in the properties of the shelf waters, such as the freshening of HSSW, are expected to have a strong impact on the mixing processes that generate AABW north of the continental shelf break (described earlier in Sects. 1.1.1 and 1.1.2), indirectly affecting the

salinity, temperature and volume of AABW.

A freshening has also been observed in the northwestern Weddell shelf, however only a few years of data exist over a shorter (1989–2006) time-period (*Hellmer et al.*, 2011). The reasons for this freshening are similarly unclear, however increased precipitation, a southward sea ice retreat and the freshwater flux from the collapse of Larsen A and B and the continued melting of Larsen C have all been proposed (*Hellmer et al.*, 2011). Only a few years of data have been collected within the HSSW forming region (along the Ronne ice front) of the Weddell Sea (*Nicholls et al.*, 2003), limiting a comparison to the freshening of HSSW in the Ross.

The waters leading into the Amundsen Sea Embayment are potentially getting warmer and saltier, which could be due to either a change in the winds, driving more CDW on to the shelf, or a change in the properties of the CDW flooding on to the shelf (*Jacobs et al.*, 2011). Pine Island Glacier (PIG) has seen a substantial increase in basal melt over recent years, although this is thought to be driven more by a stronger circulation of CDW within the cavity as opposed to the small increase in local CDW temperature (*Jacobs et al.*, 2011).

The West Antarctic Peninsula (WAP) lies further east of the area we define as the Bellingshausen shelf sea, however, this has been another well sampled oceanic region due to the location of research stations nearby, providing a further case-study to understand the potential cause of shelf sea changes. The upper ocean adjacent to the WAP has warmed by more than 1°C and increased in salinity by 0.25 from 1951 to 1994 (*Meredith and King*, 2005). *Martinson et al.* (2008) demonstrated that the heat content of UCDW being delivered to the WAP has increased in recent years. Unfortunately no long-term measurements have been taken further west in the central Bellingshausen shelf sea.

Only recently have attempts been made to understand the potential evolution of the Antarctic shelf seas over the coming decades. A recent sea ice-ocean-ice shelf modelling study of the Weddell Sea has demonstrated under a strong climate warming scenario the potential redirection of the westward flowing coastal current into the Weddell shelf; increasing the influx of warm waters, resulting in significant melting of the FRIS over the coming century (*Hellmer et al.*, 2012). Such drastic changes in the shelf seas could significantly alter HSSW/AABW

formation and could also provide a significant rise in sea levels over the coming century. A similar study has demonstrated significant shelf sea freshening and rapid melting of several other ice shelves around Antarctica under a similar, strong climate warming scenario (*Timmermann and Hellmer*, 2013).

1.1.7 Antarctic land ice

The Antarctic Ice Sheet is the largest single mass of ice on Earth, containing enough water to raise sea levels by some 58 m (*Fretwell et al.*, 2013). The ice sheet is in a continual state of flux, with fast flowing ice streams draining around 80% of the grounded ice into the ocean through its fringing ice shelves (*Pritchard et al.*, 2012), the floating extension of the ice sheet (as demonstrated by Fig. 1 in *Rignot et al.*, 2011). The loss of grounded ice to the ocean is nearly balanced by precipitation (snowfall) onto the ice sheet surface, where it compacts to form new ice.

Ice shelves gain mass through (grounded) glacier inflow, surface accumulation, or basal freezing of marine ice; and they lose mass through basal melting, iceberg calving, or top-surface sublimation/ablation. This makes them vulnerable to both atmospheric and oceanic conditions (e.g. *Pritchard et al.*, 2012; *Rignot et al.*, 2013). Recent studies have shown that ocean driven basal melting is dominating the mass export of Antarctic ice shelves (*Pritchard et al.*, 2012; *Depoorter et al.*, 2013; *Rignot et al.*, 2013), as shown in Fig. 1.8 from (*Rignot et al.*, 2013). The variability in the presence of warm CDW in the AB seas has been strongly implicated in the rapid basal melting of ice shelves fringing both seas (e.g. *Shepherd et al.*, 2004; *Holland et al.*, 2010; *Jacobs et al.*, 2011; *Fricker and Padman*, 2012; *Pritchard et al.*, 2012; *Rignot et al.*, 2013). Pine Island Glacier, especially, is thinning faster than any other ice shelf surrounding Antarctica (*Rignot and Jacobs*, 2002), due to a local feedback between basal melt and a rapid retreat of the grounding line (*Payne et al.*, 2004; *Wingham et al.*, 2009), leading to greater CDW circulation within the cavity (*Jacobs et al.*, 2011). The potential for the rapid thinning and acceleration of PIG (and the nearby Thwaites Glacier), led to the idea of this small region being the 'weak underbelly' of the West Antarctic Ice Sheet (WAIS) (*Hughes*, 1981).

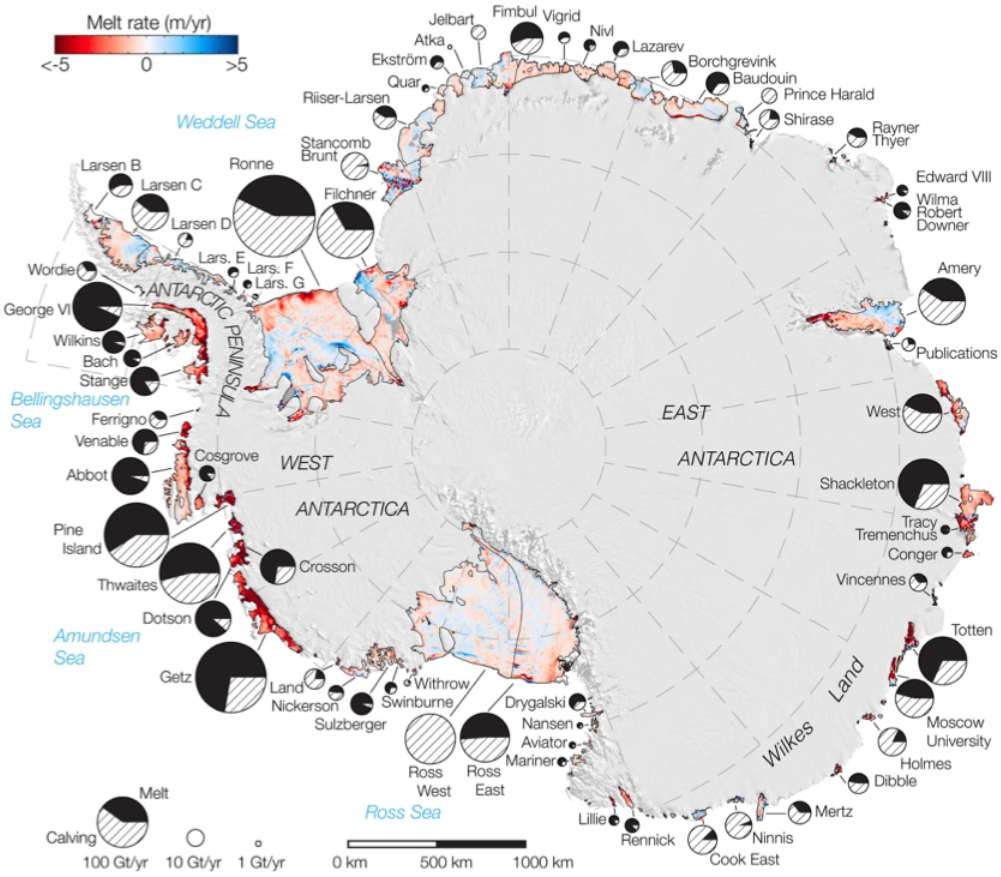

Figure 1.8: Basal melt rates and mass loss of Antarctic Ice Shelves. The colours represent the ice shelf basal melt rate (in m/yr where negative (red) values denotes ice shelf melt), while the circles represent ice shelf mass loss and are proportional in area to the total annual mass loss. Each circle is partitioned to represent the mass loss contribution from iceberg calving (hatch) and basal melt (black). Taken from *Rignot et al.* (2013).

The ice shelves fringing the AIS are out of balance, and are thinning at an estimated rate of 285 $\pm$ 50 Gt yr^{-1} between 2003-2008 (*Rignot et al.*, 2013; *Depoorter et al.*, 2013). The estimated thinning of ice shelves fringing the Amundsen Sea (160 $\pm$ 30 Gt yr^{-1}), provides roughly half of the total ice shelf imbalance, despite accounting for only 8% of the total ice shelf area (*Depoorter et al.*, 2013; *Rignot et al.*, 2013). This thinning and retreat is also thought to result in the accelerated flow of glacial ice into the ocean through reduced ice shelf buttressing (*Dupont and Alley*, 2005; *Rignot et al.*, 2008).

The WAIS is estimated to have lost (out of balance) 85 $\pm$ 22 Gt yr^{-1} (1 Gt = 10^{12} kg) of

its grounded ice between 2000 and 2011 (*Shepherd et al.*, 2012). This is similar to the total loss of grounded ice from the entire AIS, where a small mass loss from the Antarctic Peninsula balances roughly the small mass gain over East Antarctica (*Shepherd et al.*, 2012). The extent to which precipitation changes are reflected in the WAIS mass loss is unclear, however the thinning and acceleration of the fringing WAIS ice shelves makes it likely that the increased flow of previously grounded ice to the ocean is dominating the imbalance.

This large increase in the input of fresh glacial meltwater to the Amundsen Sea has been strongly implicated in the observed freshening of the Ross Sea (as discussed in Sect. 1.1.6), through the freshening of the westward flowing Antarctic coastal current (*Jacobs and Giulivi*, 2010). While the annual basal mass loss from the ice shelves fringing the Bellingshausen Sea (especially George VI) is comparable to the ice shelves fringing the Amundsen Sea, the thinning is estimated to be considerably lower (49 ± 22 Gt yr^{-1} *Depoorter et al.*, 2013; *Rignot et al.*, 2013), due to a stronger annual ice shelf mass gain (through processes mentioned earlier). This implies a smaller increase in the fresh meltwater input to the Bellingshausen Sea in recent years. The melt rate of the FRIS in the Weddell Sea shows strong spatial variability (regions of basal melting and freezing), however, it is still estimated to be thinning by 60 ± 23 Gt yr^{-1}, due in part to its considerably larger area (*Rignot et al.*, 2013). The RIS, despite being similar in size to FRIS, appears to be roughly in-balance (0 ± 5 Gt yr^{-1} *Depoorter et al.*, 2013; *Rignot et al.*, 2013). These estimated thinning rates are obtained using a relatively short (5-year) time-series. Increased temporal data-coverage and improved accuracy in the estimations are needed to provide a more accurate understanding of the mass loss from the AIS.

1.1.8 Southern Ocean trends

Significant changes have also been observed in the deep Southern Ocean, north of the shelf break. AABW, the coldest and densest water mass in the Southern Ocean (*Orsi et al.*, 1999), has warmed (*Meredith et al.*, 2008; *Purkey and Johnson*, 2010; *Meredith et al.*, 2011; *Purkey and Johnson*, 2013), freshened (*Aoki et al.*, 2005; *Rintoul*, 2007; *Johnson*, 2008; *Jacobs and Giulivi*, 2010; *Jullion et al.*, 2013; *Purkey and Johnson*, 2013) and contracted (*Purkey and Johnson*, 2012)

in recent decades, resulting in the potential slowdown of the Global Overturning Circulation (*Purkey and Johnson*, 2012). The freshening appears strongest in the southern AABW, with no observed freshening in the older AABW further north, suggesting this could be a relatively recent trend (*Purkey and Johnson*, 2013). *Purkey and Johnson* (2013) also find the strongest freshening in the Amundsen and Bellingshausen Basin and Australian-Antarctic Basin, with the Weddell Basin freshening the least, adding weight to the freshening source being the accelerating increase in glacial meltwater from WAIS and the freshening of the Ross HSSW as described in the previous sections.

The warming of the WSDW and AABW leaving the Weddell Sea (*Meredith et al.*, 2008, 2011) has been linked to changes in the strength of the Weddell Gyre. A warming of WDW, a major source of AABW formation that resides within the Weddell Gyre, was observed during the 1990s, however this was followed by a cooling in the 2000s (*Robertson et al.*, 2002; *Fahrbach et al.*, 2004; *Meredith et al.*, 2008). Changes in the WDW have also been linked to changes in atmospheric circulation patterns, changing the inflow of CDW into the Weddell Gyre and thus the resulting production of WDW (*Fahrbach et al.*, 2011).

An increase in the strength of the westerly winds circumnavigating Antarctica (linked to the positive trend in the Southern Annular Mode, described later in Sect. 1.3.2) is thought to result in: a stronger ACC transport (*Meredith et al.*, 2004b), a poleward shift in the ACC (e.g. *Gille*, 2008), and/or increased eddy activity within the ACC (*Meredith and Hogg*, 2006; *Hogg et al.*, 2008; *Boning et al.*, 2008), potentially increasing the poleward heat flux. It has been speculated that this might lead to an increase in the CDW moving onto the Antarctic continental shelf, especially in regions where the CDW is close to the shelf break (e.g. *Jacobs*, 2006). The Southern Ocean has been warming at a faster rate than the global ocean (discussed later in Sect. 1.3), with this warming taking place predominantly within the ACC (*Gille*, 2002).

1.2 Antarctic Sea Ice

The sea ice present in the polar regions covers between 3.4–4.6% of the Earth's surface (between 17.5–28.5×10^6 km^2) at any given time (*Comiso*, 2010). Antarctic sea ice forms during (austral) autumn and winter (∼April–September), extending northwards over much of the Southern Ocean. The current Antarctic sea ice extent peaks at around 18.5×10^6 km^2 (in September) and drops to a minimum of around 3.1×10^6 km^2 (in February) (*Parkinson and Cavalieri*, 2012). The mean (1979-2011) summer (January–March) and winter (July–September) ice concentration is shown in Fig. 3.3.

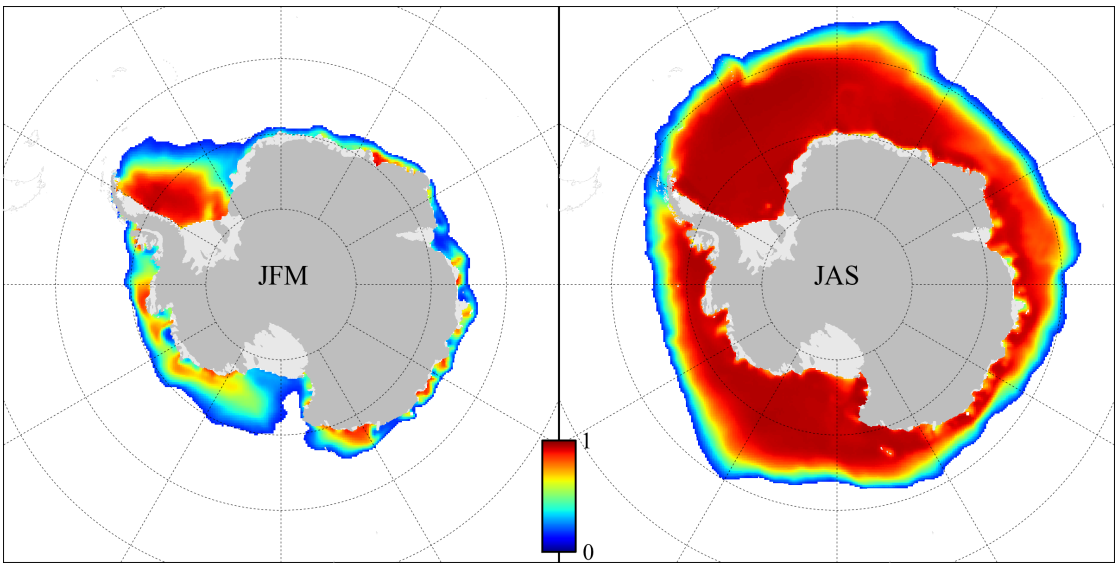

Figure 1.9: Mean (1979-2011) Antarctic sea ice concentration in summer (JFM) and winter (JAS), from passive microwave observations using from the NASA Bootstrap algorithm (*Comiso*, 1999, updated 2012). Sea ice concentrations less than 0.15 are masked.

1.2.1 Sea ice formation

Sea ice formation is a complex, multi-phase process, depending on a number of environmental factors. As sea ice plays such a fundamental role in the discussions contained throughout the thesis, a brief overview of the main stages of sea ice growth is given (for a more detailed description, see e.g. *Wadhams*, 2000).

As the ocean surface temperature falls below the salinity dependent freezing temperature of sea water (∼-1.9°C), small (mm) sized crystals of ice form, known as frazil ice. The resultant behaviour of these frazil ice crystals depends on the ocean surface conditions.

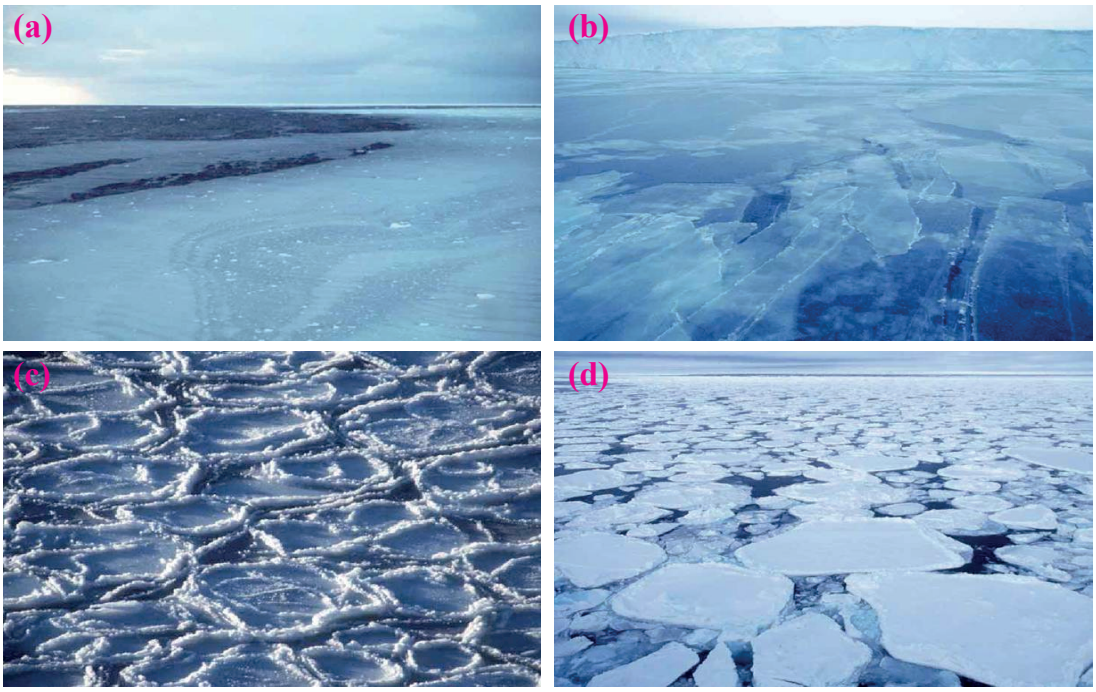

Figure 1.10: Different stages of sea ice formation. (a) Frazil ice, (b) nilas, (c) pancake ice, (d) first year ice. Images are taken from *Worby* (1999).

In calm waters, the frazil crystals rise to the surface as they increase in size and become more buoyant, producing a 'soupy' layer of frazil crystals at the surface (Fig. 1.10a), known as grease ice (so called due to its minimal light reflectance and therefore oily appearance). This soupy layer of frazil crystals then develops into a continuous sheet of ice covering the surface, known as nilas (Fig. 1.10b). The ice continues to thicken (up to several metres thick) as ice freezes onto the underside of the existing ice layer (congelation growth).

In more turbulent waters, the frazil crystals accumulate into discs of ice $O(10$ cm), known as pancake ice (due to their resemblance to pancakes, see Fig. 1.10c). These discs grow in size (up to several metres in diameter) through continuous frazil ice production, until they coalesce into large ice floes (several metres thick and up to several kilometres in diameter), forming

the signature appearance of first year ice formed in turbulent waters (Fig. 1.10d). Due to the turbulent nature of the Southern Ocean, this process is thought to dominate Antarctic sea ice growth.

Frazil ice consists of crystals of pure ice, meaning salt is expelled as the ice forms from the salty seawater. As the frazil crystals grow and bind together, some of the salty water (brine) fills the gaps between the crystals, meaning some salt is retained within the sea ice. For this reason, sea ice can be thought of as a two-phase, two-component, reactive porous medium, known as a mushy layer (*Feltham et al.*, 2006). The brine is removed from sea ice (desalination) through a variety of different mechanisms, including: salt diffusion, brine expulsion, gravity drainage, and flushing with surface meltwater, as first described by *Untersteiner* (1968), with gravity drainage and surface meltwater flushing thought to be the dominant processes of desalination (*Notz and Worster*, 2009). The salinity of sea ice is therefore thought to vary both as a function of time and the vertical depth within the sea ice layer. It is worth noting, however, that climate models tend to employ either an average 'bulk' salinity (often taken to be around 5, as used in the idealised sea ice model of Chapter 2), or a vertical salinity profile within the ice that does not change with time (such as the approach taken by CICE (v4.1), the sea ice model used in Chapters 3 and 4). Sea ice climate model components (including CICE) are now starting to incorporate time-dependent sea ice salinity parameterisations that represent the processes (mainly gravity drainage) discussed above (e.g. *Turner et al.*, 2013a).

As the salinity of sea ice is less than the salinity of the seawater it forms from, sea ice growth leads to an increase in the salinity of the ocean surface layer, through this net extraction of freshwater. Sea ice formation therefore provides a strong seasonal influence on the ocean as the surface salinates during sea ice growth (providing a negative buoyancy flux), and freshens during the respective melt as the sea ice returns the stored freshwater back to the ocean (providing a positive buoyancy flux). This process of negative and positive buoyancy fluxes, and its impact on the evolution of the ocean surface mixed layer, provides much of the discussion contained within this thesis.

As well as this ocean surface buoyancy forcing, sea ice is climatically important for several

other reasons. The presence of solid ice means that the heat transfer between the ocean and atmosphere is by thermal conduction (thermal conductivity of sea ice is salinity and temperature dependent but $\sim$2 W $m^{-1}K^{-1}$) as opposed to turbulent flow-induced heat fluxes (latent and sensible heat). This slows the heat transfer to the atmosphere; insulating the ocean from the cold polar atmosphere, where temperatures over the Antarctic sea ice can reach as low as -25°C in the austral winter (*Comiso*, 1994). The thermal conductivity of the snow that collects on sea ice is an order of magnitude lower at $\sim$0.3 W $m^{-1}K^{-1}$, (with even lower values suggested based on in-situ measurements (e.g. *Massom et al.*, 1997)), meaning snow that collects on sea ice will have a much stronger insulating effect. The sea ice, and the snow cover over sea ice, are also important due to their high albedo (how much solar radiation is reflected back into the atmosphere). The sea ice albedo-feedback mechanism, whereby a reduced sea ice cover enables the ocean to absorb more heat, resulting in additional sea ice melt, is thought to play an important role in the rapid decline of the Arctic sea ice cover (e.g. *Holland et al.*, 2006). Sea ice also plays a crucial role in the Southern Ocean uptake of CO_2 (e.g. *Takahashi et al.*, 2009), and provides a vital habitat for marine organisms (e.g. *Thomas and Dieckmann*, 2002).

1.2.2 Antarctic sea ice trends

While the Arctic sea ice cover has decreased in extent (-52×10^3 km^2y^{-1} or $\sim -4\%$ dec^{-1} for 1979-2010) over recent decades (*Parkinson et al.*, 1999; *Cavalieri et al.*, 2003; *Comiso and Nishio*, 2008; *Stroeve et al.*, 2012; *Cavalieri and Parkinson*, 2012), Antarctic sea ice has shown a smaller (magnitude) increase ($+17.5\times10^3$ km^2y^{-1} or $\sim+1.5\%$ dec^{-1}) over the same time period (*Zwally et al.*, 2002; *Comiso and Nishio*, 2008; *Turner et al.*, 2009; *Parkinson and Cavalieri*, 2012). This small increase in ice extent is the sum of stronger, but opposing regional trends, including a significant increase ($\sim+5\%$ dec^{-1}) in the Ross Sea, and a significant decrease ($\sim -5\%$ dec^{-1}) in the AB seas (*Parkinson and Cavalieri*, 2012). The Antarctic sea ice trends can also be viewed in terms of regional changes in the duration of the ice season, including a $\sim$2-3 months shorter ice-season in the AB seas, and $\sim$2 months longer ice season in the Ross Sea (*Stammerjohn et al.*, 2012). The regional pattern in ice concentration trends is similar to ice extent, with the observed

trends in the annual Antarctic ice concentration derived from passive microwave observations using the NASA Bootstrap algorithm (*Comiso*, 1999, updated 2012) shown in Fig. 1.11.

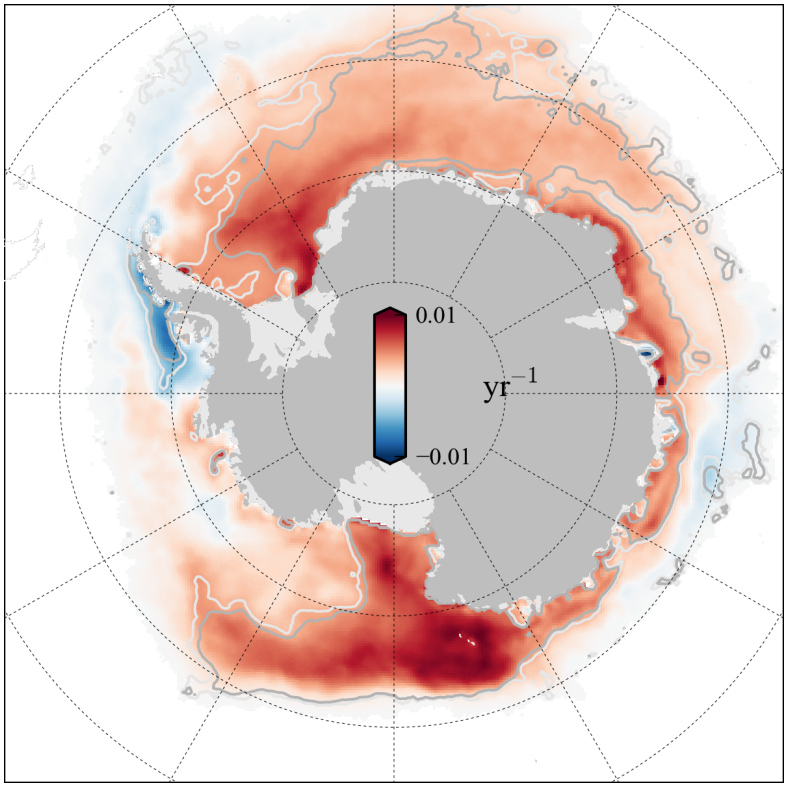

Figure 1.11: 1979-2011 linear trends (annual mean) in Antarctic sea ice concentration derived from passive microwave observations using from the NASA Bootstrap algorithm (*Comiso*, 1999, updated 2012). Significance contours are indicated by the white (90%) and grey (95%) lines.

It is currently unclear what is causing the overall increase in sea ice extent. Various forced mechanisms have been proposed, such as increased ocean stratification and reduced vertical heat flux due to: atmospheric/ocean warming slowing sea ice growth (*Zhang*, 2007); increased glacial meltwater (*Bintanja et al.*, 2013); and increased precipitation (*Liu and Curry*, 2010) (with increased snowfall providing a further potential impact through enhanced insulation). Dynamical mechanisms have also been proposed, including ozone driven changes in the near-surface winds and thus ice motion (*Turner et al.*, 2009).

The regional changes in Antarctic ice concentration have recently been shown to be driven by regional trends in the near-surface winds (*Holland and Kwok*, 2012, and Fig. 1.12 taken from

their study). The physical cause of the wind trends is still relatively unknown, however they have been linked to both the Southern Annular Mode (SAM) and El Nino-Southern Oscillation (ENSO) (*Hall and Visbeck*, 2002; *Kwok and Comiso*, 2002; *Lefebvre et al.*, 2004; *Liu et al.*, 2004; *Yuan and Li*, 2008; *Stammerjohn et al.*, 2008), which are discussed in more detail in the following section.

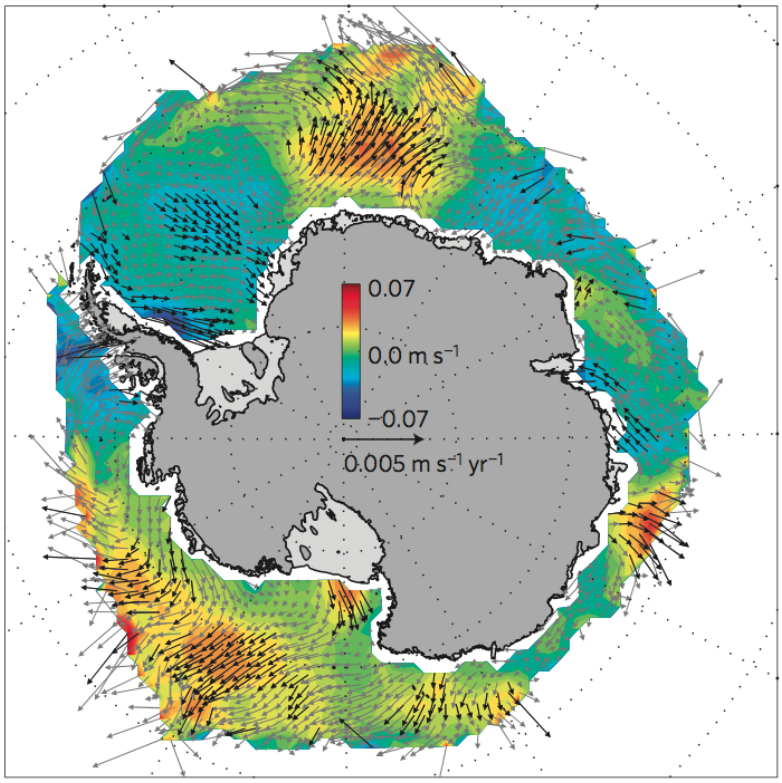

Figure 1.12: 1992-2010 linear trends (April-October mean) in sea ice motion derived from passive microwave feature-tracking. Sea ice motion trend vectors are overlaid on the 19-year change in meridional sea ice speed (positive northwards). Black vectors indicate the meridional trend is significant at 90%. Taken from (*Holland and Kwok*, 2012).

Climate models, however, have consistently predicted a decline in Antarctic sea ice extent, despite the observed increase (*Eisenman et al.*, 2011; *Turner et al.*, 2013b). *Bitz et al.* (2006) demonstrate a decrease in sea ice in response to an increase in greenhouse gases (GHG), while *Sigmond and Fyfe* (2010) and *Bitz and Polvani* (2012) show a decline in response to ozone depletion. Several recent studies have suggested that the observed increase is within the range of natural variability, although towards the more unlikely end of the distribution (*Mahlstein*

et al., 2013; *Polvani and Smith*, 2013; *Swart and Fyfe*, 2013). These results are circumpolar however (i.e. they do not simulate the strong regional trends), and rely on correct representation of natural variability within current current climate models, which is unlikely to be the case (*Turner et al.*, 2013b; *Zunz et al.*, 2013). Over longer time-scales, continued increases in GHGs are expected to cause a decrease in Antarctic sea ice, mitigated to some degree by the recovery of the ozone hole (*Smith et al.*, 2012a).

In addition to its ice area loss, the Arctic has also undergone a rapid thinning over recent decades (*Giles et al.*, 2008; *Kwok and Rothrock*, 2009; *Laxon et al.*, 2013). Unfortunately, Antarctic ice thickness is poorly sampled both temporally and spatially (*Worby et al.*, 2008), with Radar altimetry measurements unreliable in the Antarctic, due to variable snow penetration and poor knowledge of the snow thickness (*Giles et al.*, 2008). Recent studies have used the assumption that the ice snow boundary is at the sea-level to estimate a mean ice thickness (*Kurtz and Markus*, 2012), however only recent years exist, with large uncertainties. The only current method of estimating Antarctic sea ice thickness trends is therefore through modelling studies (e.g. *Holland et al.*, submitted; *Massonnet et al.*, 2013), which show regionally variable patterns in the ice thickness trends, similar to ice concentration. A more detailed description and comparison of these trends is given in Chapter 4 (Sect. 4.3.3).

1.3 Variability and Trends in the Antarctic Climate

1.3.1 Global climate trends

The Earth's climate has warmed by around 0.8°C since the later half of the 19th century (*IPCC*, 2013), due to an increase in radiative forcing. This increase (over half of that observed) is *extremely likely* (>99% confidence) to be due to human (anthropogenic) activities (e.g. through increased GHG emissions) (*IPCC*, 2013). This rapid surface temperature increase is unprecedented during the current (holocene) interglacial (as shown in Fig. 1.13, taken from *Marcott et al.*, 2013).

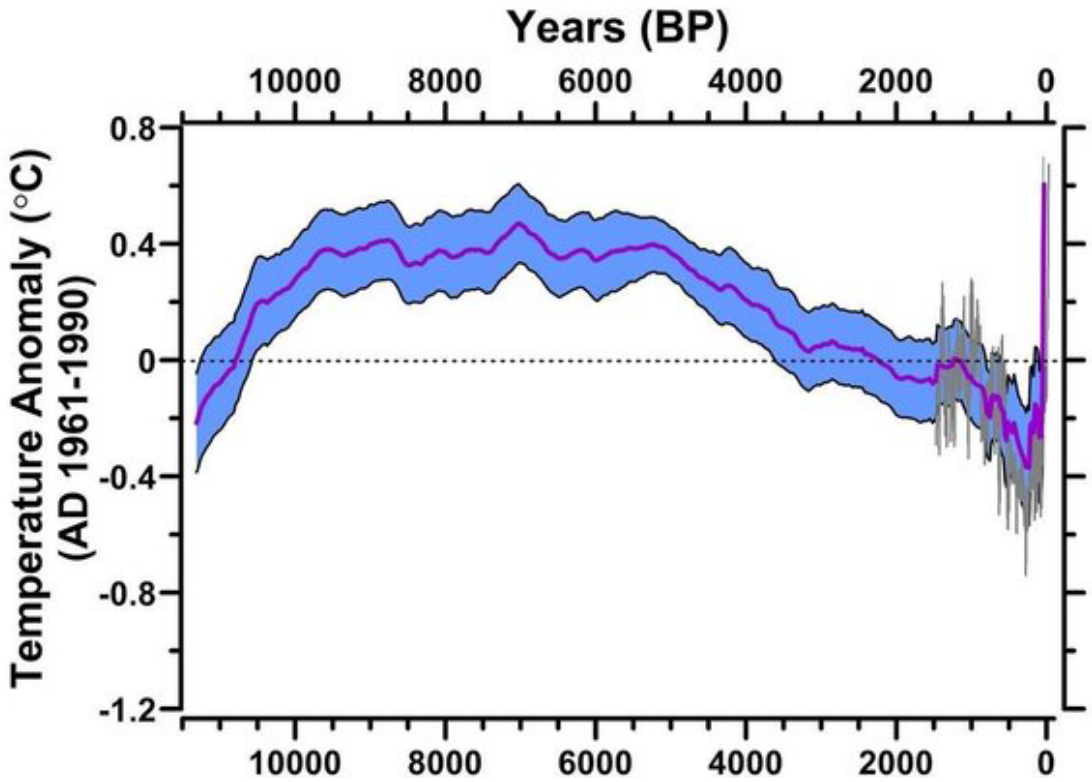

Figure 1.13: Land surface temperature reconstruction for the current (Holocene) interglacial from globally stacked temperature anomalies for the $5° \times 5°$ area-weighted mean calculation (purple line) with the 1σ uncertainty highlighted by the blue band. The *Mann et al.* (2008) CRU-EIC reconstruction over the past 1500 years is also shown (dark gray line) with this uncertainty highlighted by the light gray band. Taken from (*Marcott et al.*, 2013).

The surface temperature increase only reveals a small part of the potential climate warming, as the Earth's oceans have absorbed around 93% of the extra heat energy from this increased radiative forcing since the 1950s, as revealed by direct measurements of the ocean heat content using Argo floats (*Levitus et al.*, 2000, 2005, 2012). The small remaining fraction of this excess energy has also been used to melt the Arctic sea ice and land ice (mountain glaciers and the polar ice sheets), and warm the atmosphere and land surface (where only this last contribution is factored into the 0.8°C increase). The Earth's oceans are therefore expected to play the leading role in regulating the observed impact of anthropogenic climate change.

Despite this significant global warming, stratospheric ozone depletion is thought to have dominated southern hemisphere atmospheric circulation changes during the second half of the

20th Century (*Polvani et al.*, 2010; *Thompson et al.*, 2011). First discovered in the 1980s, a significant 'ozone hole' currently forms every spring over Antarctica (*Farman et al.*, 1985), coinciding with the return of sunlight to the cold polar stratosphere. The ozone hole refers to the breakdown of ozone (O_3) from reactions with chlorine and bromine free-radicals, (primarily) on the surface of polar stratospheric clouds, which form over the poles (but particularly the south pole) during winter (WMO, 2010). The free-radicals are produced from the photochemical breakdown of primarily anthropogenic chlorofluorocarbons (CFCs) and halons (to a lesser extent). While the emission of CFCs has reduced dramatically over the past few decades after the signing of the Montreal Protocol in 1987, the long life-time of the compounds means full recovery of the ozone hole is expected to take several more decades.

1.3.2 Antarctic climate variability

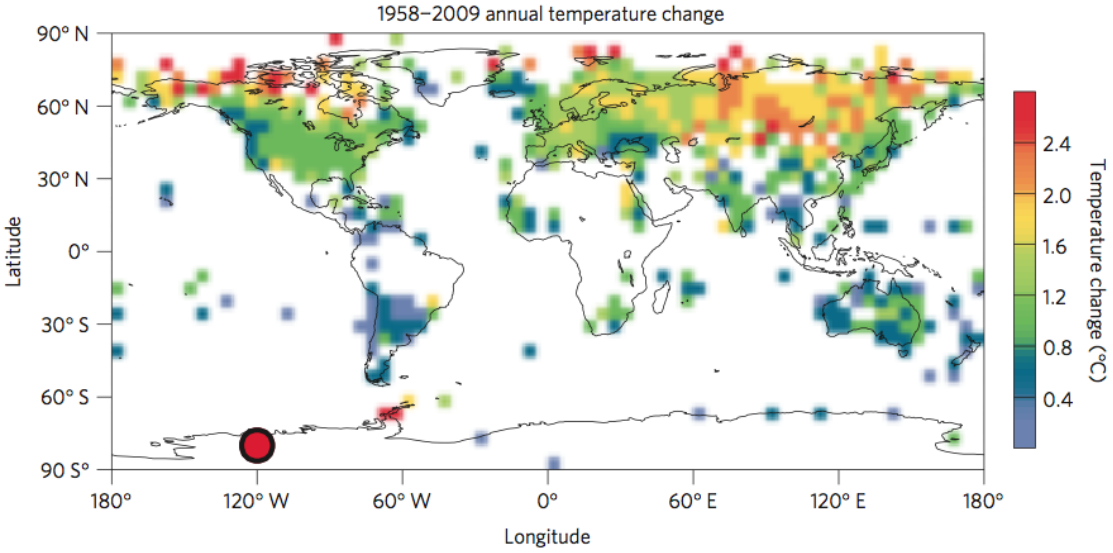

Figure 1.14: (1958-2009 linear trends in land surface temperature trends (annual mean) from Byrd Station, central West Antarctica (highlighted by the circle), and from the global CRUTEM4 dataset (*Jones et al.*, 2012). Taken from (*Bromwich et al.*, 2013).

Direct observations show that West Antarctica is warming faster than any other region on Earth, including significant warming over central West Antarctica (0.47 ± 0.23°C dec^{-1} *Bromwich et al.*, 2013) and the Antarctic Peninsula (0.56 ± 0.43°C dec^{-1} *Vaughan et al.*, 2003; *Turner et al.*,

2005), as shown in Fig. 1.14 from *Bromwich et al.* (2013). Satellite infrared radiometer data provide surface (or 'skin') temperature data for the entire Antarctic domain (*Comiso*, 2000), with the annual mean linear trend (1982-2008) shown in Fig. 1.15. This temperature trend compares well with the directly observed warming trends, and shows wide-scale significant warming over the AB seas and a cooling over the eastern and northern Ross Sea.

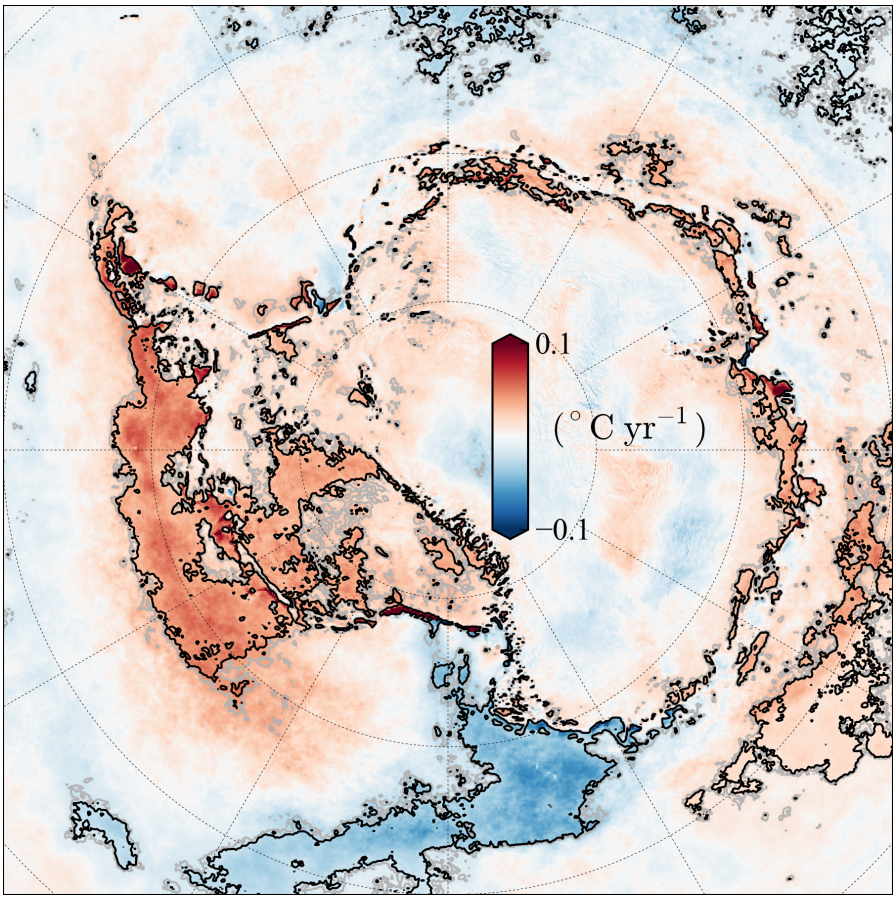

Figure 1.15: 1982-2008 linear trends (annual mean) in surface temperature, derived from satellite infrared radiometer data (*Comiso*, 2000). Significance contours are indicated by the grey (90%) and black (95%) lines.

Climate variability is mainly described using specific climate modes (a more detailed overview is given by the *IPCC*, 2007). These climate modes are quantified using an appropriate climate index, often based on differences in sea-level pressure (SLP) (or similar quantities such as geopotential height) between specific regions or latitudinal bands. Antarctic climate variability is dominated by the Southern Annular Mode (SAM) (*Thompson and Wallace*, 2000;

Marshall, 2003). The SAM index most commonly used is based on the difference between the observed difference in the zonal-mean sea level pressure (MSLP) between 40°S (mid-lattidues) and 65°S (Antarctic) (*Marshall*, 2003), as depicted in Fig. 1.16.

Antarctic climate variability has also been shown to respond to the two Pacific-South American (PSA) climate modes, associated with the El Niño Southern Oscillation (ENSO) (*Fogt and Bromwich*, 2006). The Southern Oscillation Index (SOI) describes the atmospheric response to El-Niño, where El-Niño refers to anomalous sea-surface warming in the Pacific ocean (as described in more detail by *Trenberth*, 1997), and is calculated (predominantly) using the difference in SLP between Darwin and Tahiti (*Ropelewski and Jones*, 1987).

The SAM has shifted towards a more positive polarity (decreased Antarctic MSLP and increased mid-latitude MSLP) in recent decades (as shown in Fig. 1.16), with the seasonal SAM increase significant in the austral summer and autumn (*Marshall et al.*, 2004). This trend has been linked to a combination of both stratospheric ozone depletion and increases in GHGs (*Thompson and Solomon*, 2002; *Gillett and Thompson*, 2003; *Marshall et al.*, 2004; *Shindell and Schmidt*, 2004; *Fyfe and Saenko*, 2005; *Arblaster and Meehl*, 2006; *Turner et al.*, 2009; *Thompson et al.*, 2011). Note that although the ozone hole occurs in the austral spring, the impact on the tropospheric flow is greatest during summer and autumn (*Turner et al.*, 2009).

A trend towards a more positive SAM should lead to an overall cooling of the Antarctic from increased isolation, and a strengthening of the westerly winds circumnavigating Antarctica (*Marshall*, 2002; *Thompson and Solomon*, 2002), linked to the ACC changes described earlier (Sect. 1.1.8). The SAM is also associated with a secondary zonal wave-number 3 pressure pattern, however, which produces low pressures centered in the AB seas, with the resultant meridional wind trends advecting warmer air towards the Antarctic Peninsula (*Marshall*, 2002; *Kwok and Comiso*, 2002; *Lefebvre et al.*, 2004; *Marshall et al.*, 2006), which is thought to be a major cause of the significant warming observed in the region (*Vaughan et al.*, 2003; *Turner et al.*, 2005). It has been suggested that this zonally asymmetric response is due to the potential influence of zonal asymmetries in the Antarctic landmass distribution (*Thompson and Solomon*, 2002; *Lefebvre et al.*, 2004), however this is still relatively unknown.

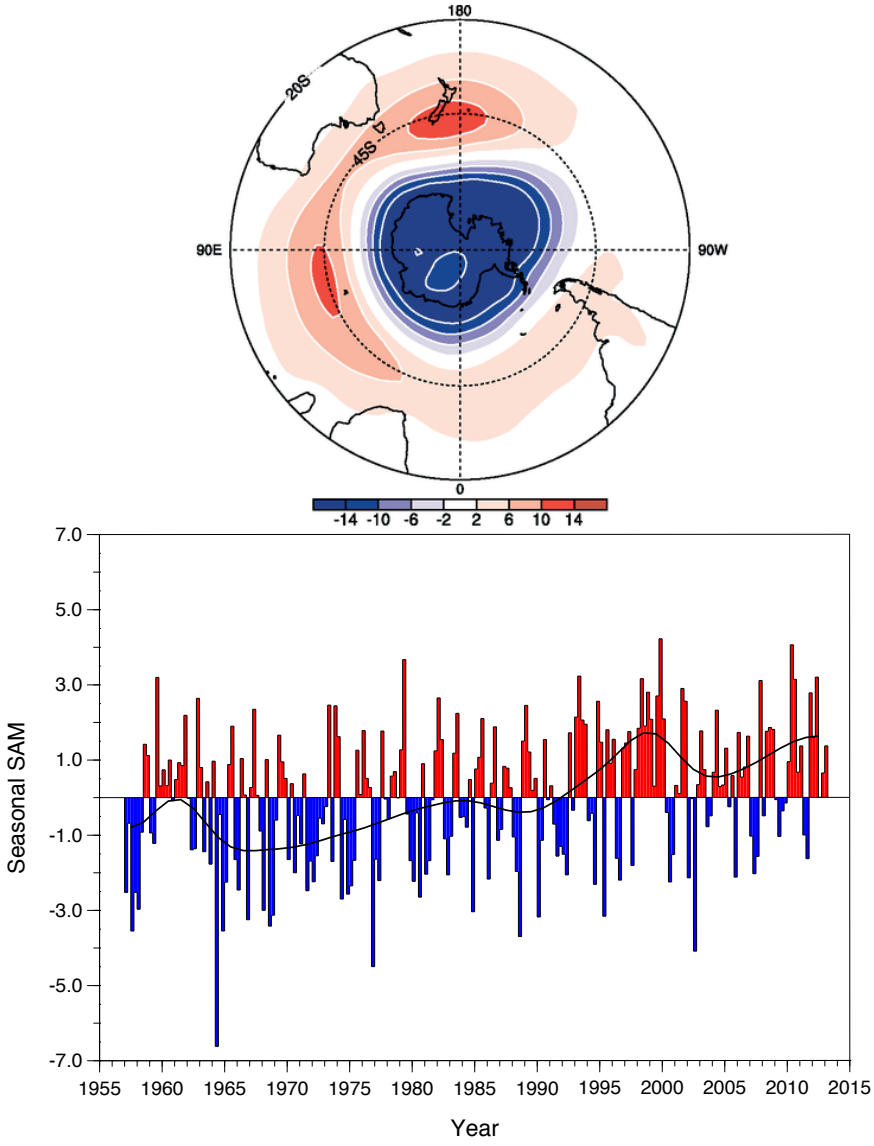

Figure 1.16: (Top) The Southern Annular Mode (SAM) geopotential height pattern as a regression based on the SAM time series for seasonal anomalies at 850 hPa. (Bottom) The SAM index from http://www.antarctica.ac.uk/met/gjma/sam.html. Updated from Fig. 3.32 from the (*IPCC*, 2007).

There is no significant trend in the winter or spring SAM index in the past 30 years, however large changes are still observed in the Antarctic sea ice (*Comiso and Nishio*, 2008), as well as significant warming over West Antarctica (*Comiso*, 2000; *Steig et al.*, 2009; *Bromwich et al.*, 2013) during these seasons. The winter/spring warming trends have been linked to ozone

depletion (*Turner et al.*, 2009; *Bitz and Polvani*, 2012) and changes in tropical Pacific sea-surface temperatures, which are linked to the El-Niño through a Rossby wave train (*Turner*, 2004; *Ding et al.*, 2011, 2012; *Schneider et al.*, 2012).

An increase in the ENSO and SAM covariance has potentially led to an increased atmospheric response to ENSO around Antarctica in recent decades (during spring/summer) (*Fogt and Bromwich*, 2006; *Stammerjohn et al.*, 2008; *Fogt et al.*, 2011). However, there is no significant trend in the SOI or other indices of the main ENSO region (that is, the eastern tropical Pacific), suggesting at most a weak contribution to the recent warming trends.

Modelling studies have indicated a continued positive SAM trend in the coming decades (*Miller et al.*, 2006), however others have suggested the recovery of the ozone hole will reduce the strengthening of the westerlies and could, in-fact, reverse the change in summer, the season of significant SAM increase over recent decades (*Perlwitz et al.*, 2008; *Son et al.*, 2008). Understanding the impact of continued greenhouse gas emissions on the SAM is still a remaining area of uncertainty in future Antarctic climate predictions. Over the next few decades, the impacts of ozone recovery and increasing greenhouse gases on the SAM could balance out during summer, although increasing greenhouse gases could still drive a positive SAM trend across all other seasons (*Thompson et al.*, 2011).

1.3.2.1 Sea level rise from Antarctica

Global sea levels have risen by around 3 mm yr^{-1} in recent decades (e.g. *Church and White*, 2011). Of this increase, around 1.1 mm yr^{-1} is thought to be due to a thermal expansion of the ocean and around 0.4 mm yr^{-1} is thought to be due to changes in land water storage (*IPCC*, 2013). The remaining half is therefore thought to be due to an increased input of continental ice from the polar ice sheets and mountain glaciers (*IPCC*, 2013). While precipitation is expected to increase in a warming climate (*Bindoff et al.*, 2007), the net mass loss from the WAIS (as described earlier, in Sect. 1.1.7) is currently thought to be greater than the smaller mass gain due to increased precipitation over East Antarctica (*Shepherd et al.*, 2012), making Antarctica a net contributor to global sea level rise. Note that as the ice shelves are already floating in

the ocean, they only have a small direct impact on global sea-levels through steric effects (ocean cooling/freshening) (*Jenkins and Holland*, 2007). Antarctica is currently contributing around 0.2 mm yr^{-1} to global sea level rise (since 1992), driven primarily though the increased loss of grounded ice from West Antarctica (Greenland is about double this at 0.4 mm yr^{-1}) (*Shepherd et al.*, 2012). Note that the contribution from mountain glaciers is currently estimated to be around 0.8 mm yr^{-1} (*Marzeion et al.*, 2012).

The WAIS is classified as a 'marine ice sheet' as the majority of the ice is grounded below sea level (*Fretwell et al.*, 2013). Much of the WAIS also rests on a reverse bed-slope (whereby the bedrock lowers towards the ice sheet interior), meaning the ice sheet has the potential for a rapid and unstable retreat (e.g. *Schoof*, 2007), increasing the potential for a total collapse of the WAIS (*Mercer*, 1978; *Hughes*, 1981). A collapse of the WAIS would raise sea levels by some 3.3 m (*Bamber et al.*, 2009), with the entire AIS holding enough ice to raise sea levels by some 58 m (*Fretwell et al.*, 2013). A relatively rapid (one to several thousand year) collapse of the WAIS from its maximum glacial extent during warm interglacials has been infered using sedimentary records (*Naish et al.*, 2009) and an ice sheet/ice shelf model (*Pollard and DeConto*, 2009), resulting in several metres of sea level rise. Further research has shown global sea levels were significantly higher (∼3-8 m) during the previous interglacial (∼ 125 thousand years ago), when the atmosphere was several degrees (∼ 3-5°C) warmer than today (*Blanchon et al.*, 2009; *Kopp et al.*, 2009), pointing to a potential future under continued anthropogenic global warming. Some recent evidence points to rapid (∼3-4 m $century^{-1}$) future sea level rise (*Blanchon et al.*, 2009), although slower rates are thought to be considerably more likely (*Kopp et al.*, 2009).

As discussed in Sects. 1.1.4, 1.1.6 and 1.1.7, the ocean, and specifically the temperature of the water masses over the shelf seas, appears to be playing the crucial role in the accelerating ice loss from West Antarctica. A deeper understanding of the processes controlling the formation of waters overlying the CDW is therefore important in understanding future ice loss from the AIS.

1.4 Thesis Aims

Five mechanisms were listed in Sect. 1.1.5 that have been used to explain the apparent bimodal distribution in the temperature of the Antarctic shelf seabed water masses. A primary objective of this thesis is to ***test hypothesis (i), that the bimodal distribution in shelf sea temperature can be explained directly by differing surface fluxes between the warm and cold regions.*** Due to the close proximity of the ACC to the AB shelf seas, this surface driven mechanism has perhaps been overlooked since it was first proposed by *Talbot* in 1988. A secondary objective is to *provide further insight into the impact of the shelf sea properties (temperature and salinity) in controlling the mixed layer deepening*, testing simplistically hypotheses (ii) and (iii). To provide additional insight into the specific controls on shelf water formation, another secondary objective is to *demonstrate the sensitivity of the mixed layer depth to specific atmospheric forcings.* In Chapter 2, an idealised sea ice-mixed layer model is developed and used to investigate these ideas further.

Following on from this broad investigation of the mean state of the shelf seas, an additional primary objective of this thesis is to ***accurately quantify the cause of regional variations in the surface-driven formation of Antarctic shelf sea waters***. There is a clear lack of observational data available within the four shelf seas and the overlying sea ice cover, meaning a modelling approach can provide crucial insight into these climatically important regions. Chapter 3 therefore uses a sophisticated sea ice model (CICE), coupled to a mixed layer model (similar to that used in the idealised study), to analyse the seasonal evolution of the sea ice and mixed layer over the Antarctic continental shelf. Through the use of a sophisticated sea ice model and realistic atmospheric forcing from reanalysis, the model should also *provide reasonable estimates of the mean fields of the annual surface salt/freshwater and heat inputs to the Southern Ocean*, which are important boundary conditions for ocean models, for which accurate observations are currently lacking. The link between specific atmospheric forcings and mixed layer deepening will also be investigated.

The final primary objective of this thesis is to ***investigate the recent and future evo-***

lution of sea ice, the surface inputs of salt/freshwater and heat, and the mixed layer depth over the Antarctic continental shelf. The cause of recently observed changes in the Antarctic shelf seas (Sect. 1.1.6) often points solely to the increasing meltwater input from the WAIS (Sect. 1.1.7). The potential contribution from ocean surface changes (e.g. sea ice and net precipitation) is still relatively uncertain, despite much discussion surrounding the issue. A secondary aim is therefore to *quantify the potential freshening signal from sea ice and net precipitation relative to the increased meltwater input from the WAIS*. The use of long-term atmospheric forcing data (under a moderate warming scenario) can also provide insight into the potential sensitivity of the Antarctic shelf seas to a continuous climate (atmospheric) warming over the coming century. This analysis is carried out in Chapter 4 using the same CICE-mixed layer model as Chapter 3.

A further, more general aim of this thesis is to ***investigate recent and future trends in the Antarctic sea ice cover***. Through the use of a sophisticated sea ice model coupled to a steady, yet realistic deep-ocean, this study can provide further insight into the recent trends in ice concentration and the potential trends in ice thickness driven by atmospheric trends alone. Ice thickness trends will be a particular focus, as this provides a more complete understanding of sea ice changes than concentration alone, and has been an overlooked subject, due predominantly to the lack of observational constraints. The analysis of a long-term climate warming simulation can also be used to demonstrate the potentially more direct response due to increases in GHGs and ozone recovery, placing the recent trends in context.

A key theme throughout this thesis is the focus on surface processes over variable ocean dynamics. Shelf sea oceanography is a crucial element of this complex climate system, however this study uses a simple mixed layer model and a prescribed deep ocean throughout, in order to simplify the results and provide a clearer understanding of the direct impact of surface processes alone in controlling the regional variations in the sea ice and shelf sea properties.

Chapter 2

The Impact of Atmospheric Forcing on Antarctic Continental Shelf Water Masses

> "Everything is on a reduced scale here in the Polar regions; we can't afford to be extravagant."
>
> — Roald Amundsen; *The South Pole*

This chapter presents the idealised sea ice-mixed layer model, used to investigate the bimodal distribution of Antarctic shelf-sea temperature. Section 2.1 describes the idealised sea ice-mixed layer model including a brief justification of the approach taken. Section 2.2 presents results from the idealised model, including various sensitivity studies. Concluding remarks are given in Sect. 2.3.

2.1 Idealised Sea Ice-Mixed Layer Modelling

The principal aim of this chapter is to test hypothesis (i) from Sect. 1.1.5, that the bimodal distribution in the Antarctic shelf-sea temperature can be explained directly by differences in the surface fluxes (atmospheric forcing) between the two regimes. A highly simplified coupled sea

ice-mixed layer model has been constructed to investigate this idea (the model was developed in FORTRAN90 and the source code is available upon request). The model is applied to Amundsen and Weddell Sea test cases to study how differences in atmospheric forcing between the two regions affect the maximum wintertime mixed layer depth (MMLD). The model uses a prescribed salinity and temperature profile below the mixed layer, providing insight into the impact on the MMLD from changes in these shelf sea properties, testing simplistically hypothesis (ii) and (iii) from Sect. 1.1.5.

Both the Weddell and Ross Seas are influenced by strong katabatic winds (*van Lipzig et al.*, 2004), resulting in low air temperatures and the formation of persistent coastal polynyas. For this study the southwestern Weddell shelf sea is chosen as the representative cold shelf sea region as it is the source of the coldest and most voluminous bottom water (*Gordon et al.*, 2010). The atmospheric conditions over the Amundsen and Bellingshausen shelf seas are also expected to be similar, and in this case the Amundsen shelf sea is chosen as the representative warm shelf sea region as it is an area of current scientific focus with the rapid thinning of Pine Island Glacier (*Jacobs et al.*, 2011). The two study-regions are shown in Fig. 2.1.

2.1.1 Comparison to previous sea-ice mixed layer modelling studies

One of the first attempts to study the ocean beneath sea ice using a bulk mixed layer model was by *Pollard et al.* (1983), who realised the need for a more accurate representation of the oceanic heat flux into the base of the sea ice. *Lemke and Manley* (1984) then examined a better representation of the pycnocline below the mixed layer, whilst imposing a fixed ice growth rate. *Lemke* (1987) included improved ice thermodynamics, whilst assuming that the mixed layer temperature is fixed to the freezing point, and *Lemke et al.* (1990) included a viscous-plastic rheology and prognostic ice concentration to study the Weddell Sea. *Martinson* (1990) considered winter mixed layer deepening of the Southern Ocean, assuming that: wind mixing can only maintain the mixed layer depth, not change it; the mixed layer cannot store heat; double diffusion is important; the forcing is steady over the winter season; and a sharp pycnocline exists below the mixed layer. The Lemke and Martinson studies demonstrate a significant improvement in the representation

of the seasonal sea ice cycle when constant deep-ocean properties are replaced with more realistic ocean profiles that vary temporally and spatially. Both studies also investigated the influence of upwelling on the mixed layer. A study by *Markus* (1999) modelled the Southern Ocean mixed layer using a prescribed sea ice concentration from satellite data. The model applied by *Tang* (1991) and *Tang and DeTracey* (1998) to the Arctic is perhaps the closest to that presented in this chapter.

The model used here builds upon these earlier studies by incorporating lateral growth of the sea ice, partitioning of the surface melt potential between lateral and basal melting, an open water surface layer that transfers heat and momentum between the atmosphere and the mixed layer, and prescribed ice divergence and ambient-ocean relaxation. The main advance, however, is the detailed examination of the bimodal distribution of Antarctic shelf seas. The use of a highly simplified model provides both a complete understanding of the results and the computational simplicity necessary for the performance of a large number of sensitivity experiments.

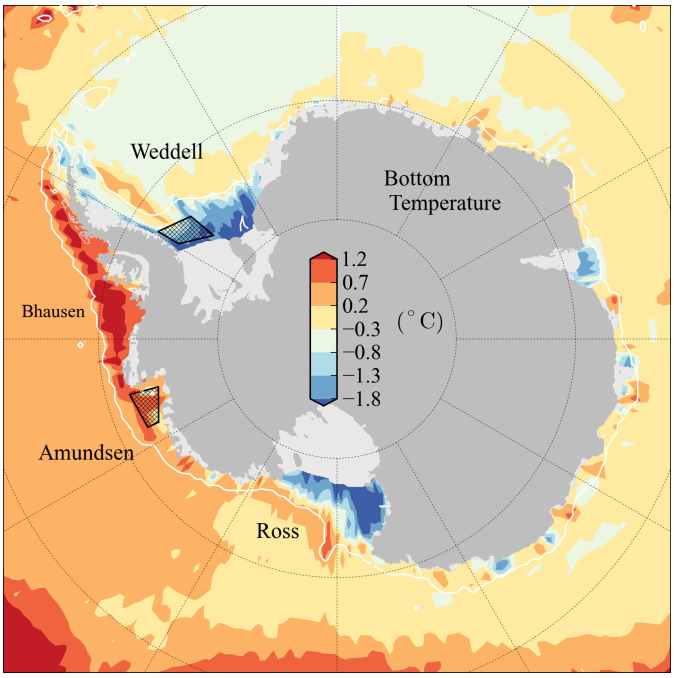

Figure 2.1: Map of the Southern Ocean bottom potential temperature as in Fig. 1.3b but with the study regions highlighted by the black hatched boxes in the Weddell and Amundsen seas.

The zero-dimensional coupled sea ice-ocean mixed layer model comprises four main com-

ponents: (a) surface energy balances at the ice-atmosphere and ocean-atmosphere interfaces; (b) a heat balance model describing the basal and lateral melting/freezing of the sea ice cover, which has a prognostic ice thickness and concentration; (c) an ocean mixed layer model, comprising balance equations that determine the evolution of the mixed layer depth, temperature and salinity; and (d) an ambient ocean profile. The model components are briefly described in the following subsections and a schematic of the sea ice, open water fraction, ocean surface layer and ocean mixed layer, is given in Fig. 2.2. Specific model parameters can be found in Table 2.1.

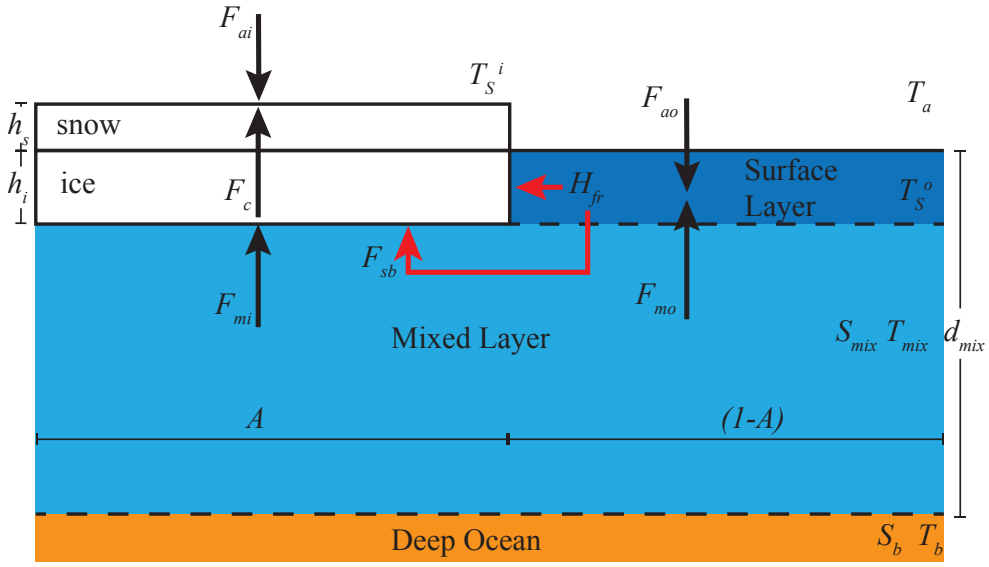

Figure 2.2: Schematic of the idealised sea ice-mixed layer model including the principal sea ice thermodynamics. Highlighted in red are the lateral and basal heat fluxes, calculated from the partitioning of the open water surface heat potential. F_{ao} and F_{ai} are the net incoming heat fluxes from the atmosphere over the open water and sea ice fractions respectively.

2.1.2 Surface heat balance

The ice and open water surface temperatures are calculated following *Maykut and Untersteiner* (1971), where the snow-covered ice surface temperature T_S^i is calculated by balancing the atmospheric surface heat fluxes (sensible, latent, blackbody, incoming longwave and incoming

shortwave heat fluxes) with the conductive heat flux through the ice as

$$\rho_a c_a C_D^i U_a (T_S^i - T_a) + \rho_a L_s C_D^i U_a (q_{sat}(T_S^i) - q_a) + \epsilon_s \sigma (T_S^i)^4 - \epsilon_s F_{lw} \downarrow \\ -(1-\alpha_s) F_{sw} \downarrow = F_c(T_S^i) \uparrow, \tag{2.1}$$

whereas the open water surface temperature T_S^o is calculated by balancing the atmospheric surface heat fluxes with the mixed layer to open water surface heat flux

$$\rho_a c_a C_D^o U_a (T_S^o - T_a) + \rho_a L_v C_D^o U_a (q_{sat}(T_S^o) - q_a) + \epsilon_w \sigma (T_S^o)^4 - \epsilon_o F_{lw} \downarrow \\ -(1-\alpha_w)(1-I_o(0)) F_{sw} \downarrow = F_{mo}(T_S^o) \uparrow, \tag{2.2}$$

where α_s is the albedo of snow (taken to be 0.8), α_w is the albedo of water (taken to be 0.06), c_a=1005 J kg^{-1} K^{-1} is the specific heat capacity of air, ϵ_o is the longwave emissivity of open water (taken to be 0.97), ϵ_s is the longwave emissivity of snow (taken to be 1), L_s=2.834 $\times$ 10^6 J kg^{-1} is the latent heat of sublimation, L_v= 2.501 $\times$ 10^6 J kg^{-1} is the latent heat of vaporisation, ρ_a=1.275 kg m^{-3} is the density of air, σ is the Stefan-Boltzmann constant, U_a is the wind speed at 10 m, q_{sat} is the saturation specific humidity, calculated following *Taylor and Feltham* (2004), q_a is the specific air humidity at 2 m, $F_{lw} \downarrow$ is the incoming longwave radiative heat flux and $F_{sw} \downarrow$ is the incoming shortwave radiative heat flux. Note that arrows are used to indicate the direction of the heat flux where necessary.

2.1.3 Sea ice thermodynamics

The *Semtner* (1976) zero-layer sea ice model is used, which assumes a linear temperature gradient through the snow and sea ice, with a conductive heat flux F_c given by

$$F_c = \frac{k_i k_s (T_f - T_S^i)}{(k_i h_s + k_s h_i)}, \tag{2.3}$$

where k_i=2.04 W m^{-1} K^{-1} is the thermal conductivity of (fresh) ice, k_s=0.31 W m^{-1} K^{-1} is the thermal conductivity of snow, h_i is the ice thickness, h_s is the thickness of the fixed snow

layer and T_f=273.15-μS_{mix} is the freezing temperature of sea water, where μ=0.054°C is the liquidus relation between the freezing temperature and salinity of the seawater.

The heat flux into the base of the sea ice at the mixed layer-sea ice boundary F_{mi} is

$$F_{mi} = \rho_w c_w c_h u^i_\star (T_{mix} - T_f), \tag{2.4}$$

where c_h=0.006 (*McPhee*, 1992) is a Stanton number describing the mixed layer to sea ice turbulent heat transfer, c_w=4190 J kg^{-1} K^{-1} is the specific heat capacity of water, ρ_w=1026 kg m^{-3} is the density of seawater, $u^i_\star$ is the friction velocity between the ice and the mixed layer and T_{mix} is the mixed layer temperature. The heat flux from the mixed layer to the open water surface layer F_{mo} is

$$F_{mo} = \rho_w c_w u^o_\star (T_{mix} - T^o_S), \tag{2.5}$$

where $u^o_\star$ is the friction velocity between the open water surface layer and mixed layer.

The rate of change of ice concentration Φ_A is calculated by balancing the ocean surface heat potential, with the latent heat released/absorbed by the ice growth/melt as

$$\Phi_A = \begin{cases} \dfrac{H_{fr}(1-A)}{L_f \rho_i h_i} & \text{for } A < A_{max} \text{ and } T^o_S < T_f \ (freezing) \\ \dfrac{H_{fr}(1-R_b)(1-A)}{L_f \rho_i h_i} & \text{for } A > 0 \text{ and } T^o_S > T_f \ (melting) \\ 0 & \text{otherwise} \end{cases}, \tag{2.6}$$

where L_f=3.340×10^5 J kg^{-1} is the latent heat of fusion, ρ_i=930 kg m^{-3} is the density of ice, A is the ice concentration and the ocean surface heat potential H_{fr} is calculated as

$$H_{fr} = F_{mo}(T^o_S) - F_{mo}(T_f) = \rho_w c_w u^o_\star (T_f - T^o_S). \tag{2.7}$$

and $F_{mo}(T_f)$ is used in the later calculation of the resultant temperature change of the mixed

layer in all cases except for when $A = 0$ and $T_S^o > T_f$. Once the ice concentration grows to a maximum value (A=A_{max}=0.95), the ocean surface heat potential is used to grow sea ice vertically. This vertical growth Φ_R is actually considered to be due to the redistribution of the sea ice grown in the persistent open water (lead) fraction, (1-A_{max}), by pressure ridging.

In the melting case, *Maykut and Perovich* (1987) suggest that a considerable amount of the ocean surface heat potential can contribute to basal melting rather than lateral melting. The melting is therefore partitioned according to a parameter R_b, where R_b=0 when all melt is lateral and R_b=1 when all melt is basal, giving a basal heat flux of

$$F_{sb} = \begin{cases} -H_{fr} R_b (1 - A) & \text{for } A > 0 \text{ and } T_S^o > T_f \\ \\ 0 & \text{otherwise} \end{cases} . \tag{2.8}$$

The rate of basal melting or freezing of ice depends on the difference in heat fluxes at the mixed layer-ice interface, such that

$$\Phi_h = (F_c - F_{mi} - F_{sb})/(\rho_i L_f), \tag{2.9}$$

where a positive (negative) value of Φ_h indicates basal ice growth (melt). Note that $h_i \geq h_{min}$, where h_{min}=0.1 m is a minimum ice thickness.

Though ice dynamics are generally neglected, ice export is parameterised in this model, as it is a sink of ice concentration that can strongly affect both the growth and the melt phases of the sea ice annual cycle. The ice concentration sink is calculated as

$$\xi = \nabla.(\mathbf{v}A), \tag{2.10}$$

where $\mathbf{v}$ is the sea ice velocity. Lateral gradients in ice concentration $\nabla.A$ are neglected here, leaving the ice sink a function of the ice velocity divergence $A\nabla.\mathbf{v}$, which is assumed to be constant and is constrained in this model by observations (Table 2.1).

2.1.4 Bulk mixed layer model

The zero-dimensional mixed layer component is based on the bulk mixed layer model of *Kraus and Turner* (1967) and *Niiler and Kraus* (1977), which assumes that temperature and salinity are uniform throughout the mixed layer, and there is a full balance in the sources and sinks of turbulent kinetic energy (TKE). An integral approach can then be taken to solve the mechanical energy budget for the entire mixed layer. More sophisticated one-dimensional models have been developed since (*Large et al.*, 1994; *Price et al.*, 1986; *Mellor and Yamada*, 1982), but as several of these mixing schemes have been shown to overestimate entrainment in the Weddell Sea region, (*Timmermann and Beckmann*, 2004; *Timmermann and Losch*, 2005), the Kraus-Turner (KT) scheme, despite also overestimating entrainment due to its stepwise treatment of the pycnocline, is chosen for a number of reasons: (i) its simplicity means physical results can be completely understood; (ii) its computational efficiency allows a large number of sensitivity studies to be performed; (iii) it is the simplest model able to reproduce reality; (iv) the neglect of horizontal variations is such a large simplification that more detailed vertical treatments would represent an inconsistent level of complexity in this case.

2.1.4.1 Surface buoyancy fluxes

The rate of mechanical energy input to the mixed layer from surface buoyancy fluxes (power input per unit area per unit density) is calculated as

$$P_B = c_2 h_{mix} \left(\frac{g\alpha}{\rho_w c_w} F_T \uparrow - g\beta F_S \uparrow \right), \tag{2.11}$$

where g=9.81 m s^{-2} is the acceleration due to gravity, α=5.82×10^{-5} K^{-1} is the thermal expansion coefficient, β=8×10^{-4} is the haline contraction coefficient, h_{mix} is the mixed layer depth and c_2 is a coefficient describing the power dissipation as a result of convective mixing and equals 1 (0.8) when the mixed layer is losing (gaining) energy (*Tang*, 1991). The heat F_T and salt F_S

fluxes out of the mixed layer are given by

$$F_T \uparrow = (1 - A)\,(F_{mo} - F_{sw}^{o} \downarrow) + AF_{mi} \tag{2.12}$$

and

$$F_S \uparrow = \frac{\rho_i}{\rho_w}(S_i - S_{mix})[(\Phi_h + \Phi_R)A + \Phi_A h_i] + (P - E)S_{mix}(1 - A), \tag{2.13}$$

where S_i is an average bulk salinity of sea ice (taken to be 5), S_{mix} is the mixed layer salinity, P is the precipitation rate and E is the evaporation rate, calculated from the latent heat flux over the open water surface. The shortwave radiation that enters the open water fraction and is absorbed within the mixed layer (longwave is assumed to be fully absorbed in the surface layer (*Maykut and Untersteiner*, 1971)), is calculated as

$$F_{sw}^{o} \downarrow = F_{sw} \downarrow \left(1 - e^{-\kappa_w h_{mix}}\right)(1 - \alpha_w) I_o(0), \tag{2.14}$$

where $I_o(0)$= 0.45 (*Niiler and Kraus*, 1977) is the fraction of shortwave radiation that penetrates the open water surface layer and κ_w=0.1 m^{-1} is an extinction coefficient of shortwave solar radiation in ocean waters (*Kara et al.*, 2005). Note that over the ice fraction, all of the incoming solar radiation is absorbed at the snow surface.

2.1.4.2 Wind mixing

The rate of turbulent kinetic energy (TKE) input to the mixed layer from wind stirring is calculated as

$$P_{wind} = c_1 e^{-h_{mix}/d_w} u_\star^3, \tag{2.15}$$

where c_1=0.8 (*Tang*, 1991) is the maximum magnitude of wind stirring in the mixed layer, d_w=10 m (*Lemke and Manley*, 1984) is a scale-depth of dissipation, and the effective friction velocity at the upper surface of the mixed layer $u_\star$ is calculated assuming free drift, such that

$$u_\star = U_a \sqrt{(\rho_a/\rho_w)[AC_D^i + (1 - A)C_D^o]}. \tag{2.16}$$

where C_D^i=0.0013 is a turbulent transfer coefficient over the ice fraction and C_D^o=0.001 turbulent transfer coefficient over the open water fraction (*Ebert and Curry*, 1993). Whilst this assumption is prone to overestimating TKE input through wind mixing, the only alternative would be to reduce this TKE input by a certain fraction. Since the model is calibrated using several other parameters to achieve a realistic reference state, a further calibration is not expected to improve the predictive capabilities of the model.

2.1.4.3 Mixed layer entrainment

The power required to entrain deep water into the mixed layer at a rate w is calculated as

$$P_E = w(h_{mix}\Delta b + c_m^2), \tag{2.17}$$

where c_m=0.03 m s^{-1} (*Kim*, 1976) is a bulk turbulent velocity scale representing the turbulent fluctuations of the mixed layer that will result in a frictional sink of TKE and Δb is the difference in the buoyancy of the waters across the mixed layer base

$$\Delta b = g\alpha(T_{mix} - T_b) - g\beta(S_{mix} - S_b), \tag{2.18}$$

where T_b and S_b are the temperature and salinity, respectively, directly below the mixed layer. This thesis only considers the evolution of a stable water column where $P_E > 0$.

Balancing Eqs.(2.11, 2.15, and 2.17) and rearranging gives the entrainment rate as

$$w = \frac{dh_{mix}}{dt} = \frac{1}{h_{mix}\Delta b + c_m^2}(P_{wind} + P_B). \tag{2.19}$$

This equation is also used to reduce the depth of the mixed layer without changing the mixed layer properties, as this represents the mixed layer reducing to a depth at which the power input from wind stirring can equal the power losses through a stabilising surface buoyancy flux.

Conservation equations for heat and salt give the temperature and salinity evolution of

the mixed layer as

$$\frac{dT_{mix}}{dt} = \begin{cases} \dfrac{-F_T \uparrow}{\rho_\omega c_w h_{mix}} + \dfrac{w}{h_{mix}}(T_b - T_{mix}) & w > 0 \\ \\ \dfrac{-F_T \uparrow}{\rho_\omega c_w h_{mix}} & w \leq 0, \end{cases} \tag{2.20}$$

and

$$\frac{dS_{mix}}{dt} = \begin{cases} -\dfrac{F_S \uparrow}{h_{mix}} + \dfrac{w}{h_{mix}}(S_b - S_{mix}) & \text{for } w > 0 \\ \\ -\dfrac{F_S \uparrow}{h_{mix}} & \text{for } w \leq 0, \end{cases} \tag{2.21}$$

which shows that when a detrainment of the mixed layer is calculated, the temperature and salinity of the mixed layer can only change through surface fluxes. This condition is also imposed when the water column is fully destratified (i.e. the surface mixed layer has deepened to the shelf seabed).

2.1.5 Ocean relaxation

The value of the salinity and temperature of the ocean below the mixed layer is updated at every time step depending upon the behaviour of the mixed layer. The ocean profiles are initially set to a representative summertime profile. When the mixed layer is subsequently present at any given depth, its properties are assigned to the ocean profile from the surface to that depth. In a simplistic representation of deep-ocean dynamics, wherever the mixed layer is not present, the ocean profile is linearly restored towards the representative summertime profile over some timescale R_T. Remnant mixed layers can then be left behind when the mixed layer retreats back to a shallower depth, forming layers of WW or dense shelf water that are slowly eroded. The representative ocean profiles are chosen to represent the water-masses being transported onto the shelf in each region, in order to test whether the forcings on-shelf are capable of destratifying these source waters in winter.

2.1.6 Model setup

2.1.6.1 Ocean profiles

In the Weddell Sea study, the aim is to model the cooling and salination of relatively warm intrusions of MWDW onto the large area of the southwestern continental shelf north of the Filchner-Ronne Ice Shelf. These intrusions appear at the mid-depth of the water column, and have temperatures of around -1.5°C and salinities of around 34.55 (*Nicholls et al.*, 2003, 2008). Similar intrusions are present on the continental shelf of the northwest Weddell Sea (*Gordon*, 1998; *Nicholls et al.*, 2004). The farthest southwest corner of the Weddell Sea features much denser HSSW with salinities as high as 34.8 (*Nicholls et al.*, 2003), but this water is believed to be the product of the polynya at the far southern boundary of the Weddell Sea, which is not the focus of this investigation. The profiles in Fig. 2.3a reflect the MWDW source waters and are used for all of the Weddell Sea simulations.

Jacobs et al. (1996) collected the first data from within the Amundsen Sea Embayment, finding almost unmodified CDW right up to the ice front of Pine Island Glacier. The profiles show a distinct (∼70 m) mixed layer near the freezing temperature with a salinity of ∼33.8. Below the mixed layer the salinity increases from ∼34 to ∼34.5 at 600 m, while temperature increases to ∼1°C; temperature and salinity are approximately constant below this. More recent data show similar profiles (*Walker et al.*, 2007; *Jacobs et al.*, 2011) with a deeper (∼200 m) near freezing surface layer of WW north of the coast. The profiles in Fig. 2.3b are a good fit to these data and are used for all of the Amundsen Sea simulations.

The density anomaly σ_θ is shown in Fig. 2.3 to illustrate the relative stability of each water column profile. The equation of state for sea water (ignoring any pressure dependence) is given by

$$\sigma_\theta(S,T,p=0) = \rho_0[1+\beta(S-S_0)-\alpha(T-T_0)]-1000, \tag{2.22}$$

where ρ_0 is a reference density calculated from a reference salinity S_0 and temperature T_0 (*UNESCO*, 1981).

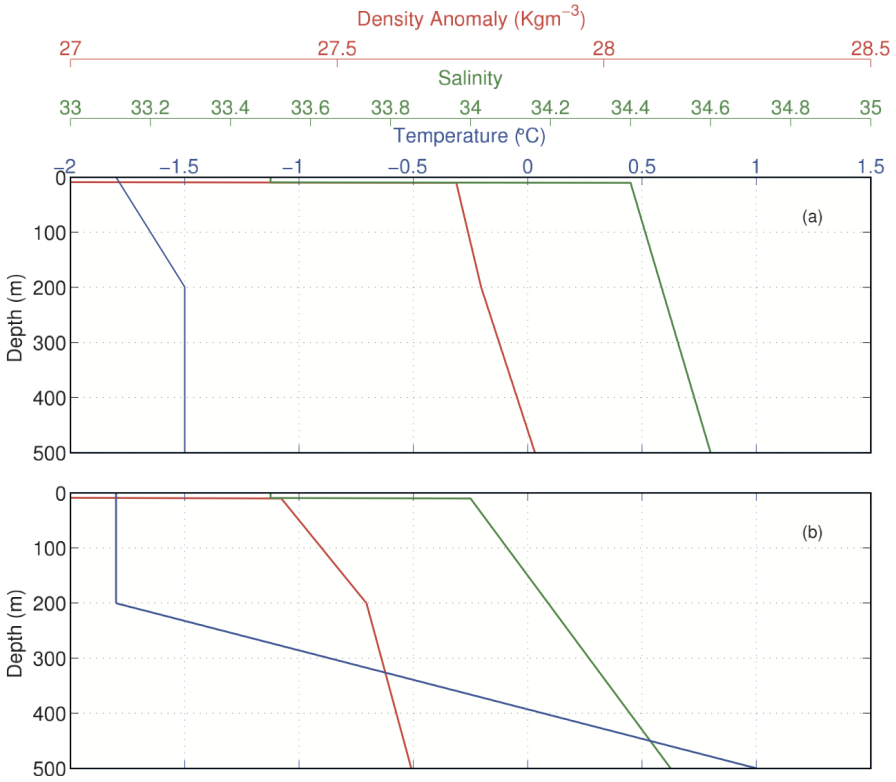

Figure 2.3: Representative summertime ocean profiles for the (a) Weddell ('cold') and (b) Amundsen ('warm') simulations.

2.1.6.2 Atmospheric forcing

The NCEP-CFSv1 atmosphere reanalysis (*Saha et al.*, 2006) provides 32 years of 6-hourly data (1979-2010) of air temperature (2 m), specific humidity (2 m), incoming longwave and shortwave radiation, wind speed (10 m) components and precipitation at a resolution of 0.3125°. The forcing data for all grid points within representative areas for the Weddell and Amundsen seas, shown in Fig. 2.1, were averaged over all 32 years to create climatologies, shown in Fig. 2.4. Note that as the wind speed is cubed to calculate the momentum transfer into the mixed layer Eq.(2.15), a second wind forcing variable was created whereby the wind speed was cubed for each grid point before the spatial and temporal averaging.

There are significant differences in the climatologies of the two regions (Fig. 2.4), which may be summarised as follows: (i) a similar summertime air temperature slightly below freezing

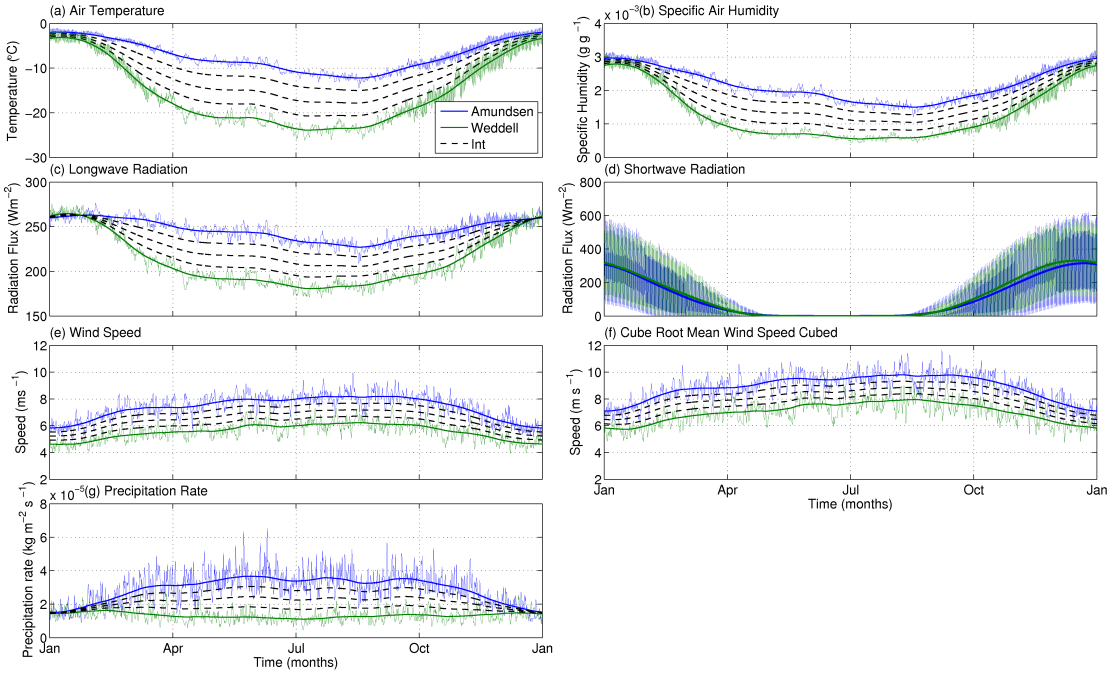

Figure 2.4: Climatological forcings calculated from the NCEP-CFSv1 reanalysis data. The forcing data have been averaged spatially over each study section shown in Fig. 2.1 and averaged over 32 years from 1979 to 2010. The light green (Weddell) and blue (Amundsen) lines are the raw climatologies, the thicker green and blue lines are the smoothed (30 day) forcings and the dashed black lines are the intermediate forcings used in the forcing sensitivity study.

(∼-1°C), but a 10°C difference in the wintertime air temperature (∼-23°C over the Weddell Sea and ∼-13°C over the Amundsen Sea); (ii) a similar summertime humidity of ∼0.003, but a 0.001 difference in the wintertime humidity (∼0.0005 over the Weddell Sea and ∼0.0015 over the Amundsen Sea); (iii) a similar summertime incoming longwave radiation of ∼260 Wm^{-2}, but a 50 Wm^{-2} difference in the wintertime longwave (∼180 Wm^{-2} over the Weddell Sea and ∼230 Wm^{-2} over the Amundsen Sea); (iv) a slight seasonal cycle in the wind speed, with an average of ∼5 m s^{-1} over the Weddell Sea and ∼7 m s^{-1} over the Amundsen Sea; (v) a precipitation rate that is fairly constant over the Weddell Sea, with an average value of $\sim 1.5\times10^{-5}$ kg $\mathrm{m}^{-2}\mathrm{s}^{-1}$, and a slight seasonal cycle over the Amundsen Sea, with an average value of $\sim 3.1\times10^{-5}$ kg $\mathrm{m}^{-2}\mathrm{s}^{-1}$; and (vi) no discernible difference in the incoming shortwave radiation.

From the raw climatologies, smoothed forcing data sets were created as shown by the thicker blue and green lines in Fig. 2.4, where a triangular smoothing procedure was used over a

30-day time period. Three intermediate forcing sets were also created for each variable (shown by the black dashed lines in Fig. 2.4) by linearly interpolating between the two smoothed climatologies at each time step. These intermediate forcing sets are used in a forcing sensitivity study, where each forcing is varied between the two smoothed climatologies whilst keeping all other forcings constant, thereby weighting each forcing change by the respective differences between each forcing variable.

2.1.6.3 Model parameters

Different model parameters were chosen to produce realistic reference cases for the two regions (Table 2.1). In particular, repeating annual cycles in ice and ocean properties were sought, since these seem a logical consequence of the application of climatological fluxes. The choices are poorly constrained due to data sparsity, so sensitivity studies were carried out to understand how each impacts the results. All simulations start on 1st January, when sea ice still covers much of the continental shelf in both Amundsen and Weddell seas (*Comiso*, 2010), so a fresh initial mixed layer is combined with an initial concentration of sea ice for both studies. Ice and snow thicknesses were based on the direct observations of *Worby et al.* (2008) which, despite sparse data in the Amundsen Sea and the southwestern Weddell Sea in winter and studies suggesting higher precipitation in the Amundsen (e.g. *van den Broeke et al.*, 2006), suggests thicker ice and snow in the Weddell Sea. This is clearly an area of large uncertainty but, as the snow sensitivity study demonstrates later, the results still hold for a large range of snow thicknesses. The partitioning of surface heat between lateral and basal melting is based on *Steele* (1992).

The ocean relaxation timescale is perhaps the least understood parameter used within the model. The relaxation is only applied to water below the mixed layer, and so will only affect the remnant water-masses left behind after the mixed layer has receded, meaning this parameter is more akin to a deep-water residence time. Due to the relaxation towards an expected summertime profile, the value is based on the time period between the mixed layer restratifying and starting to deepen again, which is taken to be three months ($R_T = 0.25$) in both simulations, representing the spring season between the end of winter and the start of summer. This parameter is examined

Parameter	Amundsen	Weddell
Initial mixed layer depth (m)	10	10
Initial mixed layer salinity	33.5	33.5
Initial mixed layer temp (°C)	-1.8	-1.8
Initial ice concentration	0.7	0.9
Initial ice thickness (m)	0.9	2.2
Snow thickness (m)	0.2	0.4
Divergence rate (yr^{-1})	0.4	1.0
Ocean profile	Fig. 2.3b	Fig. 2.3a
Relaxation timescale R_T (yr^{-1})	0.25	0.25
Basal melt fraction R_b	0.75	0.75

Table 2.1: Model parameters and initial conditions used in reference simulations.

in a sensitivity study.

By multiplying the ice concentration by an ice divergence rate, an ice concentration sink (ice export) can be calculated (Eq.2.10). Satellite-tracked ice motion vectors (*Fowler*, 2003, updated 2008), for the areas shown in Fig. 2.1 show mean (1981 - 2006) annual divergence rates of 1.1 ± 0.7 yr^{-1} for the Weddell Sea and 1.0 ± 0.6 yr^{-1} for the Amundsen Sea. The sensitivity studies presented later show the Amundsen to be only weakly sensitive to this parameter, however the lower value of 0.4 yr^{-1} was used for all Amundsen studies to prevent the full removal of ice in multi-year simulations and to ensure that a repeating cycle was obtained.

The initial mixed layer depth, salinity and temperature were based on the observed mixed layer properties at the end of preliminary simulations. All other model parameters were calibrated within the realistic ranges as discussed above to produce repeating annual cycles for the two study regions.

2.1.7 Salt and heat content of the ice-ocean column

To analyse how different processes contribute to the heat and salt content evolution of the combined sea ice, mixed layer and deep ocean (which are collectively referred to as the ice-ocean column in the rest of this paper), the integral changes of heat and salt from ice export, ocean relaxation and atmospheric surface fluxes, have been calculated by integrating with respect to time over each year.

2.1.7.1 Annual salt content changes

The annual change in the salt content of the ice-ocean column can be a result of ice export, ocean relaxation, and precipitation minus evaporation, and each are calculated respectively as

$$S_E(yr) = 0.001\rho_i \int_{yr} h_i A(S_{mix} - S_i)\xi dt, \tag{2.23}$$

$$S_R(yr) = 0.001\rho_i \int_{yr} \int_{h_{mix}}^{d_{max}} \frac{(S_{init}(z) - S_p(z))}{R_T} dz dt, and \tag{2.24}$$

$$S_P(yr) = 0.001\rho_i \int_{yr} (E - P)S_{mix}(1 - A)dt, \tag{2.25}$$

where S_{init} is the initial summertime salinity profile shown in Fig. 2.3 that the current salinity profile S_p is being relaxed towards, Δz=0.5 m is the ocean grid spacing and the factor $0.001\rho_i$ is used to convert the salinity change to a salt (mass) content change, in units of kg m^{-2}. Note that in the export case, we assume that the volume of the ice-ocean column remains constant, meaning ice export acts to increase the salt content of the ice-ocean column as the low salinity sea ice is replaced with higher salinity waters. In steady-state, the annual ice export should be roughly equal to the difference between the annual ice growth and melt.

2.1.7.2 Annual heat content changes

The yearly change in the heat content of the ice-ocean column can be a result of ice export, ocean relaxation, and atmospheric surface fluxes, and each are calculated respectively as

$$H_E(year) = \int_{yr} \rho_i L_f h_i A \xi dt \tag{2.26}$$

$$H_R(year) = \int_{yr} \int_{h_{mix}}^{d_{max}} \frac{(T_{init}(z) - T_p(z))c_w \rho_w}{R_T} dz dt, and \tag{2.27}$$

$$H_S(year) = \int_{yr} (1 - A)(F^o_{sw} \downarrow - F_{mo}(T^o_S) \uparrow) - AF_c \uparrow dt, \tag{2.28}$$

where T_{init} is the initial summertime temperature profile shown in Fig. 2.3 that the current temperature profile T_p is being relaxed towards. Note that only the export of latent heat is included as the zero-layer sea ice component has no capacity to store sensible heat. Again, an ice export should act to increase the heat content of the ice-ocean column as it removes a negative storage of latent heat.

2.2 Results and Discussion

2.2.1 Amundsen and Weddell multiyear simulations

Multiyear case studies were carried out to determine how realistically the model can simulate the annual mixed layer cycle for the two different study regions, and to provide reference states for further studies. The parameters in Table 2.1 were chosen to produce simulations that reached a cyclic steady state (ice and ocean) after several years as discussed in Sect. 2.1.6.3.

Within a single year, enhanced sea ice production leads to further brine rejection and thus a greater destratifying potential, resulting in a deeper MMLD in winter. Ice melt during the melt season causes the water column to restratify, with the mixed layer stabilising and retreating back to a shallower depth. This restratification of the water column and freshening of the mixed layer is important when it comes to the following year's destratifying phase. Therefore, conditions which lead to enhanced sea ice production and thus a deeper MMLD will also provide fresher and shallower summer mixed layers if the larger storage of fresher water in the ice melts in-situ in the subsequent melt season. It is therefore important to analyse the effects of perturbations over multiyear timescales to capture this complete mixed layer cycle.

Figure 2.5a shows a 10 year simulation using the Weddell parameters (Table 2.1) and ocean profile (Fig. 2.3a) forced by the smoothed Weddell climatology (Fig. 2.4). The result is a fully mixed water column every winter (mixed layer reaching the 500 m seabed depth). The

sea ice reaches a steady cycle, growing to a maximum thickness of 2.6 m and ice concentration of 0.9 in winter, and a minimum thickness of 2.2 m and ice concentration of 0.6 in summer. The mixed layer reaches a maximum salinity of 34.63, which is not quite saline enough to be classified as HSSW (typically around 34.75 (*Nicholls et al.*, 2009)), however this does present a realistic mechanism for converting the MWDW to near the characteristics of HSSW, with an alternative source (i.e. coastal and latent heat polynyas or shallower shelf regions) providing the final salinity increase needed.

Figure 2.5c shows a 10 year simulation using Amundsen parameters (Table 2.1) and ocean profile (Fig. 2.3b) forced by the smoothed Amundsen climatology (Fig. 2.4). The result is a repeating MMLD of 247 m every winter. The sea ice reaches a cyclic steady state, growing to a maximum thickness of 1.1 m and ice concentration of 0.95 in winter, and a minimum thickness of 0.5 m and ice concentration of 0.5 in summer.

2.2.1.1 Amundsen and Weddell switched forcings simulations

As the simplest way of testing the impact of regional differences in atmospheric forcing on the mixed layer evolution, two 10 year simulations were carried out in which the atmospheric forcing sets were switched whilst keeping all other model conditions constant. These simulations were initiated from the steady cycles of the representative simulations described above.

Figure 2.5b shows a 10 year simulation in which the Weddell reference simulation (Fig. 2.5a) is switched to Amundsen forcing. The result is a mixed layer that shallows and reaches a repeating MMLD of 390 m every winter. For the initial two years, the mixed layer continues to deepen, during which time the sea ice undergoes rapid melting. The melting of the thicker Weddell ice freshens the mixed layer, inhibiting mixed layer deepening in the subsequent winter. By the start of the third year, the ice has melted completely and the simulation becomes ice free in all subsequent summers. As there is less ice to melt and freshen the mixed layer in later years, the mixed layer is able to deepen further until the new steady state depth is reached.

Figure 2.5d shows a 10 year simulation in which the Amundsen reference simulation

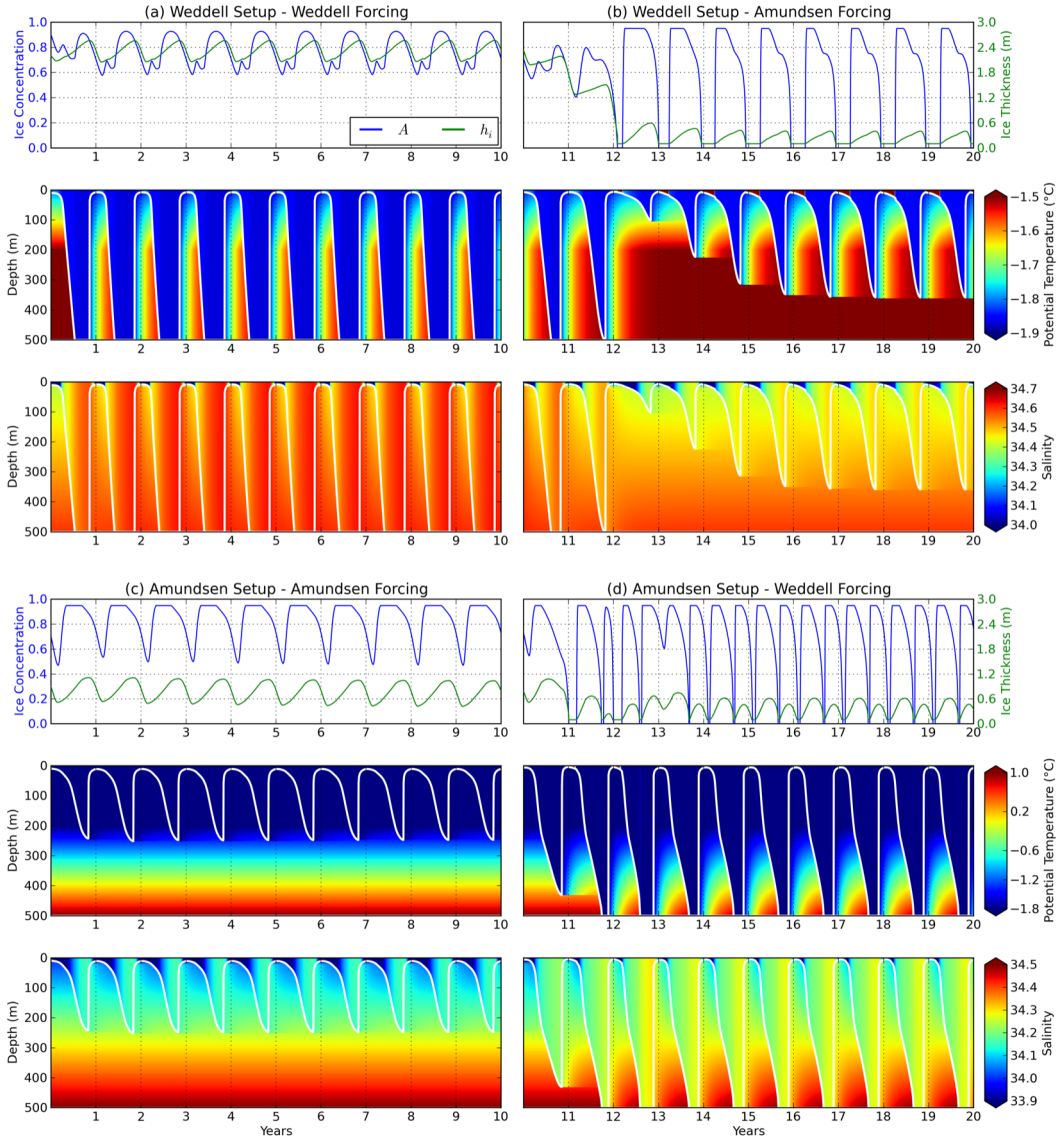

Figure 2.5: 10 year simulations using the (a) Weddell parameters, profile and forcing, (b) applied Amundsen forcing after the Weddell spinup in (a), (c) Amundsen parameters, profile and forcing, (d) applied Weddell forcing after the Amundsen spinup in (c). The top plot in each subfigure shows the ice thickness and concentration with the middle and bottom plots showing the temperature and salinity of the water column respectively. The white line shows the mixed layer depth calculated by the model.

(Fig. 2.5c) is switched to Weddell forcing. The result is a mixed layer that extends to the shelf seabed after two years of the simulation and continues to destratify the water column every winter thereafter. The maximum ice thickness and concentration reduces in the first few years as the deep ocean heat is entrained into the mixed layer and the ice adjusts to the new ocean profile. After four years, a new ice steady state is reached in which the ice begins to grow, deepening the mixed layer, only for the ice to then melt midway through winter as the mixed layer entrains the warm CDW at depth. It is only through the mixed layer destratifying the water column midway through winter that the ice is able to grow again before the summer melt period, preventing the creation of a permanent sensible heat polynya.

This biannual ice cycle in the Amundsen setup-Weddell forcing case is clearly unrealistic. The ocean profile continues to relax towards the Amundsen ocean profile, whereas in reality a well mixed water column would likely inhibit the flow of CDW onto the shelf. Nevertheless, it is interesting to note that simply switching the atmospheric forcings of the two regions appears sufficient to switch the qualitative properties of their deepest waters.

2.2.2 Salt and heat content of the ice-ocean column

To understand further the processes governing the contrasting responses discussed in the previous two sections, Fig. 2.6 shows the annual changes in the salt and heat content of the ice-ocean column, as discussed in Sect. 2.1.7.1, with Figs. 2.6a-d corresponding to the simulations shown in Figs. 2.5a-d.

2.2.2.1 Amundsen and Weddell multiyear simulations

The annual salt and heat changes of the Weddell reference simulation in Fig. 2.6a show the progression towards a cyclic steady state ocean as the net change in the annual salt and heat content tend towards zero. Initial adjustment involves a gain of salt and loss of heat which is explained by the lack of relaxation in the initial months compared with later years. For the salt content, ice export drives a large annual gain in salinity as this source of relatively fresh water

leaves the system, balancing the loss of salt from a relaxation towards a fresher summertime profile as the MWDW floods back onto the shelf every year. Open-ocean evaporation minus precipitation provides a negligible annual change in the salt content, which is likely due to the high ice concentration limiting the magnitude of both fluxes. For the heat content, both the ice export and the ocean relaxation act to increase the heat content in a similar magnitude, balancing the strong annual heat loss to the cold Weddell atmosphere.

The study by *Nicholls et al.* (2009) considered the formation of HSSW in the Weddell Sea and showed using simple calculations of the expected inflow of MWDW that the energy needed to cool and salinate these waters would require a heat loss of around 3 x 10^{20}J over the 370,000 km^2 continental shelf, giving a heat loss per unit area of around 8 x 10^8J m^{-2}. This value lies between the calculated annual heat gain of the ice-ocean column of ∼6 x 10^8J m^{-2} from ocean relaxation and the annual surface heat loss of ∼1.2 x 10^9J m^{-2}.

Comparing the Amundsen reference simulation in Fig. 2.6c to the Weddell simulation in Fig. 2.6a, highlights the much smaller annual changes in both the salt and heat content of the ice-ocean column. The contribution from ice export is reduced due to the thinner and less concentrated ice, combined with the lower ice divergence rate (0.4 s^{-1} in the Amundsen and 1.0 s^{-1} in the Weddell). The small annual change in heat from ocean relaxation is due to the shallower MMLD, with only the bottom 45 m of Winter Water relaxing back to a warmer temperature as a 200 m cold layer of Winter Water is assumed to persist perennially. Salinity relaxation freshens the surface layer and salinates the water column below around 150 m, providing a negligible net change. Unlike the Weddell simulations, the small freshening from evaporation minus precipitation could be from the greater open water fraction and stronger precipitation rate.

2.2.2.2 Amundsen and Weddell switched forcings simulations

Comparing the Amundsen forced Weddell spin-up simulation in Fig. 2.6b with the reference Weddell simulation in Fig. 2.6a shows a reduction in the magnitude of the annual changes in the salt content from ice export and ocean relaxation and a greater loss from evaporation minus

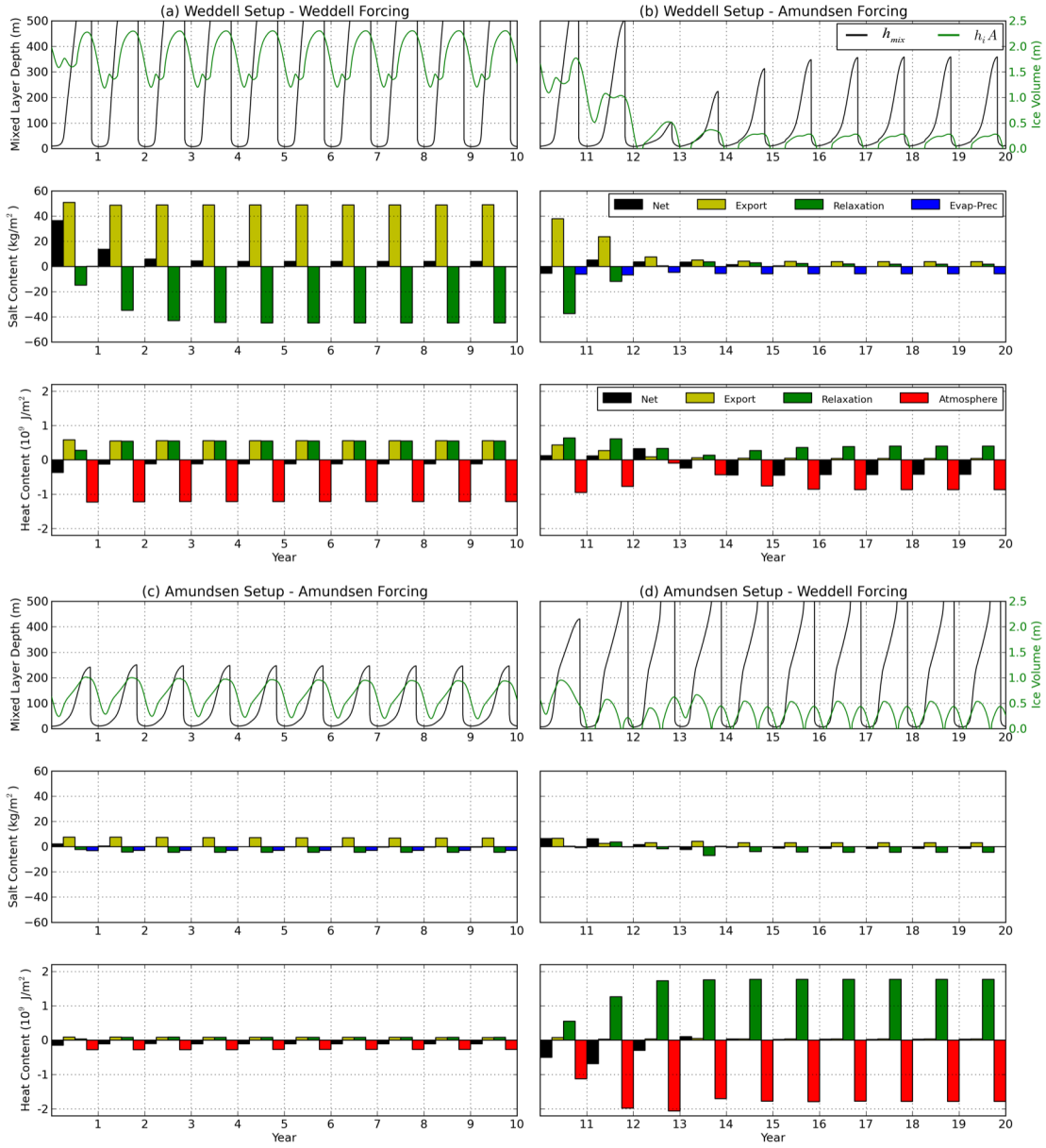

Figure 2.6: 10 year simulations, where panels (a) to (d) are the same model simulations as in Fig. 2.5. The top plot in each panel shows the mixed layer depth and ice volume (thickness multiplied by concentration). The middle plot shows the yearly salt content change of the ice-ocean column, with contributions from ice export, ocean relaxation and evaporation minus precipitation. The bottom plot shows the yearly heat content change of the ice-ocean column, with contributions from ice export, ocean relaxation and ocean-atmosphere heat flux. The net change is shown by the black bar.

precipitation, with the annual changes in salt content evolving towards the Amundsen reference state in Fig. 2.6c. The annual changes in heat content reduce in magnitude in the first few years as the ice and ocean adjust to the new forcing, after which the annual heat gain from ice export reduces to near zero due to the low volume of ice persisting in the steady state, which also explains the much larger annual heat loss to the atmosphere than in the basic Amundsen case. The annual relaxation heat gain is greater in this case than in the Amundsen reference simulation as a deeper mixed layer is relaxed back to a profile with no thick layer of Winter Water.

The Weddell forced Amundsen spin-up simulation in Fig. 2.6d shows no discernible increase in the magnitude of the annual changes in salt content, but the annual change in heat content from ocean relaxation and atmospheric surface fluxes increase in magnitude considerably. In this simulation, the mixed layer deepens and entrains the warm CDW at depth, with this heat then leaving the system through a strong atmospheric heat flux. Balancing this large loss of heat to the atmosphere is the increase in the heat content of the ice-ocean column as the thick 500 m layer of cold mixed layer waters relax to the warm Amundsen profile, creating a repeating state of heat leaving then re-entering the ice-ocean column every year.

2.2.3 Investigating the ocean profile and atmospheric forcing

In an attempt to understand in more detail the role of both the atmospheric forcing and ocean profile in controlling the mixed layer evolution in the two regions, Fig. 2.7 shows the results of the Amundsen and Weddell reference simulations with switched ocean profiles and/or the applied atmospheric forcing. Figs. 2.7a and g are the reference simulations, with all other simulations showing the results of a switch after this initial spin-up.

2.2.3.1 Switching the Weddell ocean profile and/or forcing

The following discussion relates to the simulations following the 10 year reference Weddell simulation in Fig. 2.7a.

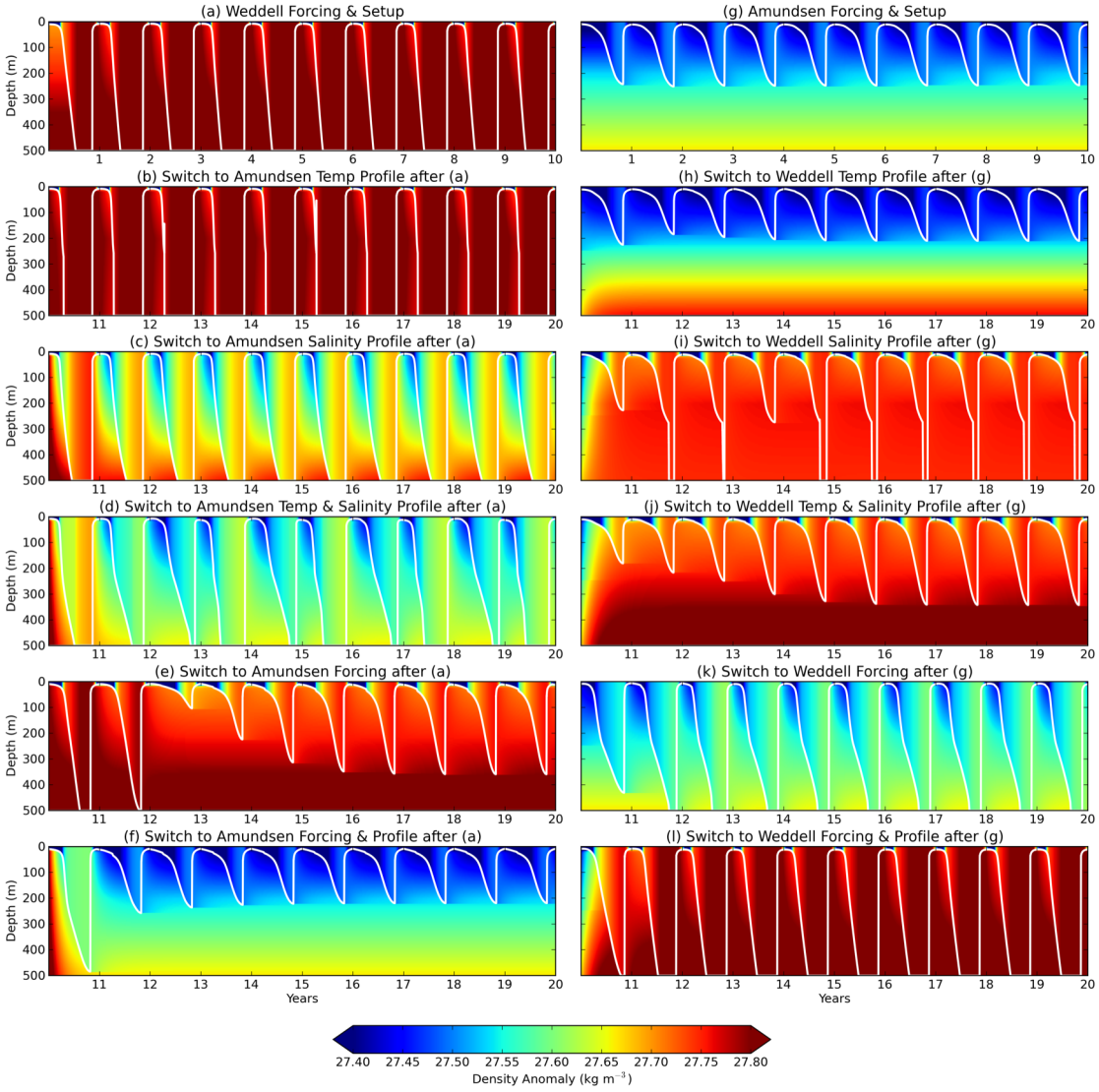

Figure 2.7: 10 year simulations, where panel (a) corresponds to the Weddell reference simulation in Fig. 2.5a and the panels below follow on from this spin-up, with the temperature profile (b), salinity profile (c), ocean profile (d), atmospheric forcing (e) and both the forcing and ocean profile (f) have been switched to the Amundsen case. Panel (g) corresponds to the Amundsen reference simulation in Fig. 2.5c and the panels below follow on from this spin-up, with the temperature profile (h), salinity profile (i), ocean profile (j), atmospheric forcing (k) and both the forcing and ocean profile (l) have been switched to the Weddell case.

Figure 2.7b shows the impact of a switch to the warmer Amundsen temperature profile. Intuitively the inclusion of warm water at depth may be expected to slow sea ice growth and limit mixed layer deepening, but the switch to the warmer and lower density temperature profile

has reduced the stability of the profile at depth, so the mixed layer entrains rapidly after a depth of around 250 m, because the mixed layer density matches that of the constant density profile below. In this specific case, ocean heat can therefore enhance mixed layer deepening while slowing sea ice growth.

Figure 2.7c shows the impact of a switch to the fresher and more stratified Amundsen salinity profile. Despite the more stable profile, which implies that a larger mixed layer density cycle is required to fully mix the water column every year, the mixed layer still deepens to the seabed at around the same time as in the reference Weddell simulation. However, by entraining into a fresher profile, the maximum mixed layer salinity (MMLS) is less than in the reference case.

Figure 2.7d shows the impact of a switch to both the Amundsen salinity and temperature profile. This profile is stable, preventing the inclusion of warm water from causing rapid deepening. The system evolves into a two year cycle, in which the sea ice is removed fully in winter through melting and ice export, with the mixed layer still deepening and salinating from the large destabilising surface temperature flux driving mixed layer entrainment. The lack of a fresh summertime profile then allows for rapid mixed layer deepening in the following year, removing all the deep ocean heat before the end of winter, allowing the ice to grow again. This then melts in the following summer, freshening the mixed layer and the cycle begins again.

Figure 2.7e shows the impact of a switch to the Amundsen forcing only and is the same as Fig. 2.5b and 2.6b so will not be discussed further.

Figure 2.7f shows the impact of a switch to both the Amundsen ocean profile (temperature and salinity) and forcing. Within one year of the simulation the system has evolved to a similar state to the reference Amundsen simulation in Fig. 2.7g, with the mixed layer reaching a depth of 220 m every winter. The difference of 25 m in the MMLD could be from differences in the model setups. The increased ice divergence rate in the Weddell can increase the open water fraction in summer, increasing the potential for summertime melting and freshening of the mixed layer. Also the thicker snow cover (0.4 m in the Weddell simulations compared to 0.2 m in the Amundsen simulations) will reduce the surface heat fluxes, limiting sea ice growth and the resultant mixed

layer deepening. This is investigated further in the model parameter sensitivity studies shown later.

2.2.3.2 Switching the Amundsen ocean profile and/or forcing

The following discussion relates to the simulations following the 10 year reference Amundsen simulation in Fig. 2.7g.

Figure 2.7h shows the impact of a switch to the colder Weddell temperature profile. Despite the Weddell profile being colder at depth, it is warmer above 200 m, which is more important in the Amundsen as only the top 200-300 m of the ocean is entrained. This warmer summertime surface layer limits sea ice growth and the resultant mixed layer deepening. The result is a repeating MMLD of 210 m.

Figure 2.7i shows the impact of a switch to the denser but less stratified Weddell salinity profile. Similar to Fig. 2.7c, the water column is now relaxing to a near constant density profile, with rapid entrainment taking place at around 250 m, when the mixed layer density matches that of the constant profile below. The mixed layer increases faster than in the reference Amundsen simulation because the fresh Winter Water layer has been replaced with relatively saline waters below the summertime mixed layer. Relaxing to an unstable profile is unrealistic, but it does highlight the importance in the Amundsen case of a well stratified salinity profile in maintaining a shallow mixed layer.

Figure 2.7j shows the impact of a switch to both the Weddell salinity and temperature profiles. This combination is stable, unlike the switch to just the Weddell salinity profile, and as a result there is no rapid deepening. The result is an evolution towards a new steady state MMLD of 340 m. This demonstrates that the Weddell salinity profile, despite being more saline, is less stratified and thus allows for deeper mixed layers, as the mixed layer increases its salinity faster by entraining this higher salinity water earlier in the year.

Figure 2.7k shows the impact of a switch to the Weddell forcing and is the same as Fig. 2.5d and 2.6d so will not be discussed further.

Figure 2.7l shows the impact of a switch to the Weddell ocean profile (temperature and salinity) and forcing. The mixed layer reaches the seabed in all winters, creating a similar ocean profile evolution to the reference Weddell simulation. The thinner snow cover and reduced divergence rate cause an annual increase in the ice volume, which does not appear to prevent the mixed layer from reaching the seabed every winter.

In both the Amundsen and Weddell simulations, a switch in the atmospheric forcing is an essential requirement in switching between a stratified or non-stratified shelf sea regime.

2.2.4 Sensitivity to changes in the atmospheric forcing

To understand the role played by each of the separate atmospheric forcing variables, a forcing sensitivity study was carried out, as shown in Fig. 2.8. For each model setup, each forcing is incremented in turn between the two forcing sets, as shown in Fig. 2.4, starting at the beginning of the two reference simulations. The MMLD is used as the diagnostic in both cases, however as the Weddell mixed layer reaches the seabed in virtually all cases, the MMLS is also used as a diagnostic for the Weddell study as it quantifies the duration and strength of the destratification phase and is of practical interest in the formation of dense shelf waters and ultimately AABW. Fig. 2.8 shows the results after 1 year, 5 years and 10 years to demonstrate the evolution of the mixed layer under each forcing change.

2.2.4.1 Amundsen forcing study

Figures 2.8a–c show the response of the Amundsen MMLD to changes in each forcing. The impacts of a switch in the precipitation, incoming longwave and shortwave, air humidity and wind speed after 1 year, 5 years and 10 years have similar magnitudes. The change in precipitation has no discernible impact on the MMLD (reference Amundsen MMLD = 247 m); switching the incoming shortwave radiation (227 m, year 10) and wind speed (236 m, year 10) switch act to reduce the MMLD slightly; switching the incoming longwave (288 m, year 10) and humidity (276 m, year 10) increases the MMLD slightly. Switching the air temperature has the biggest

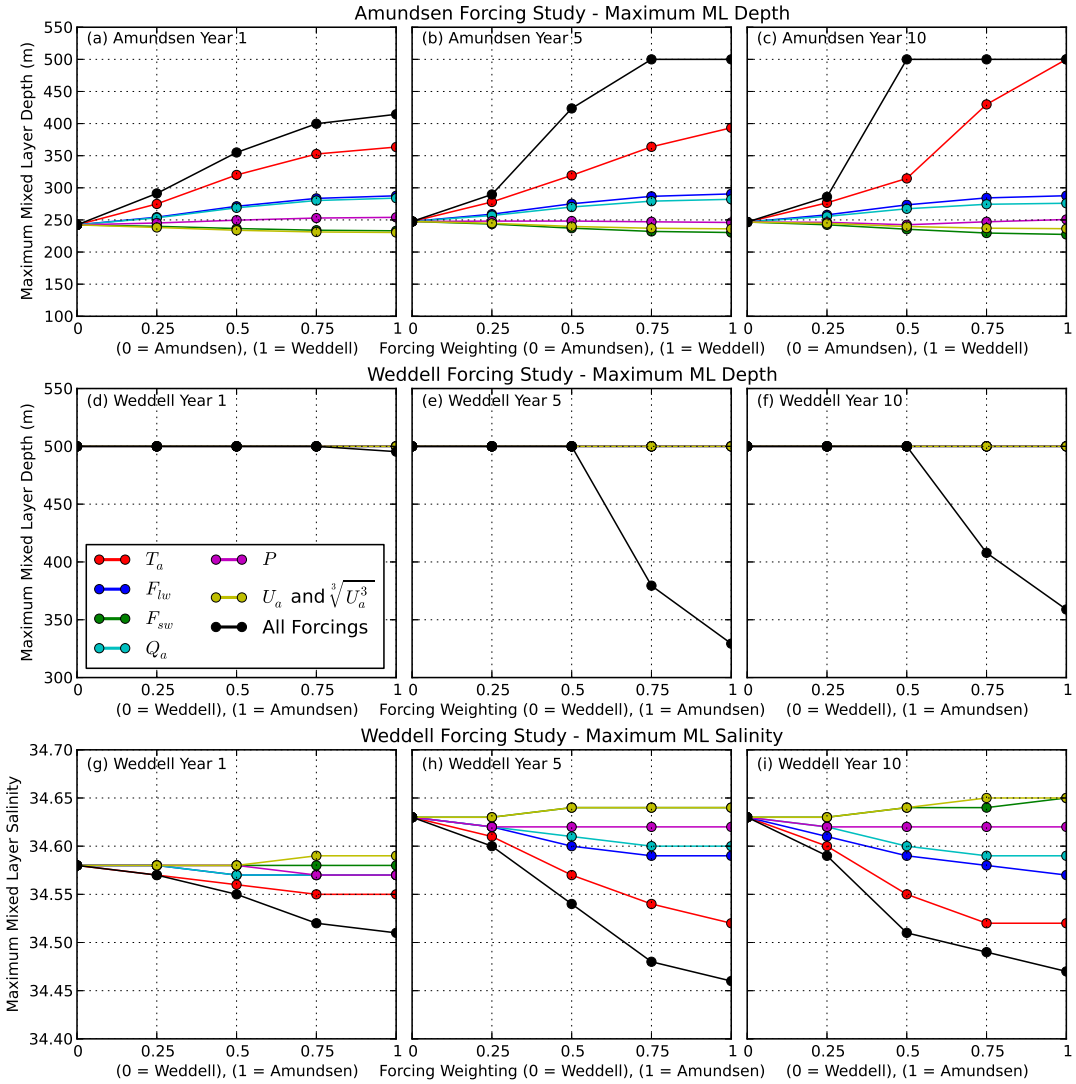

Figure 2.8: Atmospheric forcing sensitivity study for both the Weddell and Amundsen simulations. Panels (a)-(c) are the Amundsen maximum mixed layer depth sensitivities after 1 year, 5 years and 10 years respectively where the forcing for each variable (shown in the legend) is incremented towards the Weddell forcing, using the intermediate forcings shown in Fig. 2.4. Panels (d)-(f) are the Weddell maximum mixed layer depth sensitivities after 1 year, 5 years and 10 years respectively. The maximum mixed layer depths are equal to 500 m for all the individual forcing studies. Panels (g)-(i) are the Weddell maximum mixed layer salinity after 1 year, 5 years and 10 years

impact, increasing the MMLD to 363 m in the first year and causing a complete destratification (MMLD = 500 m) after 10 years. Switching all the forcings has a greater impact still, destrati-

fying the water column after 5 years with a 0.75 weighted switch and after 10 years with only a 0.50 weighted switch.

2.2.4.2 Weddell forcing study

Figures 2.8d–f show the response of the Weddell MMLD to changes in each forcing. Only through switching all the forcing variables together can the mixed layer be prevented from destratifying the water column. It may also be true that a combination of specific forcings could also prevent destratification, however this was not investigated as it would have involved a considerably greater number of simulations.

Figures 2.8g–i show the response of the Weddell MMLS. In this plot a higher salinity indicates a mixed layer that has more mixing potential, where either the rate or period of mixed layer deepening is increased. It is expected that were the seabed deeper than 500 m, the results with the highest MMLS would be more likely to fully mix the deeper water column. The order of sensitivity to the different forcings is similar to the Amundsen case, but the reference salinity increases from year 1 to year 5 before stabilising and the sensitivity to each forcing appears to increase from years 1 through to 10. The precipitation rate switch shows no discernible impact, the incoming shortwave (34.65, year 10) and wind speed (34.65, year 10) switch increase the MMLS slightly (reference Weddell MMLS of 34.63), the humidity (34.59, year 10) and incoming longwave (34.57, year 10) switch decrease the MMLS, and air temperature has the greatest impact, reducing the MMLS to 34.52 in year 10.

2.2.5 Sensitivity to model parameters

Several model parameter sensitivity studies were carried out, including the impact of the initial mixed layer depth, salinity and temperature, and initial ice thickness and concentration on the MMLD. As these initial condition sensitivity tests showed no impact on the long term (year 10) repeating solutions, the results are not shown. Instead, the impact of variations in the partitioning of surface heat between lateral and basal melt, the ocean relaxation time period,

the ice divergence rate and the snow thickness are all shown in Fig. 2.9. In a similar fashion to the forcing sensitivity study, changes in these model parameters did not prevent the Weddell mixed layer from extending to the shelf seabed in winter, so the MMLS was used to quantify the impact in the Weddell simulation. The following sensitivity studies discuss the results of a change in each parameter from the values used in both reference simulations. In some cases the range shown is greater than the range discussed to demonstrate the impact of both a decrease and increase in the given parameter.

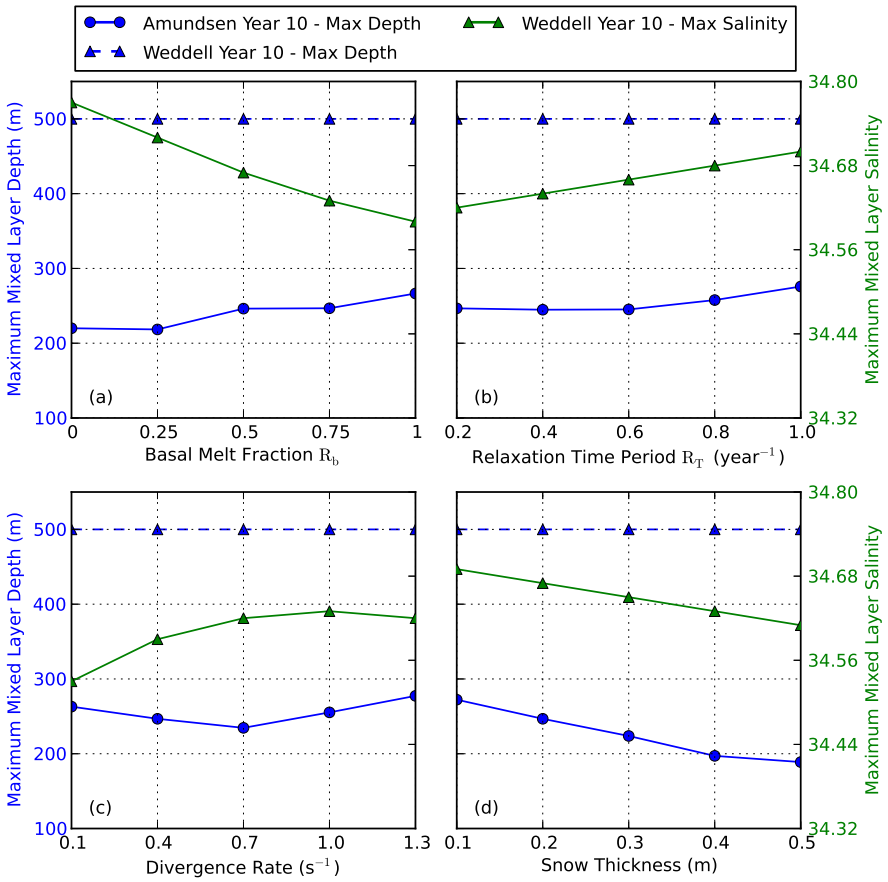

Figure 2.9: Sensitivity study of model parameters for both the Weddell and Amundsen model setups starting from the reference simulations in Figs 2.5a and 2.5c. The blue lines show the sensitivity of the maximum mixed layer depth to each parameter for both the Amundsen (solid/circles) and Weddell (dashed/triangles), while the green line shows the sensitivity of the maximum mixed layer salinity for the Weddell study only.

2.2.5.1 Sensitivity to the partitioning of surface heat R_b

Figure 2.9a shows the sensitivity of the MMLD to the partitioning of the open-ocean surface heat potential between lateral and basal melting. Using all of the surface heat to melt laterally (decreasing R_b from 0.75 to 0) in the Amundsen study results in a slight decrease in the MMLD from 247 m to 220 m. In contrast, in the Weddell, this results in an increase in the MMLS from 34.63 to 34.77.

In the Amundsen, greater lateral melting opens up more open water, which is then exposed to the warm atmosphere in the summer melt season, causing more melting. In the Weddell, minimising the ice concentration by combining the use of all the surface heat for lateral melting with the strong Weddell ice divergence rate maximised the potential heat loss to the cold Weddell atmosphere, enhancing the destratifying potential.

2.2.5.2 Sensitivity to the ocean relaxation timescale R_T

Figure 2.9b shows the sensitivity of the MMLD to the the ocean relaxation timescale. Increasing this by a factor of 4 (increasing R_T from 0.25 yr^{-1} to 1 yr^{-1}), and thus decreasing the strength of the ocean relaxation causes an increase in the Amundsen MMLD from 247 m to 275 m and an increase in the Weddell MMLS from 34.63 to 34.70.

A longer relaxation timescale is analogous to a slower erosion of the cold Winter Water towards the warmer summertime profile. Bringing less heat onto the shelf thus reduces the ocean heat flux that could inhibit sea ice growth and mixed layer deepening. It also prevents the salinity restratification that can also slow mixed layer deepening in the subsequent years.

2.2.5.3 Sensitivity to the ice divergence rate ξ

Figure 2.9c shows the sensitivity of the MMLD to the ice divergence rate. Both cases show a weak, non-monotonic response of the MMLD to this parameter. In the Amundsen case, a decrease in the divergence rate from 0.4 s^{-1} to 0.1 s^{-1} increases the MMLD from 247 m to

263 m. Increasing the divergence rate to 0.7 s^{-1} results in the minimum MMLD of 233 m, with an increase to the Weddell divergence rate of 1.0 s^{-1} increasing the MMLD to 255 m. In the Weddell case, a decrease in the divergence rate from 1.0 s^{-1} to 0.4 s^{-1} reduces the MMLS from 34.63 to 34.59, while an increase in the divergence rate to 1.3 s^{-1} also reduces the MMLS from 34.63 to 34.62.

Sea ice export is an important mechanism for creating open water, which has a strong seasonal impact on the mixed layer evolution. In winter, ice divergence acts to increase sea ice production as the open water fraction increases, through which heat is able to escape more efficiently. In summer, an increased open water fraction increases the atmosphere to surface heat flux, increasing sea ice melt and solar heating of the mixed layer. Increased sea ice growth leads to deeper mixed layers, whereas the increased melting and warming stabilises the mixed layer, inhibiting the mixed layer deepening of the following year. While it is expected that very high divergence rates (i.e. those expected in a latent heat polynya) lead to deeper mixed layers, this sensitivity study shows that small increases can have the opposite effect.

2.2.5.4 Sensitivity to the constant snow thickness h_s

Figure 2.9e shows the sensitivity of the MMLD to the constant snow thickness. An increase in the snow thickness in the Amundsen study from 20 cm to the Weddell thickness of 40 cm decreases the MMLD from 247 m to 200 m. The respective decrease in the Weddell to the Amundsen snow thickness increases the MMLS from 34.63 to 34.67.

In winter, snow prevents the rapid growth of sea ice, with the low thermal conductivity of snow insulating the ocean from the atmosphere. During the melt season, the snow cover reduces the rate of sea ice melt. This sensitivity shows that it is the impact on the ice growth that is the dominant factor.

2.3 Chapter Conclusions

In this chapter, a coupled sea ice-mixed layer model has been used to investigate the physical processes underlying the bimodal distribution in water-mass temperature over the Antarctic continental shelf. The model is able to successfully simulate realistic sea ice and mixed layer annual cycles, with complete destratification (fully mixed water column) of the Weddell Sea and only partial destratification of the Amundsen Sea. Multiyear simulations indicate the need to include realistic regional surface fluxes, relaxation to representative ocean profiles, and tuned ocean/ice parameters to produce a mixed layer annual cycle that is representative of the two study regions. The Weddell Sea simulations show a large annual loss of salt from the relaxation to a fresher Modified Warm Deep Water profile in summer, which is balanced by an annual gain in salt from the export of relatively fresh ice. The large annual loss of heat to the atmosphere is balanced equally by the heat gain from ice export and ocean relaxation. The magnitude of the annual salt and heat changes are considerably lower in the Amundsen Sea simulations.

The multiyear simulations also show a complete destratification of the Amundsen Sea by the application of Weddell Sea atmospheric forcings, while the Amundsen-forced Weddell Sea simulations reach a new equilibrium maximum mixed layer depth in winter that is shallower than the shelf seabed. In both cases, the 'cold' Weddell Sea atmospheric forcing is a necessary requirement to cause a water-column destratification, though the ocean profile is shown to play a secondary role in determining the maximum salinity of the destratified water column and the maximum depths of the shallower mixed layers. A realistic switch from one reference state to the other is only possible by combining a switch in the atmospheric forcing and ocean profile.

The model prediction of maximum mixed layer depth is most sensitive to air temperature differences between the two study regions, but differences in the incoming longwave radiation and air humidity are also important, with the difference in wind speed, precipitation and incoming shortwave radiation only providing a weak response. In the Weddell, only through switching all the forcing variables to the Amundsen forcing can a complete destratification of the water column be prevented.

This simple model cannot conclude that any single mechanism controls the observed bimodal distribution in the shelf water-mass temperature. Nevertheless, the chapter builds understanding of the many feedbacks involved, and the switched forcing results lend strong support to the hypothesis of *Talbot* (1988) that differences in atmospheric forcings are sufficient to explain the difference in water-mass temperatures over the Antarctic continental shelf.

Chapter 3

The Sea Ice and Mixed Layer over the Antarctic Continental Shelf

> "Every day some new fact comes to light - some new obstacle which threatens the gravest obstruction. I suppose this is the reason which makes the game so well worth playing."
>
> — Robert Falcon Scott

This chapter introduces the coupled CICE-mixed layer model, used to accurately quantify regional variations in the surface-driven formation of Antarctic shelf sea waters. Section 3.1 introduces the CICE-mixed layer model, including a brief description of the CICE sea ice model and the variable mixed layer model that has been newly included in CICE. Section 3.2 then presents results from the CICE-mixed layer model. Concluding remarks are given in Sect. 3.3.

3.1 CICE-Mixed Layer Modelling

Previous modelling studies have helped demonstrate the crucial role of sea ice in controlling the upper ocean characteristics of the Bellingshausen (*Meredith et al.*, 2004a; *Holland et al.*, 2010) and Amundsen (*Assmann et al.*, 2005; *Thoma et al.*, 2008) seas, and in the formation of shelf waters in the Weddell (*Timmermann et al.*, 2002) and Ross (*Assmann and Timmermann*, 2005)

seas. Despite these regional modelling studies, a detailed analysis of all four shelf sea regimes has not been undertaken to date. This chapter seeks to build on these earlier approaches by using a sophisticated sea ice model to accurately study how regional differences in the atmosphere and sea ice might control the mixed layer evolution across all four shelf sea regions. The four shelf seas are defined by the regions bounded by the Antarctic coastline and the continental shelf break (taken to be the 1000 m isobath contour) as shown in Fig. 3.9. Note that the Weddell and Bellingshausen shelf sea study regions are chosen to exclude the Antarctic Peninsular, which is not investigated in this study due to the thin width of the continental shelf. The bathymetry and bottom temperature/salinity of the four shelf seas was shown in the introduction (Fig. 1.3).

In this study, a variable mixed-layer ocean model is incorporated into the Los Alamos sea ice model CICE (version 4.1, written in FORTRAN90), within the existing CICE framework (additional FORTRAN90 source code introduced into CICE is available upon request). The standard CICE configuration divides the ice in each grid cell into five ice thickness categories, one snow thickness category and open water. A full description of the Los Alamos CICE sea ice model can be found in its user manual (*Hunke and Lipscomb*, 2010). Below is a reduced summary of the main thermodynamic/dynamic processes that are of interest to this chapter and the remaining thesis.

3.1.1 The CICE sea ice model

The previous chapter used the *Semtner* (1976) idealised zero-layer sea ice model, in which the sea ice had no capacity to store heat. In-fact, sea ice can store heat, and its specific heat capacity is given to a good approximation by *Ono* (1967) as

$$c_i(T, S) = c_0 + \frac{L_f \mu S_i}{T_i^2}, \tag{3.1}$$

where c_0=2106 J kg^{-1}K^{-1} is the specific heat capacity of fresh ice, and S_i and T_i are the internal salinity and temperature of the ice respectively.

The energy required to melt sea ice can be found by multiplying Eq.(3.1) by ρ_i and

integrating between the current temperature (T_i) and the melting temperature of sea ice ($T_m = -\mu S_i$), such that

$$Q(S_i, T_i) = \int_{T_i}^{T_m} \rho_i c_i dT. \tag{3.2}$$

The ice enthalpy is thus the solution to this equation (negative for enthalpy) plus an additional term to heat water up to its melting temperature of 0°C (from the salinity dependent freezing temperature of sea ice), such that

$$q_i(S,T) = -\rho_i[c_i(T_m - T_i) + L_f\left(1 - \frac{T_m}{T_i}\right) - c_w T_m]. \tag{3.3}$$

The snow layer over sea ice is assumed to be fresh, therefore the enthalpy of the snow layer is given simply by

$$q_s(T) = -\rho_s(c_i T_{sn} + L_f) \tag{3.4}$$

where T_{sn} is the temperature of the snow layer. The enthalpies of the ice and snow layers are then used in the calculation of ice/snow state changes, as described in Sect. 3.1.1.3.

The temperature change within the sea ice layer is governed by the heat conduction equation, given by *Maykut and Untersteiner* (1971) as

$$\rho_i c_i \frac{\partial T_i}{\partial t} = \frac{\partial}{\partial z_i}\left(k_i \frac{\partial T_i}{\partial z_i}\right) + \frac{\partial}{\partial z_i}(I_{pen}(z_i)), \tag{3.5}$$

where z_i is the vertical coordinate within the ice, $k_i(T,S)$ is the thermal conductivity of sea ice, given to a good approximation as

$$k_i(T,S) = k_0 + \frac{\beta S}{T_i}, \tag{3.6}$$

where k_0=2.03 W m^{-1}K^{-1} is the conductivity of fresh ice, β is an empirical constant (*Untersteiner*, 1964), and I_{pen} is the flux of solar radiation that penetrates to a depth z_i. The recently developed Delta-Eddington multiple scattering radiative transfer scheme is used to determine the penetrating solar flux (*Briegleb and Light*, 2007). Inherent optical properties (e.g. albedo and extinction coefficients) for bare ice, snow and ponded ice are calculated based on physical

measurements (e.g. shape, number and size of ice/snow grains), described in more detail by *Briegleb and Light* (2007). CICE employs the energy-conserving model of *Bitz and Lipscomb* (1999), which uses a finite difference form of Eq.(3.5), and a fixed number of internal ice layers to calculate the internal ice temperature evolution.

3.1.1.1 Surface heat fluxes

The heat flux from the atmosphere to the ice (upper surface) is calculated as follows (note that all fluxes are defined as positive downwards in CICE and this chapter)

$$F_{ai} = F^i_{sens} + F^i_{lat} + \epsilon F_{lw} - \epsilon\sigma(T^i_S)^4 + F^i_{swabs}, \tag{3.7}$$

where F^i_{sens} and F^i_{lat} are the sensible and latent heat flux, calculated using a stability based boundary layer parameterisation and ϵ is the emissivity of either the snow or ice surface. F^i_{swabs} is the shortwave radiation (from data) absorbed at the upper ice surface, calculated using the Delta-Eddington scheme.

3.1.1.2 Bottom and lateral heat fluxes

The heat flux from the ice to the ocean surface is given by

$$F^i_{bot} = -c_w\rho_w c_h u_\star (T_S - T^i_b) \tag{3.8}$$

where T_S is the ocean surface temperature (equal to the mixed layer temperature in the standard CICE configuration), and T^i_b is the ice bottom temperature, which is equal to the melting temperature of sea ice (based on the salinity at the base of the ice layer). Note that $F^i_{bot} \leq 0$ as this heat flux is only used for bottom melt (not freezing).

A lateral heat flux is calculated as

$$F^i_{side} = R_{side}(q_i V_i + q_s V_s)/dt, \tag{3.9}$$

where V_i is the volume (per unit area, so still in units of metres) of ice in the grid cell, V_s is the volume of snow in the grid cell and R_{side} is the fraction of ice that can be melted laterally within a given time-step, calculated using the empirical formulation of *Steele* (1992) as

$$R_{side} = w_{lat}\pi dt/(\alpha_r L_{floe}) \tag{3.10}$$

where $0 \leq R_{side} \leq 1$, α_r is an empirical constant (=0.66 in CICE), L_{floe} is an average floe diameter (=300 m in CICE), and w_{lat} is the lateral melt rate (m s^{-1}), calculated empirically following *Maykut and Perovich* (1987).

CICE calculates the total amount of heat from the ocean that is available for melting/freezing of ice as

$$H_{frzmlt} = c_w \rho_w h_{mix}(T_f - T_S)/dt. \tag{3.11}$$

F^i_{bot} and F^i_{side} are then scaled such that $H_{frzmlt} \leq F^i_{bot} + F^i_{side}$ during melting i.e. when $H_{frzmlt} \leq 0$.

3.1.1.3 Thermodynamic changes in ice state

Bottom ice growth/melt is calculated by balancing the heat flux into the ice from the ocean with F^b_c, the conductive heat flux through the ice in the bottom surface layer as

$$\frac{dh^b_i}{dt} = \frac{(F^b_c - F^i_{bot})}{q_i}. \tag{3.12}$$

In the melting case, if the calculated change in ice thickness is greater than the actual ice thickness, the remaining energy is either used to melt adjacent ice layers, or if there is no ice left to melt, the energy is returned to the ocean.

Melting at the top (ice or snow) surface is calculated by balancing the heat flux into the ice from the atmosphere with F^t_c, the conductive heat flux through the ice in the top surface layer as

$$\frac{dh^t_i}{dt} = \frac{(F_{ai} - F^t_c)}{q} \tag{3.13}$$

where q is the ice/snow enthalpy and $F_c^t < F_{ai}$ (i.e. ice/snow can only melt at the surface). Similarly, any remaining energy is used to either melt further ice/snow layers or is returned to the ocean.

R_{side} is the fraction of the ice that is melted laterally, so CICE multiplies the ice/snow state variables by 1-R_{side} to calculate the remaining amount of ice/snow left after scaling and lateral melting has taken place.

CICE forms new ice in the ocean surface layer (crudely representing frazil ice formation) as

$$\frac{V_i^{new}}{dt} = \frac{H_{frzmlt}}{q_i^{new}} \tag{3.14}$$

where q_i^{new} is the enthalpy of new ice which is (initially) assumed to be fresh, with this new ice added to the open water fraction. Note that this adds volume not just thickness as the heat available from the ocean spans the total grid cell width.

CICE also calculates sublimation and vaporisation at the surface depending on the sign of F_{lat}. The ice/snow thickness can also change through snow-ice conversion, where in the case that CICE calculates a snow thickness greater than the freeboard (using Archimedes' principle), snow is converted into ice until the snow thickness equals the freeboard (the distance from the sea-level to the upper ice/snow surface).

3.1.1.4 Salt and freshwater fluxes

In CICE, the salt/freshwater flux has been split into the direct fluxes of pure salt and fresh water (in kg $m^{-2}s^{-1}$). Processes such as evaporation therefore only contribute to the direct freshwater flux, whereas sea ice growth/melt will affect both. The different processes involved in the salt/freshwater fluxes (small, energy conserving quantities are neglected in this discussion) are thus summed together separately in CICE as

$$F_{salt}^i = 10^{-3} S_i [\rho_i A h_i R_{side} - \rho_i V_i^{new} - A\rho_i \left(dh_i^t + dh_i^b\right)]/dt \tag{3.15}$$

$$F^i_{fresh} = [(\rho_s A h_s + \rho_i A h_i) R_{side} - \rho_i V_i^{new} - \rho_s A dh_s^t - \rho_i A \left(dh_i^T t + dh_i^b\right) + \rho_s V_i^R f_R]/dt \quad (3.16)$$

where V_i^R is the volume of ice that is ridged and f_R is the fraction of the ridged snow that is lost to the ocean (=0.5 in CICE). Note that CICE assumes the ice is fresh when calculating the freshwater flux (multiplying F^i_{fresh} by 10^{-3}(1000-S_i) would be more physically consistent with F^i_{salt}, but will have a negligible impact on its absolute value). Note that the ice/snow thickness is multiplied by the ice concentration A, to represent the fluxes entering the ocean across the entire grid cell width.

The other source of freshwater that enters the ocean is from precipitation and evaporation. CICE reads in both rainfall and snowfall (changing rain to snow if $T_a \leq 0°C$), giving a net freshwater flux of

$$F^{pe}_{fresh} = F_{rain} + (1 - A)\left(F_{snow} + F^o_{lat}/L_v\right) \quad (3.17)$$

where F_{rain} and F_{snow} are the prescribed rates of rainfall and snowfall (from data). Note that rainfall over sea ice is assumed to percolate through the ice into the ocean.

3.1.1.5 Ice dynamics

Ice dynamics within CICE are based on the two-dimensional momentum equation of *Hibler* (1979)

$$m\frac{\partial \mathbf{u}}{\partial t} = \tau_a + \tau_w - \hat{k} \times mf\mathbf{u} - mg\nabla H_o - \nabla.\sigma_i \quad (3.18)$$

where $\mathbf{u}$ is the horizontal ice velocity, m is the mass per unit area of the snow and ice combined, τ_a and τ_w are the applied atmosphere and ocean wind stresses, f is the Coriolis parameter, H_o is the ocean surface tilt (this contribution is neglected), and σ_i is the internal ice stress tensor. The internal ice stresses are based on the viscous-plastic (VP) isotropic rheology (how a medium moves/deforms under a given stress) of *Hibler* (1979), updated to the more numerically efficient elastic-viscous-plastic (EVP) rheology of *Hunke and Dukowicz* (1997).

The principle equation solved by CICE is

$$\frac{\partial g}{\partial t} = -\nabla.(g\mathbf{u}) - \frac{\partial}{\partial h}(fg) + \psi \tag{3.19}$$

where g is the ice thickness distribution function (the fractional area covered by ice in a given thickness range), f is the thermodynamic growth of ice, and ψ is a ridging redistribution function.

3.1.2 Incorporating a variable mixed layer into CICE

In the standard CICE configuration, the mixed-layer depth is set to a constant value (default of 30 m), the mixed-layer salinity is prescribed, and the mixed-layer temperature is prognostic, with the option of restoring this temperature towards data. A deep ocean-mixed layer heat flux is prescribed from data. By adapting CICE to include a variable mixed layer, the mixed layer depth, temperature and salinity is allowed to evolve, based on the calculated surface and deep-ocean fluxes described below.

A bulk mixed layer model is used, based on *Kraus and Turner* (1967) and *Niiler and Kraus* (1977); similar to that described in the previous chapter. Similarly, the use of a simple bulk mixed layer reduces the computational cost of studying the formation of shelf waters, and enables a complete understanding of all aspects of the model results. The ocean below the mixed layer is relaxed towards observations, rather than modelled; removing the impact of variable ocean dynamics and isolating the effect of surface processes alone.

The sea ice has been adapted substantially from that used in the previous chapter, so the following section discusses the CICE-mixed layer model that has been developed. The mixed-layer model has no horizontal interaction, so the description below applies to each grid cell within CICE.

While CICE treats the mixed layer and surface layer as analogous, in this model, a simple 2-layer ocean is used for the temperature calculations, consisting of a fixed depth ocean surface

layer h_S (taken to be 10 m) and a variable mixed layer h_{mix} below, as shown schematically in Fig. 3.1. The surface temperature layer exchanges heat with the variable-depth mixed layer below and with the sea ice and atmosphere above, as described later in this section. Adding this surface temperature layer allows for the modelling of rapid changes in the ocean surface temperature, improving the fit of modelled ice concentration to observations, while still providing a simple and computationally efficient sea ice-mixed layer model to use for this study. Without this surface layer, the mixed layer and thus surface temperature often remained slightly above freezing when the mixed layer was deep (order of several hundred metres), hindering the formation of sea ice in winter. Note that for simplicity, the salinity calculations ignore this surface layer and treat the mixed layer salinity and surface salinity as the same, as small changes in the surface salinity will not have the same impact on the sea ice growth and melt compared to surface temperature.

The heat flux into the ocean surface layer from the ice and open-ocean fractions (all fluxes are positive downwards) is calculated as

$$F_{surface} = (1 - A)(F^o_{sens} + F^o_{lat} + F^o_{lwout} + F^o_{lw} + F^o_{sw}) + A(F^i_{bot} + F_{swthru}), \tag{3.20}$$

where F^o_{sens} is the sensible heat flux between the atmosphere to the open-ocean surface, F^o_{lat} is the latent heat flux between the atmosphere and the open-ocean surface, F^o_{lwout} is the black-body heat flux from the open-ocean surface to the atmosphere, F^o_{lw} is the downward longwave radiative heat flux, F^o_{sw} is the downward shortwave radiation absorbed by the open ocean surface, calculated as a sum over four radiative categories (direct and diffuse, visible and near-infrared) with varying albedo parameterisations, and F_{swthru} is the shortwave radiative heat flux that passes through the ice and is absorbed by the ocean. The ice-ocean heat flux F^i_{bot} is given in Eq.(3.8) and is aggregated over all ice categories/thicknesses. These are all shown schematically in Fig. 3.1 along with several other variables described below.

The heat flux from the mixed layer to the ocean surface layer is calculated as

$$F_{sm} = c_w \rho_w u_\star (T_S - T_{mix}), \tag{3.21}$$

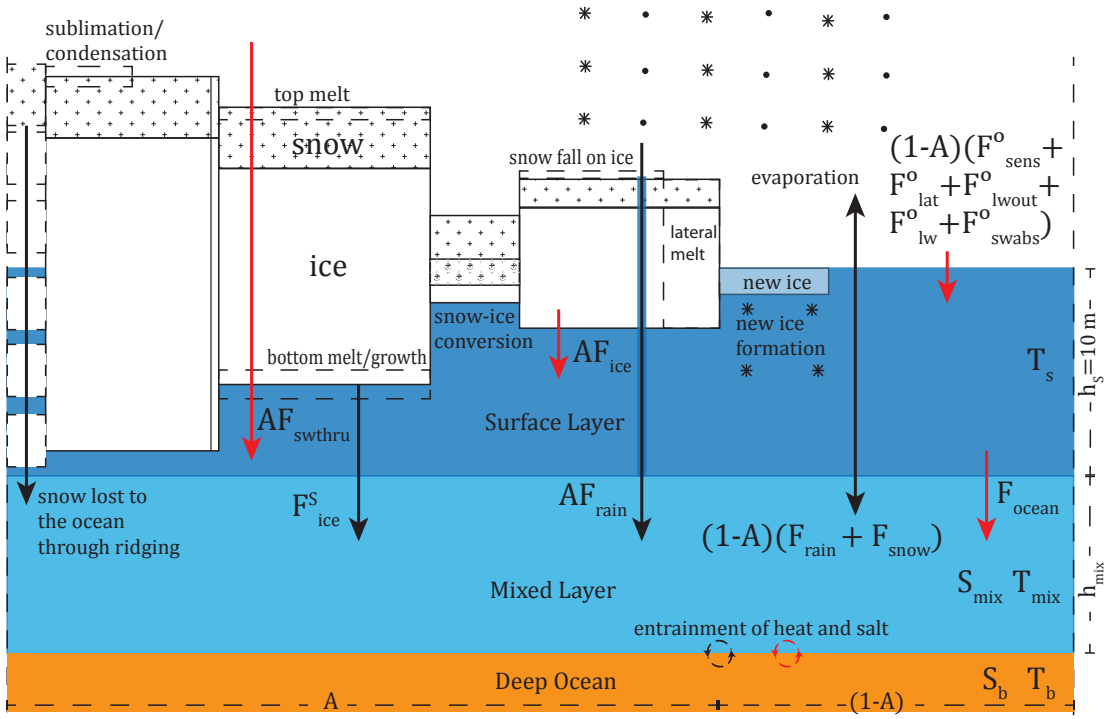

Figure 3.1: Schematic of the main thermodynamic processes included in CICE. A: total ice concentration within the grid cell, F^o_{lat}: latent heat flux over the open water fraction, F^o_{lw}: downward longwave radiative heat flux into the open water fraction, F^o_{lwout}: blackbody radiative heat flux from the open water fraction, F_{ice}: conductive heat flux through the ice, F^S_{ice}: net salt flux from ice/snow growth/melt, F_{rain}: rainfall over the grid cell, F_{ocean}: ocean surface-mixed layer heat flux, F^o_{sens}: sensible heat flux over the open water fraction, F_{snow}: snowfall over the grid cell, F^o_{swabs}: shortwave radiative heat flux absorbed by the open water fraction, F_{swthru}: shortwave radiative heat flux through the ice, S_b: salinity directly below the mixed layer, S_{mix}: mixed layer salinity, T_b: temperature directly below the mixed layer, T_S: surface layer temperature, T_{mix}: mixed layer temperature. Red arrows indicate heat fluxes while black arrows indicate salt/freshwater fluxes.

where the ocean surface layer is assumed to be in free-drift, meaning $u_\star$ is the ocean surface friction velocity, calculated through a combination of the ice-ocean wind stress τ_i and the open water wind stress τ_o as

$$u_\star = \sqrt{[A\tau_i + (1-A)\tau_o]/\rho_w}. \tag{3.22}$$

3.1.2.1 Effective salt fluxes

The salt and freshwater fluxes described in Sect. 3.1.1.4 can be combined into a net 'effective' salt flux (i.e. the freshwater flux acts as a negative salt flux, still in kg $m^{-2}s^{-1}$) as

$$\widehat{F}^i_{salt} = F^i_{salt} - \frac{F^i_{fresh} S_{mix}}{(1000 - S_{mix})} \tag{3.23}$$

$$\widehat{F}^{pe}_{salt} = -\frac{F^{pe}_{fresh} S_{mix}}{(1000 - S_{mix})} \tag{3.24}$$

This can be converted into a surface 'salinity flux' or what is sometimes called a 'virtual salt flux' (in m s^{-1}) as

$$F^i_S = \frac{(1000 - S_{mix})}{\rho_w} \widehat{F}^i_{salt} \tag{3.25}$$

$$F^{pe}_S = \frac{(1000 - S_{mix})}{\rho_w} \widehat{F}^{pe}_{salt} \tag{3.26}$$

with the net 'virtual salt flux' into the ocean equal to the sum of these two terms.

3.1.2.2 Mixed layer power input

The rate of mechanical energy input (or power) to the mixed layer from surface buoyancy fluxes is given by a combination of the following : (i) salt/freshwater flux from sea ice growth/melt P_{salt}; (ii) salt/freshwater flux from precipitation and evaporation P_{pe}; and (iii) the heat flux between the ocean surface layer and the mixed layer P_{heat}. Wind shearing (from both the ice and open water fractions) provides a direct input of power to the mixed layer P_{wind}, as in the previous chapter (Sect. 2.1.4.2). Splitting up the relative contributions to the surface power input allows each term's impact on the mixed layer evolution to be assessed. The surface power inputs (per unit density, i.e. in m^3s^{-3}) are given respectively as

$$P_{salt} = c_B g \beta h_{mix} F^i_S, \tag{3.27}$$

$$P_{pe} = c_B g \beta h_{mix} F^{pe}_S, \tag{3.28}$$

$$P_{heat} = -\frac{c_B g \alpha h_{mix}}{c_w \rho_w} F_{sm}, \tag{3.29}$$

where h_{mix} is the mixed layer depth and

$$c_B = \exp(-h_{mix}/d_B) \tag{3.30}$$

is a variable parameter describing the fraction of energy that remains in the mixed layer after convective dissipative effects are taken into account, where d_B=50 m is a scale depth of convective dissipation (*Lemke and Manley*, 1984). Note that to allow for the representation of deep (several hundred metres deep) mixed layers, this variable parameter is capped such that $c_B \geq \exp(-h_B^{max}/d_B)$ following *Lemke et al.* (1990) where a higher value of h_B^{max}=100 m is used instead of the *Lemke et al.* (1990) value of 50 m, preventing a large Weddell polynya that otherwise forms every winter near the Greenwich Meridian. This is a region of observed low ice concentrations (*Lindsay et al.*, 2004) which is due to a halo of warm waters encircling the Maud Rise at depths just below the mixed layer (*de Steur et al.*, 2007); a process that is impossible to capture in this simple model.

The input of power from wind shearing is

$$P_{wind} = \exp(-h_{mix}/d_w) u_\star^3, \tag{3.31}$$

where d_w=10 m is a scale depth of mechanical dissipation (*Lemke and Manley*, 1984). The term P_{net} is also used, which refers to the sum of the four surface power input terms described above. Note also that $P_{heat} + P_{pe} + P_{salt} = P_B$, the total power input to the mixed layer from surface buoyancy fluxes, the same term as that used in the previous chapter (Sect. 2.1.4.1). In later sections, the annual time integrals of these power input terms are used to analyse the net annual (mechanical) energy input to the mixed layer, referred to as W_{salt}, W_{pe}, W_{heat}, W_{wind}, W_{net} (not density weighted, so in units of J m^{-2}).

3.1.2.3 Mixed layer entrainment

The bulk mixed layer energy balance formulation of *Kraus and Turner* (1967) and *Niiler and Kraus* (1977) is used, which assumes that temperature and salinity are uniform throughout the mixed layer, and there is a full balance in the sources and sinks of turbulent kinetic energy (TKE) (See Sect. 2.1.4 for further details about this model choice). While the precise definition of h_{mix} varies for salinity and temperature, the error this introduces to the energy balance is expected to provide an insignificant impact on the results compared to the general assumptions made by the bulk mixed layer model. Following the previous chapter (Sect. 2.1.4.3), the mixed layer entrainment rate is calculated by balancing the energy needed to entrain water from below with the energy provided by the wind and the surface buoyancy fluxes which, when rearranged, gives the mixed layer entrainment rate as

$$w = \frac{dh_{mix}}{dt} = \frac{P_{net}}{h_{mix}\Delta b + c_m^2}. \tag{3.32}$$

The mixed layer depth is prevented from becoming too shallow (to increase numerical stability), such that $h_{mix} \geq h_{min}$, where h_{min}=10 m. Similar to the previous chapter, if the calculated mixed layer depth is greater than the seabed depth h_{bath} the entrainment rate is reduced such that the mixed layer depth equals the respective limit.

3.1.2.4 Temperature and salinity changes

Through a combination of surface and entrainment heat/salt fluxes, the change in the mixed layer temperature and salinity is calculated as

$$\frac{dT_{mix}}{dt} = \begin{cases} \dfrac{F_{sm}}{\rho_w c_w h_{mix}} + \dfrac{w}{h_{mix}}(T_b - T_{mix}) & w > 0 \\ \\ \dfrac{F_{sm}}{\rho_w c_w h_{mix}} & w \leq 0, \end{cases} \tag{3.33}$$

$$\frac{dS_{mix}}{dt} = \begin{cases} \frac{F_S^i + F_S^{pe}}{h_{mix}} + \frac{w}{h_{mix}}(S_b - S_{mix}) & \text{for } w > 0 \\ \\ \frac{F_S^i + F_S^{pe}}{h_{mix}} & \text{for } w \leq 0, \end{cases} \tag{3.34}$$

and an ocean surface temperature change given by

$$\frac{dT_S^o}{dt} = \frac{F_{surface} - F_{ms}}{c_w \rho_w h_S}. \tag{3.35}$$

The potential to freeze/melt ice in the surface layer is calculated as

$$H_{frzmlt}^S = c_w \rho_w h_S (T_f - T_S)/dt, \tag{3.36}$$

while ensuring that $T_S \geq T_f$, such that any latent heat flux from ice formation is included in the heat flux calculations. In the case that $T_{mix} < T_f$ the potential to form ice in the mixed layer (not melting as it is separated from the ice by the surface layer) is calculated as

$$H_{frzmlt}^{mix} = c_w \rho_w h_{mix} (T_f - T_{mix})/dt \text{ for } T_{mix} < T_f \tag{3.37}$$

while setting $T_{mix} = T_f$ to ensure $T_{mix} \geq T_f$. $H_{frzmlt} = H_{frzmlt}^{mix} + H_{frzmlt}^S$ is then returned to CICE as the net potential to grow/melt ice.

3.1.2.5 Deep ocean representation

A three-dimensional grid is used to represent the deep ocean, with the deep-ocean column at each horizontal (x, y) grid-cell given by

$$T_{ocean} = \{T(z_1), T(z_2), T(z_3), ...T(z_N)\} \tag{3.38}$$

$$S_{ocean} = \{S(z_1), S(z_2), S(z_3), ...S(z_N)\}, \tag{3.39}$$

where z represents the vertical ocean grid index and N is the number of vertical levels chosen. At every time-step the mixed layer temperature and salinity is assigned to the deep ocean grid within the mixed layer. The signature of Winter Water is therefore retained in the deep ocean as the mixed layer retreats back to a shallower depth. The precise depth levels and T/S data used are described in Sect. 3.1.3.

The ocean grid is used to determine the temperature and salinity of the waters entrained into the mixed layer using a linear interpolation scheme to update the value of S_b and T_b to account for the coarse ocean grid. In the case of a very shallow or deep mixed layer T_b and S_b are simply set to top or bottom values. The T/S values for depth levels deeper than the mixed layer at any given time are slowly relaxed back to their initial values to loosely represent ocean dynamics restoring the Winter Water back towards the mean (summertime) ocean conditions. A restoration timescale of $R_T = 3$ months is used as it is expected this restoration takes place predominantly through spring.

3.1.2.6 Ice dynamics

Since the model is forced with near-surface winds, the effect of the turning angle within the atmospheric Ekman layer has been accounted for. However, *Kimura* (2004) shows the angle between surface winds and ice motion to be around 10-20°, which is a result of the ocean Ekman layer. The ice-ocean drag is given by

$$\tau_w = c_d \rho_w |\mathbf{U_w} - \mathbf{u}|[(\mathbf{U_w} - \mathbf{u}) \cos\ \theta_w + \mathbf{k} \times (\mathbf{U_w} - \mathbf{u}) \sin\ \theta_w] \tag{3.40}$$

where c_d is an ice-ocean drag coefficient, $\mathbf{u}$ is the ice velocity, $\mathbf{U_w}$ is the geostrophic ocean velocity (ocean currents are neglected, meaning $\mathbf{U_w}$=0) and θ_w (=-15° in this study) is the ocean turning angle (negative for the Southern Ocean) between the geostrophic ocean currents and the ocean surface currents under the ice.

3.1.3 CICE configuration

CICE has been configured to run in stand-alone mode on a 0.5° rotated lat/lon grid (176 × 176) with the north pole at the equator (i.e. horizontal resolution of around 55 km). An Antarctic landmask and bathymetry are produced through an interpolation of the RTOPO dataset (*Timmermann et al.*, 2010). Atmospheric forcing data are taken from the ERA-Interim (ERA-I) reanalysis (*Dee et al.*, 2011) and consist of: 6-hourly fields of air temperature (2 m), specific humidity(2 m) and zonal and meridional winds (10 m); daily fields of downward shortwave and longwave radiation; and monthly fields of precipitation (snow and rain). Mean (1980-2011) winter ERA-I forcing data are shown in Fig. 3.2. Note that ERA-I forcing data was used instead of the NCEP-CFSv1 data used in the previous chapter as it is also thought to give reasonable results in the Southern Ocean (e.g. *Bracegirdle and Marshall*, 2012) and also provides accurate wind trends (*Holland and Kwok*, 2012), improving the potential accuracy of the trend analyses carried out in the following chapter.

World Ocean Atlas 09 (WOA09) temperature (*Antonov et al.*, 2010) and salinity (*Locarnini et al.*, 2010) data are used, which consist of climatological fields of *in situ* data interpolated to standard depth levels on a 1-degree grid. These data have been interpolated onto the CICE grid described above, with a weighted extrapolation procedure used to fill any missing grid points found near the coastline, and smoothed using a 9-point gaussian filter. A coarse vertical grid is used to represent the deep ocean, with depth values corresponding to z = (30, 50, 100, 150, 200, 300, 400, 600, 800, 1000) m levels. The WOA09 data at each of these z levels are initialised in the T, S deep ocean grids at each grid point and S_{mix}, T_{mix} and T_S are initialised to the z=30 m values. The mixed layer salinity is restored back to the climatological value with a period of one year, to balance any loss of salt from deep ocean relaxation.

Ice and snow thicknesses are initialised at ∼1.5 m and ∼0.2 m respectively in the grid cells where the surface temperature is below freezing. The model is initialised in March when sea ice is at its lowest extent (*Comiso*, 1999, updated 2012) and is approximately the date on which the majority of WOA09 Antarctic shelf sea measurements have been taken (due to this

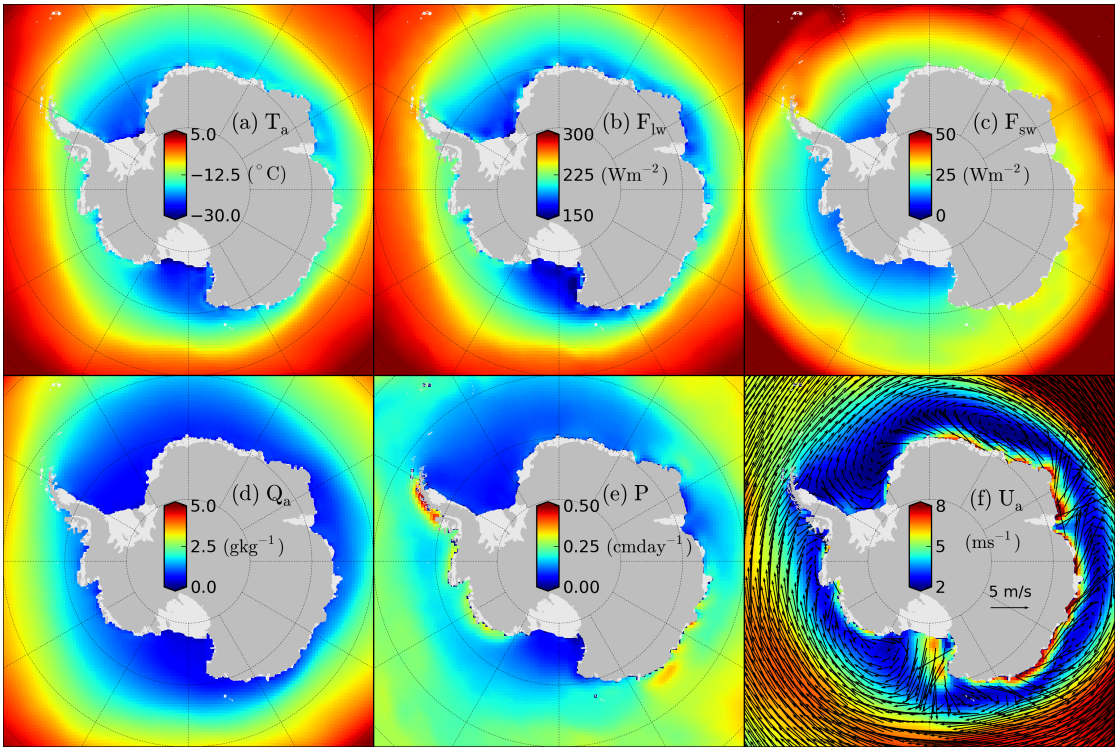

Figure 3.2: Mean (1980-2011) ERA-Interim (*Dee et al.*, 2011) winter (JAS) atmospheric forcing. (a) 2 m air temperature, (b) Incoming longwave radiation, (c) incoming shortwave radiation, (d) 2 m specific humidity, (e) total precipitation (snow and rain) and (f) 10 m wind speed, overlain with 10 m wind vectors (every third grid point).

sea ice minimum). The model is spun up for 5 years (1980-1984), before producing the analysis simulation for 27 years (1985-2011).

3.2 Results from the CICE-Mixed Layer Model

3.2.1 Sea ice state

As the focus is on the impact of the atmosphere on the shelf seas, it is important an accurate sea ice state is modelled, to validate the fluxes of freshwater, salt, heat and momentum between the atmosphere and the ocean. Figure 3.3 shows a comparison of the mean (seasonal) modelled ice concentration compared to observations derived from passive microwave emissions using the

Bootstrap algorithm (*Comiso*, 1999, updated 2012).

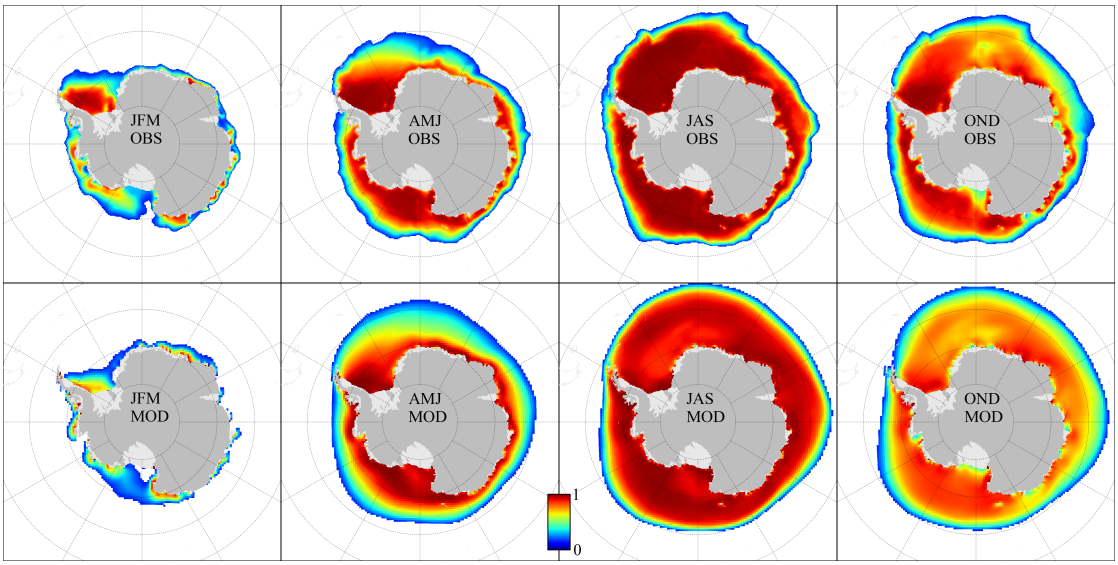

Figure 3.3: Mean (1985-2011) seasonal modelled ice concentration from the ERA-I simulation (bottom row) compared to observations (top row). Ice concentration observations calculated using the Bootstrap algorithm (*Comiso*, 1999, updated 2012). Ice concentrations less than 0.15 are masked in both datasets.

The model does a reasonable job of reproducing the seasonal sea ice cycle, with the best fit to data in autumn (April, May, June), when the mixed layer depth has the highest growth rates. There is, however, an overestimation of the seasonal cycle, with the ice extent too high in winter and too low in summer. The maximum wintertime ice extent is unlikely to be of much importance for the main aims of this study as the focus is on the impact of sea ice on the southern shelf seas, well away from the wintertime sea ice edge, but the low summer ice concentration is a concern as this extra ice melt will probably over-stratify the shelf seas in summer. In the Weddell Sea, the low ice concentration in summer appears to be linked to low ice concentrations in winter and spring, while in the Amundsen Sea Embayment, a polynya forms in spring leading to an ice-free region in summer. The Ross and Bellingshausen seas appear to have the best fit to observations.

Figure 3.4 shows the mean (seasonal) modelled ice motion. In most regions, the ice follows the pattern of the near-surface winds, with a slight leftward deflection due to the ocean turning angle. There is a strong northward ice motion in the Ross and westward coastal current in East

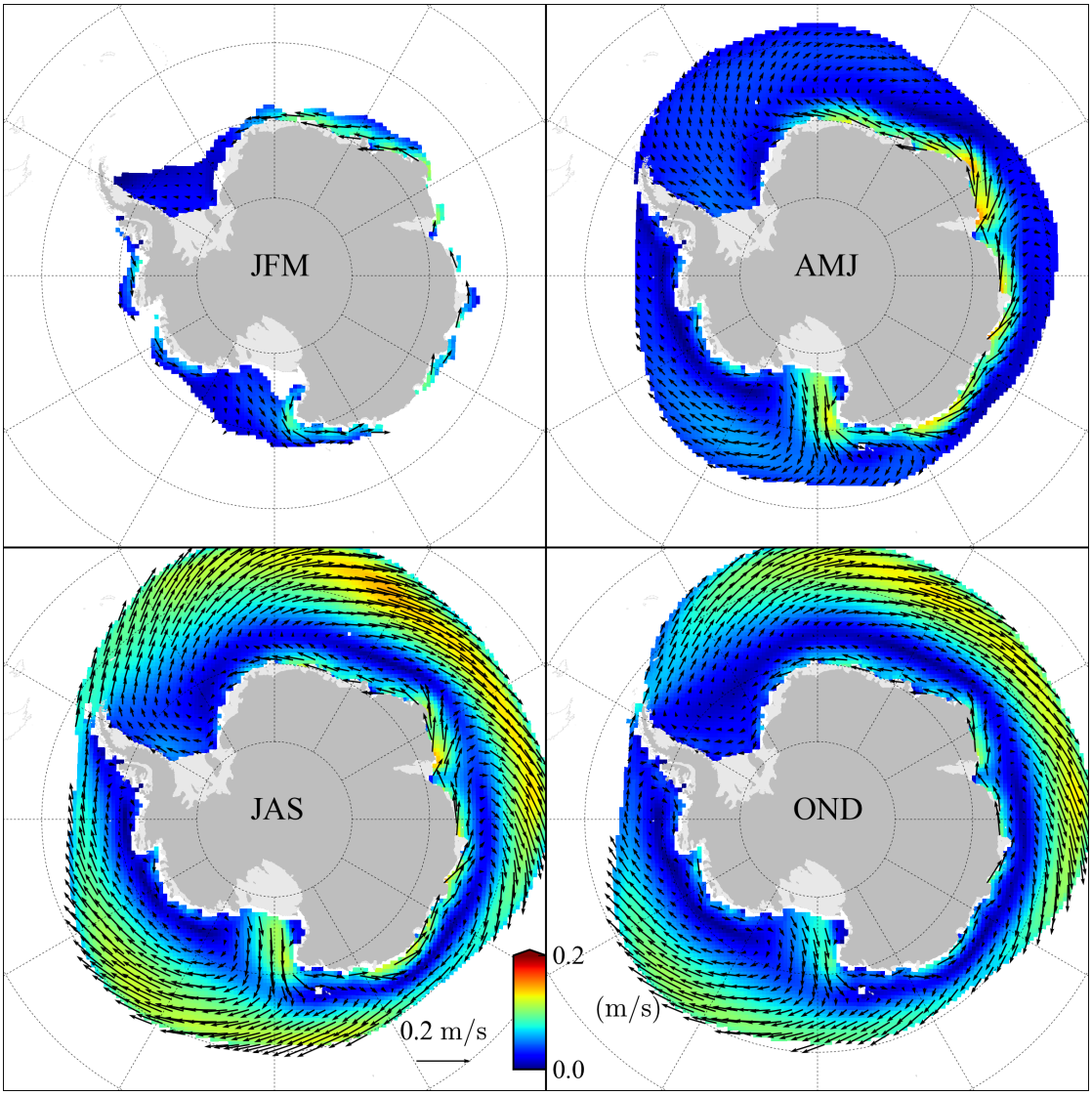

Figure 3.4: Mean (1985-2011) seasonal modelled ice motion (ice speed overlain with ice motion vectors) from the ERA-I simulation. Regions corresponding to a mean ice concentration less than 0.15 are masked in both datasets.

Antarctica as expected from both the near surface winds (Fig. 3.2) and by comparing to ice motion derived from passive microwave feature-tracking (*Holland and Kwok*, 2012).

Figure 3.5 shows the mean (seasonal) modelled ice thickness compared to observations of ice thickness from the 2003-2008 ICESat laser altimetry freeboard measurements (*Kurtz and Markus*, 2012), which assumes that the ice-snow interface is at sea level, i.e. that all freeboard is

snow and all draft is solid ice. Note that here and throughout the rest of the thesis, ice thickness refers the volume of ice per unit grid cell area. The modelled results agree well in the general location of regions of thicker and thinner ice, although the absolute values of ice thickness show differences across all seasons and regions. The modelled Weddell Sea ice thickness shows the best fit to observations throughout the year, especially in spring. The model shows a perennially thicker (∼1 m) sea ice cover in the Bellingshausen Sea which will result in lower growth and melt rates and could also prevent the advection of ice into the Amundsen Sea Embayment, where the modelled ice thickness remains very low throughout the year. The model shows perennially thin ice in the Ross Sea, however in spring this is only over the southern half of the shelf sea whereas the observations suggest it could cover a much higher fraction of the shelf sea area.

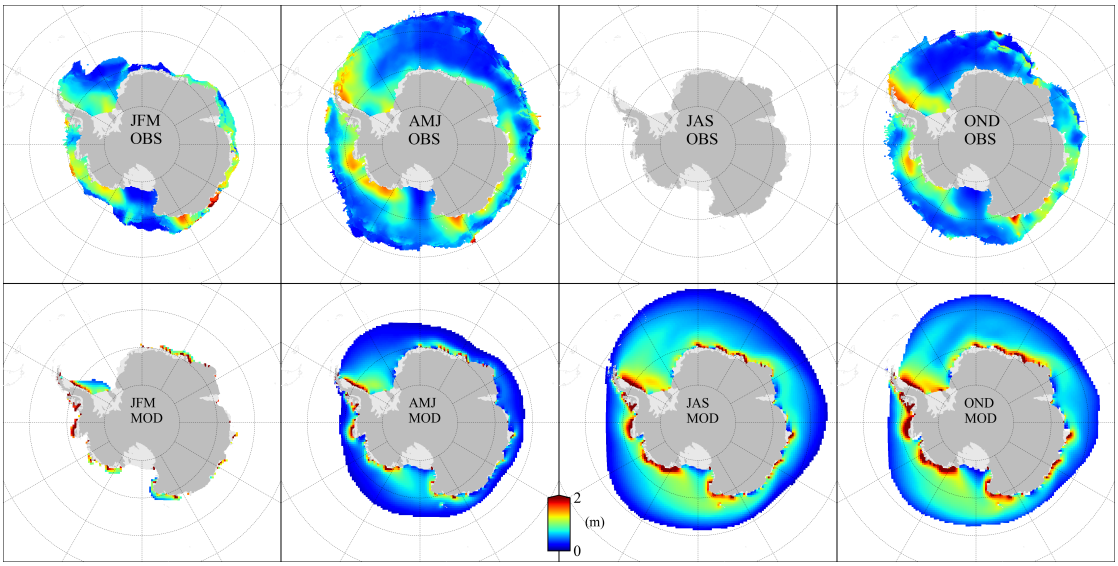

Figure 3.5: Mean (1985-2011) seasonal modelled ice thickness (volume of ice per unit grid cell area) from the ERA-I simulation (bottom row) compared to mean (2003-2008) seasonal observed ice thickness (top row). Ice thickness observations taken from ICESat measurements (*Kurtz and Markus*, 2012). Note that no observations were obtained during winter (JAS). Regions with a respective ice concentration less than 0.5 are masked in both datasets.

Only ice and not snow thickness is compared (*Kurtz and Markus*, 2012, also provides estimates of snow thickness, which is equal to the freeboard based on their methodology), as modelled snow thickness is generated using uncertain reanalysis data and carries a higher relative uncertainty in the observational estimates. Snow is important due to both its low thermal conductivity and contribution to ice volume through snow-ice conversion (*Powell et al.*, 2005),

providing a potentially large source of uncertainty within this study and similar analyses of Antarctic sea ice.

3.2.2 Mixed layer depth and shelf water formation

Figure 3.6a shows the mean (1985-2011) maximum mixed layer depth in each grid cell, demonstrating the ability of this simple mixed layer model to produce the expected pattern of shelf water formation over the Antarctic continental shelf. The mixed layer maximum (which mostly occurs in winter) is deepest in the Weddell and Ross (WR) seas, with the black crosses highlighting grid cells where the maximum mixed layer depth is greater than 90% of the water column depth. To further highlight this destratification, Fig. 3.6b shows the fraction of the water column occupied by the maximum mixed layer depth. Figure 3.6c shows the mean winter ice thickness, demonstrating a clear relationship between thin ice, high ice production, and deep mixed layers. Figure 3.7 shows the bottom salinity in summer and winter in the WR shelf seas. The summer minimum salinity fields show the data that the deep ocean is restored towards, while the winter maximum fields show that the model is producing dense waters in sensible areas and with realistic properties.

In the Weddell Sea, Figs. 3.6a and 3.7 show a complete destratification along the Ronne Ice Front, over the shallow (∼300 m) Berkner Bank in the centre of the shelf and along the Luitpold Coast up to the Brunt Ice Shelf. The summer bottom salinity in Fig. 3.7 is effectively WOA09 salinity data, due to the relatively rapid (3 month) relaxation time period, showing the highest salinities (∼34.8) in the southwest corner of the shelf (reflecting the summertime measurements of *Nicholls et al.*, 2003), fresher waters (∼34.6) over the Berkner Bank, near HSSW (∼34.7) waters in the Filchner Depression, fresher waters (∼34.6) along the Luitpold coast and lower salinity waters (≤34.5) near the Brunt Ice Shelf. In winter, complete destratification along the Ronne Ice Front causes the bottom salinity to increase to ∼34.9 in a few grid cells, due to the rapid sea ice production (discussed in more detail later). The large region of complete destratification over the shallow Berkner Bank results in little change in salinity, which is still too low to be classified as HSSW, matching well the wintertime observations of this region (*Nicholls et al.*, 2008). Both

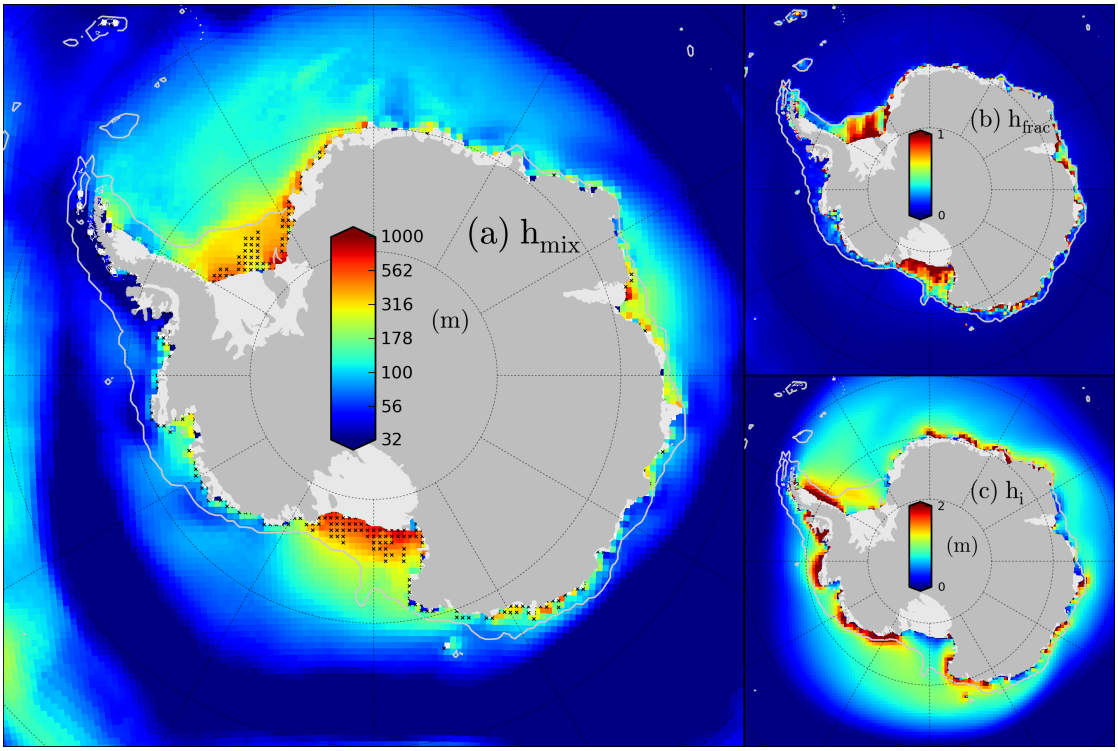

Figure 3.6: Mean (1985-2011) (a) maximum mixed layer depth, (b) fractional depth of (a) as a function of the water column depth and (c) wintertime (JAS) ice thickness (same as in Fig. 3.5) from the ERA-I simulation. Note that the colour scale and colour bar in (a) use a logarithmic (base 10) scale. The black crosses highlight grid cells where the maximum mixed layer depth is greater than 90% of the water column depth.

these results also fit well with the idea discussed by *Nicholls et al.* (2009), that Modified Warm Deep Water is modified heavily over much of the shelf, mixing with more saline waters formed close to the Ronne Ice Front to give the HSSW signature that is eventually advected off the shelf. Complete destratification along the Luitpold coast has also been observed in recent seal-tag CTD measurements (*Årthun et al.*, 2012), which, in agreement with the model, show a destratified yet low-salinity (∼34.4) water column, which is often classified as Eastern Shelf Water (ESW); salinification is suppressed by fresh Ice Shelf Water (ISW) present in the region (*Fahrbach et al.*, 1994a).

In the Ross Sea, Figs. 3.6a and 3.7 show a complete destratification over much of the southern shelf. The summertime bottom salinity in Fig. 3.7 shows LSSW along the eastern half of the Ross Ice Front (RIF) and HSSW in the western half, similar to the Weddell shelf and

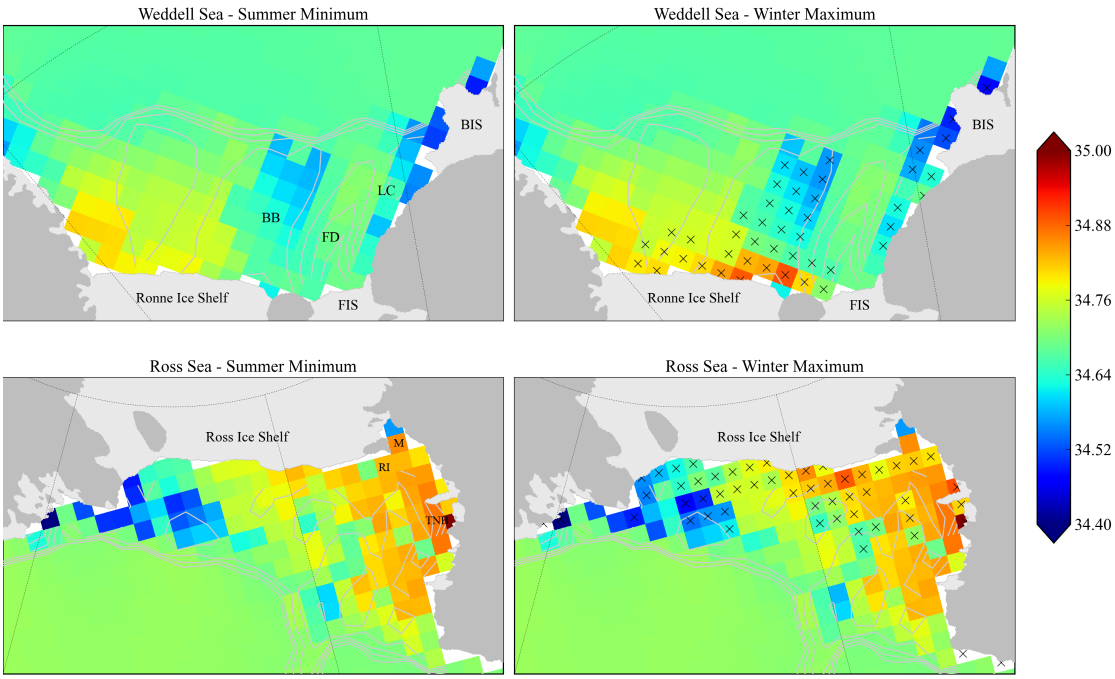

Figure 3.7: Mean (1985-2011) summer minimum and winter maximum bottom salinity of the Weddell and Ross shelf seas from the ERA-I simulation. The crosses indicate grid cells where the mean maximum mixed layer depth is greater than 90% of the water column depth. BB: Berkner Bank, FD: Filchner Depression, FIS: Filchner Ice Shelf, BIS: Brunt Ice Shelf, LC: Luitpold Coast, RI: Ross Island, M: McMurdo Sound, TNB: Terra Nova Bay.

as summarised by *Orsi and Wiederwohl* (2009). In winter, the water column destratifies along much of the RIF and towards the centre of the shelf, also in regions with a shallow water column. Similar to the Weddell Sea, there are only a few regions in which the bottom salinity increases markedly from its summertime value, despite the large region of destratification, with the deep (800-1000 m) water column possibly limiting the potential salinity increase.

Figure 3.6 shows that the winter maximum mixed layer remains very shallow (<100 m) in the Bellingshausen Sea, with the deepest (200-300 m) mixed layers found in a small coastal region of Eltanin Bay, where the observations of *Tamura et al.* (2008) show polynya formation. Deep convection from winter polynyas in Eltanin Bay is discussed in the modelling study of *Holland et al.* (2010). Observations of winter mixed layers from thermistor moorings between 2007 and 2010 (*Martinson and McKee*, 2012) show a mixed layer extending down to around 100-150 m every winter in the Marguerite Bay, while *Meredith et al.* (2010) find shallower mixed

layers further inshore. Observations of the Winter Water depth in summer (*Martinson et al.*, 2008; *Jenkins and Jacobs*, 2008) show that maximum mixed layer depths are 100-200 m over a much wider area.

The Amundsen Sea, in general, has deeper modelled maximum mixed layers in winter than the Bellingshausen Sea, with mixed layers in the embayment reaching depths of around 200-300 m and the majority of the remaining shelf sea showing mixed layers reaching depths of 100-200 m. No wintertime oceanographic sections are thought to exist from this region, however summertime observations of the Winter Water depth suggest that the mixed layer depth in the embayment, and the deepening tendency towards the coast, are accurate (*Jacobs et al.*, 2011, 2012). Modelled mixed layer depths near the shelf break are too shallow however, and a deepening to the west (*Jacobs et al.*, 2012) is not captured. These features are probably driven by Ekman convergence, which is neglected here.

3.2.3 Surface inputs of salt/freshwater and heat

This model also provides a useful tool for estimating the annual surface inputs of heat and salt into the Southern Ocean. The annual surface input of effective salt into the mixed layer is calculated from the fluxes due to ice processes and net precipitation given in Eqs.(3.23, 3.24) as

$$S_{ice}(year) = \int_{year} \widehat{F}^{i}_{salt} dt \tag{3.41}$$

$$S_{pe}(year) = \int_{year} \widehat{F}^{pe}_{salt} dt \tag{3.42}$$

where the variable S_{net} is also used in the following discussion, which is the sum of S_{ice} and S_{pe}. The annual surface input of heat to the mixed layer is calculated from the surface layer to mixed layer heat flux given in Eq.(3.21) as

$$H_S(year) = \int_{year} \widehat{F}_{sm} dt. \tag{3.43}$$

The mean annual (1985-2011) surface input of each of these variables is shown in Fig. 3.8.

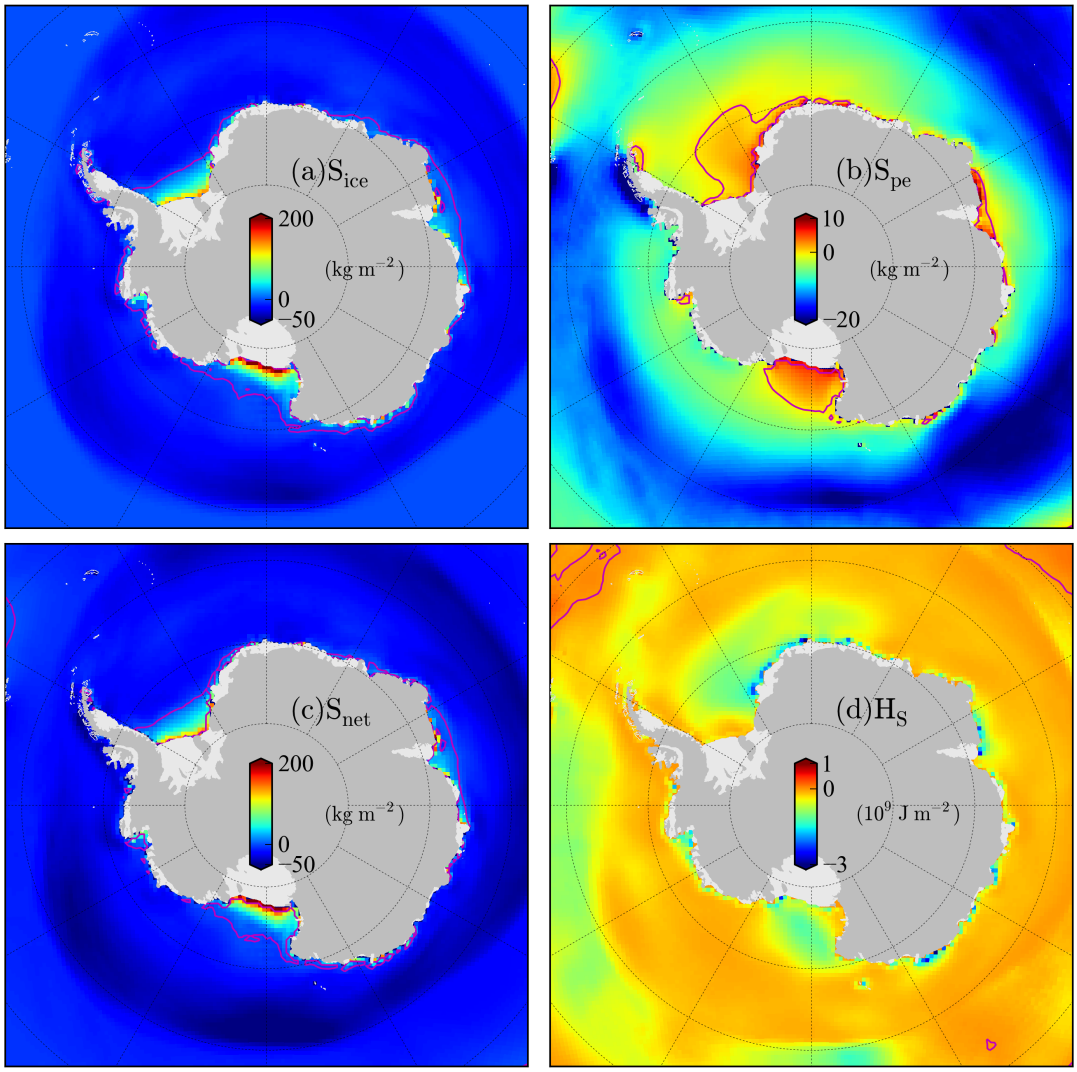

Figure 3.8: Mean (1985-2011) annual surface (effective) salt input from (a) ice/snow processes, (b) net precipitation (P-E) and the (c) the sum of these two contributions. (d) shows the mean annual surface to mixed layer heat input. All taken from the ERA-I simulation.

Figures. 3.8a–c show sea ice processes dominating the net annual effective salt input to the Antarctic shelf seas (discussed in more detail in the following section), with the net input peaking at ∼100-200 kg m^{-2} along the FRIS and RIS ice fronts. Note that the zero-contour (both from sea ice and the total) closely tracks the continental shelf break in the WR seas (as

well as off the Adélie Land coast and Cape Darnley in East Antarctica); the regions of shelf water formation around Antarctica. A small region within the Amundsen Sea Embayment also shows a net annual salt input, but this does not appear sufficient to create shelf water as demonstrated earlier. The WR also gain salt from S_{pe} (although small in comparison with S_{ice}), likely due to a combination of low precipitation (as shown in Fig. 3.2), the virtually perennial sea ice cover preventing snowfall into the shelf seas, and the strong winds increasing evaporation. The fractional contribution from net precipitation increases north of the shelf break. Virtually the entire Southern Ocean mixed layer undergoes a net annual loss of heat to the surface, with the greatest heat loss occurring in cold southern regions covered with thinner ice (compare with Fig. 3.5).

Such quantities are required boundary conditions for stand-alone ocean models, and are predominantly obtained from the results of coupled atmosphere-ocean models that often contain a simpler sea ice model (if any). A recent study by *Tamura et al.* (2011) looked at providing these quantities using a combination of ERA-I (and also NCEP2/ERA-40) atmospheric forcing data and passive microwave observations of thin ice (averaged over 1992-2007). While this approach has been shown to be useful in detecting polynya regions (e.g. *Tamura et al.*, 2008), it is highly-questionable for regions with ice thicker than several centimetres, and is therefore not thought to be an accurate method of analysing the salt flux from the more gradual pack ice growth north of the polynyas. While noting these concerns, the *Tamura et al.* (2011) study shows a peak net annual salt input of $\sim$100 kg m^{-2} along the RIF, similar to this study. The region of high salt input in the *Tamura et al.* (2011) study is within a narrow coastal region (representing the coastal polynya) and drops off rapidly, unlike the more gradual decrease towards the WR shelf break as shown in this study. A net annual effective salt input of around zero is then found over the rest of the Weddell shelf, a result that is questionable due to both the significant amounts of shelf waters (fully mixed water column) formed here, and the strong ice divergence (net export) as discussed in more detail in Sect. 3.2.5. Converting the mean surface heat flux into a mean heat energy input shows a value of $\sim$-0.5–1$\times10^9$J m^{-2} over much of the shelf, peaking at $\sim$-1.5$\times10^9$ J m^{-2} along the RIS and the northern Amundsen and Bellingshausen (AB) seas, similar to this study.

3.2.4 Mixed layer evolution

To understand in more detail the causes of the mixed layer evolution, Fig. 3.9a-d shows the (2000-2011) deconstructed input of power from the ocean surface to the mixed layer, from the following: the surface heat flux (including the transfer of latent heat from ice growth and melt) in red; the net salt flux from ice processes in blue; the freshwater flux from evaporation and precipitation in magenta; and wind shearing in green, as described in Sect. 3.1.2.2. Note that during mixed layer deepening, these terms are the fraction of power remaining after dissipative effects are taken into account. The evolution of the mean mixed layer depth over the study regions is also shown (in black) to demonstrate how the surface power input drives the mixed layer evolution. Figure 3.9 shows that in all four regions the net power input (in grey) closely follows the power input from the net salt flux due to ice growth and melt. There is a small contribution from the heat flux term, with wind mixing and precipitation minus evaporation providing a negligible impact.

Figure 3.9e shows the mean (2000-2011) net surface power input annual cycle for all four regions, highlighting the extremely low autumn/winter mixed layer power input to the AB seas compared to the WR seas. This result demonstrates that the deep mixed layers that form in the WR seas can potentially be attributed simply to a greater input of power at the surface in autumn/winter, providing further evidence to support the hypothesis of *Talbot* (1988), that regionally varying surface fluxes can directly explain the bimodal distribution in the shelf seabed temperature. However, the simplicity of the model means that a contribution to this distribution from ocean dynamics still cannot be ruled out.

In Fig. 3.9e the mean Weddell Sea surface power input appears to be roughly symmetric, with no clear winter peak. The Ross Sea mean surface power input has a more pronounced peak in August and a similar inter-annual monthly variability to the Weddell. The Amundsen Sea mean surface power input tends to peak in April, when the mixed layer is shallow, thereby reducing any dissipative effects, while the Bellingshausen Sea shows no real pattern in the peak surface power input across autumn/winter. The mean Ross surface power input is almost double the

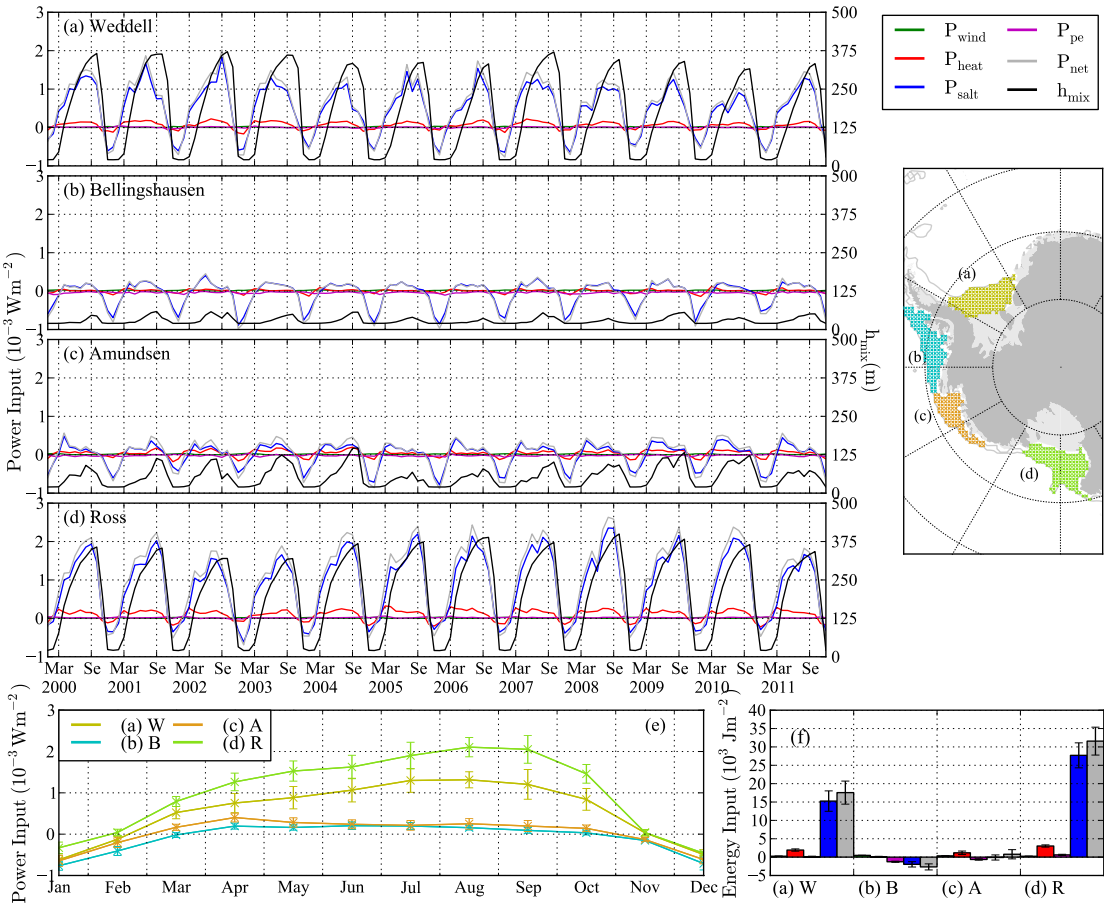

Figure 3.9: 2000-2011 regional (mean) contributions to the mixed layer evolution from the ERA-I simulation. (a) - (d) power input from wind mixing (green), the ocean-surface layer heat flux (red), the salt flux from sea ice growth/melt (blue), net precipitation minus evaporation (pink), net power input from the addition of all these four terms (grey) and the mixed layer depth (black) averaged spatially over each of the four study regions highlighted in the map shown, (e) mean 2000-2011 regional net power input annual cycle, (f) mean 2000-2011 regional energy input to the mixed layer from the time integral of each power input term (same colours as (a)-(d)). The error bars shown in panels (e) and (f) correspond to one standard deviation from the mean. The surface power inputs are described in Sect.(3.1.2.2), where the terms have been multiplied by ρ_w to express each in more suitable units.

Weddell throughout autumn/winter, however there is large inter-annual variability in the value of this maximum. The Amundsen and Bellingshausen seas experience a similar surface power input in July, with a lower surface power input in the Bellingshausen across all other months. The AB seas both experience a greater surface power output (removal of mechanical energy from the mixed layer) in summer, causing a stronger stratification and further reducing the potential

mixed layer deepening in the following winter. This effect is strongest in the Bellingshausen Sea, which has both the lowest power input and largest power output of the four regions.

Figure 3.9f shows the mean annual energy balance of the mixed layer, calculated through a time integral of the mean power input contributions for each region (as stated in Sect. 3.1.2.2), with the colours corresponding to the same terms as in Figs. 3.9a-d. A positive value denotes a net yearly input of energy to the mixed layer, with the deep ocean relaxation removing the excess energy (mainly during spring/summer, representing the advection of more saline waters off the shelf). There is a large input of energy to the WR shelf seas, driven mainly by the salt flux from sea ice growth. The Amundsen shelf sea surface energy input is well balanced, whereas the Bellingshausen shelf sea experiences a net loss of energy due to the large summer freshwater flux from ice convergence and melt and also from the freshwater flux due to precipitation. In this case, the loss of energy from the mixed layer must be balanced by diapycnal mixing, represented simply in this model by the relaxation of the mixed layer towards higher salinities.

Figures 3.9e and 3.9f show the Ross shelf atmosphere provides the greatest input of energy to the ocean, predominantly through the salt flux from ice formation, which may appear to contradict with the observation that the Weddell Sea generates the coldest and most voluminous bottom waters (*Gordon et al.*, 2010). This observation could be explained by either a difference in the waters advecting into the shelf seas that mix with the shelf waters, such as the large flux of freshwater from the Amundsen to the Ross Sea (*Assmann and Timmermann*, 2005; *Jacobs and Giulivi*, 2010), or the deeper bathymetry in the Ross Sea along the ice front (Fig. 1.3a), limiting the duration of complete wintertime destratification and thus the rate of salinification. The increase in the flux of fresh glacial meltwater into the Amundsen Sea has been implicated in the recent Ross Sea freshening, as described in Sect. 1.1.7, highlighting the additional contribution of this process, which is not explicitly included in this study of surface buoyancy fluxes.

3.2.5 Regional sea ice mass balance

As sea ice has been shown to be the dominant driver of the mixed layer evolution over the Antarctic shelf seas, the sea ice mass balance for the four separate regions is now analysed, to highlight the differences in the growth, melt and export of ice from each region. The annual difference in ice growth and melt should equal the ice exported out of the region if the ice is assumed to be in a regional steady state. The relative contributions to this balance, however, are important as they will influence the mixed layer deepening in winter and freshening in summer. If a large fraction of the ice produced in winter is exported away before it can melt in summer, deeper mixed layers would be expected than the more stable case of ice growth equalling ice melt. Alternatively a net import of ice could provide more ice to melt in summer than was produced the previous winter, providing a fresher summer mixed layer that could inhibit wintertime mixed layer deepening.

The annual ice growth and melt in a specific region (in m^3) is calculated as

$$G_i(year) = \int\int_R \int_{year} \frac{\partial V_i^T}{\partial t}\ dtdxdy \quad \text{where } \frac{\partial V_i^T}{\partial t} > 0 \tag{3.44}$$

$$M_i(year) = \int\int_R \int_{year} \frac{\partial V_i^T}{\partial t}\ dtdxdy \quad \text{where } \frac{\partial V_i^T}{\partial t} < 0 \tag{3.45}$$

where R is the regional shelf sea spatial domain and

$$\frac{\partial V_i^T}{\partial t} = A\frac{\partial h_i^T}{\partial t} + h_i\frac{\partial A^T}{\partial t} \tag{3.46}$$

where V_i is the volume of ice per unit area (in m) and the superscript T denotes the change in ice state is due to thermodynamic processes only.

The annual ice export out of a specific region (also in m^3) is calculated in a similar fashion as

$$E_i(year) = \int\int_R \int_{year} (\nabla \cdot (\mathbf{u}V_i))\ dtdxdy. \tag{3.47}$$

3.2.5.1 Results and discussion

Figure 3.10 shows the sea ice mass balance of the four study regions, with the results summarised in Table 3.1. The annual ice growth in Fig. 3.10a (converted to volume in Table 3.1) shows that the Weddell (1020±110 km^3) and Ross (1280±92 km^3) shelf seas grow 2-3 times as much ice each year compared to the Amundsen (382±23 km^3) and Bellingshausen (481±43 km^3) shelf seas. Considering the difference in the size of each shelf sea region, it is also useful to compare this in terms of the mean thickness of ice grown, which normalises the results by the area of each region. The factor of three difference in ice volume growth between the Ross and the Amundsen seas changes to a factor of two when the mean ice thickness growth is considered (2.78±0.2 m and 1.39±0.1 m respectively), due to the relatively small Amundsen shelf sea region. Switching between volume and thickness also changes the region of lowest ice growth, with the lowest mean ice volume growth in the Amundsen, but the lowest mean thickness growth in the Bellingshausen (1.20±0.1 m).

	Weddell	**B'hausen**	**Amundsen**	**Ross**
Shelf sea area (10^3 km^2)	445	398	271	462
Ice growth (m)	2.29±0.3	1.20±0.1	1.41±0.1	2.78±0.2
Ice melt (m)	0.74±0.1	0.98±0.2	0.79±0.1	0.44±0.1
Ice export (m)	1.55±0.5	0.26±0.4	0.60±0.4	2.34±0.3
Ice growth (km^3)	1020±110	481±43	382±23	1285±92
Ice melt (km^3)	330±61	389±66	214±34	203±49
Ice export (km^3)	690±240	103±150	163±120	1082±150
Polynya area (10^3 km^2)	52.0	-	-	96.8
Polynya growth (m)	4.96±0.7	-	-	5.98±0.4
Polynya growth (km^3)	258±34	-	-	578±40

Table 3.1: Mean (1985-2011) annual regional sea ice mass balance contributions from the ERA-I simulation, taken from Fig. 3.10. The errors shown correspond to one standard deviation in the inter annual variability.

Since these results are compared to studies of polynya ice growth below, an attempt has been made to estimate the ice growth from coastal polynyas. Due to the coarse grid (∼55 km) polynyas are not expected to be fully resolved by this model, so instead, grid cells with a 'high' mean monthly ice growth rate (taken to be 4 m yr^{-1}) are highlighted. This value corresponds to the lower end of the *Tamura et al.* (2008) and *Drucker et al.* (2011) scales and provides 'polynya'

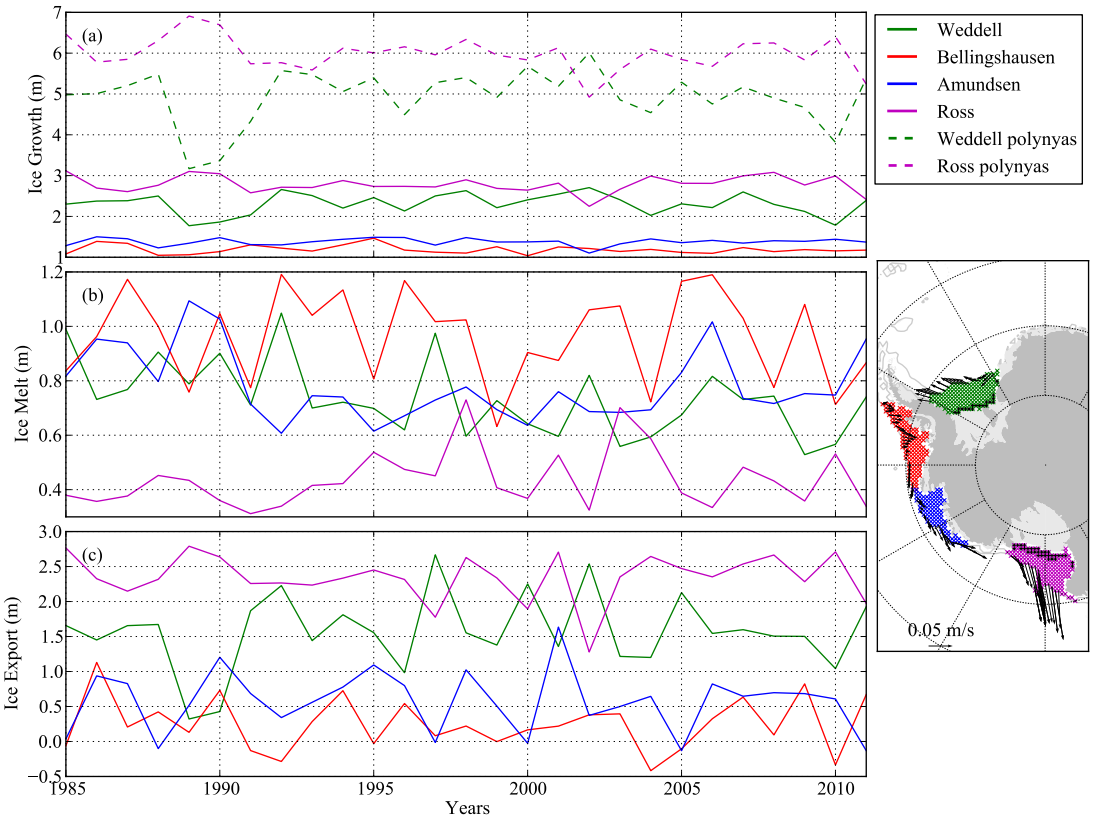

Figure 3.10: Annual (1985-2011) regional sea ice mass balance (same regions as Fig. 3.9) from the ERA-I simulation. (a) Annual regional ice production, including the contribution from rapid sea ice growth 'polynya' grid cells (marked by the black crosses) , (b) annual regional ice melt, (c) annual regional net ice export. Mean ice motion vectors for the outer grid cells of each region are shown in the map.

grid cells in reasonable locations along the Ross and Ronne ice fronts (Fig. 3.11). This gives a mean Weddell 'polynya' growth of 258±34 km^3 and a mean Ross mean growth of 578±40 km^3. To examine how sea ice growth is distributed within the shelf seas, Fig. 3.11 shows the mean (1985-2011) annual ice growth. Within the WR shelf seas, the ice growth increases towards the southern coastal ice fronts. The cause of this spatial distribution is investigated in more detail in Sect. 3.2.6. It is expected that latent heat polynyas form in these coastal regions through the strong northward advection of ice away from the coast. Despite the thin ice in the Ross Sea, it is too thick to be classified as a polynya according to the definition of *Martin et al.* (2004), who extend the definition of a polynya to include thin ice (<10-20 cm). *Markus et al.* (1998) show that the width of the coastal polynyas in the Weddell Sea can be as low as 5 km in winter,

considerably less than the grid cell width of ∼55 km used in this study, meaning the simulation of either thin ice (<0.20 m) or a near-zero ice concentration is very unlikely. The Ross Sea polynya is much wider (see Fig. 2 in *Drucker et al.*, 2011), which is why more evidence of 'polynya' activity is observed along the Ross Ice front in spring. Figure 3.11 shows the highest modelled mean annual ice growth at around 8 m per year, less than the maximum values found in the observational study of *Drucker et al.* (2011), which calculates a maximum growth of ∼15 m yr^{-1} in the Weddell and ∼28 m yr^{-1} in the Ross, however the larger area the modelled ice growth is calculated over balances the lower area-averaged growth rate.

The precise role and importance of coastal polynyas in shelf-water formation is still under investigation, and a number of recent observational studies have attempted to quantify the ice growth from coastal polynyas in the Weddell Sea (*Markus et al.*, 1998; *Renfrew et al.*, 2002; *Drucker et al.*, 2011), Ross Sea (*Martin et al.*, 2007; *Comiso et al.*, 2011; *Drucker et al.*, 2011) and the entire Antarctic (*Tamura et al.*, 2008). *Renfrew et al.* (2002) calculate a mean (1992-1998) ice growth in the Ronne Polynya (adjacent to the Ronne Ice Shelf) of 110±30 km^3, similar to the *Markus et al.* (1998) mean (1992-1994) growth of ∼87 km^3, the *Tamura et al.* (2008) mean (1992-2001) growth of 85 ± 25 km^3, and the *Drucker et al.* (2011) mean (1992-2008) growth of 100±12 km^3. *Drucker et al.* (2011) also calculate the ice grown in the Eastern Weddell Polynya (EWP) adjacent to the Brunt Ice Shelf, along with a small contribution from a stationary iceberg A23, finding a mean total Weddell polynya ice growth of 240±30 km^3. This compares well to the simulated Weddell polynya growth of 258±34 km^3 found in this study. Comparing to the modelled shelf sea ice growth of 1020±110 km^3 shows the mean observed Ronne polynya growth accounts for around 10% of the total ice growth and the total Weddell polynya growth from both observations and this study accounts for around 20% of the total ice growth. This matches well the salt/heat budget calculation made by *Nicholls et al.* (2009), who showed that the heat loss from the Ronne polynya of around 3.5×10^{19}J from the *Renfrew et al.* (2002) study accounts for only 10% of the 3×10^{20}J heat loss needed to convert MWDW to HSSW, as mentioned in the introduction (Sect. 1.1.1). Including an additional 10% of the total heat loss from the EWP, the remaining 80% of ice growth occurs more gradually over the broader shelf sea and is a process lacking in observational analyses. The close fit to this theoretical ratio is an encouraging

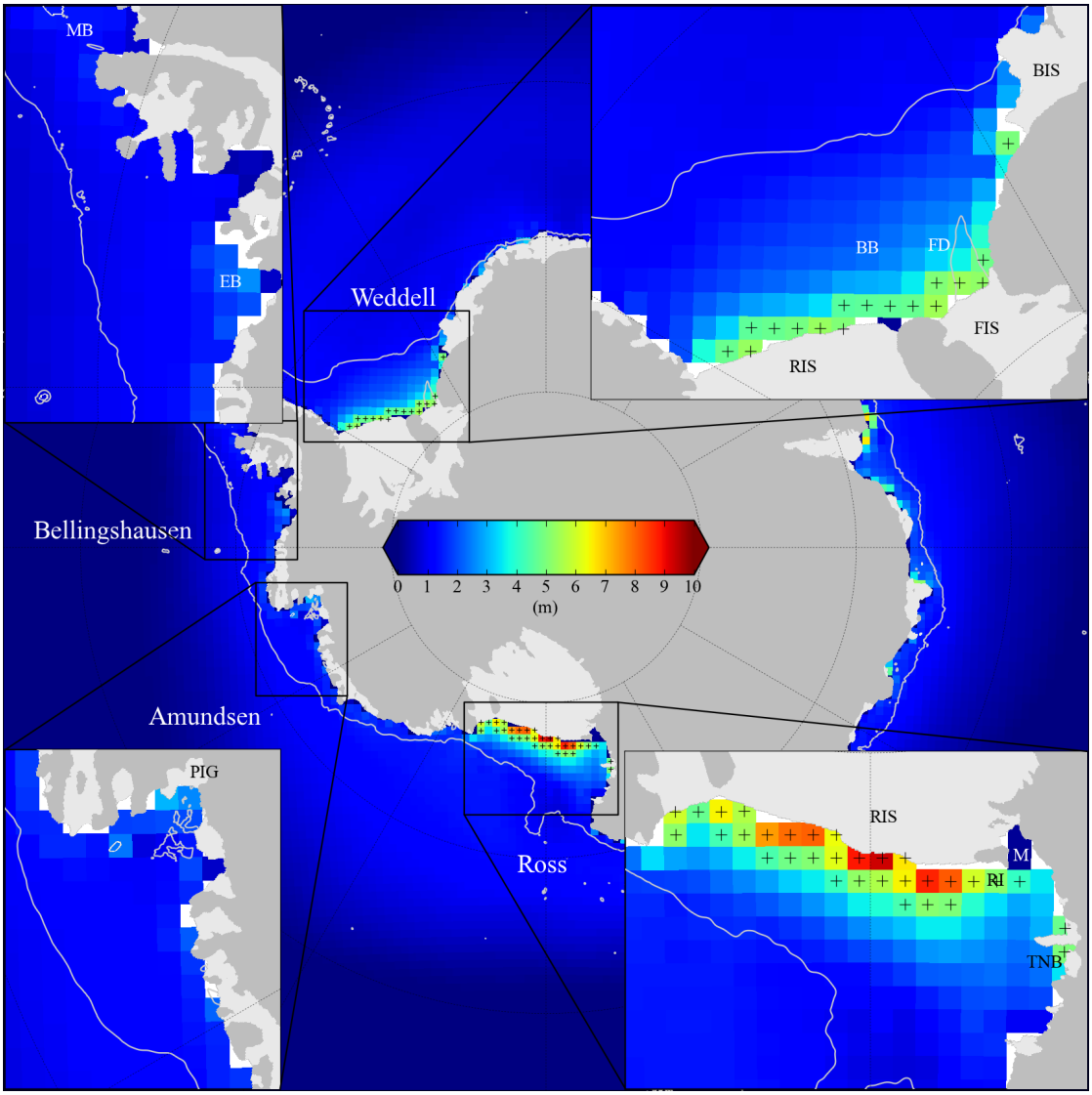

Figure 3.11: Mean (1985-2011) annual ice growth from the ERA-I simulation. Crosses mark the grid cells where the mean annual ice growth is greater than 4 m. The white line is the 1000 m isobath contour taken from the RTOPO dataset (*Timmermann et al.*, 2010). BB: Berkner Bank, FD: Filchner Depression, FIS: Filchner Ice Shelf, BIS: Brunt Ice Shelf, MB: Marguerite Bay, EB: Eltanin Bay, PIG: Pine Island Glacier, RIS: Ross Ice Shelf, RI: Ross Island, MS: McMurdo Sound, TNB: Terra Nova Bay.

validation of the model.

In the Ross Sea, *Martin et al.* (2007) calculate a mean (1992-2002) ice growth in the coastal polynyas (Ross, McMurdo Sound and Terra Nova Bay polynyas) of 500±160 km^3, similar to the

Tamura et al. (2008) mean (1992-2001) growth of 450±140 km^3, while *Drucker et al.* (2011) calculate a higher mean (2003-2008) growth of 740±90 km^3. In all cases, the Ross Sea Polynya (RSP) dominates, providing ∼80-90% of the total polynya ice growth. The earlier polynya studies are within error of the modelled polynya estimate of 578±40 km^3 and comparing these values to the modelled total Ross shelf sea ice growth of 1285±92 km^3 shows the Ross polynyas contributing around half of the total sea ice growth.

Using this same ice growth calculation procedure, the total ice growth of the Weddell (0-60°W) and Ross (135°W-195°W) seas, including over the deep ocean, can be estimated, resulting in a mean (1985-2011) growth of 4,580±280 km^3 in the Weddell, and 4,564±270 km^3 in the Ross, considerably higher than the 1,800 km^3 Weddell ice volume estimate of *Renfrew et al.* (2002). In this study, the Weddell shelf sea contributes around 20% to the total Weddell ice growth and the Ross shelf sea contributes around 30% to the total Ross ice growth.

Comparing the mean annual ice growth map in Fig. 3.11 with the shelf water formation in Fig. 3.7, it is clear that high rates of ice growth are not strictly necessary to cause a complete destratification of the water column. In both regions, the formation of shelf waters (where the water column is fully mixed) extends further north by several grid points from the coast, with an even larger destratification region over the relatively shallow Berkner Bank in the Weddell, which sees only 1-2 m of ice grown each year. It is worth noting, however, that despite the destratification, this does not lead directly to the formation of HSSW but is indirectly important in HSSW formation through the conversion of large volumes of Modified Warm Deep Water to near HSSW. The consistent growth rate along the Ronne Ice Front demonstrates the impact of bathymetry on shelf water formation, as briefly discussed in the previous section, which shows HSSW formation occurring in regions where the water column is at its shallowest (at the southern Berkner Bank). This highlights the potential impact bathymetry can have on HSSW formation, providing further evidence to the claim that the deeper water column along the Ross Ice Front prevents the Ross from producing more HSSW than the Weddell.

Figure 3.10b shows the annual regional ice melt. The Bellingshausen shelf sea has the highest mean annual melt (0.98±0.2 m) despite having the lowest mean annual ice growth,

compared to the Amundsen (0.79±0.1 m), Weddell (0.74±0.1 m) and Ross (0.44±0.1 m) seas. No observational studies of Antarctic ice melt are thought to currently exist, preventing validation of these modelled results. The high Bellingshausen ice melt is due to the strong import of ice (discussed in more detail in the next paragraph) combined with a warm summertime atmosphere. The Amundsen shelf sea also experiences a relatively warm summer and there is a ready supply of ice to melt through the continuous advection of ice from the Bellingshausen Sea. The Ross Sea rapidly advects ice away from the shelf, reducing the amount of ice available to melt in summer. The Weddell Sea also advects ice northwards but at a slower rate than the Ross, increasing the amount of ice available to melt. Both the Ross and the Weddell shelf seas are forced by a colder atmosphere in summer than the AB seas.

The annual regional ice export is shown in Fig. 3.10c. Note the high inter-annual variability in ice export compared to the other two terms in the sea ice mass balance. There is a large export of ice from the Weddell (1.55±0.5 m) and Ross (2.34±0.3 m) shelf seas and a low export from the Amundsen (0.60±0.4 m) and Bellingshausen (0.26±0.4 m) shelf seas. The ice is advected to the north of the WR shelf seas (shown by the ice motion vectors at the shelf edge in Fig. 3.10c), driven by strong meridional winds, especially in the Ross, as shown in Fig. 3.2, removing much of the ice that is grown in winter before it is able to melt in summer (except for a period in the late 1980s where the Weddell export reduces dramatically to near the AB export). Considering the significantly higher meridional wind speed in the Ross, it is perhaps surprising that the difference between the WR export is not greater. An important factor here is the thickness of the ice that is being exported (shown in Fig. 3.5) with the thicker ice in the Weddell compensating to some degree the reduced meridional ice speed. In contrast, the eastern AB shelf seas show a net import of ice, which is strongest in the eastern Bellingshausen sea, although this is exceeded by a net export of ice to the west of each region. Despite a mean net export of ice out of the Bellingshausen shelf sea, a net import (negative export) is within one standard deviation of the mean. Ice advection between the Bellingshausen and Amundsen seas likely plays an important role in each regional mass balance, however due to the thin width of the connecting shelf sea and the complex coastal geometry of the Amundsen Sea Embayment, it is unlikely this model will capture the process accurately, as discussed earlier in Sect. 3.2.1.

Comparing the modelled ice export with observations in the Weddell Sea, *Drucker et al.* (2011) calculate a mean (1992-2008) export of 390±130 km^3 (through a straight-line flux-gate centred over the 1000 m deep shelf break) using the motion-tracking area flux estimation of *Kwok* (2005) combined with an ICESat estimate of Weddell shelf sea ice thickness (0.75±3 m) of *Yi et al.* (2011). This is the only known estimate of Weddell shelf ice export and is lower than, but within error of, the 690±240 km^3 value found in this study.

Drucker et al. (2011) calculate a mean (1992-2008) Ross ice export of 700±350 km^3 using the motion tracking area flux estimation of *Kwok* (2005) and in-situ Ross shelf sea ice thickness (0.6±0.3 m) of *Jeffries and Adolphs* (1997). This is similar to the *Comiso et al.* (2011) value of 600±470 km^3 which used a similar method and dataset. These values are lower than, but within error of, the 1082±150 km^3 value found in this study. In both cases, the *Kwok* (2005) flux-gate used lies to the north of the shelf break in the east, where there is a tendency for ice import, and to the south of the shelf break in the west ,where there is a tendency for export. It is therefore expected that the *Comiso et al.* (2011) and *Drucker et al.* (2011) estimates are a lower bound of the expected export past the 1000 m isobath contour. The only other known estimate of Ross export is that of *Jacobs et al.* (2002), which used a simple calculation involving NCEP surface winds and the *Jeffries and Adolphs* (1997) ice thickness to obtain an estimated export of 1000±300 km^3, closer to the value found in this study.

There has been little observational analysis of the AB shelf sea ice growth and export. *Tamura et al.* (2008) show that there are potentially small coastal polynyas in the Eltanin Bay in the Bellingshausen Sea, corresponding to the peak region of ice growth in the Bellingshausen shelf sea shown in Fig. 3.11, and in the Amundsen Sea Embayment, which is not apparent in this study. *Assmann and Timmermann* (2005) is the only study known that has attempted to quantify the ice transport through the Amundsen Sea, using the Bremerhaven Regional Ice Ocean Simulations (BRIOS) model, calculating a mean (1978-2001) annual ice export of 536±350 km^{-3}. This value is higher than, but within error of, the calculated export of 163±120 km^3 found in this study. The region in *Assmann and Timmermann* (2005) for which ice export is calculated, extends further north of the shelf break, increasing the potential advection of ice to the north.

3.2.6 Linear regression analysis

To understand the link between spatial and temporal atmospheric variability on the surface-driven deepening of the mixed layer, this section investigates the linear correlation between various atmospheric variables and the net surface power input to the mixed layer in autumn/winter (April-September). Specifically, Table 3.2 demonstrates the spatial correlation between the mean (1985-2011) autumn/winter atmospheric forcing and the mean (1985-2011) autumn/winter surface power input, with one point used for each grid cell within the regions shown in Fig. 3.9. Figure 3.12 demonstrates the temporal correlation between the shelf-sea mean autumn/winter atmospheric forcing to the shelf-sea mean autumn/winter net surface power input, with one point used for each year for each region. This regression is shown graphically to demonstrate the variability in the mean atmospheric forcing over each of the shelf seas. The potential for summer stratification preconditioning the following winter mixed layer deepening has been discussed previously (e.g. by *Meredith et al.*, 2004a, in the Bellingshausen Sea) and so it is included as a further variable in both studies. All variables are regressed against the mean net surface power input in autumn/winter (April-September) as this represents both the mixed layer deepening and potential salinification of the mixed layer. Note that in the following discussion, a 'weak' correlation implies an $r^2 < 0.2$, a 'moderate' correlation implies an r^2 of 0.2-0.5, and a 'strong' correlation implies an $r^2 > 0.5$. Correlations discussed are significant at 99% unless otherwise stated (correlations $< 99\%$ are also listed in the table/figure).

Considering the significant intra-regional spatial correlations (r^2 values) listed in Table 3.2, the temporal mean Weddell autumn/winter net surface power input shows: strong spatial correlation to the summer (January-March) net surface power input (0.55); moderate correlation to incoming shortwave radiation (0.43), specific humidity (0.30) and air temperature (0.24); and weak correlation to the zonal wind speed (0.18) and meridional wind speed (0.07). The Bellingshausen autumn/winter net surface power input shows: moderate correlation to the meridional wind speed (0.33), air temperature (0.27), incoming longwave radiation (0.25) and specific humidity (0.23); and weak correlation to the incoming shortwave radiation (0.18) and zonal wind speed (0.18). The Amundsen autumn/winter net surface power input shows: moderate correla-

P_{net}^{A-S}	**Weddell**	**Bellingshausen**	**Amundsen**	**Ross**
T_a	**0.25** (−)	**0.28** (−)	**0.12** (−)	**0.54** (−)
Q_a	**0.31** (−)	**0.23** (−)	**0.13** (−)	**0.44** (−)
F_{lw}	0.04 (−)	**0.26** (−)	**0.13** (−)	0.02 (−)
F_{sw}	**0.42** (−)	**0.21** (−)	**0.12** (−)	**0.36** (−)
P	0.00 (+)	0.02 (−)	0.00 (+)	**0.09** (−)
U_m	**0.19** (+)	**0.32** (+)	0.01 (+)	0.00 (+)
V_z	**0.06** (−)	**0.34** (+)	0.04 (+)	0.00 (−)
P_{net}^{J-M}	**0.54** (+)	0.00 (+)	**0.27** (+)	**0.81** (+)

Table 3.2: Spatial linear regression (from the ERA-I simulation) of the temporal mean (1985-2011) autumn/winter (April-September) net surface power input to the mixed layer against the temporal mean (1985-2011) autumn/winter: 2 m air temperature, 2 m specific humidity, incoming longwave radiation, incoming shortwave radiation, total precipitation (rain and snow), 10 m zonal (positive eastwards) wind speed, 10 m meridional (positive northwards) wind speed, and summer net surface power input, for the regions shown in Fig. 3.9. Each regressed data point corresponds to a specific grid cell and represents the anomaly between the grid point temporal mean value and the spatial/temporal mean shelf sea value. The coefficient of determination (r^2) is shown in the table, where significant (>99%) correlations are highlighted in bold. The sign in the bracket indicates the sign of the respective r-value.

tion to the summer net surface power input (0.26); and weak correlation to the specific humidity (0.14), air temperature (0.14), incoming longwave radiation (0.14) and incoming shortwave radiation (0.13). The Ross autumn/winter net surface power input shows: strong correlation to the summer (January-March) net surface power input (0.81) and air temperature (0.54); moderate correlation to specific humidity (0.44) and incoming shortwave radiation (0.36); and weak correlation to precipitation (0.09) and the zonal wind speed (0.08).

It was expected that the air temperature would show a strong spatial correlation to the autumn/winter net surface power input, based on the previous chapter, which demonstrated the strong impact of air temperature on mixed layer depth variability. However, the previous chapter carried out an inter-regional sensitivity study as opposed to the intra-regional correlations shown above. The more sophisticated 2-D ice dynamics of CICE complicates the results of the simple sea ice model further by advecting ice into neighbouring grid cells, affecting their resultant thermodynamic behaviour. A combination of low air temperatures, high ice growth and strong net export of ice out of a grid cell should lead to a consistently stronger winter destratification, i.e. the process taking place along the coastal ice fronts, where ice is only advected northwards without any import of ice from the south. The perennially thin ice cover in the Ross Sea probably

explains the greater correlation between intra-regional atmospheric variability and the net surface power input, with the thicker ice present in the other shelf seas insulating them against any intra-regional atmospheric variability. The lack of strong spatial correlation with the winds is unsurprising, as it is the ice divergence that plays the crucial role locally, where the divergence is expected to be at a maximum near the coast, which might not necessarily correspond to regions of stronger winds. The high ice growth rates near to the coast and the continuous export of ice to the north in the Weddell and Ross Seas (as described earlier in Sect. 3.2.5) will lead to a greater autumn/winter net surface power input and will reduce the availability of ice to melt in summer. This could also explain the strong correlation between the summer net surface power input and autumn/winter surface power input as opposed to the causative impact of less summer melt and therefore a less stratified summer water column on the subsequent mixed layer deepening. However, this could also be an additional positive feedback.

Considering the significant spatial (shelf-sea) mean temporal correlations (r^2 values) shown in Fig. 3.12, the spatial mean Weddell autumn/winter net surface power input shows: strong temporal correlation to the meridional wind speed (0.59); moderate correlation to the summer net surface power input (0.35), specific humidity (0.34), incoming longwave radiation (0.35), precipitation (0.30) and air temperature (0.28); and weak correlation to the zonal wind speed (0.18, 97%). The mean Bellingshausen autumn/winter net surface power input shows strong correlation to the incoming longwave radiation (0.68), air temperature (0.66), precipitation (0.64), specific humidity (0.63) and meridional wind speed (0.60). The mean Amundsen autumn/winter power input shows: strong correlation to the meridional wind speed (0.77), air temperature (0.76), incoming longwave radiation (0.71) and specific humidity (0.70); moderate correlation to precipitation (0.49); and weak correlation to the incoming shortwave radiation (0.16, 96%) and summer net surface power input (0.15, 95%). The mean Ross autumn/winter net surface power input shows: moderate correlation to the zonal wind speed (0.47), precipitation (0.39), incoming shortwave radiation (0.38) and incoming longwave radiation (0.37); and weak correlation to the specific humidity (0.26), air temperature (0.24) and summer net surface power input (0.22, 98%). Note that all variables in this temporal correlation show less variance than in the spatial correlations described above (i.e. atmospheric and summer power input show greater spatial

variance within each shelf sea compared to the mean shelf sea temporal variability).

The mean shelf sea autumn/winter net surface power input shows a strong temporal correlation to most of the thermodynamic forcing variables in the AB shelf seas, especially for air temperature, specific humidity, incoming longwave radiation and precipitation, which are all strongly coupled through cloud formation. The weaker correlation to these variables in the WR may be due to ocean feedbacks as a result of deeper mixed layers such as an enhanced ocean heat flux, or the weaker correlation between the atmospheric variables due to stronger winds. The strong correlation to meridional winds compared to zonal winds in the AB can be explained by the mean ice motion and geometry of the regions (Fig. 3.4). Only a more northward (positive) meridional wind anomaly could increase divergence, as a more westward (negative) zonal flow would simply increase both the import of ice from the east and export to the west of each region.

An interesting result is the lack of correlation between the net surface power input and the meridional wind speed in the Ross Sea. Intuitively, stronger meridional winds might be expected to result in greater net ice divergence and thus increased ice production, as seen in the Weddell. Figure 3.13 shows the correlations of further temporal linear regressions that were carried out to investigate this in more detail. Figure 3.13a shows the correlation between the annual Ross ice export (E_i) and the spatial mean autumn/winter zonal and meridional wind speed, demonstrating a moderate correlation between the ice export and the zonal wind speed (0.28), but no correlation to the meridional wind speed. Figure 3.13b then shows a moderate anti-correlation (0.27) between the autumn/winter meridional and zonal wind speeds. These results are thought to be due to the location of the Amundsen/Ross Sea pressure low (as discussed in more detail by *Comiso et al.*, 2011), where specific locations of the low change the orientation of the isobars across the shelf, meaning greater meridional winds thus appear to reduce the zonal component of the wind (less eastward) and vice versa. Cape Adare in the east of the Ross shelf sea appears to hinder the export of ice out of the shelf, as demonstrated by the thick ice produced along the coast here (Fig. 3.5). A more eastward wind direction will result in ice being advected more perpendicular to both the ice front and shelf break, away from the Cape Adare coast, potentially increasing ice export. The ocean turning angle (Eq. 3.40) probably

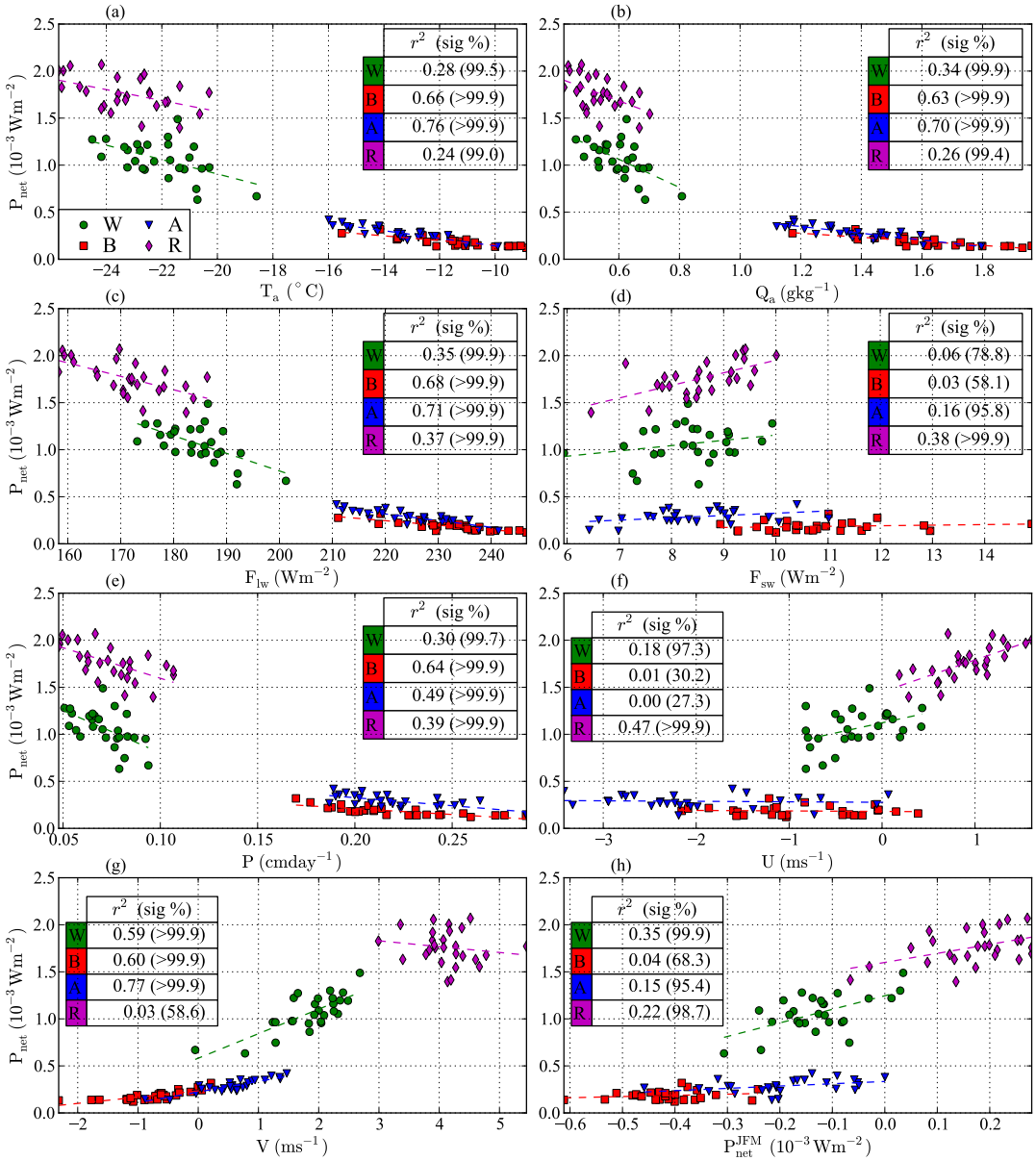

Figure 3.12: Linear temporal correlation (from the ERA-I simulation) of the spatial (shelf sea) mean autumn/winter (April-September) net surface power input to the mixed layer against the spatial mean autumn/winter (a) 2 m air temperature, (b) 2 m specific humidity, (c) incoming longwave radiation, (d) incoming shortwave radiation, (e) total precipitation (rain and snow), (f) 10 m zonal wind speed, (g) 10 m meridional wind speed and (h) summer net surface power input, for the grid points representing each region shown in Fig. 3.9. Each coloured data point represents a shelf sea and corresponds to the shelf sea annual value. The linear regression lines of each shelf sea dataset are shown by the dashed lines, with the coefficient of determination (r^2) and significance of the correlation shown in the tables within each panel.

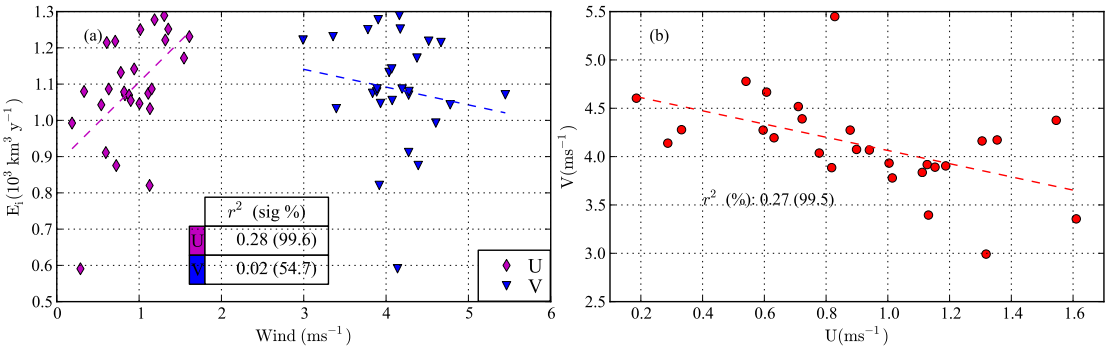

Figure 3.13: Linear temporal correlation (from the ERA-I simulation) of the (a) annual Ross ice export against the spatial mean autumn/winter 10 m zonal (purple diamonds) and meridional (blue triangles) wind speed, and (b) the spatial mean Ross autumn/winter 10 m zonal wind speed against the spatial mean Ross autumn/winter 10 m meridional wind speed. Each data point corresponds to the Ross shelf annual value.

plays an important role here due to the leftward deflection of the ice motion in response to the predominantly meridional winds (see Figs. 3.2 and 3.4). The mean zonal wind speed shows greater variance than the meridional winds, making the process described more likely to generate an observable difference in ice export compared to changes in the meridional winds. Another complicating factor in this discussion is the impact of ice thickness on the resultant link between winds and export, which was highlighted by *Comiso et al.* (2011) as a key area of uncertainty in such discussions.

3.3 Chapter Conclusions

In this chapter, a prognostic mixed layer model has been incorporated into the Los Alamos sea ice model CICE, to investigate the cause of regional variations in the formation of Antarctic shelf sea waters. This model captures reasonably well the expected ice concentration and sea ice thickness distribution through comparison to observations and produces deep (>500 m) mixed layers in the Weddell and Ross shelf seas each winter as expected. This results in a fully mixed (destratified) water column along the southern coastal ice fronts in both seas, leading to HSSW formation. The water column is also destratified in shallow regions further north (e.g. the Berkner Bank in the central Weddell shelf), which do not lead to HSSW formation but do provide an important

mechanism through which Modified Warm Deep Water (MWDW) is converted to near HSSW. Shallow mixed layers form in the Amundsen (∼200 m) and Bellingshausen (<100 m) shelf seas. Southern Ocean maps of the effective salt input at the surface show sea ice processes dominating the total surface input, with the entire Weddell and Ross shelf seas receiving an annual input of effective salt each year.

Deconstructing the surface power input to the mixed layer, shows the effective salt flux from sea ice growth/melt dominates the evolution of the mixed layer in all regions, with a smaller contribution from the surface heat flux. The Weddell and Ross shelf seas receive a net input of energy at the surface (mainly through the autumn/winter salt flux), which is used to convert MWDW to HSSW, with the excess energy removed each year through deep-ocean restoring, which represents ocean dynamics neglected by this model. The Amundsen shelf sea is well-balanced, with the surface input of energy in autumn/winter balanced by the loss of energy from surface forcing in spring/summer. The Bellingshausen shelf sea experiences an annual surface energy deficit, due primarily to a strong freshwater flux in spring/summer.

An analysis of the sea ice mass balance demonstrates the contrasting growth, melt and export of ice in each region. The Ross shelf sea has the highest mean annual ice growth, followed by the Weddell shelf sea, with the two regions growing two/three times as much ice as the Amundsen and Bellingshausen shelf seas. Despite this, the Bellingshausen shelf sea has the highest mean annual ice melt of the shelf seas, driven in large part by the warm summer atmosphere and continuous ice import from the northeast, which explains the strong summer stratification and shallow mixed layers that form here in winter. In contrast, a large fraction of the ice that is grown over the Weddell and Ross shelves is exported to the north each year ($\gtrsim$40% and $\gtrsim$70% respectively). These results compare well to the estimated ice growth needed for MWDW-HSSW conversion in the Weddell Sea calculated by *Nicholls et al.* (2009), and both the Weddell and Ross export estimates lie within the range calculated by *Drucker et al.* (2011). Comparing the modelled ice growth estimates to the polynya ice growth observations suggest the coastal polynyas contribute ∼20% of the Weddell shelf sea ice growth and around half of the Ross shelf sea ice growth. Sea ice growth outside the Ross and Weddell coastal polynyas is therefore expected to be an important shelf sea process that currently lacks much observational

analysis.

A linear regression analysis is performed to determine the temporal and spatial correlations between the autumn/winter mixed layer power input and several atmospheric variables. The Weddell and Ross temporal mean autumn/winter power input shows strong spatial correlation to the summer power input and moderate correlation to the autumn/winter air temperature, specific humidity and incoming shortwave radiation. The Bellingshausen temporal mean autumn/winter power input shows moderate spatial correlation to the autumn/winter air temperature, specific humidity, incoming shortwave, incoming longwave and the meridional wind speed. The Amundsen temporal mean autumn/winter power input only shows a moderate correlation to the summer power input.

The Amundsen and Bellingshausen spatial (shelf-sea) mean autumn/winter power input shows strong temporal correlation to the autumn/winter air temperature, specific humidity, incoming longwave radiation and precipitation. The Weddell and Ross spatial (shelf-sea) mean autumn/winter power input show only a moderate correlation to the same atmospheric variables. All regions show strong temporal correlation between the spatial (shelf-sea) mean autumn/winter surface power input and the meridional wind speed except the Ross, which instead shows moderate correlation to the zonal wind speed. Further regressions demonstrate that this may be due to the Ross shelf-sea geometry and impact of the ocean turning angle on ice motion, with a more zonal wind preventing ice build up along the Cape Adare coast in the eastern Ross shelf sea.

Chapter 4

Recent and Future Trends in the Antarctic Sea Ice and Mixed Layer

> "Ice contains no future, just the past, sealed away. As if [it's] alive, everything in the world is sealed up inside, clear and distinct. Ice can preserve all kinds of things that way - cleanly, clearly. That's the essence of ice, the role it plays."
>
> — Haruki Murakami; *Blind Willow, Sleeping Woman*

This chapter uses the CICE-mixed layer model to investigate recent and future trends in the sea ice and mixed layer over the Antarctic continental shelf. The ERA-I simulation of the previous chapter is used to examine recent trends, while the atmospheric forcing output from the HadGEM2-ES General Circulation Model (GCM) is used to simulate long-term trends. Section 4.1 presents the HadGEM2-ES forced simulation, including a comparison to the ERA-I forced simulation. Section 4.2 analyses the trends in both atmospheric forcings. Section 4.3 investigates the resulting trends in the Antarctic sea ice concentration, thickness and motion, comparing to observations where possible. Sections 4.4–4.6 analyse trends in the sea ice mass balance, the surface input of salt and heat, and the mixed layer depth, within each of the four shelf sea study regions. Concluding remarks are given in Sect. 4.7.

4.1 Results from the HadGEM2-ES Forced Simulation

The atmospheric forcing output of a single climate model involved in the Coupled Model Intercomparison Project - Phase 5 (CMIP5), part of the upcoming IPCC Fifth Assessment Report (AR5), is used to investigate long-terms trends in the Antarctic sea ice and mixed layer. Using just one climate model output allows for the thorough analysis of the atmospheric forcing trends and the direct impact of the regional forcing trends on the Antarctic sea ice and mixed layer. Unfortunately, General Circulation Models (GCMs) have been shown to do a poor job of reproducing observed trends in Antarctic sea ice extent (*Turner et al.*, 2013b) and even in correctly simulating Antarctic shelf water and thus bottom water formation (*Heuzé et al.*, 2013). Note that this does not include reanalyses, such as the ERA-I output presented in the previous chapter, as these are constrained by available observations. Despite these concerns, GCMs provide the only method of investigating long-term (future) trends in the Antarctic climate system. The validity and potential accuracy of the long-term trends are discussed throughout the chapter, however at the very least, the forcing provides a physically consistent climate projection over the coming century, which can be used to understand the potential sensitivity of the sea ice and mixed layer to a moderate climate warming signal. The sea ice and mixed layer trends resulting from this long-term moderate warming signal will also provide an interesting context to the trends found in the short-term (1985-2011) ERA-I simulation, which are also investigated in this chapter.

Long-term (1980–2099) atmospheric forcing data are taken from the Hadley Centre Global Environmental Model, version 2, Earth System (HadGEM2-ES) configuration GCM (*Jones et al.*, 2011), under the Representative Concentration Pathway 4.5 (RCP4.5). HadGEM2-ES was chosen as it was shown to be one of the best CMIP5 models in simulating observed sea ice trends and bottom water formation, although the model still differs substantially from reality (*Turner et al.*, 2013b; *Heuzé et al.*, 2013). RCP4.5 is a 'moderate' scenario of increased greenhouse gas emissions and land-use change, which stabilises radiative forcing at 4.5 W m^{-2} (approximately 650 ppm CO2e) by 2100 (a more detailed summary of this pathway is given by *Thomson et al.*, 2011). As HadGEM2-ES was part of the CMIP5, the representation of a realistic decline and recovery of stratospheric ozone was also required. The HadGEM2-ES atmospheric forcing data consist

of: daily fields of air temperature (2 m), specific humidity (2 m), zonal and meridional winds (10 m), and downward shortwave and longwave radiation; and monthly fields of precipitation (snow and rain). The usefulness of any future climate projection is limited by its ability to reproduce at least a reasonable initial (mean) state, therefore the following sub-sections compare the HadGEM2-ES simulation to the ERA-I simulation (over the same 1980-2011 time-period). The comparison also provides a simple yet useful demonstration of the potential importance of atmospheric forcing in accurately simulating the observed Antarctic sea ice state.

4.1.1 HadGEM2-ES and ERA-I atmospheric forcing comparison

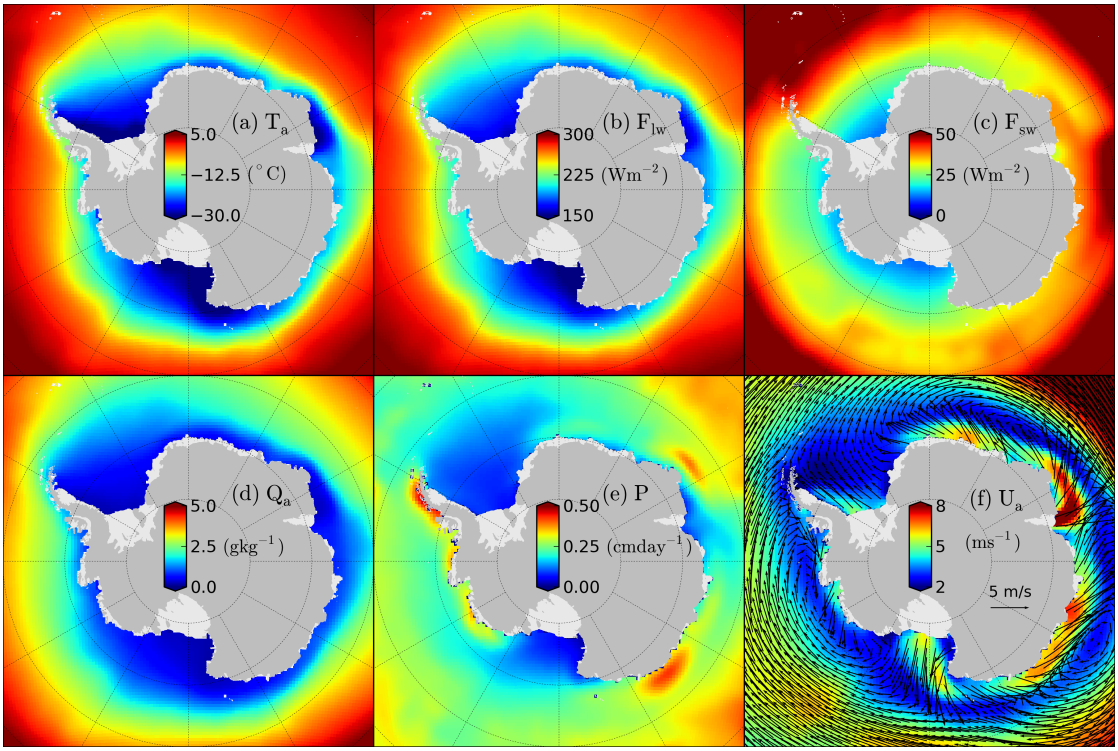

Figure 4.1: Mean (1980-2011) winter (JAS) atmospheric forcing from HadGEM2-ES. (a) 2 m air temperature, (b) Incoming longwave radiation, (c) incoming shortwave radiation, (d) 2 m specific humidity, (e) total precipitation (snow and rain) and (f) 10 m wind speed, overlain with 10 m wind vectors (every third grid point).

Figure 4.1 shows the mean (1980-2011) winter HadGEM2-ES atmospheric forcing. Comparing this to the ERA-I forcing, over the same time period (shown previously in Fig. 3.2),

demonstrates, in general, a good agreement across all forcing variables. The HadGEM2-ES forcing captures the key bimodal pattern over the shelf seas, with lower air temperature, incoming longwave radiation, specific humidity and precipitation over the Weddell and Ross (WR) shelf seas. It appears the bimodal distribution is enhanced in the HadGEM2-ES forcing, with even lower air temperatures (∼-30°C) observed over the WR shelf seas. The winds show differences between the two forcings, with stronger off-shore winds over the Weddell shelf and weaker winds over the Ross shelf in the HadGEM2-ES forcing. The impact of this difference in winds on ice motion is discussed in Sect. 4.1.2.2.

4.1.2 Modelled sea ice comparison

4.1.2.1 Ice concentration

Figure 4.2 shows the mean (seasonal) modelled ice concentration from the ERA-I and HadGEM2-ES simulations (1985-2011) compared to observations derived from passive microwave emissions using the Bootstrap algorithm (*Comiso*, 1999, updated 2012) (note that the ERA-I comparison to observations was also shown previously in Fig. 3.3).

The HadGEM2-ES forced simulation also does a reasonable job of reproducing the observed seasonal sea ice cycle (over recent decades). There is an improvement of the winter and spring ice concentration over the ERA-I simulation, although this is not of great importance considering the primary aims of this study as the ice extent during these months is well away from the shelf break, as previously discussed. There is a slight underestimation of the ice concentration in autumn, especially in the Weddell, Bellingshausen and Amundsen seas. The summer results are similar to ERA-I and also suffer from lower than observed concentrations.

4.1.2.2 Ice motion

Figure 4.3 shows the mean (seasonal) modelled ice motion using the HadGEM2-ES forcing (the ERA-I results were shown previously in Fig. 3.4).

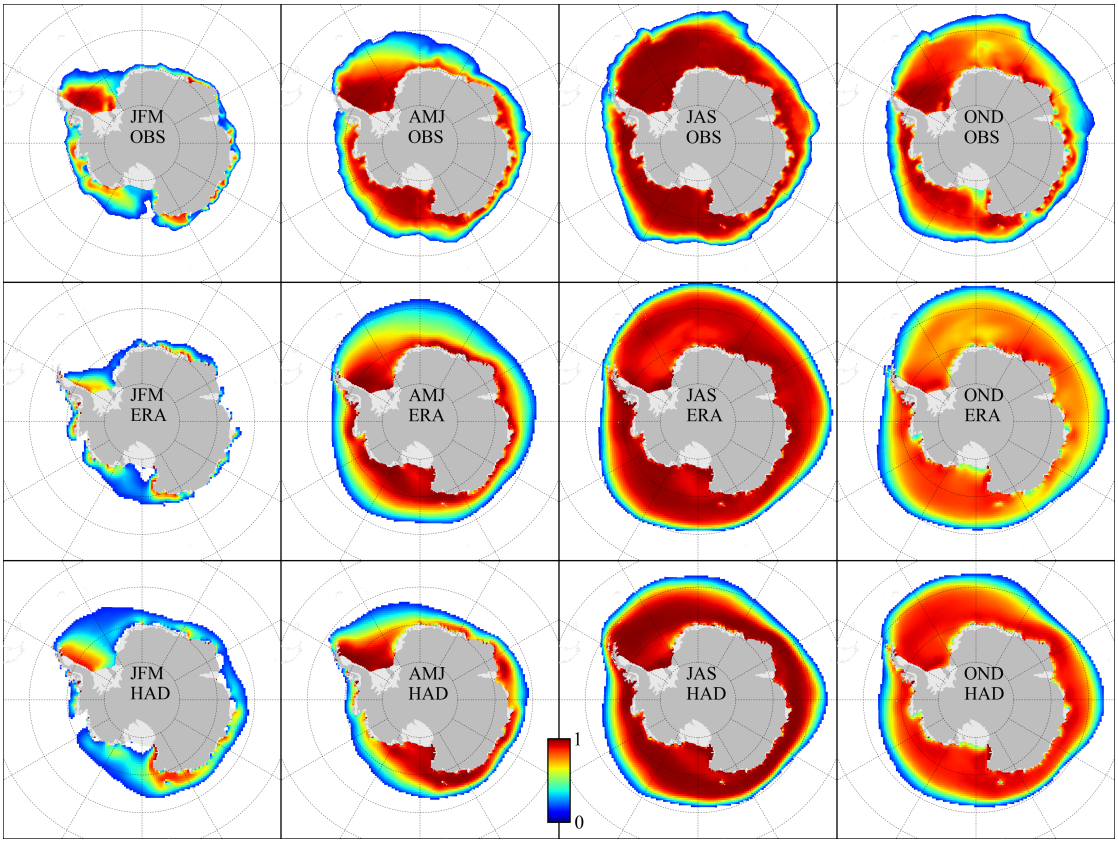

Figure 4.2: Mean (1985-2011) seasonal ice concentration from observations (top row), the ERA-I simulation (middle row), and the HadGEM2-ES simulation (bottom row).Observations are calculated using the Bootstrap algorithm (*Comiso*, 1999, updated 2012). Ice concentrations less than 0.15 are masked in all datasets.

The clear difference between the HadGEM2-ES and ERA-I ice motion is the lack of strong circumpolar ice motion in the HadGEM2-ES results, which could explain the reduced ice extent in autumn/winter (which actually leads to a better fit to observations). The strong circumpolar ice motion, however, is clearly evident in observations of ice motion derived from passive microwave feature-tracking (*Holland and Kwok*, 2012). There is a particularly strong advection of ice originating from Cape Darnley through autumn and winter, however this is not a region of concern in this study. The Weddell shelf sea ice motion is stronger (more meridional) in the HadGEM2-ES simulation; a potential overestimation when compared to observations. In the Ross Sea, it appears that the majority of the ice turns westward after it is advected past the shelf break. The *Holland and Kwok* (2012) observations and the ERA-I results suggest instead that a

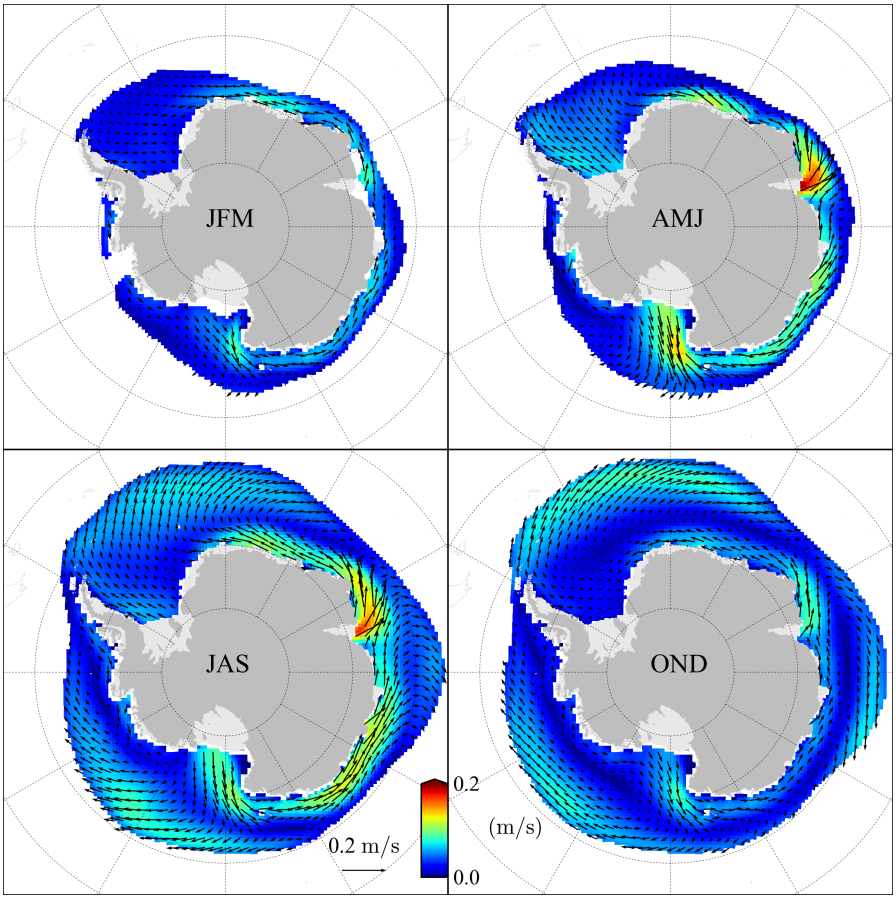

Figure 4.3: Mean (1985-2011) seasonal modelled ice motion (ice speed overlain with ice motion vectors) from the HadGEM2-ES simulation. Regions corresponding to a mean ice concentration less than 0.15 are masked in both datasets.

small fraction should turn eastward and circulate back towards the Bellingshausen sea. A more eastward location of the Amundsen/Ross Sea pressure low is the probable explanation.

4.1.2.3 Ice thickness

Figure 4.4 shows the mean (seasonal) modelled ice thickness using ERA-I and HadGEM2-ES forcing, compared to observations of ice thickness from the 2003-2008 ICESat laser altimetry freeboard measurements (*Kurtz and Markus*, 2012). Note that the ERA-I comparison was also shown previously in Fig. 3.5.

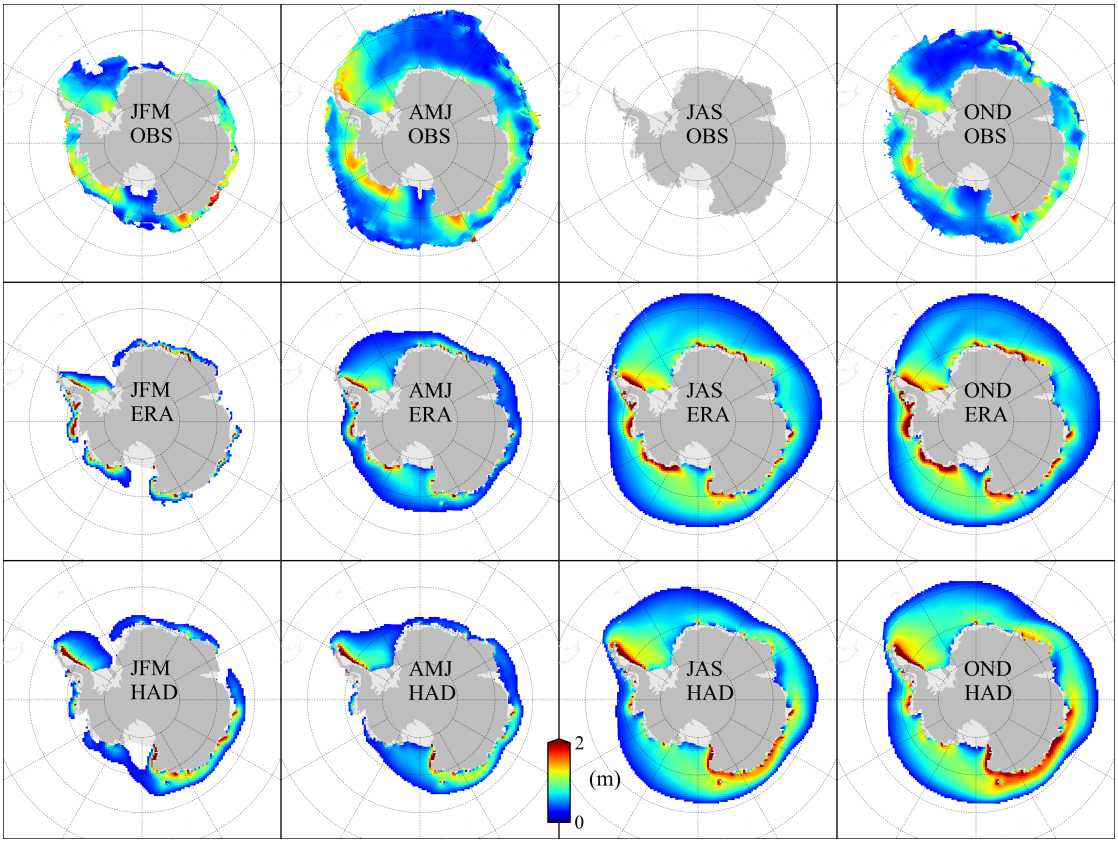

Figure 4.4: Mean (2003-2008) seasonal observed ice thickness (top row) compared to mean (1985-2011) seasonal modelled ice thickness from the ERA-I (middle row) and HadGEM2-ES (bottom row) simulations. Ice thickness observations taken from ICESat measurements (*Kurtz and Markus*, 2012). Note that no observations were obtained during winter (JAS). Regions with a respective ice concentration less than 0.5 are masked in all datasets.

The HadGEM2-ES results also agree reasonably well in the general location of regions of thicker and thinner ice. The differences between the HadGEM2-ES and ERA-I results follow a similar pattern to ice concentration. This acts to decrease the ice thickness in the Amundsen and Bellingshausen (AB) seas, bringing the thickness results more in line with observations. However, as this appears to be linked to unrealistically low ice concentrations, this does not imply a more physically realistic behaviour in the HadGEM2-ES simulation. Both simulations are seemingly unable to capture the expected distribution of thinner ice in only the southwestern and northeastern corner of the Weddell and the apparent northward extension of the thin ice cover over the entire Ross shelf during winter. The thick ice present along Cape Adare in the Ross shelf

sea extends southwards to the western Ross Ice Front in the HadGEM2-ES simulation.

The HadGEM2-ES simulation shows, in general, a good agreement to the ERA-I simulation, despite the lack of constraint to observations, providing some moderate level of confidence in the ability of this long-term forcing set to provide reasonable results.

4.2 Atmospheric Forcing Trends

As the primary focus of this chapter is on the impact of atmospheric forcing trends on the sea ice and mixed layer, this section presents and analyses trends in the ERA-I and HadGEM2-ES forcings. Inter-annual trends at each grid point are calculated using a simple linear regression from the time-series of annual (or seasons when stated) means. In the following discussion, a significant trend implies a significance greater than 90%, as highlighted in the following figures. Annual forcing trends are shown in general, as changes occurring across all seasons play an important role in the sea ice and mixed layer evolution, as demonstrated by the previous chapter.

4.2.1 Recent ERA-I atmospheric forcing trends

Linear trends in the ERA-I atmospheric forcing are shown in Fig. 4.5, demonstrating a regionally variable trend (in both magnitude and direction) across all forcings. There is a significant region of cooling over the southwestern Weddell shelf, and a small region of warming along the Ross Ice Front. There are no regions of significant warming or cooling over the Amundsen or Bellingshausen shelf seas. North of the shelf seas, there is a large significant region of cooling over the Ross Sea. Incoming longwave radiation and specific humidity show a similar regional pattern, which is unsurprising considering their strong coupling, as discussed in the previous chapter. Incoming shortwave radiation increases significantly over the central Ross shelf, and further north, showing a strong anti-correlation to air temperature, incoming longwave and specific humidity, due to the expected impact of changes in the cloud cover. Precipitation decreases significantly in the eastern Ross and shows the greatest spatial variability of all forcings.

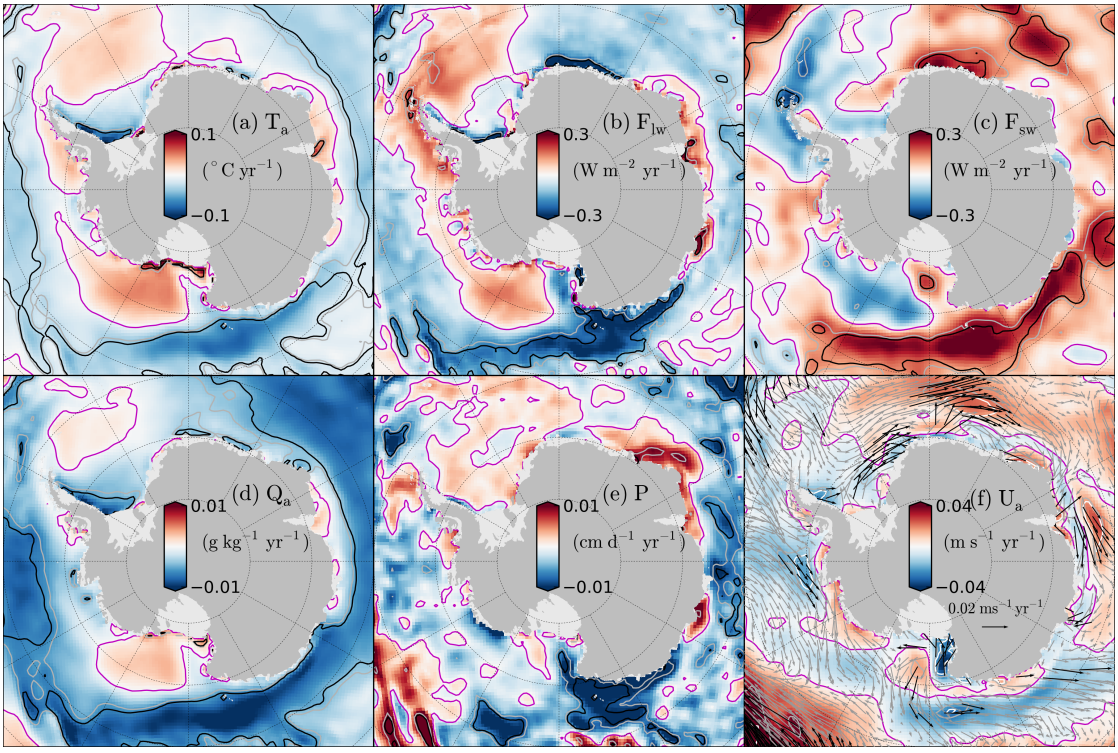

Figure 4.5: 1985-2011 linear trends in the mean (annual) ERA-I atmospheric forcing for the same variables as in Fig. 3.2. In (a)-(e), the grey and black contours indicate the significance at 90% and 95%. In (f), the grey and white contours indicate the wind speed significance at 90% and 95%, while the black vectors (arrows) indicate either the zonal or meridional wind component is significant at >90%. The magenta contour indicates the zero-trend.

The Southern Annular Mode (SAM) was discussed in the introduction (Sect. 1.3.2) as being the dominant driver of Antarctic climate variability. However, the winds show no strong evidence of the increased circumpolar westerlies north of the shelf, expected from the recent positive trend in the SAM (e.g. *Marshall*, 2002). Instead, there is stronger evidence of the zonally asymmetric pattern (e.g. a significant southward trend towards the Antarctic Peninsula and northward trend from the Ross Sea) linked to secondary modes of the SAM (e.g. *Lefebvre et al.*, 2004; *Turner et al.*, 2009). This, however, appears insufficient to generate the strong annual warming that has been observed over the Antarctic Peninsula in recent decades (*Vaughan et al.*, 2003; *Turner et al.*, 2005). The small significant northward wind trend from the central Ross shelf is balanced by a southward trend over the western shelf.

ERA-I trends have been shown to provide one of the most reliable estimates of Antarctic

climate trends (in near-surface air temperature and mean sea-level pressure), compared to other reanalyses (*Bracegirdle and Marshall*, 2012). *In situ* meteorological data coverage of Antarctica and the surrounding seas is severely limited. However, measurements of the mean sea level pressure over the Bellingshausen Sea using ice-drifiting buoys, also show ERA-I trends to be the most accurate of several reanalyses, implying a similar level of accuracy in the neighbouring Amundsen Sea (*Bracegirdle*, 2013).

The ERA-I near-surface air temperature trends can also be compared with surface temperature trends derived from satellite infrared radiometer data (*Comiso*, 2000), shown in the introduction (Fig. 1.15 in Sect 1.3.2). It is important to note the difference between the ERA-I and satellite-derived temperature variables before carrying out the comparison. While ERA-I data refers to the near-surface (2 m) air temperature, the *Comiso* (2000) satellite-derived data provides the temperature of the surface or 'skin' layer directly, meaning changes to the properties of the surface (i.e. changes in ice concentration) will likely have a significant impact (e.g. as open water can increase above the freezing temperature). Despite these concerns, the satellite-derived trends compare reasonably well with the ERA-I trends in several important locations, including the warming on the western side of the Antarctic Peninsula and cooling over the western Ross Sea. Figure 1.15 shows the satellite-derived surface warming trend is significant and extends down from the western Antarctic Peninsula to the Amundsen Sea, including a strong warming signal within the Amundsen Sea Embayment, which is not apparent in Fig. 4.5a.

To investigate this in more detail, Fig. 4.6 shows a comparison of the mean seasonal trends (1985-2008) between the two datasets (the time-period of coincident data access). Figure 4.6 demonstrates a generally good level of agreement between the ERA-I and satellite-derived temperature trends, despite the difference between the two variable definitions. The best agreement appears to be in autumn, when the sea ice growth rate is at its peak. The trends start to differ in spring, and show the biggest disagreement in summer where, for example, the seasonally consistent warming trend over the AB seas, shown in the satellite-derived trend is not apparent in the ERA-I trends. The significant cooling in the ERA-I forcing over the southern Weddell Sea, does not appear (in any season) in the satellite-derived trends. These temperature trends are expected to be strongly influenced by sea ice trends, through e.g. changes in open water, as

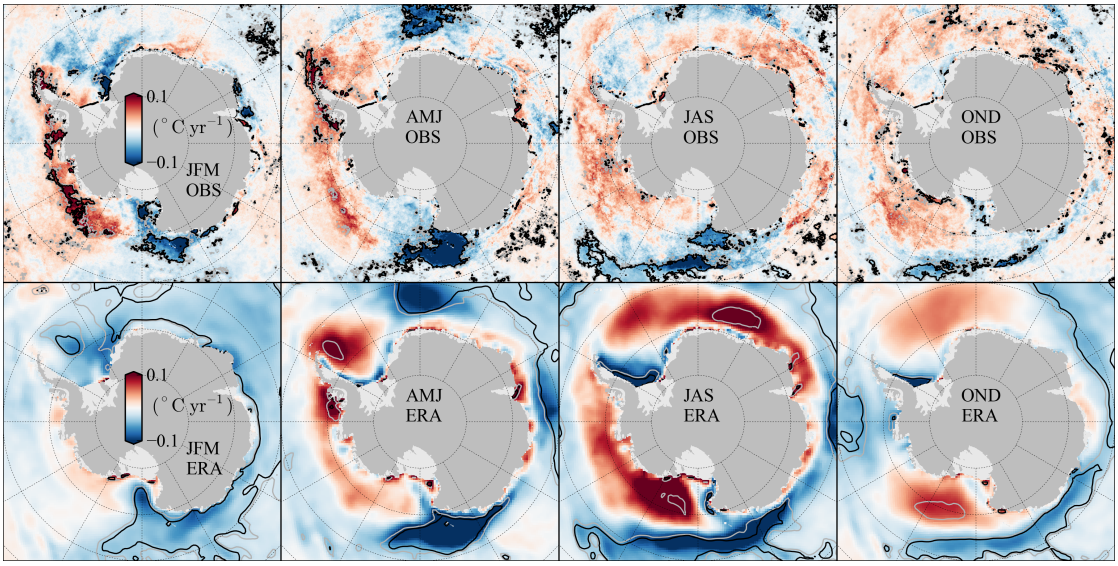

Figure 4.6: 1985-2008 linear trends (seasonal) in near-surface (2 m) air temperature from the ERA-I forcing and surface ('skin') temperature from satellite infrared radiometer data (*Comiso*, 2000). The grey and black contours indicate the significance at 90% and 95%.

discussed previously.

Along with air temperature, ERA-I was shown to offer the most reliable trends in precipitation compared to several global reanalyses (*Bromwich et al.*, 2011), although this is still expected to provide large uncertainties as it is notoriously the least accurate of all forcing variables.

4.2.1.1 ERA-I wind trends

As discussed in the introduction (Sect. 1.3.2), wind trends are thought to play the fundamental role in controlling the recent, regional trends in ice concentration (*Holland and Kwok*, 2012). It is worth noting, however, that due to inconsistencies in the retrievals during the warmer summer months, the *Holland and Kwok* (2012) study was limited to the April-October analysis period. The mean seasonal trends in the ERA-I winds are shown in Fig. 4.7 to understand potential seasonal variability in the strength and direction of the wind trends.

Figure 4.7 clearly demonstrates the strong seasonal variability in the ERA-I winds, such as

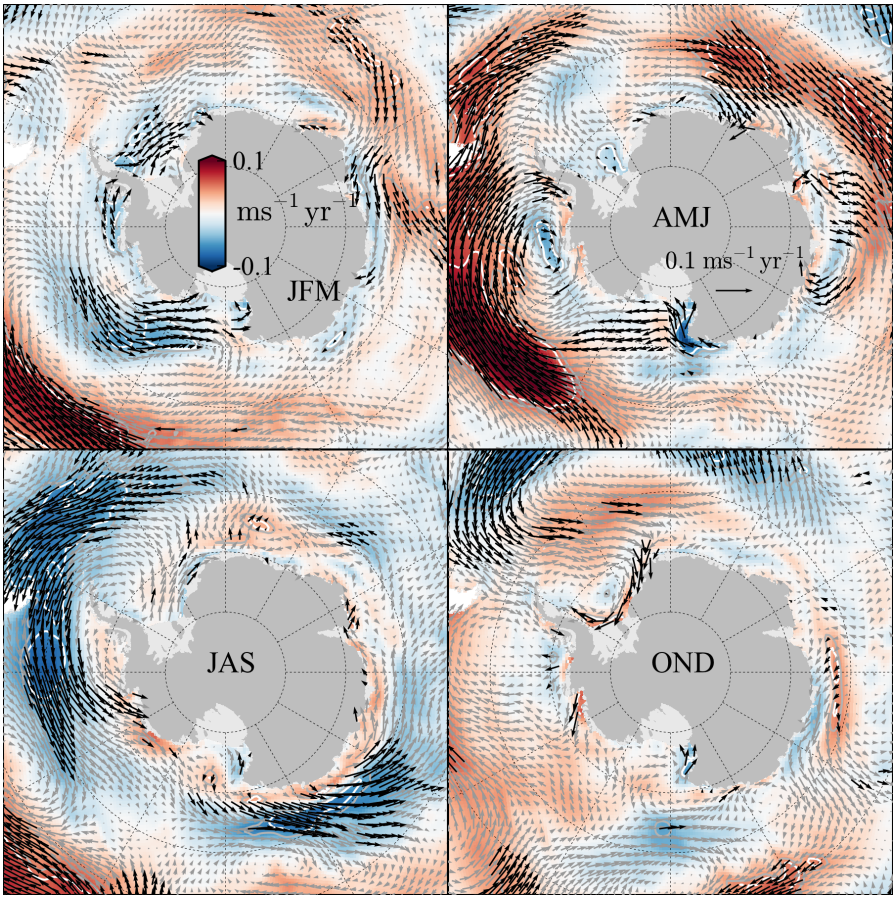

Figure 4.7: 1985-2011 linear trends (seasonal) in near-surface (2 m) winds from the ERA-I forcing. The grey and white contours indicate the wind speed significance at 90% and 95%, while the black vectors (arrows) indicate either the zonal or meridional wind component is significant at >90%.

the strong significant eastward trend in autumn and strong significant westward trend in winter around West Antarctica. There is strong evidence of both the zonally symmetric (increased westerlies) and zonally asymmetric patterns in autumn, a season of significant SAM increase (*Marshall et al.*, 2004). No such pattern is shown across the other seasons however, meaning other factors or simply natural variability are dominating the signal.

4.2.2 Recent HadGEM2-ES atmospheric forcing trends

The recent trends in the HadGEM2-ES forcing are shown in Fig. 4.8 to: demonstrate the difference between the two forcing trends; demonstrate the potential ability of the HadGEM2-ES forcing to reproduce recent atmospheric/sea ice trends; and to place the future HadGEM2-ES forcing trends in context.

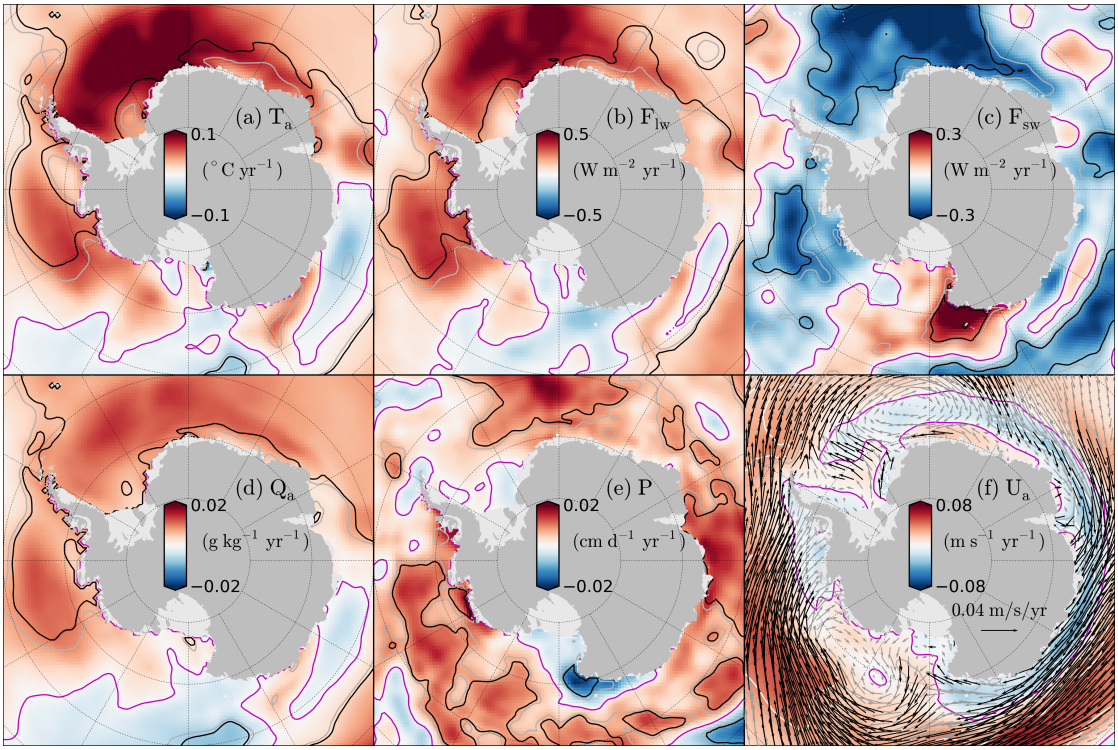

Figure 4.8: As in Fig. 4.5, but for the 1985-2011 trend in the HadGEM2-ES forcing. Note the different colour scales used in several of the panels compared to those in Fig. 4.5.

Fig. 4.8 shows large differences in the HadGEM2-ES trends compared to the ERA-I forcing. There is, in general, less regional variability, and instead a strong warming signal is observed (especially over the Weddell Sea), along with similar trends in incoming longwave, specific humidity and incoming longwave. The winds show a stronger, more significant increase in the westerlies, as expected from the positive SAM trend. However, analysing the seasonal wind trends (not shown) demonstrates that this mean annual increase takes place predominantly through spring, a season not thought to be undergoing a significant SAM increase (*Marshall et al.*, 2004), mak-

ing the physical cause of this trend inconsistent with predictions. These forcing trends further demonstrate the inability of this specific GCM to simulate realistic recent atmospheric trends around Antarctica. The impact of these trends on the Antarctic sea ice are still analysed in the following sections to demonstrate the impact of the erroneous forcing trends on the sea ice, and to place the ERA-I sea ice trends in context.

4.2.3 Future HadGEM2-ES atmospheric forcing trends

Figure 4.9 shows the long-term (1985-2099) trends in the HadGEM2-ES atmospheric forcing, demonstrating a consistent and significant trends (e.g. warming) across virtually all regions and variables, except for the Ross Sea.

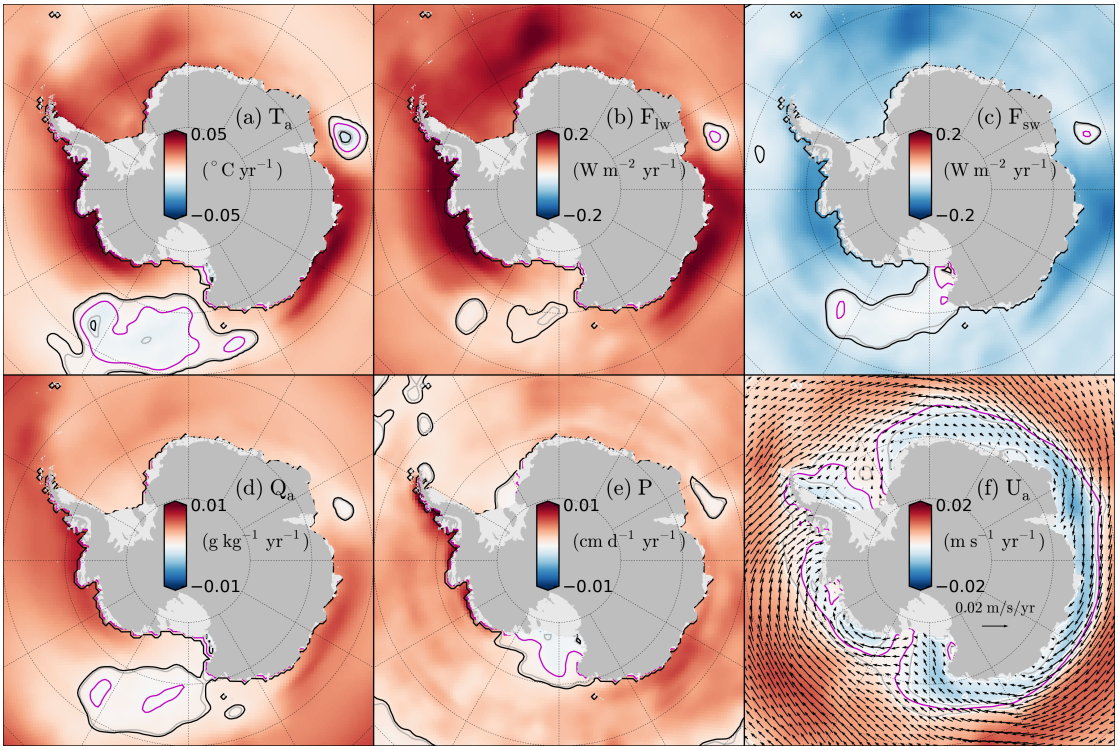

Figure 4.9: As in Fig. 4.5, but for the 1985-2099 trend in the HadGEM2-ES forcing. Note the different colour scales used in several of the panels compared to those in Fig. 4.5.

Air temperature, incoming longwave radiation and specific humidity all show a significant positive trend in the AB seas, with the Weddell Sea showing a positive but weaker trend.

These trends are of a similar magnitude to the strongest trends observed in the ERA-I forcing, despite the significantly longer time-period. The Ross Sea shows the weakest response, with large insignificant regions north of the shelf break. It is interesting to note that there are large regions that remain virtually constant, despite the long-term, moderate climate warming signal. Incoming shortwave radiation shows a similar regional pattern but with the sign of the trend reversed (consistently negative). Precipitation shows a similar (positive) regional pattern, with the strongest trends observed over the AB shelf seas, and no significant trend over the Ross shelf sea. The wind trend shows a clearer strengthening of the westerlies north of the shelf, compared to the ERA-I wind trends shown in Fig. 4.5, but with the zonally asymmetric pattern less pronounced. The seasonal wind trends (not shown) demonstrate that this westerly trend is consistent across all seasons, unlike the recent HadGEM2-ES forcing, which was dominated by the stronger trend during spring. A significant eastward (reduced) wind trend is observed over the eastern Amundsen shelf sea and a southward (reduced) wind trend over the entire Ross shelf sea.

Figure 4.10 shows the seasonal trends in the HadGEM2-ES near-surface air temperature forcing. This figure demonstrates the absence of any significant warming over the Ross shelf in winter and spring despite the moderate climate warming signal. It also demonstrates the spatial variability in the air temperature trend, with the strongest warming in autumn over the Weddell Sea, and the strongest warming in winter over the AB shelf seas.

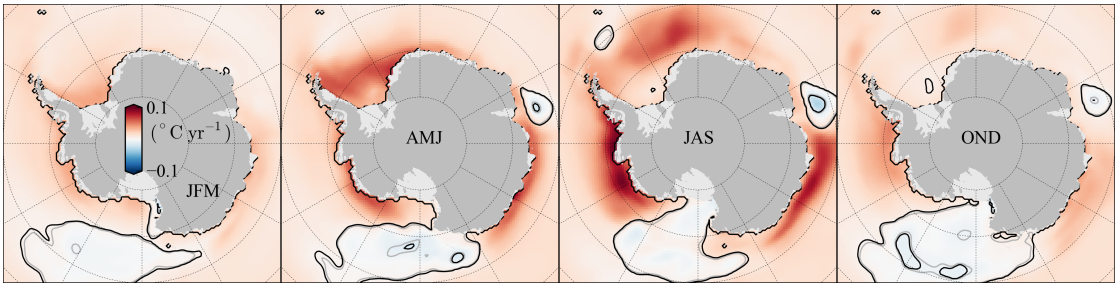

Figure 4.10: 1985-2099 linear trends (seasonal) in the near-surface air temperature from the HadGEM2-ES forcing. The grey and black contours indicate the significance at 90% and 95%.

4.3 Modelled Sea Ice Trends

In this section, the impact of the recent ERA-I and HadGEM2-ES forcing trends on the Antarctic sea ice concentration (Sect. 4.3.1), ice motion (Sect. 4.3.2), and ice thickness (Sect. 4.3.3) is analysed, before looking at future ice concentration and thickness trends from the HadGEM2-ES simulation (Sect. 4.3.4).

4.3.1 Recent ice concentration trends

Figure 4.11 shows the linear trends (1985-2011) in (seasonal) ice concentration from the ERA-I and HadGEM2-ES simulations, and observations derived from passive microwave emissions using the Bootstrap algorithm (*Comiso*, 1999, updated 2012).

The observations show, in general, a tendency for increased ice concentration in the Ross and eastern Weddell seas, and decreases in the western Weddell and Bellingshausen seas. The southern Amundsen and southeastern Ross show a decreasing trend during summer, autumn and spring, and small increases further north during autumn, winter and spring.

The ERA-I simulation agrees reasonably well with observations, showing an increase in concentration in the Ross and Amundsen seas, and a small decrease in the Bellingshausen and western Weddell seas (except in summer). The ERA-I simulation fails to produce the strong trends observed in summer, including the significant decrease over the AB shelf seas, and the significant increase in the western Ross. The ERA-I simulation does show a significant summer increase over the Weddell shelf, similar to observations, however this is not as strong as the observations suggest. As the ERA-I forcing data is constrained by observations including ice concentration, it is perhaps surprising that this simulation does not show more accurate trends. The cause of this discrepancy is unclear, however further research (e.g. through a different model configuration, using the same forcing and time-period) could be useful.

The HadGEM2-ES simulation (over the same 1985-2011 period) shows poor agreement

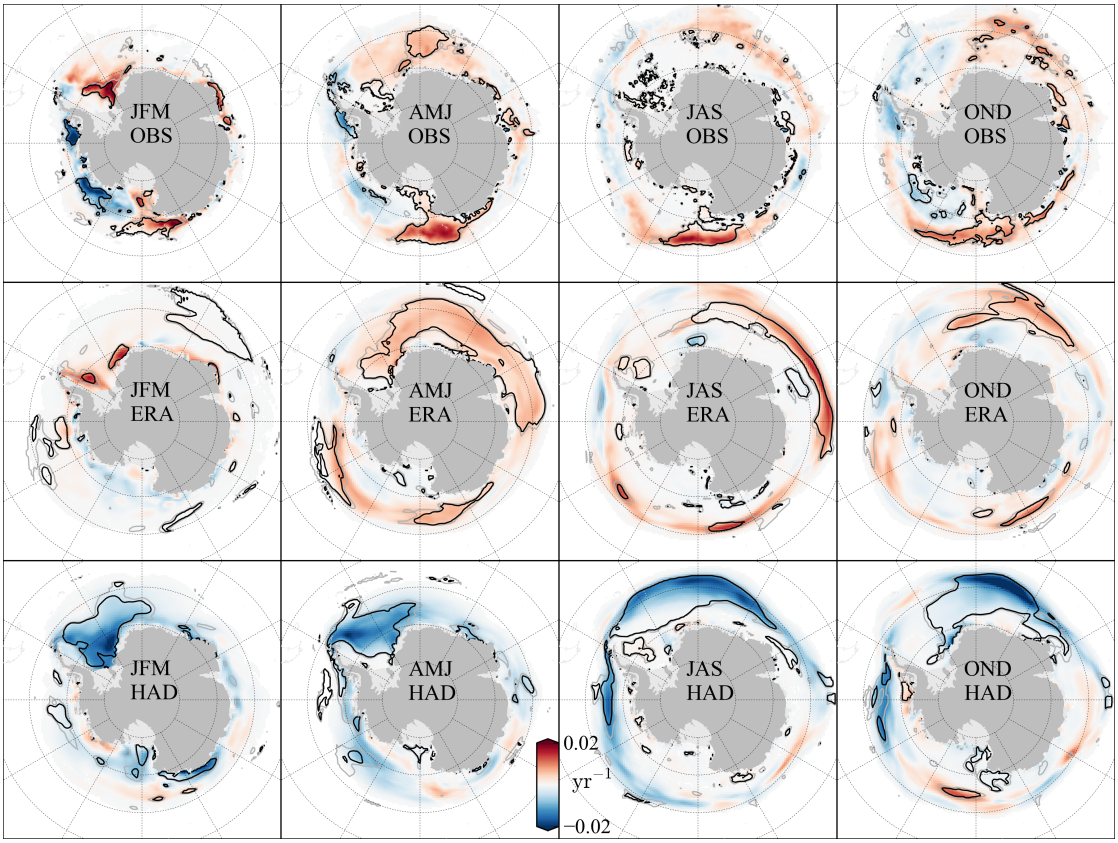

Figure 4.11: 1985-2011 linear trends (seasonal) in ice concentration from observations (top row), the ERA-I simulation (middle row), and the HadGEM2-ES simulation (bottom row). Observations are calculated using the Bootstrap algorithm (*Comiso*, 1999, updated 2012). The grey and black contours indicate the significance at 90% and 95%.

with the observed trends in ice concentration. This is unsurprising, as GCMs have consistently failed to simulate the observed trends in Antarctic sea ice extent over recent decades (*Eisenman et al.*, 2011; *Turner et al.*, 2013b). The large disagreement between the ERA-I and HadGEM2-ES winds, as shown in the previous section, is expected to be a major reason for the poor representation of concentration trends in the HadGEM2-ES simulation, due to the importance of wind-driven trends in ice concentration (*Holland and Kwok*, 2012). The following section therefore analyses the modelled trends in ice motion from both simulations.

4.3.2 Recent ice motion trends

Figure 4.12 shows the modelled trends in ice motion from the ERA-I simulation. Ice motion trends derived from passive microwave feature-tracking (*Holland and Kwok*, 2012) provide the best observational comparison, although as stated previously, surface melt leads to inaccuracies in the data during summer and spring and the need for continuous daily sampling limits the period to April-October 1992-2010, preventing a more complete comparison (the observed trends in ice motion, taken from *Holland and Kwok* (2012) were shown in Fig. 1.12).

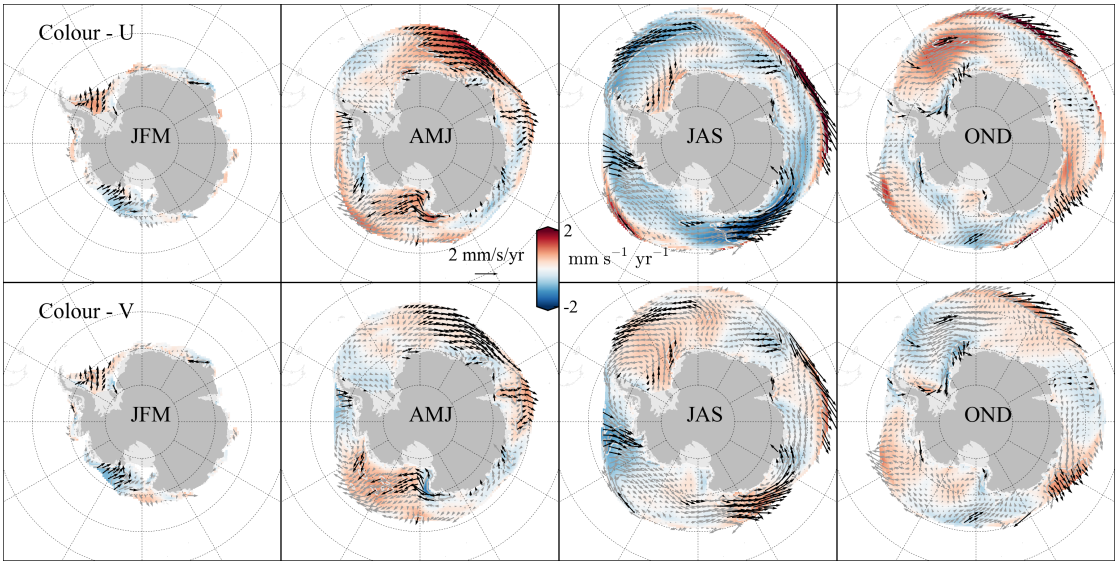

Figure 4.12: 1985-2011 linear trends (seasonal) in ice motion from the ERA-I simulation. The top row colour highlights the zonal (U) ice motion trend component (positive eastwards), while the bottom row colour highlights the meridional (V) ice motion trend component (positive northwards). Regions with a respective mean ice concentration less than 0.15 are masked. The grey and white contours indicate the significance of the relevant ice motion component at 90% and 95%, while the black vectors (arrows) indicate either the zonal or meridional component is significant at >90%.

Despite the difference in time-period, the ERA-I simulation reproduces many of the main observed ice motion features, including a northward trend in the Amundsen and Ross seas (Pacific sector) during autumn, and a southward trend in the Bellingshausen Sea (and Amundsen Sea to a lesser extent) during autumn and winter. Note that the *Holland and Kwok* (2012) study focusses on meridional ice motion trends as these are expected to play a bigger role in controlling

regional trends in ice extent. However, as the main focus of this chapter is on the ice export out of the shelf seas, zonal wind trends are expected to play an equally important role (especially in the AB shelf seas due to coastal geometry), so are also shown in Fig. 4.12. The zonal component highlights the strong westward ice motion trend in the AB seas (including over the continental shelf), and in the Ross and Weddell seas (north of the shelf break) during winter. Both the zonal and meridional trends show strong seasonal variability.

It is also worth noting that the magnitude of the modelled trends (up to ∼2 mm $s^{-1}yr^{-1}$) is lower than the *Holland and Kwok* (2012) observed trends (up to ∼5 mm $s^{-1}yr^{-1}$). This may be expected from the difference in the regression time-periods, however carrying out the analysis for the same time-period and monthly range (not shown) still results in an underestimation. While CICE is one of the most sophisticated sea ice models available, the rheology and wind drag parameterisations, which play a crucial role in the coupling between wind and ice motion, are still an active area of research (e.g. *Tsamados et al.*, 2013). In this study, ocean currents are neglected, which could also provide a significant impact on the magnitude and direction of the ice motion trends, although observations of even the mean ocean currents surrounding Antarctica remain sparse.

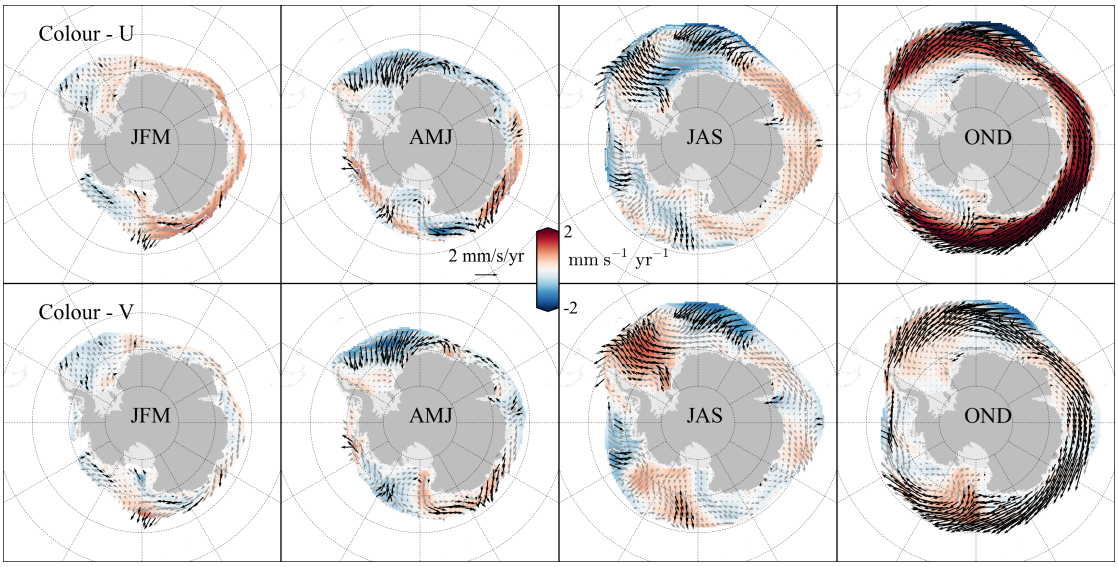

Figure 4.13: As Fig. 4.12, but for the HadGEM2-ES simulation (over the same 1985-2011 time period)

Figure 4.13 shows the modelled trends in ice motion using the HadGEM2-ES forcing (over the recent 1985-2011 period). As the HadGEM2-ES simulation does a poor job of modelling the observed trends in ice concentration (Fig. 4.11), it is not expected to compare well with the observed regional ice motion trends. In fact, the HadGEM2-ES meridional trends do capture the observed southward trend in the Bellingshausen Sea, of a similar magnitude to the ERA-I simulation, however this is only in winter, and the results suffer from the unrealistically low ice extent in this region. The strong eastward ice motion trend during spring stands out. While a strong eastward ice motion trend is expected from an increasing SAM and stronger westerly winds, as stated in the wind trend discussion, the SAM trend is only thought to be significant in the austral summer and autumn, meaning the physical driver of this strong trend is unclear. There is insufficient evidence to suggest that unrealistic ice motion trends play much of a role in the modelled HadGEM2-ES ice concentration decrease (Fig. 4.11), with instead the thermodynamic impact of over-zealous warming (and strong trends in other forcings) (Fig. 4.8) likely dominating the response. The underlying physical cause of the recent wind trends is still highly uncertain, as discussed in Sect. 1.3.2.

4.3.3 Recent ice thickness trends

Ice thickness trends signify the more complete sea ice response to atmospheric forcing trends. As ice thickness in this study refers to the volume of ice per unit grid-cell area, concentration trends are explicitly included in the results. Current understanding of even the mean Antarctic ice thickness is severely lacking, however, and suffers from the current inability of satellites to reliably measure ice freeboard, as discussed in Sect. 4.1.2.3. A qualitative comparison to recent modelling studies is given instead. The linear trends (1985-2011) in (seasonal) ice thickness from both the ERA-I and HadGEM2-ES forced simulations are shown in Fig. 4.14.

The ERA-I simulation shows a spatially variable and, in some cases, seasonally variable trend in ice thickness. There is a significant thickening trend in the western and eastern Weddell shelf sea, across all seasons. The thinning trend (in winter and spring) along the Ronne Ice Front is not significant. Along the Bellingshausen Sea coastline, there are small regions of significant

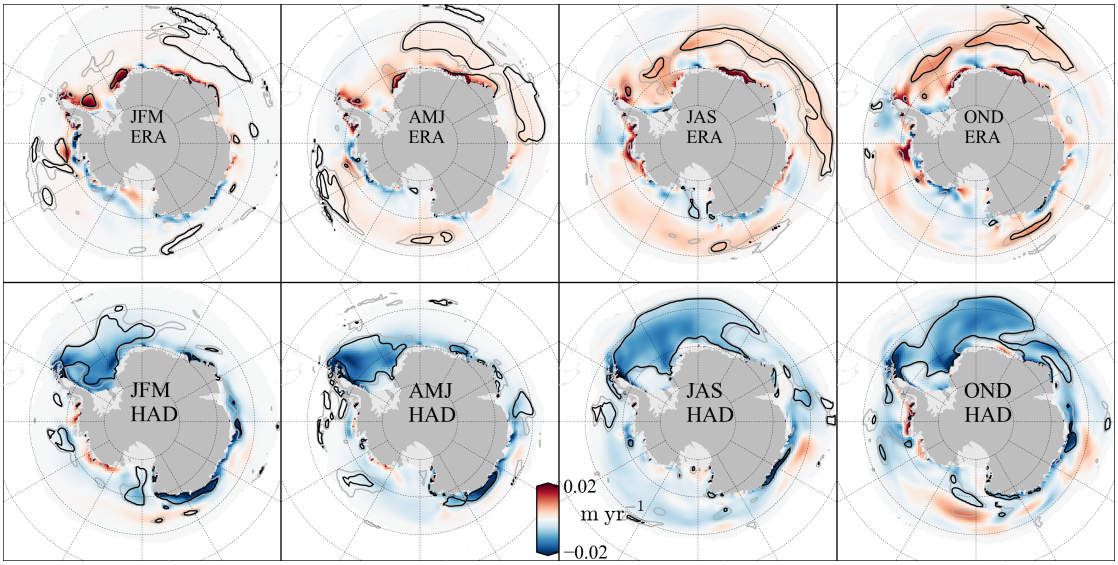

Figure 4.14: 1985-2011 linear trends (seasonal) in ice thickness from the ERA-I (top row) and HadGEM2-ES (bottom row) simulations. Regions with a respective mean ice concentration less than 0.15 are masked in both datasets. The grey and black contours indicate the significance at 90% and 95%.

thickening during winter and spring, probably due to the southward ice motion trends described earlier, as well as a thinning in summer. There is a similar pattern in the Amundsen Sea, with only small regions of significance, which vary both spatially and seasonally. There are small regions of weak thinning in the Ross Sea, across all seasons, with the strong northward ice motion potentially reducing the impact of the significant atmospheric trends in this region. The magnitude of the trends are ∼0-2 cm year^{-1}, implying increases and decreases of up to ∼50 cm over the 27 year study period, a significant fraction of the mean ice thickness of ∼1-2 m. The lack of large regions of significance highlights the large inter-annual variability in Antarctic ice thickness.

The recent HadGEM2-ES simulation, in-contrast, shows a virtually consistent thinning signal across all seasons and regions, with the strongest thinning taking place in the Weddell Sea. There are small regions of thickening, especially along the AB coastline, which are again thought to be driven by the increased southward ice motion trend (during winter and spring) as previously shown in Fig. 4.13.

Due to the lack of ice thickness observations, the only data to compare these results with are from the data assimilation study of *Massonnet et al.* (2013) and the high-resolution modelling study of *Holland et al.* (submitted). The *Massonnet et al.* (2013) study computes the annual mean (1980-2008) thickness trends using an ensemble Kalman filter to improve the estimate of ice thickness by assimilating observed ice concentration data. The limitations of this study are: the lack of direct physical origin to the results due to the statistical optimisation of model variables at each time step; and the coarse resolution (2°) required to run 25 ensemble members, which is problematic when a main focus of this chapter is on the smaller scale, regional trends within the shelf seas. The *Holland et al.* (submitted) study computes the autumn and winter mean (1992-2010) thickness trends, and in contrast, uses a high resolution (0.25°) ocean-sea ice model, meaning all trends have a physical origin, however the sea ice model uses only the 'zero-layer' *Semtner* (1976) thermodynamics (ice has no capacity to store heat) as in Chapter 2, and the results are unconstrained by observations.

The *Massonnet et al.* (2013) study finds a thickening trend of ∼1 cm yr^{-1} in the Weddell Sea (including along the Ronne Ice Front) and in much of the Ross Sea (greater in the western Ross). They also find a thinning (with a lower magnitude of ∼0.5–1 cm yr^{-1}) in the Bellingshausen and Amundsen Seas, and a thickening (∼0.5 cm yr^{-1}) along the western Bellingshausen and Amundsen Sea coast. The *Holland et al.* (submitted) study finds a stronger thickening trend of ∼3 cm yr^{-1} in the Weddell Sea (over both seasons), a thinning (∼1-2 cm yr^{-1}) in the Bellingshausen Sea in autumn, thickening (∼3 cm yr^{-1}) along the AB coast in winter, a thinning (∼2-3 cm yr^{-1}) along the western Weddell (eastern Antarctic Peninsula) coastline in winter, and no strong thickness trends in the Ross Sea.

The ERA-I modelled trends in ice thickness presented here are broadly in-line with those of *Holland et al.* (submitted), where again, it is expected the difference in time-period may explain some of the difference in the magnitude of the trends. This agreement is unsurprising as both studies use the same (ERA-I) atmospheric forcing. The large thickening trend over the Ross in the *Massonnet et al.* (2013) study is not found in this or the *Holland et al.* (submitted) modelling study. Clearly more research is needed to understand the potential accuracy and physical origin of these ice thickness trends.

4.3.4 Future ice concentration and thickness trends

While the previous discussion highlighted the inability of the HadGEM2-ES forced simulation to reproduce the recent trends in ice concentration, motion and potentially thickness, the primary reason for introducing the HadGEM2-ES simulation was to extend this trend analysis into the coming century. While the forcing may be either struggling to capture current natural variability or overestimating the forced response, the long-term simulation can still provide useful information about the impact of a long-term moderate warming on the Antarctic sea ice and mixed layer. The validity of the results, however, is highly questionable. Figure 4.15 therefore shows the long-term (1985-2099) ice concentration and thickness trends from the HadGEM2-ES forced simulation.

As expected from the consistent warming trends (along with similar trends in the other atmospheric forcing variables) shown previously in Fig. 4.9, the simulation results in a significant decrease in ice concentration and thickness over much of the Antarctic sea ice domain. Only the Ross Sea shows regions undergoing no significant changes, due to the absence of significant forcing trends in these regions (shown in Figs. 4.9 and 4.10). Increased westerlies should lead to an increase in ice extent due to the impact of the ocean turning angle. This is not apparent in either the concentration or thickness trends, implying that the impact of thermodynamic trends (e.g. atmospheric warming) is dominating over dynamical trends. The magnitude of the long-term trends remain relatively high, despite the extended time-period (up to $\sim$0.005 year^{-1} in concentration and up to $\sim$0.005 m year^{-1} in thickness) implying a reduction in ice concentration of up to $\sim$0.5 and thinning of up to $\sim$0.5 m by the end of the century.

To demonstrate the impact of these trends on the Antarctic sea ice state, Fig. 4.16 shows the mean (2080-2099) sea ice concentration and thickness at the end of the HadGEM2-ES simulation. Comparing this to the recent (1985-2011) mean HadGEM2-ES simulated ice concentration and thickness shown in Figs. 4.2 and 4.4 demonstrates the less concentrated and thinner ice in the WR seas and the less concentrated and perennially thin ice cover in the AB seas by the end of the century. While this is not an attempt to predict the likely fate of the Antarctic sea

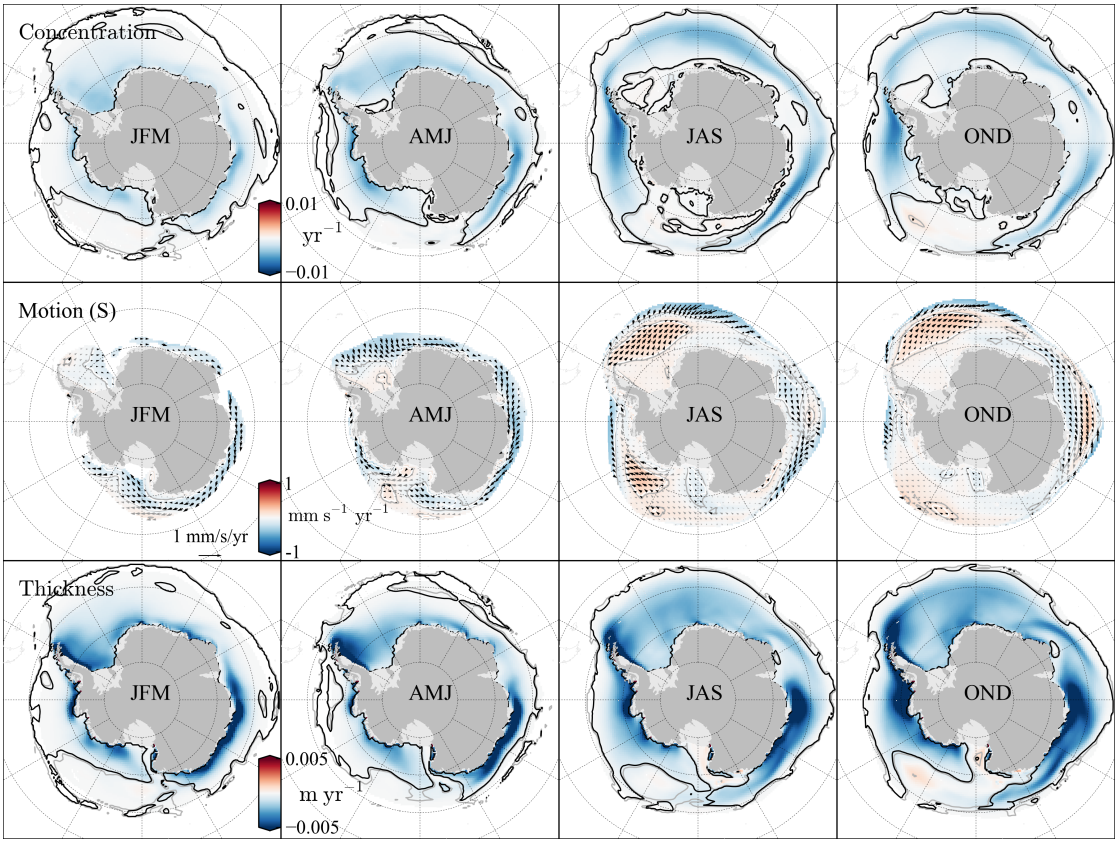

Figure 4.15: 1985-2099 linear trends (seasonal) in ice concentration (top row), motion (middle row) and thickness (bottom row), from the HadGEM2-ES simulation. In the top and bottom rows, the grey and black contours indicate the significance at 90% and 95%. In the middle row, the grey and white contours indicate the wind speed significance at 90% and 95%, while the black vectors (arrows) indicate either the zonal or meridional ice motion is significant at >90%.

ice cover, this simulation does demonstrate a physically consistant mechanism through which a moderate and continued global warming signal can lead to dramatic changes in Antarctic sea ice by the end of this century. Section 4.4 analyses the more direct sea ice mass balance within each of the shelf seas.

4.3.5 Extended linear regression analysis

The longer time-period (1985-2099) of the HadGEM2-ES simulation also provides a more stringent test of the conclusions drawn from the linear regression analysis of the previous chapter

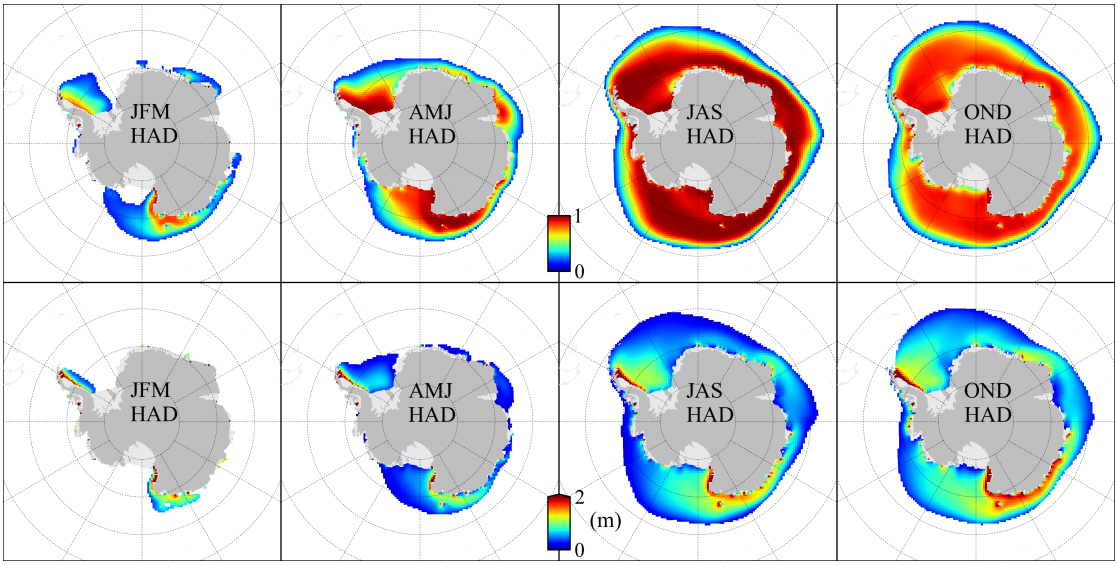

Figure 4.16: Mean (2080-2099) seasonal ice concentration (top row) and thickness (bottom row) from the HadGEM2-ES simulation. Ice concentrations less than 0.15 and ice thicknesses with a respective ice concentration less than 0.5 m are masked.

(Sect. 3.2.6). Only the temporal correlation is investigated further as this regression benefits directly from additional yearly data points, whereas regressing long-term mean intra-regional values is less physically meaningful. Figure 4.17 therefore demonstrates the temporal correlation between the shelf-sea mean autumn/winter atmospheric forcing (including the summer net surface power input to the mixed layer) and the shelf-sea mean autumn/winter net surface power input to the mixed layer, with one point used for each year for each region (similar to Fig. 3.12 in the previous chapter). As in the previous discussion, a weak correlation implies an $r^2 < 0.2$, a moderate correlation implies an r^2 of 0.2-0.5, and a strong correlation implies an $r^2 > 0.5$. All correlations discussed are significant at 99% unless otherwise stated.

Considering the significant spatial (shelf-sea) mean temporal correlations (r^2 values) shown in Fig. 4.17, the spatial mean Weddell autumn/winter net surface power input shows: strong temporal correlation to precipitation (0.70); moderate correlation to incoming longwave radiation (0.44), zonal wind speed (0.37), specific humidity (0.32) and air temperature (0.22); and weak correlation to the meridional wind speed (0.18), net summer surface power input (0.17) and incoming shortwave radiation (0.11). The mean Bellingshausen autumn/winter net surface

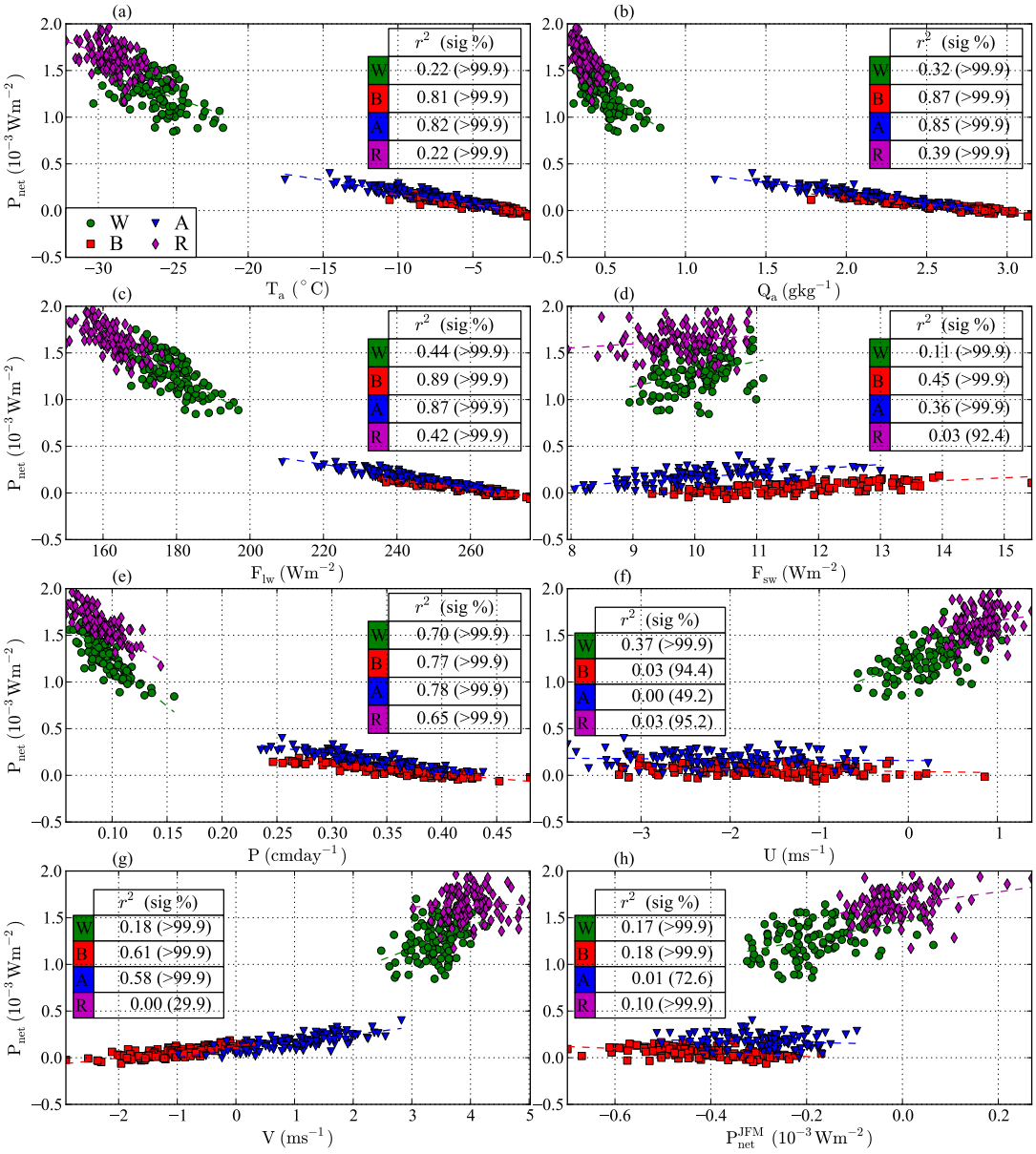

Figure 4.17: Temporal linear regressions, as in Figure 3.12 but for the extended (1985-2099) HadGEM2-ES simulation.

power input shows: strong correlation to the incoming longwave radiation (0.89), specific humidity (0.87), air temperature (0.81), precipitation (0.77) and meridional wind speed (0.61); moderate correlation to incoming shortwave radiation (0.45); and weak correlation to the net summer surface power input (0.18). The mean Amundsen autumn/winter net surface power

input shows: strong correlation to the incoming longwave radiation (0.87), specific humidity (0.85), air temperature (0.82), precipitation (0.78) and meridional wind speed (0.58); and moderate correlation to incoming shortwave radiation (0.36). The mean Ross autumn/winter net surface power input shows: strong temporal correlation to precipitation (0.65); moderate correlation to incoming longwave radiation (0.42), specific humidity (0.39) and air temperature (0.22); and weak correlation to the net summer surface power input (0.10).

These results compare well with the regional pattern of correlations found and discussed in the previous chapter from the shorter ERA-I simulation, with generally greater, and more significant correlations across all regressions. The clearest difference between the simulations is in the WR zonal and meridional wind regressions. Specifically, in the Ross, the correlation between the autumn/winter net power input to the mixed layer and the mean zonal wind decreases from a moderate/strong correlation in the ERA-I simulation to no significant correlation in the HadGEM2-ES simulation, meaning the Ross shows no correlation to either wind speed component. In the Weddell, the correlation between the autumn/winter net power input and the mean meridional wind changes from a strong correlation in the ERA-I simulation to a weak correlation in the HadGEM2-ES simulation, while the correlation with the mean zonal wind increases from weak to moderate.

Similar to the previous chapter, two further temporal regressions are carried out to investigate this in more detail. Figure 4.18a shows the correlation between the annual Ross ice export and the mean autumn/winter zonal and meridional wind speed, demonstrating no significant correlation between the ice export and either wind speed component. Figure 4.18b shows a similar moderate anti-correlation (0.27) between the autumn/winter meridional and zonal wind speeds to the ERA-I simulation.

As the zonal-meridional wind anti-correlation is still believed to be due to the location of the Amundsen/Ross Sea pressure low, the consistency of this result is encouraging yet unsurprising. The earlier hypothesis that a more zonal wind field might increase ice export as it avoids the potential land barrier of the Cape Adare coast is not demonstrated in this extended regression, despite the additional thick ice build-up. Ice export out of the shelf appears to be uncorrelated to

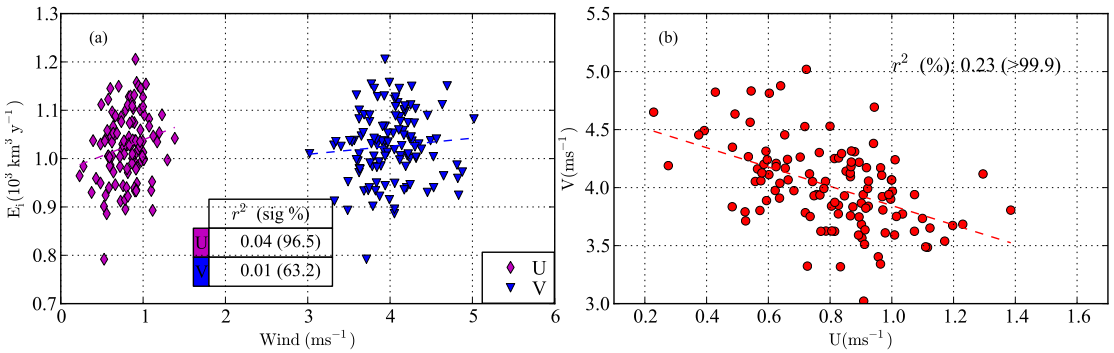

Figure 4.18: Additional Ross Sea temporal regressions from the extended (1985-2099) HadGEM2-ES simulation, as in Figure 3.13

the mean shelf sea winds, with the changing winds appearing to only alter the angle at which the ice is exported out of the shelf. Thermodynamic feedbacks may also be influencing the results, e.g. through the wind variability influencing the amount of sea ice available to export. A finer resolution, regional model and/or improved physics in the sea ice momentum balance (Eq. 3.18) is probably required to investigate these ideas in more detail.

4.4 Regional Sea Ice Mass Balance Trends

The previous chapter demonstrated the strong regional differences in the annual growth, melt and export of sea ice within the four Antarctic shelf seas (Sect. 3.2.5), and the crucial role of sea ice in controlling the seasonal mixed layer evolution (Sect. 3.2.4). This section therefore investigates recent and future trends in the sea ice mass balance contributions within each of the shelf seas. Figure 4.19 is an extension of Fig. 3.10 from the previous chapter, including, and focussing on, the long-term HadGEM2-ES trends (Fig. 3.10 shows the ERA-I results more clearly). Annual 'polynya' trends (regions with an annual growth rate greater than 4 m yr^{-1}) are also discussed, as these regions contribute a significant fraction of the total shelf sea ice growth (especially in the Ross Sea, as discussed in the previous chapter), and are experiencing some of the strongest trends in the atmospheric forcing. Results are summarised in Table 4.1.

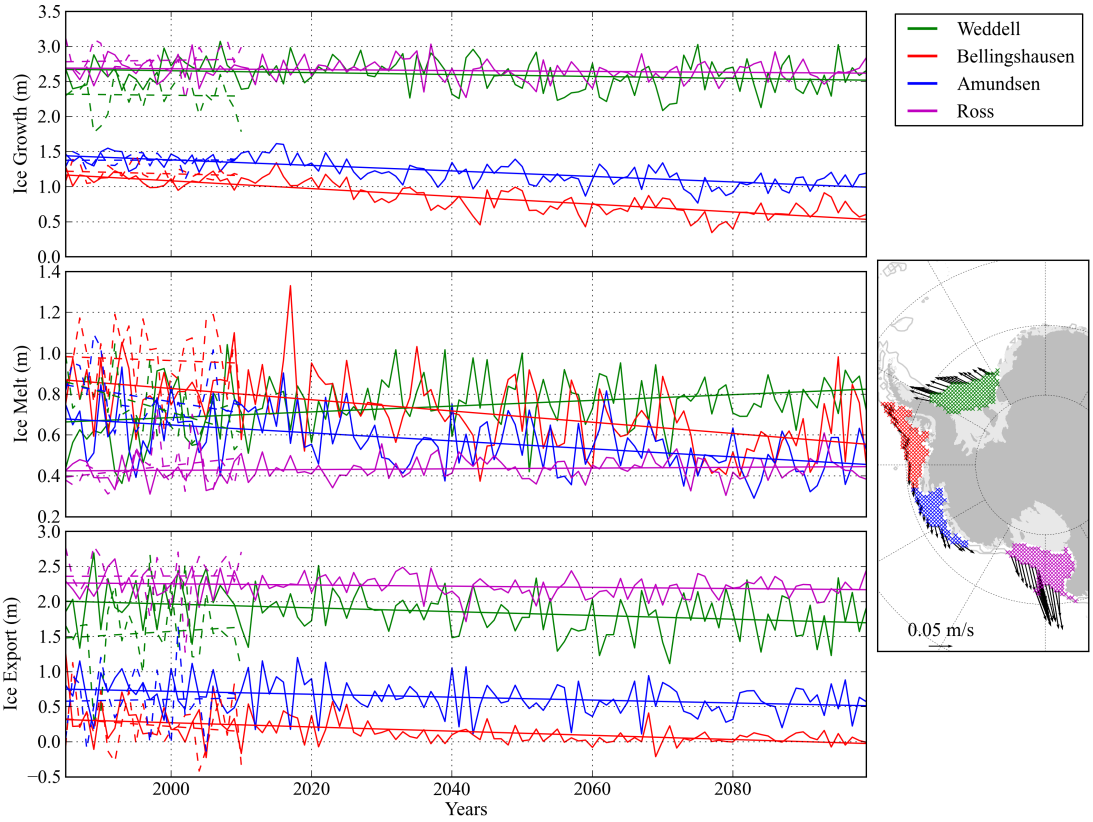

Figure 4.19: Regional sea ice mass balance from both the ERA-I (1985-2011 - dashed lines) and HadGEM2-ES (1985-2099 - solid lines) simulations. (a) Annual regional ice production, (b) annual regional ice melt, (c) annual regional net ice export. Both the annual values and linear trend lines are plotted. Mean ice motion vectors of the outer grid cells of each region from the HadGEM2-ES simulation are shown in the map as well as the polynya grid cells from the HadGEM2-ES simulation (marked by the black crosses); the trends of which are given in Table 4.1

4.4.1 Recent trends from the ERA-I simulation

In the ERA-I simulation, the only significant trends are in the Weddell Sea, which experiences a significant decrease in the annual Weddell ice melt (-0.10 m dec^{-1}). This decrease is probably due to the significant spring cooling along the Ronne Ice Front in the ERA-I forcing (shown in Fig. 4.6), with incoming longwave and specific humidity probably contributing also. It was expected that the significant winter cooling over much of the southern Weddell shelf would lead to an increase in the annual ice growth, however this is not observed in the results. This could be

due to the potentially thicker summer ice cover (due to the reduced annual ice melt) slowing the following autumn/winter ice growth, the competing impact of other forcing trends (not apparent), the warming trend to the north of the shelf sea during autumn (not significant), the thicker winter sea ice showing less sensitivity to atmospheric forcing trends through increased insulation, or a combination of these different factors. There is a near-significant decrease in the annual Weddell 'polynya' ice melt (-0.08 m dec^{-1}, 93%), with the decreasing volume trend (-4.43 km^3 dec^{-1}, 93%) around 10% of the total shelf sea decrease (-44.1 km^3 dec^{-1}), implying the decreasing Weddell ice melt is a more shelf-wide process. *Massonnet et al.* (2013) simulate a strong annual thickening over the Weddell shelf, however much of this is not significant (<95%), which they link to the large inter-annual variability of the thick Weddell sea ice cover. There is a large decrease in the annual Ross 'polynya' ice growth (-0.10 m dec^{-1}), however, this is not significant, implying large variability (the polynya export shows a similar result). The lack of significant trends in the sea ice mass balance contributions is unsurprising considering the lack of consistent and significant shelf-wide ERA-I forcing trends, and the competing thermodynamic/dynamic impact of the various forcings.

While sea ice thickness observations are lacking, recent studies have attempted to estimate the annual ice growth within the WR polynyas using a combination of satellite observations and reanalysis data, as summarised in Sect. 3.2.5 of the previous chapter. As well as the mean values discussed in the previous chapter, *Comiso et al.* (2011) and *Drucker et al.* (2011) also report an increasing trend (1992-2008) in the annual Ross Polynya ice growth of $\sim$20 km^{3}yr^{-1}. *Drucker et al.* (2011) also investigate the Weddell Sea, but find no significant trend overall. The Ross Polynya trend is an order of magnitude greater than any of the trends found in this study. The *Comiso et al.* (2011) and *Drucker et al.* (2011) studies use a shorter time period than this study, although shortening the time-period of this analysis did not greatly increase the magnitude of the trend (not shown). The *Tamura et al.* (2008) study (included in the previous chapter's discussion) also investigates trends in polynya growth, and instead report a decreasing trend (using a shorter time period of 1992-2001) in the annual Ross (~ -8.5 km^{3}yr^{-1}) and Weddell (~ -3 km^{3}yr^{-1}) polynya ice growth. While this demonstrates a considerably difference in the expected trend from both polynyas, *Comiso et al.* (2011) conclude this is likely to be a function of the different

methods used to derive the iceberg masks, and their inclusion of secondary polynyas that form downwind of the icebergs. Despite these concerns, the drastic difference in the estimated polynya trends highlights the potential uncertainty of such analyses. Another key difference between this study and the observational studies is in the polynya classification, where the *Tamura et al.* (2008), *Comiso et al.* (2011) and *Drucker et al.* (2011) studies use a thin-ice ($\leq$15 cm) detection method to calculate the polynya region, then use relatively coarse (1.125°) reanalysis data to calculate the heat flux and expected sea ice growth. Regions with ice thicker than 15 cm are thus excluded from their annual ice growth estimate. In this study, the coastal polynya region is defined by a fixed area along the ice front (based on a mean annual ice growth threshold), meaning the annual ice growth within a specific region is tracked. While this representation of a polynya is not as accurate as the observational studies, there is perhaps more consistency in the physical quantity being regressed.

These observational studies, along with several others studies (e.g. *Jacobs et al.*, 2002), often infer that the increase in Ross ice extent is a strong indicator of increasing ice export from the Ross shelf sea, primarily through an increase in the Ross Polynya ice growth/export. Figure 4.11 shows significant increases in ice concentration/extent north of the Ross Sea, however the simulation does not also demonstrate any significant increases in ice export from the Ross shelf or polynya. Inferring shelf sea changes from regions north of the shelf is therefore thought to be a potentially misleading approach.

4.4.2 Future trends from the HadGEM2-ES simulation

The HadGEM2-ES simulation shows greater and more significant trends across all sea ice mass balance contributions. There is a significant decrease in the annual Weddell ice export (-0.03 m dec^{-1}) and a significant increase in the annual Weddell ice melt ($+0.01$ m dec^{-1}), as well as a near-significant decrease in the annual ice growth (-0.01 m dec^{-1}, 97%). There is a significant decrease in the annual Weddell 'polynya' ice growth (-0.04 m dec^{-1}) and export (-0.05 m dec^{-1}), with the 'polynya' export volume decrease (-3.67 km^3 dec^{-1}) a significant fraction (around 30%) of the total Weddell export decrease (-12.0 km^3 dec^{-1}). The wind trends over the Wed-

ERA-I	**Weddell**	**B'hausen**	**Amundsen**	**Ross**
G_i (km^3 dec^{-1})	-4.84	-9.81	0.40	6.56
G_i (m dec^{-1})	-0.01	-0.02	0.002	0.01
M_i (km^3 dec^{-1})	**-44.1**	-5.09	-14.9 (90)	17.4
M_i (m dec^{-1})	**-0.10**	-0.01	-0.06 (90)	0.04
E_i (km^3 dec^{-1})	27.3	-28.4	4.82	1.30
E_i (m dec^{-1})	0.06	-0.07	0.02	0.003
'Polynya' area (10^3 km^2)	55.1	-	-	96.9
G_i^p (km^3 dec^{-1})	1.90	-	-	-10.4
G_i^p (m dec^{-1})	0.03	-	-	-0.10
M_i^p (km^3 dec^{-1})	-4.43 (93)	-	-	2.22
M_i^p(m dec^{-1})	-0.08 (93)	-	-	0.02
E_i^p (km^3 dec^{-1})	3.57	-	-	-10.9
E_i^p (m dec^{-1})	0.07	-	-	-0.11
HadGEM2-ES				
G_i (km^3 dec^{-1})	-6.05 (97.3)	**-22.1**	**-10.6**	-2.94
G_i (m dec^{-1})	-0.01 (97.3)	**-0.055**	**-0.041**	-0.01
M_i (km^{3}dec^{-1})	**6.25**	**-11.0**	**-5.28**	0.84
M_i (m dec^{-1})	**0.01**	**-0.03**	**-0.02**	0.002
E_i (km^3 dec^{-1})	**-12.0**	**-11.9**	**-5.60**	-3.90 (94.9)
E_i (m dec^{-1})	**-0.03**	**-0.03**	**-0.02**	-0.01 (94.9)
'Polynya' area (10^3 km^2)	76.5	-	-	93.9
G_i^p (km^3 dec^{-1})	**-3.16**	-	-	**-3.57**
G_i^p (m dec^{-1})	**-0.04**	-	-	**-0.04**
M_i^p (km^3 dec^{-1})	0.55	-	-	-0.27
M_i^p(m dec^{-1})	0.01	-	-	-0.003
E_i^p (km^3 dec^{-1})	**-3.67**	-	-	**-3.29**
E_i^p (m dec^{-1})	**-0.05**	-	-	**-0.04**
Shelf sea area (10^3 km^2)	433	398	261	459

Table 4.1: Linear trends in the regional sea ice mass balance contributions from the ERA-I (1985-2011) and HadGEM2-ES (1985-2099) simulations. The area-weighted trends (in m) are produced by dividing by the listed shelf sea area. Shelf sea regions are shown in Fig. 4.19. All trends in bold are significant at 99%, with significance values between 90% and 99% included in parentheses. The mass balance trends from the WR polynyas are also included (denoted by the superscript p)

dell shelf during this period (shown in Fig. 4.9) are small, which, combined with the significant warming signal throughout all seasons (Fig. 4.10), means these trends are probably more due to thermodynamic trends (i.e. thinner ice is being exported at a similar rate).

There is a significant decrease in the annual Bellingshausen ice growth (-0.06 m dec^{-1}), melt (-0.03 m dec^{-1}) and export (-0.03 m dec^{-1}). There is a similar pattern in the Amundsen, with a significant decrease in the annual ice growth (-0.04 m dec^{-1}), melt (-0.02 m dec^{-1})

and export (-0.02 m dec^{-1}). In both cases, the decrease in ice melt is at first surprising, considering the significant warming, including summer (as shown in Fig. 4.10), over the AB shelf seas. However, the decreasing ice growth and the resulting ice free summer in this region by the end of the century (as shown in Fig. 4.16) means there is likely insufficient ice available to melt in summer. The ice melt balances the ice growth in the Bellingshausen shelf sea by 2099, meaning there is no observable annual export or import of ice.

The only significant trend in the Ross is in the polynya, which shows a significant decrease in the annual ice growth (-0.04 m dec^{-1}). There is also a near significant decrease in the annual ice export over the wider shelf (-0.01 m dec^{-1}, 95 %). The decrease in the annual volume of ice exported (-3.90 km^3 dec^{-1}) is similar to the decrease in the volume of ice exported from the coastal polynya (-3.29 km^3 dec^{-1}), implying the polynya trend is controlling the total shelf sea export decrease. The weak warming trend appears to be insufficient to generate a strong thermodynamic response in the Ross, while the decreased meridional winds in the western Ross do not appear to cause any significant trends in the ice exported from the Ross. This was also highlighted in the previous linear regression analysis (see Figure 4.18), which showed no correlation between the annual Ross ice export and the meridional (or zonal) winds.

4.5 Shelf Sea Salinity and Temperature Trends

As discussed in the introduction (Sect. 1.1.6), the southwestern Ross shelf sea has freshened by around 0.03 dec^{-1} since the 1950s (*Jacobs and Giulivi*, 1998; *Jacobs et al.*, 2002; *Jacobs and Giulivi*, 2010) and the northwestern Weddell shelf sea has freshened by around 0.09 dec^{-1} (over a shorter time period of 1989-2006 and with only three years of data) (*Hellmer et al.*, 2011). Sea ice changes have been implicated and discussed in relation to these freshening signals, however the dominant process appears to be the freshwater input from increasing ice shelf melt in nearby locations. The following section investigates the possible impact on the properties of the shelf seas from trends in the surface input of salt/freshwater and heat, excluding ice shelf meltwater trends. A greater focus is given to the WR shelf seas due to the shelf waters that form here and

the available comparison to recently observed trends.

Shelf sea temperature trends are limited by the formation of sea ice at the ocean surface freezing temperature, with the observed warming trend in the Ross Sea close to the expected change in freezing temperature from the observed salinity decline over the same period (*Jacobs and Giulivi*, 2010). Despite this, trends in the annual surface heat input are also discussed as this could still provide a significant signal over the longer-term simulation, and the values also provide a useful comparison to the mean annual surface heat input results from the idealised modelling study (Sect. 2.1.7.1).

The annual effective salt input (over the Southern Ocean) was introduced in Sect. 3.2.3, with the regional salt input calculated in a similar fashion (by integrating the effective surface salt fluxes given in (Eqs. 3.23 and 3.24)) as

$$S_{ice}(year, R) = \frac{1}{A_S} \int\int_{R} \int_{year} \widehat{F}^{ice}_{salt} \; dtdxdy \tag{4.1}$$

$$S_{pe}(year, R) = \frac{1}{A_S} \int\int_{R} \int_{year} \widehat{F}^{pe}_{salt} \; dtdxdy \tag{4.2}$$

where A_S is the shelf sea area. The sum of these two contributions, S_{net} is also used and discussed in the following analysis. The WR polynya regions are also investigated as these correspond to the primary regions of HSSW formation, and are denoted by the superscript p (e.g. S^p_{net}) in Table 4.2. It is worth noting that in the idealised study (Sect. 2.1.7.1), ice export was used to infer changes in the salt content as it is roughly equal to the residual of ice growth and melt, and was easily diagnosed in the model. This approach differs somewhat, as instead, the annual input of salt is calculated from the effective salt fluxes from sea ice growth/melt. This was seen to be a more accurate approach; however, the results should be broadly inline with those presented in the earlier chapter.

To express these trends in more intuitive units, Eq. (3.25) and the mean maximum mixed layer depth (MMLD - $\overline{h}_{max}$) are used to provide a rough estimate of the annual change in the

salinity of the wintertime mixed layer as

$$\widehat{S}(year, R) = \frac{(1000 - S_{mix})}{\rho_w \overline{h}_{max}} S(year, R) \tag{4.3}$$

The benefit of this approach is that it provides the freshening signal of the winter mixed layer from surface processes alone, avoiding the competing signal of ocean restoring, providing a useful comparison to the freshening signals currently being observed within the Antarctic shelf seas.

As stated previously, the more likely contributor to shelf sea freshening is thought to be from the increased input of fresh glacial meltwater (discussed in Sect. 1.1.7 of the introduction). Equation (3.24) is used to convert the effective salt input trends into freshwater equivalent units (Gt yr^{-1} of fresh glacial ice/meltwater entering the ocean) as

$$FWE_{net}(year, R) = -\frac{(1000 - S_{mix})A_S}{10^{12} S_{mix}} S_{net}(year, R). \tag{4.4}$$

where 10^{12} is used to convert from kg to Gt of meltwater.

The annual (regional) surface heat input (in J m^{-2}) to the mixed layer (note this is the heat input from the surface layer h_S and not the atmosphere) is calculated using the mixed layer-ocean heat flux given in Eq. (3.21) as

$$H_S(year, R) = \int_R \int_{year} F_{sm} \; dtdxdy. \tag{4.5}$$

Similar to the salt input, the surface heat input trend can be used to provide a rough estimate of the annual change in the temperature of the winter-time mixed layer as

$$\widehat{H}(year, R) = \frac{H_S(year, R)}{\rho_w c_p \overline{h}_{max}}. \tag{4.6}$$

Direct trends in the salinity and temperature of the shelf seas (as opposed to inferred from surface trends) are also calculated by averaging all grid cells bounded by the shelf break, the

Antarctic coastline and the shelf seabed. While this provides a direct time-series of the shelf sea salinity and temperature, the value will be modified by both the surface fluxes described above and also by the impact of ocean restoring towards the summertime profile. The deep ocean restoring is thus likely to provide a negative feedback to the potential trends in the surface fluxes, as the ocean restoring rate is linearly proportional to the difference between the current state and the reference state (described in Sect. 3.1.2.5). While this is a simplistic representation of off-shelf/on-shelf ocean advective processes, it does pose a valid question as to the expected relation between these two effects i.e. does the residence time of HSSW increase as the off-shelf flow decreases from a reduced density gradient? Carrying out this direct shelf sea analysis is also a useful way of highlighting the seasonal variability in the salinity and temperature of the shelf seas.

The trends in both the annual surface salt/heat input contributions and the estimated and direct shelf sea salinity/temperature are shown in Fig. 4.20, with all trends summarised in Tables 4.2 and 4.3.

4.5.1 Surface salt input and shelf sea salinity trends

4.5.1.1 Recent trends from the ERA-I simulation

The ERA-I simulation shows no significant (>99%) trends in the annual effective salt input at the surface, with the lack of significant sea ice trends directly preventing any trends due to sea ice processes (S_{ice}). S_{pe} trends are indirectly linked to the sea ice through changes in the open water fraction (e.g. potential for enhanced snowfall into the ocean), although the trends in ice concentration over the shelf (Fig. 4.11) appear small compared to the ice thickness trends (Fig. 4.14).

There is a near-significant increase in the Weddell S_{ice} (+3.60 kg m^{-2}dec^{-1}, 95%), resulting in an estimated mean MMLD salination of 0.01 dec^{-1}. The trend in the Weddell S^{p}_{ice} is larger (+4.75 kg m^{-2}dec^{-1}), however it is not significant. There is a strong, near-significant decrease in the Ross S^{p}_{net} (−5.70 kg m^{-2}dec^{-1}, 91%), resulting in an estimated mean MMLD freshening

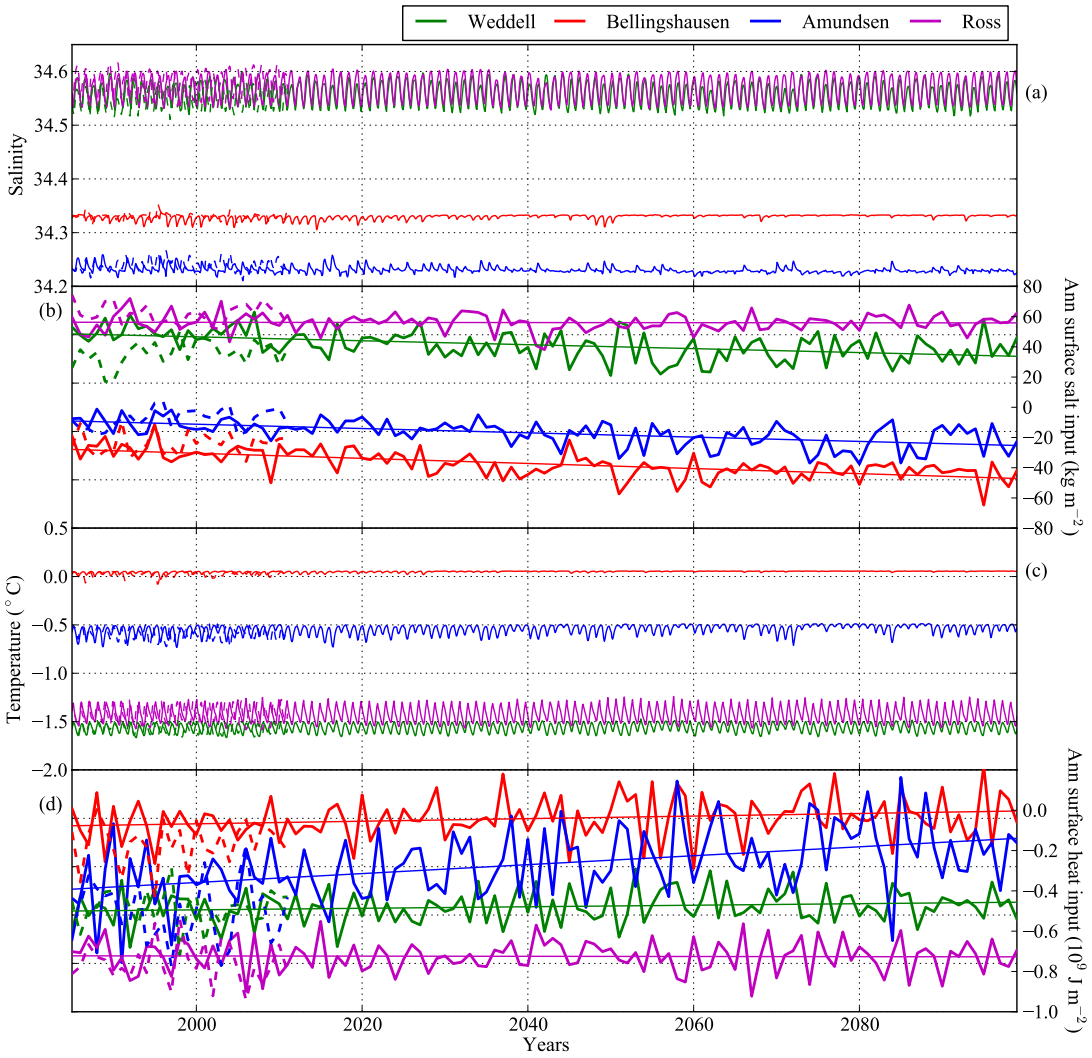

Figure 4.20: Mean shelf sea salinity (a), annual mean surface salt input (b), Mean shelf sea temperature (c) and annual mean surface heat input (d) for the HadGEM2-ES (1985-2099) simulation (solid lines). The ERA-I results (1985-2011) are also shown (dashed lines). The straight lines in (b) and (d) indicate the linear trend of the interannual values.

of 0.01 dec^{-1}. There is a near-significant increase in the Amundsen S_{pe} (+0.63 kg m^{-2}dec^{-1}, 93%) which contributes around 30% of the near-significant increase in S_{net} (+2.78 kg m^{-2}dec^{-1}, 92%), resulting in an estimated mean MMLD salination of 0.02 dec^{-1}. There are no significant trends in the effective salt input to the Bellingshausen shelf sea.

ERA-I	**Weddell**	**B'hausen**	**Amundsen**	**Ross**
Shelf sea area (10^3 km^2)	433	398	261	459
$\overline{h}_{max}$ (m)	340	50	110	360
S_{ice} (kg m^{-2}dec^{-1})	3.60 (95)	0.33	2.16	-0.61
S_{pe} (kg m^{-2}dec^{-1})	-0.16	0.36	0.63 (93)	-0.03
S_{net} (kg m^{-2}dec^{-1})	3.50 (92)	0.70	2.78 (92)	-0.63
FWE_{net} (Gt dec^{-1})	-43.1 (92)	-7.91	-20.6 (92)	8.20
$\widehat{S}_{net}$ (dec^{-1})	0.01 (92)	0.01	0.02 (92)	-0.002
Shelf sea salinity (dec^{-1})	2e-4 (97)	-1e-4 (92)	1e-4	2e-5
'Polynya' area (10^3 km^2)	55.1	-	-	96.9
$\overline{h}^p_{max}$ (m)	520	-	-	590
S^p_{net} (kg m^{-2}dec^{-1})	4.75	-	-	-5.70 (91)
FWE^p_{net} (Gt dec^{-1})	-7.46	-	-	15.7 (91)
$\widehat{S}^p_{net}$ (dec^{-1})	0.01	-	-	-0.01 (91)
HadGEM2-ES				
$\overline{h}_{max}$ (m)	350	30	90	350
S_{ice} (kg m^{-2}dec^{-1})	**-1.14**	-0.32 (96)	**-0.43**	-0.010
S_{pe} (kg m^{-2}dec^{-1})	-0.04 (93)	**-1.29**	**-0.93**	-0.020
S_{net} (kg m^{-2}dec^{-1})	**-1.18**	**-1.60**	**-1.37**	-0.040
FWE_{net} (Gt dec^{-1})	**14.5**	**18.1**	**10.1**	0.48
$\widehat{S}_{net}$ (dec^{-1})	**-0.003**	**-0.05**	**-0.01**	-1e-4
Shelf sea salinity (dec^{-1})	**-4e-5**	**5e-5**	**-5e-5**	6e-6
'Polynya' area (10^3 km^2)	76.5	-	-	93.9
$\overline{h}^p_{max}$ (m)	550	-	-	590
S^p_{net} (kg m^{-2}dec^{-1})	**-1.79**	-	-	-0.69 (98)
FWE^p_{net} (Gt dec^{-1})	**3.88**	-	-	1.84 (98)
$\widehat{S}^p_{net}$ (dec^{-1})	**-0.003**	-	-	-0.001 (98)

Table 4.2: Effective surface salt input, ice shelf mass loss equivalent, estimated salinity and direct shelf sea salinity trends from both ERA-I (1985-2011) and HadGEM2-ES (1985-2011) simulations. Shelf sea regions are shown in Fig. 4.19. All trends in bold are significant at 99%, with significance values between 90% and 99% included in parentheses. The Weddell and Ross polynya trends are also included (denoted by the superscript p)

The estimated Weddell MMLD salination (+0.01 dec^{-1}), despite being an order of magnitude lower than the observed northwestern Weddell shelf sea freshening (-0.09 dec^{-1}), is distributed over the entire shelf sea, and occurs over a longer time-period. This appears to be driven primarily by the direct impact of the significant decrease in the annual ice melt (M_i). The annual ice melt is the only near-significant sea ice trend in the Amundsen, and is therefore thought to be the cause of the near-significant increase in S_{pe} and increase in S_{ice} (significant at 88%) through the direct increase in salt input from less sea ice melt, the expected decrease in snow melt, and the increase in summer ice concentration, reducing snowfall into the ocean. Ice

melt has perhaps been a process ignored in previous analyses, however through enhanced storage of freshwater in summer and reduced snowfall/melt into the ocean, it appears possible this could have a large impact on the properties of the shelf sea below.

The estimated Ross polynya MMLD freshening (-0.01 dec^{-1}), while only near-significant, provides physical evidence of significant freshening of shelf waters driven purely by surface trends, of a similar order of magnitude to recent observations. The trend in the salt input under the Ross polynya is dominated by S_{ice}, with S_{pe} trends small and insignificant in comparison under both polynya regions (not shown). The Ross polynya ice mass balance trends are large but insignificant. It therefore appears that the variability in this signal is smoothed when considered as the annual salt input, which factors in the combined trend in growth and melt as well as the additional feedbacks of changes in snowfall/melt into the ocean. A strong surface-driven freshening is more likely within a smaller region such as the polynya, which is also more likely to undergo bigger changes in magnitude due to the enhanced sea ice cycle.

4.5.1.2 Future trends from the HadGEM2-ES simulation

The HadGEM2-ES simulation shows stronger and more significant trends in the annual effective salt input at the surface, as expected from the regional sea ice trends discussed in the previous section. In the Weddell, there is a significant decrease in S_{ice} (-1.14 kg m^{-2}dec^{-1}), which dominates the decrease in S_{net} (-1.18 kg m^{-2}dec^{-1}), resulting in an estimated mean MMLD freshening of 0.003 dec^{-1}. The decrease in the Weddell S^{p}_{net} is stronger (-1.79 kg m^{-2}dec^{-1}), however the deeper mean MMLD (shelf waters form here in winter) means the estimated freshening signal is similar (-0.003 dec^{-1}). The only significant Ross trend is in S^{p}_{net} (-0.69 kg m^{-2}dec^{-1}, 98%) which results in an estimated mean MMLD freshening of 0.001 dec^{-1}. In the Bellingshausen, there is a significant decrease in S_{pe} (-1.29 kg m^{-2}dec^{-1}) and a near-significant decrease in S_{ice} (-0.32 kg m^{-2}dec^{-1}, 96%). Due to the shallow mean Bellingshausen MMLD (30 m), the estimated freshening in this surface layer is very strong (0.05 dec^{-1}). There is a similar pattern (with a smaller magnitude) in the Amundsen, which shows a significant decrease in S_{pe} (-0.93 kg m^{-2}dec^{-1}) and S_{ice} (-0.43 kg m^{-2}dec^{-1}), resulting in an estimated mean

MMLD freshening of 0.01 dec^{-1}.

The strong decrease in S_{ice} in the Weddell is likely caused by the significant decrease in ice export (a sum of an increase in ice melt and decrease in ice growth as shown in Table 4.1). Again, an expected increase in snow melt (through the enhanced ice melt) or snowfall into the ocean will likely lead to an additional positive feedback in the decreasing effective salt input. The Ross S^p_{net} trend is also expected to be dominated by the decrease in the polynya ice export.

It is interesting to observe that in the AB seas, the trend in S_{pe} dominates over S_{ice}. As discussed in Sect. 4.3.4, the decrease in ice concentration is limited by the amount of sea ice available, with Fig. 4.16 demonstrating the virtually complete removal of ice by the end of the century in the AB seas. The strong increase in S_{pe} is likely the result of both an increase in open water and the strong significant increase in precipitation over the AB seas, as shown in Fig. 4.9e.

It is interesting to note that despite the continuous long-term warming signal, the magnitude of the ERA-I trends are generally stronger, especially under the WR polynyas, implying natural variability can result in stronger trends than the impact from a more direct/persistent forced warming signal.

4.5.1.3 Potential contribution of ice shelves to shelf sea freshening

As discussed in Sect. 1.1.7, the ice shelves fringing the Amundsen Sea are estimated to be losing mass (thinning) by 160 ± 30 Gt yr^{-1} in recent years (*Depoorter et al.*, 2013; *Rignot et al.*, 2013), while the WAIS is estimated to be losing grounded ice (through the expected acceleration of the same ice shelves fringing the Amundsen Sea) at a rate of 85 ± 22 Gt yr^{-1} over the last decade (*Shepherd et al.*, 2012). The total increase in the input of continental ice into the Amundsen Sea is therefore thought to be ∼250 Gt yr^{-1} in recent years. This additional fresh glacial meltwater has been implicated in the freshening (0.08 dec^{-1}) of the upper 200 m of the Antarctic coastal current, which connects the Amundsen Sea (upstream) to the Ross (downstream) (*Jacobs and Giulivi*, 2010; *Jacobs et al.*, 2013), as discussed in Sect. 1.1.6, with

the freshening signal thought to be mixed down to the seabed in the southwestern corner of the Ross shelf during HSSW formation. The equivalent freshwater trend from surface changes within the Ross polynya found in this study is ∼1.5 Gt yr^{-1}, considerably smaller (by two orders of magnitude) than the additional meltwater from the WAIS. Despite the clear disparity in the magnitude of the additional freshwater input, the surface-driven trend directly enters the region of shelf water formation, whereas the additional meltwater input to the Amundsen Sea is distributed within both shelf seas (including the significant area underneath the ice shelves). An unknown fraction also potentially advects northwards past the shelf-break and into the broader Southern Ocean directly. However, only 1% of the additional fresh glacial meltwater needs to enter the region of HSSW formation to provide a similar response to the surface driven trends derived in this study. More research is clearly needed to understand the pathway of the glacial meltwater entering the Amundsen Sea.

Ice shelves fringing the Bellingshausen Sea, are thought to be more in-balance, despite losing similar volumes of ice through basal melt (*Rignot et al.*, 2013). The more ready access to the warm UCDW means ice shelves here are unlikely to have thinned or accelerated through additional ocean melt in recent years. George VI ice shelf appears to be thinning the most (–21 ± 20 Gt yr^{-1} *Depoorter et al.*, 2013; *Rignot et al.*, 2013), meaning the surface input of freshwater equivalent of ∼1.8 Gt yr^{-1} from the surface-driven trends is around an order of magnitude less (although within one standard deviation) and is potentially comparable to the thinning of some of the smaller ice shelves in the region.

The Weddell shelf sea is the most isolated of the four shelf seas due to the geometry of the Antarctic Peninsular. The Filchner-Ronne Ice Shelf is currently estimated to be thinning by 60 ± 23 Gt yr^{-1} (*Rignot et al.*, 2013). It is unclear how much this is due to enhanced basal melt or iceshelf calving, however the impact on the Weddell shelf sea from either process is thought to be relatively low. Much of the ice lost though iceberg calving could advect away from the shelf sea before melting, due to the relatively strong southerly winds over the shelf. Increased ice lost through basal melt will provide additional volumes of Ice Shelf Water (ISW), however, as discussed in Sect. 1.1.1. much of this is thought to be transferred directly off the shelf through the Filchner Depression (*Foldvik et al.*, 2004; *Wilchinsky and Feltham*, 2009). The

equivalent freshwater input from surface processes, such as the 4 Gt yr^{-1} increase in the ERA-I simulation could therefore provide a significant signal in relation to any potential increase in glacial meltwater from the FRIS. The freshening in the northwestern Weddell was linked to the collapse of Larsen B, which took place before the *Depoorter et al.* (2013) and *Rignot et al.* (2013) observations, meaning its contribution to the shelf seas is still relatively unclear (*Jullion et al.*, 2013).

There are large uncertainties attached to this kind of discussion, predominantly in understanding the ocean circulation within the shelf seas, and the future stability of the WAIS over the coming century. While in general, sea ice trends appear small in comparison to the estimated increase in glacial meltwater, strong, localised trends could still provide significant impacts in important shelf sea regions. Again, further modelling, potentially through the use of a more sophisticated sea ice-ocean-ice shelf model is required to investigate this in more detail.

4.5.2 Surface heat input and shelf sea temperature trends

ERA-I	**Weddell**	**B'hausen**	**Amundsen**	**Ross**
$\overline{h}_{max}$ (m)	340	50	110	360
H_{ML} (10^6 J $m^{-2}dec^{-1}$)	-1.47	13.8	-23.8	-10.2
$\widehat{H}_{ML}$ (°C dec^{-1})	0.001	0.07	-0.05	-0.01
Shelf sea (°C dec^{-1})	-2e-4	2e-4	-6e-4 (93.1)	-2e-4
HadGEM2-ES				
$\overline{h}_{max}$ (m)	350	30	90	350
H_{ML} (10^6 J $m^{-2}dec^{-1}$)	3.31	5.63 (95)	**21.8**	-0.42
$\widehat{H}_{ML}$ (°C dec^{-1})	0.002	0.05 (95)	**0.06**	-3e-4
Shelf sea (°C dec^{-1})	**1.2e-4**	**1.4e-4**	**4.2e-4**	2e-5

Table 4.3: Annual surface-mixed layer heat input, estimated and direct shelf sea temperature trends from both ERA-I (1985-2011) and HadGEM2-ES (1985-2099) simulations. Regions taken from Fig. 3.10. All trends in bold are significant at 99%, with significance values between 90% and 99% included in parentheses.

The ERA-I simulation shows no significant trends in the annual surface-mixed layer heat input. The sea ice is thought to provide much of the thermodynamic response to atmospheric forcing trends over the shelf seas, due to the virtually perennial sea ice cover. The surface layer h_S will also provides some inertia to the transfer of heat from the atmosphere to the mixed

layer (this was the principal reason for introducing the surface layer to the CICE-mixed layer model). The changing mixed layer depth in response to the surface heat flux is also expected to provide a negative feedback to some degree, in response to changes in the surface-mixed layer heat flux.

The HadGEM2-ES simulation shows greater and more significant trends in the annual surface-mixed layer heat input, although only in the AB shelf seas. Again, it appears the forcing trends are not large enough to generate a significant response in the WR for the same reasons listed above. The strongest increase is in the Amundsen surface heat input ($+21.8 \times 10^6$ J m^{-2}dec^{-1}), which results in an estimated mean MMLD warming of 0.06 °C dec^{-1} or ∼0.6 °C by the end of the century. This is a large warming signal, and is thought to be due primarily to the removal of the insulating sea ice cover by the end of the century. The Bellingshausen shelf sea experiences a smaller increase in the surface-mixed layer heat input ($+5.63 \times 10^6$ J m^{-2}dec^{-1}, 95%) however the shallower mean MMLD (30 m) results in a similar estimated rate of warming (+0.05 °C dec^{-1}, 95%).

The direct warming of the mixed layer could be an important mechanism in providing additional heat to the ice shelves fringing the AB seas. Indeed, *Holland et al.* (2010) demonstrated, using a regional model, that the melt rates of George VI Ice Shelf correlate strongly with the mixed layer temperature (albeit in the same localised region). In that study, years of deep convection (through enhanced sea ice growth) around the shelf break caused additional mixing of heat towards the surface, resulting in mixed layer temperature increases adjacent to the ice shelf of up to 0.5 °C dec^{-1} as the heat mixed southwards. This mechanism, however, simply changed the distribution of heat within the shelf as it bought more heat from depth to above the ice shelf draft. The mechanism described here is different, in that the significant long-term changes in the sea ice cover cause an addition of heat into the ocean from the atmosphere. This is, in-effect, another mechanism through which surface processes can have a major impact on the future stability of ice shelves in the region.

As stated previously, this annual surface-mixed layer heat input provides a useful validation and expansion of the surface heat input calculations shown in the idealised modelling study

(Sect. 2.1.7.2). In this study, the ERA-I simulation shows a mean annual surface heat input of $\sim -0.8\times10^9$ J m^{-2} in the Ross, $\sim -0.5\times10^9$ J m^{-2} in the Weddell, $\sim -0.4\times10^9$ J m^{-2} in the Amundsen, and $\sim -0.1\times10^9$ J m^{-2} in the Bellingshausen Sea. This differs somewhat with the results of the idealised modelling study, which found a mean annual surface heat input of $\sim -1.2\times10^9$ J m^{-2} in the Weddell and $\sim -0.2\times10^9$ J m^{-2} in the Amundsen Sea (Fig. 2.6). It is worth noting that the quantity measured is slightly different, due to the inclusion of a fixed depth surface layer (h_S=10 m) in this study which has some capacity to store heat. The regions are also different, with the previous idealised study using the southwestern corner of the Weddell shelf sea, which is expected to be significantly colder and more prone to stronger winds than the wider shelf sea, increasing the heat loss to the atmosphere. As both the Ross and Weddell have similar atmospheric forcings, the difference calculated here is thought to be primarily due to the reduced (thinner and lower concentration) ice cover over the Ross shelf, decreasing insulation (especially during autumn/winter). The close fit between the Amundsen and Weddell is interesting, as the Weddell grows significantly more sea ice each autumn/winter (Fig. 3.10), although the Amundsen loses a similar quantity of heat to the surface, probably due to the entrainment of warmer waters from below the mixed layer, with this heat hindering ice formation.

4.5.2.1 Direct shelf sea salinity and temperature trends

Figure 4.20a and 4.20c show the salinity and temperature time-series (monthly means) for each of the four shelf seas. The direct trends in the shelf sea salinity (Table 4.2) and temperature (Table 4.3) are, in general, at least an order of magnitude lower than the estimated impact from the annual surface trends (of heat and effective salt), demonstrating the strong negative feedback due to ocean restoring, as discussed at the start of this section. Figure 4.20 demonstrates qualitatively that in the AB shelf seas, the reduced magnitude of the seasonal variability is the primary effect of the decreasing surface trends. This analysis is merely an attempt to highlight the potentially strong negative feedback that could be provided through changes in ocean advection, which is crudely parametrized by ocean restoring in this study. An ocean model able to accurately represent shelf sea oceanography is needed to understand the actual impact on the shelf seas due

to changes in the residence time of shelf waters and the horizontal advection of waters within the mixed and winter water layers.

4.6 Mixed Layer Depth Trends

This section investigates trends in the mixed layer due to the annual heat and effective salt input trends described above. Fig. 4.21 shows the trends in the MMLD and the contributions to the annual surface (mechanical) energy input to the mixed layer (W_{heat}, W_{ice}, W_{pe} and W_{net}) for both the ERA-I and HadGEM2-ES simulations, with the results summarised in Table 4.4. The annual energy input to the mixed layer (given in Sect. 3.1.2.2) is used in this analysis for the same reasons given in Sect. 3.2.4. Note that due to the weak impact of wind shearing on mixed layer deepening, as demonstrated in the previous chapter, this process is ignored in the following analysis. Polynya regions are also ignored in this analysis as a large fraction of these regions remain fully mixed, meaning only a change in the properties of the water column (as estimated in the previous section) are likely to be of interest.

ERA-I	**Weddell**	**B'hausen**	**Amundsen**	**Ross**
MMLD (m dec^{-1})	5.48	-2.93	-0.35	-0.78
W_{heat} (10^2J m^{-2}dec^{-1})	0.17	-0.27	0.65	0.67
W_{ice} (10^2J m^{-2}dec^{-1})	8.54	-0.11	1.60	-8.21
W_{pe} (10^2J m^{-2}dec^{-1})	-0.19	0.50	0.80	0.06
W_{net} (10^2J m^{-2}dec^{-1})	8.47	0.12	2.90	-7.52
HadGEM2-ES				
MMLD (m dec^{-1})	**-1.19**	**-1.98**	**-4.73**	0.46
W_{heat} (10^2J m^{-2}dec^{-1})	**-0.37**	**-0.26**	**-0.81**	-0.09
W_{ice} (10^2J m^{-2}dec^{-1})	**-3.16**	-0.003	-0.40 (93.5)	-1.15
W_{pe} (10^2J m^{-2}dec^{-1})	**-0.09**	**-1.76**	**-1.30**	-0.03
W_{net} (10^2J m^{-2}dec^{-1})	**-3.57**	**-1.77**	**-2.30**	-1.25

Table 4.4: Linear trends in the regional annual energy input contributions (given in Sect. 3.1.2.2) and the maximum mixed layer depth for both the ERA-I and HadGEM2-ES simulations (annual values shown in Fig. 4.21). All trends in bold are significant at 99%, with significance values between 90% and 99% included in parentheses.

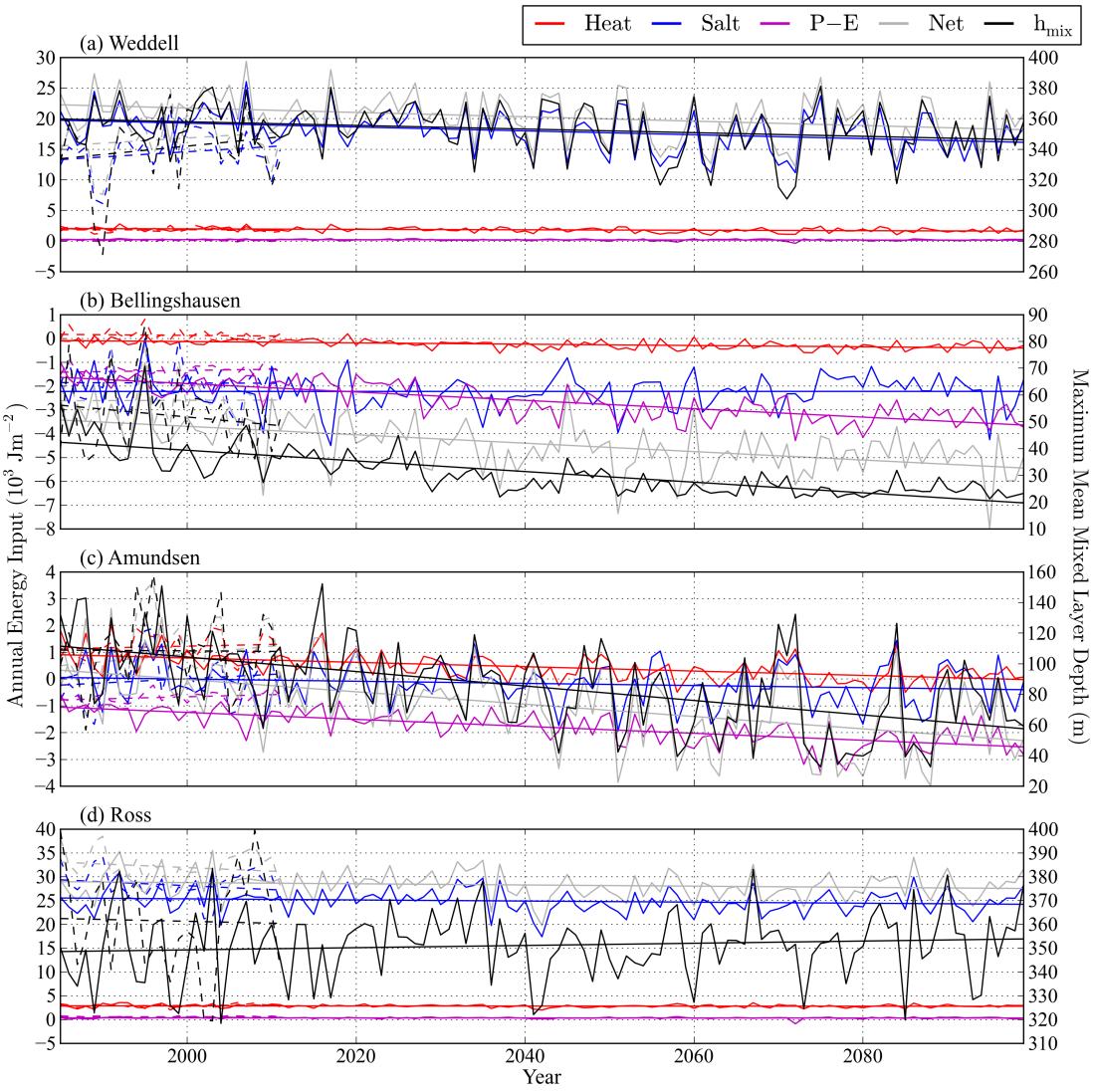

Figure 4.21: Regional annual mixed layer energy input contributions (given in Sect. 3.1.2.2), for both the ERA-I (1985-2011 - dashed lines) and HadGEM2-ES (1985-2099 - solid lines) simulations. The straight lines show the linear trends of the corresponding annual mixed layer energy input contributions. Also shown in black is the maximum mixed layer depth. The linear trends are listed in Table 4.4.

4.6.1 Recent and future trends in the mixed layer and surface energy input

The ERA-I simulation shows no significant or near-significant (>90%) trends in the MMLD or annual surface energy input contributions as highlighted in Table 4.4. Based on the near-significant decrease in the annual Weddell ice melt, it was expected that this would result in a decrease in the energy lost during spring/summer, increasing the overall energy input. There is, in fact, a strong positive trend in W_{ice} ($+8.54\times10^2$ J m^{-2}dec^{-1}), and the MMLD ($+5.48$ m dec^{-1}), however neither are significant. Fig. 3.9 shows the large internal variability in both signals, which prevents a significant trend being observed within this relatively short time-period.

The HadGEM2-ES simulation shows large and significant trends in both the MMLD and the surface energy input contributions across all regions except the Ross Sea, as expected from the previous trend analyses. There is a significant decrease in the Weddell MMLD (-1.19 m dec^{-1}), however this implies only a $\sim$10 m decrease by the end of the century. This appears to be driven primarily by a decrease in W_{ice} (-3.16×10^2 J m^{-2}dec^{-1}), which dominates the total W_{net} decrease (-3.57×10^2 J m^{-2}dec^{-1}).

There is a significant decrease in the Bellingshausen MMLD (-1.98 m dec^{-1}), resulting in a decrease from $\sim$40 m to $\sim$20 m (around 50%) by the end of the century. This is a large reduction and is driven primarily by a decrease in W_{pe} (-1.76×10^2 J m^{-2}dec^{-1}). The small decreasing trend in W_{heat} implies evaporation is likely providing only a small response compared to precipitation.

There is a stronger significant decrease in the Amundsen MMLD (-4.73 m dec^{-1}), resulting in an overall decrease from $\sim$115 m to $\sim$60 m (also around 50%) by the end of the century. This reduction is a result of significant decreases in W_{pe} (-1.30×10^2 J m^{-2}dec^{-1}) and W_{heat} (-0.81×10^2 J m^{-2}dec^{-1}), with W_{ice} contributing a smaller, near-significant decrease (-0.40×10^2 J m^{-2}dec^{-1}, 94%) . This results in a change from a small net surface energy input at the start of the simulation (1985) to a large net loss of energy at the surface by the end of the century (2099), similar to the current Bellingshausen mixed layer energy balance.

The Ross shelf sea does not show any significant trend, consistent with the lack of significant trends shown in the HadGEM2-ES simulation throughout the previous sections.

4.6.1.1 Mixed layer trend discussion

The energy input terms are a function of the mixed layer depth itself, both directly (to convert the buoyancy flux into a power) and through the calculation of energy dissipation, meaning the mixed layer depth trends should differ somewhat from the more direct impact of trends in the surface input of salt and heat discussed previously.

The regional pattern in the mixed layer trends is similar to that of the trends in the annual sea ice mass balance, and the heat and effective salt input trends discussed earlier, as expected. The absence of any near-significant trends in either the ERA-I simulation or Ross HadGEM2-ES results implies a weaker linear response in the mixed layer to atmospheric forcing trends. Any potential atmospheric forcing trend has been influenced by both the non-linearity of the thermodynamic/dynamic sea ice response and the internal mixed layer dynamics (through dissipation and mixed layer entrainment), increasing the variability and thereby decreasing the significance of any potential linear trend.

The importance of the MMLD or WW layer in controlling the basal melt rate of ice shelves fringing the AB seas has been discussed throughout this thesis. It is worth nothing, however, that localised processes can also play a strong role, such as the recent observations of *Padman et al.* (2012), which show a small halo of relatively deep WW surrounding the Wilkins Ice Shelf (WIS). Also, as discussed previously (Sect. 4.5.2), the *Holland et al.* (2010) modelling study linked the George VI Ice Shelf melt rate variability to specific years of enhanced mixed layer deepening, bringing heat from depth to above the ice shelf draft. The process described here, of a shelf-wide shoaling MMLD instead implies the potential for increased access to UCDW. A direct warming of the mixed layer through surface heat input trends (Sect. 4.5.2) could also be an important mechanism. The lack of significant trends in the ERA-I simulation implies this process is unlikely to be implicit in the current increase in the thinning of ice shelves fringing the AB seas, although a significant shelf sea trend may not even be required due to the strong

positive feedbacks associated with enhanced ice shelf melt (as discussed in Sect. 1.1.7). The HadGEM2-ES simulation, however, implies this mechanism could become more important in future decades.

While the Bellingshausen shelf appears to be flooded by the warmer UCDW (*Martinson and McKee*, 2012), the Amundsen shelf sea appears to be flooded predominantly by the colder LCDW, with UCDW (which overlies the LCDW) potentially blocked by the relatively deep WW layer near the shelf break (*Wåhlin et al.*, 2010; *Jacobs et al.*, 2011; *Arneborg et al.*, 2012; *Jacobs et al.*, 2012, 2013). The significant decrease in the Amundsen MMLD and the shift towards a more Bellingshausen like upper ocean state, could imply the potential for on-shelf advection of the shallower and warmer UCDW onto the Amundsen shelf in the coming century (under this moderate climate warming scenario). Such a process is highly uncertain but has been discussed in recent studies of the Amundsen Sea (e.g. *Dinniman et al.*, 2012; *Jacobs et al.*, 2013).

The AB shelf seas are strongly implicated in the rapid basal melting of the ice shelves fringing the coastline (e.g. *Pritchard et al.*, 2012; *Depoorter et al.*, 2013; *Rignot et al.*, 2013) and these results suggest that changing surface conditions (e.g. through a reduced sea ice cover) could increase the access of oceanic heat to ice shelves fringing the AB seas in the coming century, additional to the potential warming of CDW through increased ocean heat uptake,changes in the wind-driven transport on shelf (*Thoma et al.*, 2008) and changes in the ACC (e.g. *Gille*, 2002, 2008), as discussed in the introduction (Sect. 1.3.2).

In the WR seas, the physical meaning of a change in the MMLD is perhaps less clear considering the shelf waters that form here. A decrease in the MMLD signifies either a reduction in the regions forming shelf waters, a decrease in the depth of the shallower mixed layers that form further north, or the likely combination of both factors . The previous chapter discussed the importance of shelf waters (not HSSW) that form further north, in shielding the FRIS and RIS from intrusions of Modified Warm/Circumpolar Deep Waters (MWDW/MCDW) onto the shelf. A reduction in the MMLD implies the reduced ability of the shelf sea to cool these warmer water intrusions, potentially increasing their reach into the shelf sea. Strong conclusions cannot be drawn from the potential impact of such a process as there are likely to be strong

ocean feedbacks (e.g. changes in the summertime deep-shelf ocean properties - not a constant summertime relaxation profile) that will determine the total impact.

It was proposed by *Nicholls* (1997) that a surface warming induced slow-down of HSSW formation could, in fact, reduce basal ice shelf melt through reduced down-slope advection of HSSW towards the FRIS grounding line (where the HSSW is warmer than the freezing temperature at this pressure). However, as discussed by *Hellmer et al.* (2012), this neglects the potential impact of increased on-shelf advection of warm MWDW, which could provide much more heat than changes in HSSW formation, as the MWDW intrusions are significantly warmer. While the *Hellmer et al.* (2012) study proposed a potential redirection of the Antarctic coastal current in bringing warmer waters onto the shelf, this study indicates the potential for reduced mixing over the Weddell shelf, which could more indirectly increase the potential intrusions of warmer waters from north of the shelf break.

4.7 Chapter Conclusions

In this chapter, the CICE-mixed layer model has been used to investigate recent and future trends in the Antarctic sea ice cover, and the mixed layer over the Antarctic continental shelf. The ERA-I simulation of the previous chapter has been used to examine recent trends, while the atmospheric forcing output from the HadGEM2-ES GCM (under a moderate climate warming scenario) was used to simulate long-term trends. The recent mean HadGEM2-ES atmospheric forcing compares well with the ERA-I forcing and produces a reasonable mean ice concentration and thickness distribution compared to observations over recent decades.

Recent ERA-I forcing trends show strong spatial variability (in both magnitude and direction). Comparing the ERA-I trends to satellite inferred surface temperature trends demonstrate reasonable agreement with observations. The recent trends in the HadGEM2-ES forcing show poor agreement with ERA-I and observed atmospheric trends, highlighting the inability of current GCMs to simulate recent trends in the Antarctic climate. The long-term trends in the HadGEM2-ES forcing demonstrate a virtually circumpolar warming signal, except over the Ross

Sea, which appears to be well-shielded from the climate warming signal (with a similar pattern across all other forcing variables).

The ERA-I simulation captures much of the recently observed regional trends in concentration and ice motion. The ERA-I simulation shows strong spatially variable trends in ice thickness, especially along the Antarctic coastline within the shelf seas. The results agree well with the magnitude and regional variability shown in recent modelling studies (*Holland et al.*, submitted; *Massonnet et al.*, 2013), providing further insight to this crucial, yet largely unknown, Antarctic climate indicator. The HadGEM2-ES simulation shows a more consistent thinning trend, although there are some regions of thickening along the coast in the recent, short-term analysis, highlighting the important role of dynamical trends. The long-term HadGEM2-ES simulation shows significant, virtually circumpolar decreases in ice concentration and thickness (except in the Ross Sea) over the coming century, leading to the virtually complete loss of ice in the Amundsen and Bellingshausen seas, with the thermodynamic response thought to dominate over this time-scale.

An extended linear regression analysis using the longer-term HadGEM2-ES simulation showed similar correlations to the ERA-I simulation. The notable exception is in the wind regressions, with the Ross showing no correlation between the mixed layer deepening and either mean shelf sea wind component in the HadGEM2-ES simulation. The role of Cape Adare in preventing ice export, as discussed in the previous chapter, is unclear.

The ERA-I simulation shows a significant decrease in the annual Weddell shelf sea ice melt, but weak, insignificant trends in the annual shelf sea ice growth, melt and export, across the remaining shelf seas. The decrease in the annual Weddell ice melt leads to a near-significant increase in the annual effective salt input over the Weddell shelf, along with a moderate estimated freshening of the mean maximum mixed layer depth (MMLD). A near-significant decrease in the annual effective salt input under the Ross polynya is simulated, driven primarily by sea ice changes, resulting in a freshening of the same order of magnitude as those currently being observed. This is in contrast to the estimated increase in polynya growth from the observational studies of *Comiso et al.* (2011) and *Drucker et al.* (2011). There are no significant trends in

the MMLD or annual mixed layer energy input contributions in the ERA-I simulation, with the MMLD demonstrating large inter-annual variability.

The HadGEM2-ES simulation shows more significant (although not necessarily stronger) trends across all shelf-sea regions, due to the moderate climate warming signal and extended time-period. The Weddell shelf sea experiences: strong and significant decreases in the annual ice growth and export, and an increase in the annual ice melt; a decrease in the input of effective salt at the surface, resulting in a significant estimated freshening of the mean MMLD; and a significant (although small) decrease in the MMLD/destratifying potential. The Ross shelf sea experiences: a near-significant decrease in the annual Ross ice export, caused predominantly by a significant decrease in the annual Ross polynya ice growth; and a near-significant decrease in the annual input of effective salt under the polynya resulting in a freshening of the water column under the polynya (where the mixed layer reaches the shelf seabed). The Amundsen and Bellingshausen shelf seas experience: strong and significant decreases in the annual ice melt, growth and export; a decrease in the annual input of effective salt resulting in a strong estimated freshening of the mean (albeit shallow) MMLD; a significant increase in the annual surface-mixed layer heat input; and a strong, significant decrease ($\sim$50%) in the MMLD by the end of the century. The shoaling of the Amundsen and Bellingshausen mixed layers and the strong surface warming, could provide a significant increase in ocean heat carried towards the ice shelves fringing both seas.

The freshening signals were placed in context of the rapid thinning and acceleration of the West Antarctic ice shelves. This demonstrated that the large input of fresh glacial meltwater dominates over changes in freshwater from sea ice/precipitation trends. However, strong freshening was estimated in localised regions (e.g. polynyas) of a similar order of magnitude to the recently observed freshening (e.g. *Jacobs and Giulivi*, 2010). More research is needed to understand the potential pathway of increased fresh glacial meltwater, to fully understand the impact on the shelf seas and regions of HSSW formation.

Chapter 5

Concluding Remarks

> "We can only sense that in the deep and turbulent recesses of the sea are hidden mysteries far greater than any we have solved."
>
> — Rachel Carson; *The Sea Around Us*

While chapter conclusions are given throughout the thesis, this final chapter summarises the approaches taken, results found, and main conclusions drawn, based on the objectives listed in the introduction (Sect. 1.4). Following on from the discussion surrounding each objective is a summary of the main limitations of the work and the potential future work that could provide further insight.

Primary objective: Test whether the apparent bimodal distribution in the temperature of the Antarctic shelf seabed water masses can be explained directly by differing surface fluxes between the warm and cold regions.

A coupled sea ice-mixed layer model was used in Chapter 2 to investigate the physical processes underlying this bimodal distribution. The use of a highly simplified model provided both a complete understanding of the results, and the computational simplicity needed for the performance of a large number of sensitivity studies. The chapter built understanding of the many processes and feedbacks involved, and the switched forcing results lent strong support to the hypothesis of *Talbot* (1988), that differences in atmospheric forcings are sufficient to explain the difference in water-mass temperature over the Antarctic continental shelf.

Secondary objective: Provide further insight into the impact of the shelf sea properties (temperature and salinity) in controlling the mixed layer deepening

This same model could then be used to simplistically investigate whether the bimodal distribution could also be explained by: a difference in the rate, and/or temperature, of warm-water transport onto the shelf (*Dinniman et al.*, 2011); or the impact of warm water on-shelf, through the entrainment of heat into the mixed layer hindering sea ice formation (*Martinson*, 1990). Through the strong support given to the hypothesis of *Talbot* (1988) based on the results of the switched forcing simulations, the chapter indirectly showed that the regional variations in the shelf water properties were potentially less important than the strong regional differences in atmospheric forcing. Also, the Amundsen setup - Weddell forced simulation showed that while the entrainment of CDW caused significant changes to the sea ice, deep mixed layers still formed. In both cases, the 'cold' Weddell Sea atmospheric forcing was a necessary requirement for the formation of shelf waters. A switch in both the atmosphere and ocean, however, was required to provide a realistic switch in the shelf seas, implying an important role of the deeper-ocean. The simple nature of the ocean restoring, representing on-shelf flow of warmer-waters, and the lack of atmospheric feedbacks meant these hypotheses could not be tested in great detail.

Secondary objective: Investigate the sensitivity of the mixed layer depth to specific atmospheric forcings.

The model provided a simple way of testing the sensitivity of the maximum mixed layer depth to variations in specific atmospheric forcings. By varying the applied forcing between the smoothed representative Amundsen and Weddell forcings the model prediction of maximum mixed layer depth was shown to be most sensitive to air temperature. Differences in the incoming longwave radiation and air humidity were also shown to be important, with the difference in wind speed, precipitation and incoming shortwave radiation providing only a weak response.

Limitations and future work

Due to its inherent simplicity, the model could not conclude that any single mechanism controls the observed bimodal distribution in the shelf water-mass temperature. Also, of the five mechanisms listed in Sect. 1.1.5 used to explain the apparent bimodal distribution, the following mechanisms were not tested in this thesis: the presence of dense cold water on-shelf reduces the import of less-dense warm waters (*Talbot*, 1988); and, warmer waters induce a greater flux of ice-shelf meltwater, stratifying the water column and suppressing mixed layer deepening (*Jenkins and Jacobs*, 2008). Both raise the potentially important role of variations in shelf sea oceanography and remain fully untested in this model as the impact of surface fluxes was isolated from variable ocean dynamics.

Shelf water formation is expected to be strongly influenced by the potentially non-linear ocean feedbacks from off-shelf/on-shelf transport, represented simplistically by a linear restoring between the current salinity/temperature and the summertime properties in both the idealised and CICE-mixed layer models. Even the most sophisticated climate models have historically struggled to accurately model shelf water formation (*Heuzé et al.*, 2013) (although HadGEM2-ES was shown to be one of the best). Using a simple prescribed deep-ocean removed this potential problem, however this then meant such mechanisms remained untested. Investigating this and the potential for increasing ice shelf melt in response to ocean warming probably require the use of a fine-resolution and highly sophisticated sea ice-ocean-ice shelf model. Such models are in use (e.g. *Hellmer et al.*, 2012; *Holland et al.*, submitted; *Timmermann and Hellmer*, 2013), however maintaining reasonable shelf sea conditions and isolating individual mechanisms from these more complex models is a serious challenge.

Primary objective: Accurately quantify the cause of regional variations in the surface-driven formation of Antarctic shelf sea waters.

A prognostic mixed layer model (similar to that used in the idealised study) was incorporated into the Los Alamos sea ice model CICE in Chapter 3 to more accurately investigate the cause of regional variations in the formation of Antarctic shelf sea waters. The majority of previous

studies have attempted to accurately model the sea ice and shelf sea evolution within specific regions. The main advance of this study was in the use of a single Southern Ocean domain to analyse consistently the contrasting behaviour of the four shelf seas. Through the use of a highly idealised ocean model, the study also sought to isolate the impact of surface fluxes (as opposed to variable ocean dynamics) on mixed layer deepening and shelf water formation, similar to the approach taken in the idealised study. Through extensive comparison to observations, the model was shown to produce reasonably accurate estimates of the sea ice concentration, thickness and motion, while the mixed layer evolved as expected within each of the shelf seas.

Deconstructing the surface mechanical power input to the mixed layer demonstrated that the effective salt flux from sea ice growth/melt dominates the evolution of the mixed layer across all regions of interest. These results provided further evidence of the bimodal nature of the surface forcing over the shelf seas, investigated using the idealised model.

An analysis of the sea ice mass balance demonstrated the contrasting growth, melt and export of ice in each region. A linear regression analysis was also carried out, demonstrating significant spatial and temporal correlation between the mixed layer deepening and several atmospheric variables.

Secondary objective: Provide estimates of the annual surface salt/freshwater and heat inputs to the Southern Ocean.

Maps of the heat and effective salt input are useful quantities for ocean model surface boundary conditions and in understanding the surface forcing of the Southern Ocean. They also provided a useful validation of the model results. The effective salt input demonstrated the dominant role of sea ice growth/melt over net precipitation within the Antarctic shelf seas. This study showed a stronger effective salt input north of the polynya regions compared to other studies, a result that makes sense considering the shelf waters that form in these locations.

Limitations and future work

Validation of model results

This analysis suffered from a lack of observational data to compare the modelled results to. Antarctic sea ice concentration data are relatively accurate (above 0.15) and provide good temporal and spatial coverage. Antarctic sea ice and snow thickness is poorly sampled both temporally and spatially, however, and suffers from large uncertainties due to problems with accurately measuring the interface between the ice and snow layers (as discussed in Sect. 4.3). Ice motion data are fairly well sampled spatially and temporally, although it suffers from large differences between datasets (e.g. *Fowler*, 2003, updated 2008; *Holland and Kwok*, 2012), and summer estimates are hindered by inaccuracies due to surface melt. There is also a lack of direct oceanographic observations from within the shelf seas, due in large part to the overlying sea ice cover, preventing a more thorough validation of the mixed layer results.

The link between ice export and the mean shelf-sea winds provided interesting results in the Ross Sea, whereby the different forcing sets showed slightly contrasting results. It is still not clear whether the Cape Adare coast is providing any impact on ice export, or whether the winds do in fact, only change the angle at which the ice is exported out of the shelf seas. A more quantitative validation of the modelled ice motion would be useful.

The modelling approach

A key theme throughout this thesis was the focus on surface processes over variable ocean dynamics. Shelf sea oceanography is a crucial element of this complex climate system, however this study used a simple mixed layer model and a prescribed deep ocean throughout to simplify the results and provide a clearer understanding of the direct impact of surface processes alone. The reasons for this bulk mixed layer modelling approach were discussed in Sect. 2.1.4, whereby the simplicity of other aspects of the approach was argued to mean that a more thorough representation of mixing would represent an inconsistent level of complexity. Simply improving the mixing

scheme would therefore not help in answering many of the remaining questions. Instead, the coupling of a sophisticated ocean model (e.g. the Nucleus for European Modelling of the Ocean (NEMO) model) would therefore provide the more sensible next stage in a follow-up study.

Improvements in the representation of sea ice would probably be of more use in increasing the accuracy and reliability of the results presented in this study. While CICE returns the direct fluxes of salt and freshwater to the ocean at the onset of ice melt, in reality the sea ice loses brine through a variety of processes of differing time-scales (although brine drainage is thought to dominate, as discussed in Sect. 1.2.1). Recent modelling studies have shown the incorporation of a simple parameterisation of brine entrapment and drainage can have a significant impact on the mixed layer depth through the horizontal transport of brine contained within the sea ice (e.g. *Vancoppenolle et al.*, 2009). A brine drainage parameterisation is currently being incorporated into CICE (*Turner et al.*, 2013a), which could provide an improvement to the conclusions drawn in this study.

Another key area of uncertainty in this analysis was in the role of coastal polynyas in the shelf sea ice mass balance. The relatively coarse grid (∼55 km) meant polynyas (which have a width of only several kilometres in the Weddell Sea(*Markus et al.*, 1998)) were not fully resolved. A much finer-resolution grid is therefore required to understand in more detail the role of the polynyas relative to the more gradual growth of sea ice in shelf water formation. Increasing the grid resolution would likely provide further benefits too, such as improved ice motion along the coast, preventing large isolated grid cells that tend to cause erroneous thick ice build-up.

Primary objective: Investigate the recent and future evolution of the sea ice and mixed layer over the Antarctic continental shelf.

The CICE-mixed layer model was used in Chapter 4 to investigate recent (using the ERA-I forcing) and future (using the HadGEM2-ES forcing under a moderate climate warming scenario) trends in the sea ice, the surface inputs of heat and effective salt, and the mixed layer depth. By isolating the impact of surface trends alone, this approach provided valuable insight into the direct impact on the shelf seas from changes in the surface conditions (e.g. sea ice and net precipitation). Trends in the sea ice mass balance, the surface inputs of heat and effective salt,

and the mixed layer depth were investigated showing, in general, insignificant trends in the recent ERA-I simulation compared to the long-term HadGEM2-ES future projection.

Secondary objective: Quantify the potential shelf sea freshening from sea ice and net precipitation, in relation to the increased ice loss (meltwater) from the WAIS.

The results indicate that the recent increase in fresh glacial meltwater probably dominates over recent changes in freshwater from sea ice/precipitation trends. With the West Antarctic ice shelves likely to continue thinning and accelerating over the coming decades (e.g. *IPCC*, 2013), it is expected this dominance will continue. Strong freshening was estimated in localised regions (e.g. polynyas) however, of a similar order of magnitude to recently observed freshening trends (e.g. *Jacobs and Giulivi*, 2010), meaning the impact of sea ice on the shelf seas still cannot be neglected. These results differed considerably to recent observational estimates of polynya growth trends, however (*Comiso et al.*, 2011; *Drucker et al.*, 2011). Improvements in the representation of polynyas could again be useful.

Secondary objective: Investigate recent and future trends in the Antarctic sea ice cover

An analysis of the trends in the Antarctic sea ice concentration, motion and thickness was also carried out in Chapter 4, demonstrating the importance of accurate atmospheric forcing (e.g. through reanalysis) in reproducing the regional pattern in Antarctic sea ice trends. The ERA-I simulation provided further, crucial insight into the recent trends in Antarctic sea ice thickness, showing a strong spatially variable trend, especially along the Antarctic coastline, similar to other recent modelling studies (*Holland et al.*, submitted; *Massonnet et al.*, 2013). The long-term HadGEM2-ES simulation provided a future projection of the sea ice state under a moderate climate warming signal, showing a continued thinning and reduction in ice concentration circumpolar Antarctica, resulting in a perennially thin ice cover over the AB seas.

Limitations and future work

As discussed in Sect. 4.3.2, a key uncertainty surrounding studies of Antarctic sea ice trends is the potential ability of climate models to accurately simulate the wind-driven trends in ice motion shown in the study of *Holland and Kwok* (2012). The modelled trends in ice motion will be strongly influenced by the choice of ice rheology and drag parameterisations. CICE currently employs, as a default, the viscous-plastic (isotropic) rheology typical of most advanced sea ice models, as well as constant drag coefficients. A new anisotropic rheology and variable drag coefficients have now been incorporated into the latest (v5) CICE release (*Tsamados et al.*, 2013, submitted). Investigating modelled trends in ice motion using these improvements could provide valuable insight into the abilities of this sophisticated sea ice model to simulate the dynamically-driven trends in ice concentration (around West Antarctica). Such efforts could also improve the estimated trends in ice thickness, for which modelled simulations provide crucial insight considering the lack of observations, and could also improve the estimated trends in the annual surface inputs of salt and heat found in this study.

Question marks still remain over the results of future GCM projections (including the one presented in this thesis) that are unable to reproduce current trends. Increased evidence of the current trends being driven purely by natural variability will increase confidence that the future projection presented here, and in other studies (e.g. *Hellmer et al.*, 2012), may represent a reasonable projection of Antarctic sea ice and the resultant impact on the Antarctic shelf seas from increases in GHGs over the coming decades. While several recent studies have suggested that the observed increase in sea ice extent is within the range of natural variability (*Mahlstein et al.*, 2013; *Polvani and Smith*, 2013; *Swart and Fyfe*, 2013), the result does not hold for regional trends, and GCMs appear unable to correctly simulate natural variability anyway (*Turner et al.*, 2013b; *Zunz et al.*, 2013).

This study has demonstrated the potential increase in the access of warm ocean waters to ice shelves fringing the Amundsen and Bellingshausen seas from decreases in the wintertime mixed layer depth. Changes in the wind-driven transport on-shelf (*Thoma et al.*, 2008) and the potential

warming and poleward shift of the ACC (*Gille*, 2002, 2008) could provide further, potentially more dominant sources of additional ocean heat, however. Understanding the potential stability of the Filchner-Ronne Ice Shelf in the Weddell Sea is of great importance for future sea level rise projections, through its connections to the much larger East Antarctic Ice Sheet (*Bamber et al.*, 2000). Reduced destratification over the Weddell shelf, as found in the future HadGEM2-ES simulation, demonstrates a potential mechanism for increased access of the FRIS to warmer waters north of the shelf break, however more research is needed to understand the likelihood and potential impact of such a mechanism.

While the impact of increases in glacial meltwater have been offered as a potential mechanism for the recent sea ice increase (*Bintanja et al.*, 2013), *Swart and Fyfe* (2013) suggest this only contributes a small fraction of the observed increase. Continued and possible accelerations of the continental ice loss could yet provide a significant impact on the sea ice cover, however. While this thesis was unable to simulate changes in ice shelf melt, this process is expected to provide a significant impact on shelf water and thus bottom water formation over the coming decades. Improved measurements of continental ice loss; fine-resolution, coupled (sea ice-ocean-atmosphere-ice shelf) climate models; and more oceanographic measurements are all urgently required to improve our understanding of the mean state and future stability of the Antarctic shelf seas.

Bibliography

Ainley, D. G., and S. S. Jacobs (1981), Sea-bird affinities for ocean and ice boundaries in the antarctic, *Deep Sea Research Part A. Oceanographic Research Papers*, *28*(10), 1173–1185.

Antonov, J. I., D. Seidov, T. P. Boyer, R. A. Locarnini, A. V. Mishonov, H. E. Garcia, O. K. Baranova, M. M. Zweng, and D. R. Johnson (2010), World Ocean Atlas 2009, Volume 2: Salinity, p. 184, NOAA Atlas NESDIS 68, U.S. Government Printing Office,Washington, D.C.

Aoki, S., S. R. Rintoul, S. Ushio, S. Watanabe, and N. L. Bindoff (2005), Freshening of the Adélie Land Bottom Water near 140 °E, *Geophys. Res. Lett.*, *32*, L23601, doi:10.1029/2005GL024246.

Arblaster, J. M., and G. A. Meehl (2006), Contributions of external forcings to Southern Annular Mode trends, *J. Climate*, *19*(12), 2896–2905, doi:10.1175/JCLI3774.1.

Arneborg, L., A. K. Wåhlin, G. Björk, B. Liljebladh, and A. H. Orsi (2012), Persistent inflow of warm water onto the central Amundsen shelf, *Nature Geosci*, *5*(12), 876–880, doi:10.1038/ngeo1644.

Årthun, M., K. W. Nicholls, and L. Boehme (2012), Wintertime water mass modification near an Antarctic ice front, *J. Phys. Oceanogr.*, *43*(2), 359–365, doi:10.1175/JPO-D-12-0186.1.

Assmann, K., and R. Timmermann (2005), Variability of dense water formation in the Ross Sea, *Ocean Dynamics*, *55*(2), 68–87, doi:10.1007/s10236-004-0106-7.

Assmann, K. M., H. H. Hellmer, and S. S. Jacobs (2005), Amundsen sea ice production and transport, *J. Geophys. Res.*, *110*, C12013, doi:10.1029/2004JC002797.

Bamber, J. L., D. G. Vaughan, and I. Joughin (2000), Widespread complex flow in the interior of the Antarctic Ice Sheet, *Science*, *287*(5456), 1248–1250, doi:10.1126/science.287.5456.1248.

Bamber, J. L., R. E. M. Riva, B. L. A. Vermeersen, and A. M. LeBrocq (2009), Reassessment of the potential sea-level rise from a collapse of the West Antarctic Ice Sheet, *Science*, *324*(5929), 901–903, doi:10.1126/science.1169335.

Bindoff, N., et al. (2007), Observations: oceanic climate and sea level, in *Climate change 2007: The physical science basis. Contribution of working group I to the fourth assessment report of the Intergovernmental Panel on Climate Change [Solomon, S. and D. Qin and M. Manning and Z. Chen and M. Marquis and K.B. Averyt and M.Tignor and H.L. Miller (eds.)]*, Cambridge University Press.

Bintanja, R., G. J. van Oldenborgh, S. S. Drijfhout, B. Wouters, and C. A. Katsman (2013), Important role for ocean warming and increased ice-shelf melt in Antarctic sea-ice expansion, *Nature Geosci*, *6*(5), 376–379, doi:10.1038/ngeo1767.

Bitz, C. M., and W. H. Lipscomb (1999), An energy-conserving thermodynamic model of sea ice, *J. Geophys. Res.*, *104*(C7), 15,669–15,677, doi:10.1029/1999JC900100.

Bitz, C. M., and L. M. Polvani (2012), Antarctic climate response to stratospheric ozone depletion in a fine resolution ocean climate model, *Geophys. Res. Lett.*, *39*(20), L20705, doi:10.1029/2012GL053393.

Bitz, C. M., P. R. Gent, R. A. Woodgate, M. M. Holland, and R. Lindsay (2006), The influence of sea ice on ocean heat uptake in response to increasing CO_2, *J. Climate*, *19*(11), 2437–2450, doi:10.1175/JCLI3756.1.

Blanchon, P., A. Eisenhauer, J. Fietzke, and V. Liebetrau (2009), Rapid sea-level rise and reef back-stepping at the close of the last interglacial highstand, *Nature*, *458*(7240), 881–884, doi:10.1038/nature07933.

Boning, C. W., A. Dispert, M. Visbeck, S. R. Rintoul, and F. U. Schwarzkopf (2008), The response of the Antarctic Circumpolar Current to recent climate changes, *Nature Geosci*, *1*(12), 864–869, doi:10.1038/ngeo362.

Bracegirdle, T. J. (2013), Climatology and recent increase of westerly winds over the Amundsen Sea derived from six reanalyses, *Int. J. Climatol.*, *33*(4), 843–851, doi:10.1002/joc.3473.

Bracegirdle, T. J., and G. J. Marshall (2012), The reliability of Antarctic tropospheric pressure and temperature in the latest global reanalyses, *J. Climate*, *25*(20), 7138–7146, doi:10.1175/JCLI-D-11-00685.1.

Briegleb, B. P., and B. Light (2007), A Delta-Eddington multiple scattering parameterization for solar radiation in the sea ice component of the Community Climate System Model., *NCAR Tech. note NCAR/TN- 472+STR*, National Center for Atmospheric Research, Boulder, Colorado.

Bromwich, D. H., J. P. Nicolas, and A. J. Monaghan (2011), An assessment of precipitation changes over Antarctica and the Southern Ocean since 1989 in contemporary global reanalyses*, *J. Climate*, *24*(16), 4189–4209, doi:10.1175/2011JCLI4074.1.

Bromwich, D. H., J. P. Nicolas, A. J. Monaghan, M. A. Lazzara, L. M. Keller, G. A. Weidner, and A. B. Wilson (2013), Central West Antarctica among the most rapidly warming regions on Earth, *Nature Geosci*, *6*(2), 139–145, doi:10.1038/ngeo1671.

Cavalieri, D. J., and C. L. Parkinson (2012), Arctic sea ice variability and trends, 1979-2010, *The Cryosphere*, *6*(4), 881–889, doi:10.5194/tc-6-881-2012.

Cavalieri, D. J., C. L. Parkinson, and K. Y. Vinnikov (2003), 30-year satellite record reveals contrasting Arctic and Antarctic decadal sea ice variability, *Geophys. Res. Lett.*, *30*(18), 1970, doi:10.1029/2003GL018031.

Church, J. A., and N. J. White (2011), Sea-level rise from the late 19th to the early 21st Century, *Surveys in Geophysics*, *32*(4-5), 585–602, doi:10.1007/s10712-011-9119-1.

Comiso, J. (1999, updated 2012), Bootstrap sea ice concentrations from Nimbus-7 SMMR and DMSP SSM/I-SSMIS. Version 2, Boulder, Colorado USA: NASA DAAC at the National Snow and Ice Data Center.

Comiso, J. (2010), *Polar Oceans from Space*, Springer, New York.

Comiso, J. C. (1994), Surface temperatures in the polar regions from Nimbus 7 temperature humidity infrared radiometer, *J. Geophys. Res.*, *99*(C3), 5181–5200, doi:10.1029/93JC03450.

Comiso, J. C. (2000), Variability and trends in Antarctic surface temperatures from in situ and satellite infrared measurements, *J. Climate*, *13*(10), 1674–1696, doi:10.1175/1520-0442(2000)013⟨1674:VATIAS⟩2.0.CO;2.

Comiso, J. C., and F. Nishio (2008), Trends in the sea ice cover using enhanced and compatible AMSR-E, SSM/I, and SMMR data, *J. Geophys. Res.*, *113*, C02S07, doi:10.1029/2007JC004257.

Comiso, J. C., R. Kwok, S. Martin, and A. L. Gordon (2011), Variability and trends in sea ice extent and ice production in the Ross Sea, *J. Geophys. Res.*, *116*, C04021.

Cunningham, S. A., S. G. Alderson, B. A. King, and M. A. Brandon (2003), Transport and variability of the Antarctic Circumpolar Current in Drake Passage, *J. Geophys. Res.*, *108*(C5), 8084, doi:10.1029/2001JC001147.

de Steur, L., D. Holland, R. Muench, and M. McPhee (2007), The warm-water Halo around Maud Rise: Properties, dynamics and impacts, *Deep Sea Research Part I: Oceanographic Research Papers*, *54*(6), 871–896, doi:10.1016/j.dsr.2007.03.009.

Deacon, G. (1937), The hydrology of the Southern Ocean., *Discovery Reports*, *15*, 1–124.

Dee, D. P., et al. (2011), The ERA-Interim reanalysis: configuration and performance of the data assimilation system, *Q.J.R. Meteorol. Soc.*, *137*(656), 553–597, doi:10.1002/qj.828.

Depoorter, M. A., J. L. Bamber, J. A. Griggs, J. T. M. Lenaerts, S. R. M. Ligtenberg, M. R. van den Broeke, and G. Moholdt (2013), Calving fluxes and basal melt rates of Antarctic ice shelves, *Nature*, *advance online publication*, doi:10.1038/nature12567.

Ding, Q., E. J. Steig, D. S. Battisti, and M. Kuttel (2011), Winter warming in West Antarctica caused by central tropical Pacific warming, *Nature Geosci*, *4*(6), 398–403, doi:10.1038/ngeo1129.

Ding, Q., E. J. Steig, D. S. Battisti, and J. M. Wallace (2012), Influence of the Tropics on the Southern Annular Mode, *J. Climate*, *25*(18), 6330–6348, doi:10.1175/JCLI-D-11-00523.1.

Dinniman, M. S., and J. M. Klinck (2004), A model study of circulation and cross-shelf exchange on the West Antarctic Peninsula continental shelf, *Deep Sea Research Part II: Topical Studies in Oceanography*, *51*(1719), 2003–2022, doi:10.1016/j.dsr2.2004.07.030.

Dinniman, M. S., J. M. Klinck, and W. O. Smith Jr. (2011), A model study of Circumpolar Deep Water on the West Antarctic Peninsula and Ross Sea continental shelves, *Deep Sea Research Part II: Topical Studies in Oceanography*, *58*(1316), 1508–1523, doi:10.1016/j.dsr2.2010.11.013.

Dinniman, M. S., J. M. Klinck, and E. E. Hofmann (2012), Sensitivity of Circumpolar Deep Water transport and ice shelf basal melt along the West Antarctic Peninsula to changes in the winds, *J. Climate*, *25*(14), 4799–4816, doi:10.1175/JCLI-D-11-00307.1.

Drucker, R., S. Martin, and R. Kwok (2011), Sea ice production and export from coastal polynyas in the Weddell and Ross seas, *Geophys. Res. Lett.*, *38*(17), L17502, doi:10.1029/2011GL048668.

Dupont, T. K., and R. B. Alley (2005), Assessment of the importance of ice-shelf buttressing to ice-sheet flow, *Geophys. Res. Lett.*, *32*, L04503, doi:10.1029/2004GL022024.

Ebert, E. E., and J. A. Curry (1993), An intermediate one-dimensional thermodynamic sea ice model for investigating ice-atmosphere interactions, *J. Geophys. Res.*, *98*(C6), 10,085–10,109, doi:10.1029/93JC00656.

Eisenman, I., T. Schneider, D. S. Battisti, and C. M. Bitz (2011), Consistent changes in the sea ice seasonal cycle in response to global warming, *J. Climate*, *24*(20), 5325–5335, doi: 10.1175/2011JCLI4051.1.

Fahrbach, E., R. Peterson, G. Rohardt, P. Schlosser, and R. Bayer (1994a), Suppression of bottom water formation in the southeastern Weddell Sea, *Deep Sea Research Part I: Oceanographic Research Papers*, *41*(2), 389–411, doi:10.1016/0967-0637(94)90010-8.

Fahrbach, E., G. Rohardt, M. Schröder, and V. Strass (1994b), Transport and structure of the Weddell Gyre, *Annales Geophysicae*, *12*(9), 840–855, doi:10.1007/s00585-994-0840-7.

Fahrbach, E., M. Hoppema, G. Rohardt, M. Schroder, and A. Wisotzki (2004), Decadal-scale variations of water mass properties in the deep Weddell Sea, *Ocean Dynamics*, *54*(1), 77–91, doi:10.1007/s10236-003-0082-3.

Fahrbach, E., M. Hoppema, G. Rohardt, O. Boebel, O. Klatt, and A. Wisotzki (2011), Warming of deep and abyssal water masses along the Greenwich meridian on decadal time scales: The

Weddell Gyre as a heat buffer, *Deep Sea Research Part II: Topical Studies in Oceanography*, *58*(2526), 2509–2523, doi:10.1016/j.dsr2.2011.06.007.

Farman, J. C., B. G. Gardiner, and J. D. Shanklin (1985), Large losses of total ozone in Antarctica reveal seasonal ClOx/NOx interactions, *Nature*, *315*(6016), 207–210, doi:10.1038/315207a0.

Feltham, D. L., N. Untersteiner, J. S. Wettlaufer, and M. G. Worster (2006), Sea ice is a mushy layer, *Geophys. Res. Lett.*, *33*(14), L14501, doi:10.1029/2006GL026290.

Fogt, R., D. Bromwich, and K. Hines (2011), Understanding the SAM influence on the south pacific ENSO teleconnection, *Clim Dyn*, *36*(7-8), 1555–1576, doi:10.1007/s00382-010-0905-0.

Fogt, R. L., and D. H. Bromwich (2006), Decadal variability of the ENSO teleconnection to the high-latitude South Pacific governed by coupling with the Southern Annular Mode*, *J. Climate*, *19*(6), 979–997, doi:10.1175/JCLI3671.1.

Foldvik, A., T. Gammelsrød, and T. Tørresen (1985), Hydrographic observations from the Weddell Sea during the Norwegian Antarctic Research Expedition 1976/77, *Polar Research*, *3*, 177–193, doi:10.1111/j.1751-8369.1985.tb00506.x.

Foldvik, A., T. Gammelsrød, S. Østerhus, E. Fahrbach, G. Rohardt, M. Schroder, K. W. Nicholls, L. Padman, and R. A. Woodgate (2004), Ice shelf water overflow and bottom water formation in the southern Weddell Sea, *J. Geophys. Res.*, *109*, C02015, doi:10.1029/2003JC002008.

Foster, T. D., and E. C. Carmack (1976), Frontal zone mixing and Antarctic Bottom Water formation in the southern Weddell Sea, *Deep Sea Research*, *23*(4), 301–317, doi:10.1016/0011-7471(76)90872-X.

Fowler, C. (2003, updated 2008), Polar Pathfinder daily 25 km EASE-grid sea ice motion vectors, [1981 - 2006], Boulder, Colorado USA: NASA DAAC at the National Snow and Ice Data Center.

Fretwell, P., et al. (2013), Bedmap2: improved ice bed, surface and thickness datasets for Antarctica, *The Cryosphere*, *7*(1), 375–393, doi:10.5194/tc-7-375-2013.

Fricker, H. A., and L. Padman (2012), Thirty years of elevation change on Antarctic Peninsula ice shelves from multimission satellite radar altimetry, *J. Geophys. Res.*, *117*, C02026, doi:10.1029/2011JC007126.

Fyfe, J. C., and O. A. Saenko (2005), Human-induced change in the Antarctic Circumpolar Current, *J. Climate*, *18*(15), 3068–3073, doi:10.1175/JCLI3447.1.

Giles, K. A., S. W. Laxon, and A. L. Ridout (2008), Circumpolar thinning of Arctic sea ice following the 2007 record ice extent minimum, *Geophys. Res. Lett.*, *35*(22), L22502, doi:10.1029/2008GL035710.

Gill, A. E. (1973), Circulation and bottom water production in the Weddell Sea, *Deep Sea Research and Oceanographic Abstracts*, *20*(2), 111–140, doi:10.1016/0011-7471(73)90048-X.

Gille, S. T. (2002), Warming of the Southern Ocean since the 1950s, *Science*, *295*(5558), 1275–1277, doi:10.1126/science.1065863.

Gille, S. T. (2008), Decadal-scale temperature trends in the Southern Hemisphere oceans, *J. Climate*, *21*(18), 4749–4765, doi:10.1175/2008JCLI2131.1.

Gillett, N. P., and D. W. J. Thompson (2003), Simulation of recent Southern Hemisphere climate changes, *Science*, *302*(5643), 273–275, doi:10.1126/science.1087440.

Gordon, A. L. (1971), Oceanography of Antarctic waters, in *Antarct. Res. Ser.*, vol. 15, edited by J. L. Reid, pp. 169–203, AGU, Washington, DC, doi:10.1029/AR015p0169.

Gordon, A. L. (1998), Western Weddell Sea thermohaline stratification, in *Antarct. Res. Ser.*, vol. 75, pp. 215–240, AGU, Washington, DC, doi:10.1029/AR075p0215.

Gordon, A. L., B. Huber, D. McKee, and M. Visbeck (2010), A seasonal cycle in the export of bottom water from the Weddell Sea, *Nature Geosci*, *3*(8), 551–556, doi:10.1038/ngeo916.

Hall, A., and M. Visbeck (2002), Synchronous variability in the Southern Hemisphere atmosphere, sea ice, and ocean resulting from the Annular Mode*, *J. Climate*, *15*(21), 3043–3057, doi:10.1175/1520-0442(2002)015⟨3043:SVITSH⟩2.0.CO;2.

Hellmer, H. H., S. S. Jacobs, and A. Jenkins (1998), Oceanic erosion of a floating Antarctic glacier in the Amundsen Sea, *Ocean, Ice, and Atmosphere: Interactions at the Antarctic Continental Margin, Antarct. Res. Ser*, *75*, 83–99, doi:10.1029/AR075p0083.

Hellmer, H. H., O. Huhn, D. Gomis, and R. Timmermann (2011), On the freshening of the northwestern Weddell Sea continental shelf, *Ocean Science*, *7*(3), 305–316, doi:10.5194/os-7-305-2011.

Hellmer, H. H., F. Kauker, R. Timmermann, J. Determann, and J. Rae (2012), Twenty-first-century warming of a large Antarctic ice-shelf cavity by a redirected coastal current, *Nature*, *485*(7397), 225–228, doi:10.1038/nature11064.

Heuzé, C., K. J. Heywood, D. P. Stevens, and J. K. Ridley (2013), Southern Ocean bottom water characteristics in CMIP5 model, *Geophys. Res. Lett.*, *40*(7), 1409–1414, doi:10.1002/grl.50287.

Heywood, K. J., A. C. Naveira Garabato, D. P. Stevens, and R. D. Muench (2004), On the fate of the Antarctic Slope Front and the origin of the Weddell Front, *J. Geophys. Res.*, *109*, C06021, doi:10.1029/2003JC002053.

Hibler, W. D. (1979), A dynamic thermodynamic sea ice model, *J. Phys. Oceanogr.*, *9*(4), 815–846, doi:10.1175/1520-0485(1979)009⟨0815:ADTSIM⟩2.0.CO;2.

Hofmann, E. E., D. P. Costa, K. Daly, M. S. Dinniman, J. M. Klinck, M. Marrari, L. Padman, and A. Pinones (2009), Results from the US Southern Ocean GLOBEC synthesis studies, *GLOBEC Int. Newsl*, *15*, 43–48.

Hogg, A. M. C., M. P. Meredith, J. R. Blundell, and C. Wilson (2008), Eddy heat flux in the Southern Ocean: Response to variable wind forcing, *J. Climate*, *21*(4), 608–620, doi:10.1175/2007JCLI1925.1.

Holland, M. M., C. M. Bitz, and B. Tremblay (2006), Future abrupt reductions in the summer Arctic sea ice, *Geophys. Res. Lett.*, *33*, L23503, doi:10.1029/2006GL028024.

Holland, P. R., and R. Kwok (2012), Wind-driven trends in Antarctic sea-ice drift, *Nature Geosci*, *5*(12), 872–875, doi:10.1038/ngeo1627.

Holland, P. R., A. Jenkins, and D. M. Holland (2010), Ice and ocean processes in the Bellingshausen Sea, Antarctica, *J. Geophys. Res.*, *115*, C05020.

Holland, P. R., N. Bruneau, C. Enright, M. Losch, N. T. Kurtz, and R. A. Kwok (submitted), Modelled trends in Antarctic sea ice thickness, *Journal of Climate*.

Hughes, T. J. (1981), The weak underbelly of the West Antarctic Ice-Sheet, *Journal of Glaciology*, *27*, 581–525.

Hunke, E. C., and J. K. Dukowicz (1997), An elastic viscous plastic model for sea ice dynamics, *J. Phys. Oceanogr.*, *27*(9), 1849–1867, doi:10.1175/1520-0485(1997)027⟨1849:AEVPMF⟩2.0.CO; 2.

Hunke, E. C., and W. H. Lipscomb (2010), CICE: the Los Alamos sea ice model documentation and software user's manual version 4.1, *LA-CC-06-012*, T-3 Fluid Dynamics Group, Los Alamos National Laboratory, Los Alamos.

IPCC (2007), *Climate Change 2007: The Physical Science Basis. Contribution of Working Group I to the Fourth Assessment Report of the Intergovernmental Panel on Climate Change [Solomon, S. and D. Qin and M. Manning and Z. Chen and M. Marquis and K.B. Averyt and M.Tignor and H.L. Miller (eds.)]*, 235–337 pp., Cambridge University Press, Cambridge, United Kingdom and New York, USA.

IPCC (2013), *Summary for Policymakers. In: Climate Change 2013: The Physical Science Basis. Contribution of Working Group I to the Fifth Assessment Report of the Intergovernmental Panel on Climate Change [Stocker, T.F., D. Qin, G.-K. Plattner, M. Tignor, S. K. Allen, J. Boschung, A. Nauels, Y. Xia, V. Bex and P.M. Midgley (eds.)]*, Cambridge University Press, Cambridge, United Kingdom and New York, NY, USA.

Jacobs, S. (2006), Observations of change in the Southern Ocean, *Philosophical Transactions of the Royal Society A: Mathematical, Physical and Engineering Sciences*, *364*(1844), 1657–1681, doi:10.1098/rsta.2006.1794.

Jacobs, S., C. Giulivi, P. Dutrieux, E. Rignot, F. Nitsche, and J. Mouginot (2013), Getz ice shelf melting response to changes in ocean forcing, *J. Geophys. Res. Oceans*, *118*, doi:10.1002/jgrc. 20298.

Jacobs, S., S., A. Jenkins, H. Hellmer, C. Giulivi, F. Nitsche, B. Huber, and R. Guerrero (2012), The Amundsen Sea and the Antarctic Ice Sheet, *Oceanography*, *25*(3), 154–163, doi:10.5670/oceanog.2012.90.

Jacobs, S. S. (1991), On the nature and significance of the antarctic slope front, *Marine Chemistry*, *35*(14), 9–24.

Jacobs, S. S. (2004), Bottom water production and its links with the thermohaline circulation, *Antarctic Science*, *16*(4), 427–437, doi:10.1017/S095410200400224X.

Jacobs, S. S., and C. F. Giulivi (1998), Interannual ocean and sea ice variability in the Ross Sea, in *Antarct. Res. Ser.*, vol. 75, pp. 135–150, AGU, Washington, DC, doi:10.1029/AR075p0135.

Jacobs, S. S., and C. F. Giulivi (2010), Large multidecadal salinity trends near the Pacific-Antarctic continental margin, *J. Climate*, *23*(17), 4508–4524, doi:10.1175/2010JCLI3284.1.

Jacobs, S. S., A. F. Amos, and P. M. Bruchhausen (1970), Ross Sea oceanography and Antarctic Bottom Water formation, *Deep Sea Research and Oceanographic Abstracts*, *17*(6), 935–962, doi:10.1016/0011-7471(70)90046-X.

Jacobs, S. S., R. G. Fairbanks, and Y. G. Horibe (1985), Origin and evolution of water masses near the Antarctic continental margin: Evidence from $H_2^{18}O/H_2^{16}O$ ratios in seawater, in *Antarct. Res. Ser.*, vol. 43, pp. 59–85, AGU, Washington, DC, doi:10.1029/AR043p0059.

Jacobs, S. S., H. H. Hellmer, and A. Jenkins (1996), Antarctic Ice Sheet melting in the Southeast Pacific, *Geophys. Res. Lett.*, *23*(9), 957–960, doi:10.1029/96GL00723.

Jacobs, S. S., C. F. Giulivi, and P. A. Mele (2002), Freshening of the Ross Sea during the late 20th Century, *Science*, *297*(5580), 386–389, doi:10.1126/science.1069574.

Jacobs, S. S., A. Jenkins, C. F. Giulivi, and P. Dutrieux (2011), Stronger ocean circulation and increased melting under Pine Island Glacier ice shelf, *Nature Geosci*, *4*(8), 519–523, doi:10.1038/ngeo1188.

Jeffries, M. O., and U. Adolphs (1997), Early winter ice and snow thickness distribution, ice structure and development of the western Ross Sea pack ice between the ice edge and the Ross Ice Shelf, *Antarctic Science*, *9*(02), 188–200, doi:10.1017/S0954102097000242.

Jenkins, A., and D. Holland (2007), Melting of floating ice and sea level rise, *Geophys. Res. Lett.*, *34*(16), L16609, doi:10.1029/2007GL030784.

Jenkins, A., and S. Jacobs (2008), Circulation and melting beneath George VI Ice Shelf, Antarctica, *J. Geophys. Res.*, *113*, C04013, doi:10.1029/2007JC004449.

Johnson, G. C. (2008), Quantifying Antarctic Bottom Water and North Atlantic Deep Water volumes, *J. Geophys. Res.*, *113*, C05027, doi:10.1029/2007JC004477.

Jones, C. D., et al. (2011), The HadGEM2-ES implementation of CMIP5 centennial simulations, *Geosci. Model Dev.*, *4*(3), 543–570, doi:10.5194/gmd-4-543-2011.

Jones, P. D., D. H. Lister, T. J. Osborn, C. Harpham, M. Salmon, and C. P. Morice (2012), Hemispheric and large-scale land-surface air temperature variations: An extensive revision and an update to 2010, *J. Geophys. Res.*, *117*(D5), D05127, doi:10.1029/2011JD017139.

Jullion, L., A. C. Naveira Garabato, M. P. Meredith, P. R. Holland, P. Courtois, and B. A. King (2013), Decadal freshening of the Antarctic Bottom Water exported from the Weddell Sea, *J. Climate*, *26*(20), 8111–8125, doi:10.1175/JCLI-D-12-00765.1.

Kara, A. B., A. J. Wallcraft, and H. E. Hurlburt (2005), A new solar radiation penetration scheme for use in ocean mixed layer studies: An application to the Black Sea using a fine-resolution hybrid coordinate ocean model (HYCOM), *J. Phys. Oceanogr.*, *35*(1), 13–32, doi:10.1175/JPO2677.1.

Kim, J.-W. (1976), A generalized bulk model of the oceanic mixed layer, *J. Phys. Oceanogr.*, *6*(5), 686–695, doi:10.1175/1520-0485(1976)006⟨0686:AGBMOT⟩2.0.CO;2.

Kimura, N. (2004), Sea ice motion in response to surface wind and ocean current in the Southern Ocean:, *Journal of the Meteorological Society of Japan. Ser. II*, *82*(4), 1223–1231, doi:10.2151/jmsj.2004.1223.

Klinck, J., E. Hofmann, R. Beardsley, B. Salihoglu, and S. Howard (2004), Water-mass properties and circulation on the west Antarctic Peninsula continental shelf in austral fall and winter 2001, *Deep Sea Research Part II: Topical Studies in Oceanography*, *51*(17), 1925–1946, doi:10.1016/j.dsr2.2004.08.001.

Klinck, J. M., and M. S. Dinniman (2010), Exchange across the shelf break at high southern latitudes, *Ocean Sci.*, *6*(2), 513–524, doi:10.5194/os-6-513-2010.

Kopp, R. E., F. J. Simons, J. X. Mitrovica, A. C. Maloof, and M. Oppenheimer (2009), Probabilistic assessment of sea level during the last interglacial stage, *Nature*, *462*(7275), 863–867, doi:10.1038/nature08686.

Kraus, E. B., and J. S. Turner (1967), A one-dimensional model of the seasonal thermocline II. the general theory and its consequences, *Tellus*, *19*(1), 98–106, doi:10.1111/j.2153-3490.1967.tb01462.x.

Kurtz, N. T., and T. Markus (2012), Satellite observations of Antarctic sea ice thickness and volumes, *J. Geophys. Res.*, *117*, C08025, doi:10.1029/2012JC008141.

Kwok, R. (2005), Ross sea ice motion, area flux, and deformation, *J. Climate*, *18*(18), 3759–3776, doi:10.1175/JCLI3507.1.

Kwok, R., and J. C. Comiso (2002), Spatial patterns of variability in Antarctic surface temperature: Connections to the Southern Hemisphere Annular Mode and the Southern Oscillation, *Geophys. Res. Lett.*, *29*(14), 1705–, doi:10.1029/2002GL015415.

Kwok, R., and D. A. Rothrock (2009), Decline in Arctic sea ice thickness from submarine and ICESat records: 1958-2008, *Geophys. Res. Lett.*, *36*(15), L15501, doi:10.1029/2009GL039035.

Large, W. G., J. C. McWilliams, and S. C. Doney (1994), Oceanic vertical mixing: A review and a model with a nonlocal boundary layer parameterization, *Rev. Geophys.*, *32*(4), 363–403, doi:10.1029/94RG01872.

Laxon, S. W., et al. (2013), CryoSat-2 estimates of Arctic sea ice thickness and volumes, *Geophys. Res. Lett.*, *40*(4), 732–737, doi:10.1002/grl.50193.

Lefebvre, W., H. Goosse, R. Timmermann, and T. Fichefet (2004), Influence of the Southern Annular Mode on the sea ice-ocean system, *J. Geophys. Res.*, *109*, C09005, doi:10.1029/2004JC002403.

Lemke, P. (1987), A coupled one-dimensional sea ice-ocean model, *J. Geophys. Res.*, *92*(C12), 13,164–13,172, doi:10.1029/JC092iC12p13164.

Lemke, P., and T. O. Manley (1984), The seasonal variation of the mixed layer and the pycnocline under polar sea ice, *J. Geophys. Res.*, *89*(C4), 6494–6504, doi:10.1029/JC089iC04p06494.

Lemke, P., W. B. Owens, and W. D. Hibler (1990), A coupled sea ice-mixed layer-pycnocline model for the Weddell Sea, *J. Geophys. Res.*, *95*(C6), 9513–9525, doi:10.1029/JC095iC06p09513.

Levitus, S., J. I. Antonov, T. P. Boyer, and C. Stephens (2000), Warming of the World Ocean, *Science*, *287*(5461), 2225–2229, doi:10.1126/science.287.5461.2225.

Levitus, S., J. Antonov, and T. Boyer (2005), Warming of the World Ocean, 1955-2003, *Geophys. Res. Lett.*, *32*(2), L02604, doi:10.1029/2004GL021592.

Levitus, S., et al. (2012), World ocean heat content and thermosteric sea level change (0-2000 m), 1955-2010, *Geophys. Res. Lett.*, *39*, L10603, doi:10.1029/2012GL051106.

Lindsay, R. W., D. M. Holland, and R. A. Woodgate (2004), Halo of low ice concentration observed over the Maud Rise seamount, *Geophys. Res. Lett.*, *31*(13), L13302, doi:10.1029/2004GL019831.

Liu, J., and J. A. Curry (2010), Accelerated warming of the Southern Ocean and its impacts on the hydrological cycle and sea ice, *Proceedings of the National Academy of Sciences*, pp. –, doi:10.1073/pnas.1003336107.

Liu, J., J. A. Curry, and D. G. Martinson (2004), Interpretation of recent Antarctic sea ice variability, *Geophys. Res. Lett.*, *31*, L02205, doi:10.1029/2003GL018732.

Locarnini, R. A., A. V. Mishonov, J. I. Antonov, T. P. Boyer, H. E. Garcia, O. K. Baranova, M. M. Zweng, and D. R. Johnson (2010), World Ocean Atlas 2009, Volume 1: Temperature, NOAA Atlas NESDIS 68, U.S. Government Printing Office,Washington, D.C.

Lumpkin, R., and K. Speer (2007), Global ocean meridional overturning, *J. Phys. Oceanogr.*, *37*(10), 2550–2562, doi:10.1175/JPO3130.1.

Mahlstein, I., P. R. Gent, and S. Solomon (2013), Historical Antarctic mean sea ice area, sea ice trends, and winds in CMIP5 simulations, *J. Geophys. Res. Atmos.*, *118*(11), 5105–5110, doi:10.1002/jgrd.50443.

Mann, M. E., Z. Zhang, M. K. Hughes, R. S. Bradley, S. K. Miller, S. Rutherford, and F. Ni (2008), Proxy-based reconstructions of hemispheric and global surface temperature variations over the past two millennia, *Proceedings of the National Academy of Sciences*, *105*(36), 13,252–13,257, doi:10.1073/pnas.0805721105.

Marcott, S. A., J. D. Shakun, P. U. Clark, and A. C. Mix (2013), A reconstruction of regional and global temperature for the past 11,300 years, *Science*, *339*(6124), 1198–1201, doi:10.1126/science.1228026.

Markus, T. (1999), Results from an ECMWF-SSM/I forced mixed layer model of the Southern Ocean, *J. Geophys. Res.*, *104*(C7), 15,603–15,620, doi:10.1029/1999JC900080.

Markus, T., C. Kottmeier, and E. Fahrbach (1998), Ice formation in coastal polynyas in the Weddell Sea and their impact on oceanic salinity, in *Antarctic Sea Ice: Physical Processes, Interactions and Variability*, *Antarct. Res. Ser.*, vol. 74, edited by O. Jeffries, pp. 273–292, AGU, Washington, D. C., doi:10.1029/AR074p0273.

Marshall, G. J. (2002), Analysis of recent circulation and thermal advection change in the northern Antarctic Peninsula, *Int. J. Climatol.*, *22*(12), 1557–1567, doi:10.1002/joc.814.

Marshall, G. J. (2003), Trends in the Southern Annular Mode from observations and reanalyses, *J. Climate*, *16*(24), 4134–4143, doi:10.1175/1520-0442(2003)016⟨4134:TITSAM⟩2.0.CO;2.

Marshall, G. J., P. A. Stott, J. Turner, W. M. Connolley, J. C. King, and T. A. Lachlan-Cope (2004), Causes of exceptional atmospheric circulation changes in the Southern Hemisphere, *Geophys. Res. Lett.*, *31*(14), L14205, doi:10.1029/2004GL019952.

Marshall, G. J., A. Orr, N. P. M. van Lipzig, and J. C. King (2006), The impact of a changing Southern Hemisphere Annular Mode on Antarctic Peninsula summer temperatures, *J. Climate*, *19*(20), 5388–5404, doi:10.1175/JCLI3844.1.

Marshall, J., and K. Speer (2012), Closure of the meridional overturning circulation through Southern Ocean upwelling, *Nature Geosci*, *5*(3), 171–180, doi:10.1038/ngeo1391.

Martin, S., R. Drucker, R. Kwok, and B. Holt (2004), Estimation of the thin ice thickness and heat flux for the Chukchi Sea Alaskan coast polynya from Special Sensor Microwave/Imager data, 1990-2001, *J. Geophys. Res.*, *109*, C10012, doi:10.1029/2004JC002428.

Martin, S., R. S. Drucker, and R. Kwok (2007), The areas and ice production of the western and central Ross Sea polynyas, 1992-2002, and their relation to the B-15 and C-19 iceberg events of 2000 and 2002, *Journal of Marine Systems*, *68*(12), 201–214, doi:10.1016/j.jmarsys.2006.11.008.

Martinson, D. G. (1990), Evolution of the Southern Ocean winter mixed layer and sea ice: Open ocean deepwater formation and ventilation, *J. Geophys. Res.*, *95*(C7), 11,641–11,654, doi:10.1029/JC095iC07p11641.

Martinson, D. G., and D. C. McKee (2012), Transport of warm Upper Circumpolar Deep Water onto the western Antarctic Peninsula continental shelf, *Ocean Sci.*, *8*(4), 433–442, doi:10.5194/os-8-433-2012.

Martinson, D. G., S. E. Stammerjohn, R. A. Iannuzzi, R. C. Smith, and M. Vernet (2008), Western Antarctic Peninsula physical oceanography and spatio-temporal variability, *Deep Sea Research Part II: Topical Studies in Oceanography*, *55*(1819), 1964–1987, doi:10.1016/j.dsr2.2008.04.038.

Marzeion, B., A. H. Jarosch, and M. Hofer (2012), Past and future sea-level change from the surface mass balance of glaciers, *The Cryosphere*, *6*(6), 1295–1322, doi:10.5194/tc-6-1295-2012.

Massom, R. A., M. R. Drinkwater, and C. Haas (1997), Winter snow cover on sea ice in the Weddell Sea, *J. Geophys. Res.*, *102*(C1), 1101–1117, doi:10.1029/96JC02992.

Massonnet, F., P. Mathiot, T. Fichefet, H. Goosse, C. Knig Beatty, M. Vancoppenolle, and T. Lavergne (2013), A model reconstruction of the Antarctic sea ice thickness and volume changes over 1980-2008 using data assimilation, *Ocean Modelling*, *64*, 67–75, doi:10.1016/j.ocemod.2013.01.003.

Maykut, G. A., and D. K. Perovich (1987), The role of shortwave radiation in the summer decay of a sea ice cover, *J. Geophys. Res.*, *92*(C7), 7032–7044, doi:10.1029/JC092iC07p07032.

Maykut, G. A., and N. Untersteiner (1971), Some results from a time-dependent thermodynamic model of sea ice, *J. Geophys. Res.*, *76*(6), 1550–1575, doi:10.1029/JC076i006p01550.

McPhee, M. G. (1992), Turbulent heat flux in the upper ocean under sea ice, *J. Geophys. Res.*, *97*(C4), 5365–5379, doi:10.1029/92JC00239.

Mellor, G. L., and T. Yamada (1982), Development of a turbulence closure model for geophysical fluid problems, *Rev. Geophys.*, *20*(4), 851–875, doi:10.1029/RG020i004p00851.

Mercer, J. H. (1978), West Antarctic ice sheet and CO2 greenhouse effect: a threat of disaster, *Nature*, *271*(5643), 321–325, doi:10.1038/271321a0.

Meredith, M. P. (2013), Oceanography: Replenishing the abyss, *Nature Geosci*, *6*(3), 166–167, doi:10.1038/ngeo1743.

Meredith, M. P., and A. M. Hogg (2006), Circumpolar response of Southern Ocean eddy activity to a change in the Southern Annular Modes, *Geophys. Res. Lett.*, *33*, L16608, doi:10.1029/2006GL026499.

Meredith, M. P., and J. C. King (2005), Rapid climate change in the ocean west of the Antarctic Peninsula during the second half of the 20th century, *Geophys. Res. Lett.*, *32*, L19604, doi:10.1029/2005GL024042.

Meredith, M. P., I. A. Renfrew, A. Clarke, J. C. King, and M. A. Brandon (2004a), Impact of the 1997/98 ENSO on upper ocean characteristics in Marguerite Bay, western Antarctic Peninsula, *J. Geophys. Res.*, *109*, C09013, doi:10.1029/2003JC001784.

Meredith, M. P., P. L. Woodworth, C. W. Hughes, and V. Stepanov (2004b), Changes in the ocean transport through Drake Passage during the 1980s and 1990s, forced by changes in the Southern Annular Modes, *Geophys. Res. Lett.*, *31*, L21305, doi:10.1029/2004GL021169.

Meredith, M. P., A. C. N. Garabato, A. L. Gordon, and G. C. Johnson (2008), Evolution of the deep and bottom waters of the Scotia Sea, Southern Ocean, during 1995-2005*, *J. Climate*, *21*(13), 3327–3343, doi:10.1175/2007JCLI2238.1.

Meredith, M. P., M. I. Wallace, S. E. Stammerjohn, I. A. Renfrew, A. Clarke, H. J. Venables, D. R. Shoosmith, T. Souster, and M. J. Leng (2010), Changes in the freshwater composition of the upper ocean west of the Antarctic Peninsula during the first decade of the 21st century, *Progress in Oceanography*, *87*(14), 127–143, doi:10.5194/os-8-433-2012.

Meredith, M. P., A. L. Gordon, A. C. Naveira Garabato, E. P. Abrahamsen, B. A. Huber, L. Jullion, and H. J. Venables (2011), Synchronous intensification and warming of Antarctic Bottom Water outflow from the Weddell Gyre, *Geophys. Res. Lett.*, *38*, L03603, doi:10.1029/2010GL046265.

Miller, R. L., G. A. Schmidt, and D. T. Shindell (2006), Forced annular variations in the 20th century Intergovernmental Panel on Climate Change Fourth Assessment Report models, *J. Geophys. Res.*, *111*, D18101, doi:10.1029/2005JD006323.

Moffat, C., B. Owens, and R. C. Beardsley (2009), On the characteristics of Circumpolar Deep Water intrusions to the west Antarctic Peninsula Continental Shelf, *J. Geophys. Res.*, *114*, C05017, doi:10.1029/2008JC004955.

Naish, T., et al. (2009), Obliquity-paced Pliocene West Antarctic ice sheet oscillations, *Nature*, *458*(7236), 322–328, doi:10.1038/nature07867.

Nicholls, K. W. (1997), Predicted reduction in basal melt rates of an Antarctic ice shelf in a warmer climate, *Nature*, *388*(6641), 460–462, doi:10.1038/41302.

Nicholls, K. W., L. Padman, M. Schröder, R. A. Woodgate, A. Jenkins, and S. Østerhus (2003), Water mass modification over the continental shelf north of Ronne Ice Shelf, Antarctica, *J. Geophys. Res.*, *108*(C8), 3260, doi:10.1029/2002JC001713.

Nicholls, K. W., C. J. Pudsey, and P. Morris (2004), Summertime water masses off the northern Larsen C Ice Shelf, Antarctica, *Geophys. Res. Lett.*, *31*, L09309, doi:10.1029/2004GL019924.

Nicholls, K. W., L. Boehme, M. Biuw, and M. A. Fedak (2008), Wintertime ocean conditions over the southern Weddell Sea continental shelf, Antarctica, *Geophys. Res. Lett.*, *35*, L21605, doi:10.1029/2008GL035742.

Nicholls, K. W., S. Østerhus, K. Makinson, T. Gammelsrød, and E. Fahrbach (2009), Ice-ocean processes over the continental shelf of the southern Weddell Sea, Antarctica: A review, *Rev. Geophys.*, *47*, RG3003, doi:10.1029/2007RG000250.

Niiler, P., and E. B. Kraus (1977), One-dimensional models of the upper oceans, in *Modelling and Prediction of the Upper Layers of the Ocean*, edited by E. B. Kraus, pp. 143–172, Pergamon Press, New York.

Notz, D., and M. G. Worster (2009), Desalination processes of sea ice revisited, *J. Geophys. Res.*, *114*, C05006, doi:10.1029/2008JC004885.

Ohshima, K. I., et al. (2013), Antarctic Bottom Water production by intense sea-ice formation in the Cape Darnley polynya, *Nature Geosci*, *6*(3), 235–240, doi:10.1038/ngeo1738.

Ono, N. (1967), Specific heat and heat of fusion of sea ice, in *Physics of Snow and Ice*, vol. 1, edited by H. Oura, pp. 599–610, Institute of Low Temperature Science, Hokkaido, Japan.

Orsi, A., G. Johnson, and J. Bullister (1999), Circulation, mixing, and production of Antarctic Bottom Water, *Progress In Oceanography*, *43*(1), 55–109, doi:10.1016/S0079-6611(99)00004-X.

Orsi, A. H., and C. L. Wiederwohl (2009), A recount of Ross Sea waters, *Deep Sea Research Part 2: Topical Studies in Oceanography*, *56*(13-14), 778–795, doi:10.1016/j.dsr2.2008.10.033.

Orsi, A. H., T. Whitworth III, and W. D. Nowlin Jr. (1995), On the meridional extent and fronts of the Antarctic Circumpolar Current, *Deep Sea Research Part I: Oceanographic Research Papers*, *42*(5), 641–673, doi:10.1016/0967-0637(95)00021-W.

Orsi, A. H., S. S. Jacobs, A. L. Gordon, and M. Visbeck (2001), Cooling and ventilating the Abyssal Ocean, *Geophys. Res. Lett.*, *28*(15), 2923–2926, doi:10.1029/2001GL012830.

Orsi, A. H., W. M. Smethie, and J. L. Bullister (2002), On the total input of antarctic waters to the deep ocean: A preliminary estimate from chlorofluorocarbon measurements, *J. Geophys. Res.*, *107*(C8), 31–1–31–14.

Padman, L., et al. (2012), Oceanic controls on the mass balance of Wilkins Ice Shelf, Antarctica, *J. Geophys. Res.*, *117*, C01010, doi:10.1029/2011JC007301.

Parkinson, C. L., and D. J. Cavalieri (2012), Antarctic sea ice variability and trends, 1979-2010, *The Cryosphere*, *6*(4), 871–880, doi:10.5194/tc-6-871-2012.

Parkinson, C. L., D. J. Cavalieri, P. Gloersen, H. J. Zwally, and J. C. Comiso (1999), Arctic sea ice extents, areas, and trends, 1978-1996, *J. Geophys. Res.*, *104*(C9), 20,837–20,856, doi:10.1029/1999JC900082.

Payne, A. J., A. Vieli, A. P. Shepherd, D. J. Wingham, and E. Rignot (2004), Recent dramatic thinning of largest West Antarctic ice stream triggered by oceans, *Geophys. Res. Lett.*, *31*, L23401, doi:10.1029/2004GL021284.

Perlwitz, J., S. Pawson, R. L. Fogt, J. E. Nielsen, and W. D. Neff (2008), Impact of stratospheric ozone hole recovery on Antarctic climate, *Geophys. Res. Lett.*, *35*(8), L08714, doi:10.1029/2008GL033317.

Pollard, D., and R. M. DeConto (2009), Modelling West Antarctic ice sheet growth and collapse through the past five million years, *Nature*, *458*(7236), 329–332, doi:10.1038/nature07809.

Pollard, D., M. Batteen, and Y. Han (1983), Development of a simple upper-ocean and sea-ice model, *J. Phys. Oceanogr*, *13*(5), 754–768, doi:10.1175/1520-0485(1983)013⟨0754:DOASUO⟩2.0.CO;2.

Polvani, L. M., and K. L. Smith (2013), Can natural variability explain observed Antarctic sea ice trends? new modeling evidence from CMIP5, *Geophys. Res. Lett.*, *40*(12), 3195–3199, doi:10.1002/grl.50578.

Polvani, L. M., D. W. Waugh, G. J. P. Correa, and S.-W. Son (2010), Stratospheric ozone depletion: The main driver of twentieth-century atmospheric circulation changes in the Southern Hemisphere, *J. Climate*, *24*(3), 795–812, doi:10.1175/2010JCLI3772.1.

Powell, D. C., T. Markus, and A. Stssel (2005), Effects of snow depth forcing on Southern Ocean sea ice simulations, *J. Geophys. Res.*, *110*(C6), C06001, doi:10.1029/2003JC002212.

Price, J. F., R. A. Weller, and R. Pinkel (1986), Diurnal cycling: Observations and models of the upper ocean response to diurnal heating, cooling, and wind mixing, *J. Geophys. Res.*, *91*(C7), 8411–8427, doi:10.1029/JC091iC07p08411.

Pritchard, H. D., S. R. M. Ligtenberg, H. A. Fricker, D. G. Vaughan, M. R. van den Broeke, and L. Padman (2012), Antarctic ice-sheet loss driven by basal melting of ice shelves, *Nature*, *484*(7395), 502–505, doi:10.1038/nature10968.

Purkey, S. G., and G. C. Johnson (2010), Warming of global abyssal and deep Southern Ocean waters between the 1990s and 2000s: Contributions to global heat and sea level rise budgets*, *J. Climate*, *23*(23), 6336–6351, doi:10.1175/2010JCLI3682.1.

Purkey, S. G., and G. C. Johnson (2012), Global contraction of Antarctic Bottom Water between the 1980s and 2000s*, *J. Climate*, *25*(17), 5830–5844, doi:10.1175/JCLI-D-11-00612.1.

Purkey, S. G., and G. C. Johnson (2013), Antarctic Bottom Water warming and freshening: Contributions to sea level rise, ocean freshwater budgets, and global heat gain*, *J. Climate*, *26*(16), 6105–6122, doi:10.1175/JCLI-D-12-00834.1.

Renfrew, I. A., J. C. King, and T. Markus (2002), Coastal polynyas in the southern Weddell Sea: Variability of the surface energy budget, *J. Geophys. Res.*, *107*(C6), 3063, doi:10.1029/2000JC000720.

Rignot, E., and S. S. Jacobs (2002), Rapid bottom melting widespread near Antarctic ice sheet grounding lines, *Science*, *296*(5575), 2020–2023, doi:10.1126/science.1070942.

Rignot, E., J. L. Bamber, M. R. van den Broeke, C. Davis, Y. Li, W. J. van de Berg, and E. van Meijgaard (2008), Recent Antarctic ice mass loss from radar interferometry and regional climate modelling, *Nature Geosci*, *1*(2), 106–110, doi:10.1038/ngeo102.

Rignot, E., J. Mouginot, and B. Scheuchl (2011), Ice flow of the Antarctic Ice Sheet, *Science*, *333*(6048), 1427–1430, doi:10.1126/science.1208336.

Rignot, E., S. Jacobs, J. Mouginot, and B. Scheuchl (2013), Ice shelf melting around Antarctica, *Science*, *341*, 266–270, doi:10.1126/science.1235798.

Rintoul, S., C. Hughes, and D. Olbers (2001), The Antarctic Circumpolar Current system, in *Ocean Circulation and Climate*, edited by G. Siedler, J. Church, and J. Gould, pp. 271–302, Academic Press, New York.

Rintoul, S. R. (2007), Rapid freshening of Antarctic Bottom Water formed in the Indian and Pacific oceans, *Geophys. Res. Lett.*, *34*(6), L06606, doi:10.1029/2006GL028550.

Robertson, R., M. Visbeck, A. L. Gordon, and E. Fahrbach (2002), Long-term temperature trends in the deep waters of the Weddell Sea, *Deep Sea Research Part II: Topical Studies in Oceanography*, *49*(21), 4791–4806, doi:10.1016/S0967-0645(02)00159-5.

Ropelewski, C. F., and P. D. Jones (1987), An extension of the Tahiti-Darwin Southern Oscillation Index, *Mon. Wea. Rev.*, *115*(9), 2161–2165, doi:10.1175/1520-0493(1987)115⟨2161:AEOTTS⟩2.0.CO;2.

Saha, S., et al. (2006), The NCEP Climate Forecast System, *J. Climate*, *19*(15), 3483–3517, doi:10.1175/JCLI3812.1.

Schmitz, W. J. (1995), On the interbasin-scale thermohaline circulation, *Rev. Geophys.*, *33*(2), 151–173, doi:10.1029/95RG00879.

Schneider, D., C. Deser, and Y. Okumura (2012), An assessment and interpretation of the observed warming of West Antarctica in the austral spring, *Clim Dyn*, *38*(1-2), 323–347, doi:10.1007/s00382-010-0985-x.

Schodlok, M. P., D. Menemenlis, E. Rignot, and M. Studinger (2012), Sensitivity of the ice-shelf/ocean system to the sub-ice-shelf cavity shape measured by NASA IceBridge in Pine Island Glacier, West Antarctica, *Annals of Glaciology*, *53*(60), 156–162, doi:10.3189/2012AoG60A073.

Schoof, C. (2007), Ice sheet grounding line dynamics: Steady states, stability, and hysteresis, *J. Geophys. Res.*, *112*, F03S28, doi:10.1029/2006JF000664.

Semtner, A. J. (1976), A model for the thermodynamic growth of sea ice in numerical investigations of climate, *J. Phys. Oceanogr*, *6*(3), 379–389, doi:10.1175/1520-0485(1976)006⟨0379:AMFTTG⟩2.0.CO;2.

Shepherd, A., D. Wingham, and E. Rignot (2004), Warm ocean is eroding West Antarctic Ice Sheet, *Geophys. Res. Lett.*, *31*, L23402, doi:10.1029/2004GL021106.

Shepherd, A., et al. (2012), A reconciled estimate of ice-sheet mass balance, *Science*, *338*(6111), 1183–1189, doi:10.1126/science.1228102.

Shindell, D. T., and G. A. Schmidt (2004), Southern Hemisphere climate response to ozone changes and greenhouse gas increases, *Geophys. Res. Lett.*, *31*(18), L18209, doi:10.1029/2004GL020724.

Sigmond, M., and J. C. Fyfe (2010), Has the ozone hole contributed to increased Antarctic sea ice extent?, *Geophys. Res. Lett.*, *37*, L18502, doi:10.1029/2010GL044301.

Skinner, L. C., S. Fallon, C. Waelbroeck, E. Michel, and S. Barker (2010), Ventilation of the deep Southern Ocean and deglacial CO2 rise, *Science*, *328*(5982), 1147–1151, doi:10.1126/science.1183627.

Smith, K. L., L. M. Polvani, and D. R. Marsh (2012a), Mitigation of 21st century Antarctic sea ice loss by stratospheric ozone recovery, *Geophys. Res. Lett.*, *39*(20), L20701, doi:10.1029/2012GL053325.

Smith, W. J., P. Sedwick, K. Arrigo, D. Ainley, and A. Orsi. (2012b), The Ross Sea in a sea of changes, *Oceanography*, *25*(3), doi:10.5670/oceanog.2012.80.

Son, S.-W., et al. (2008), The impact of stratospheric ozone recovery on the Southern Hemisphere westerly jet, *Science*, *320*(5882), 1486–1489, doi:10.1126/science.1155939.

Stammerjohn, S., R. Massom, D. Rind, and D. Martinson (2012), Regions of rapid sea ice change: An inter-hemispheric seasonal comparison, *Geophys. Res. Lett.*, *39*(6), L06501, doi:10.1029/2012GL050874.

Stammerjohn, S. E., D. G. Martinson, R. C. Smith, X. Yuan, and D. Rind (2008), Trends in Antarctic annual sea ice retreat and advance and their relation to El Niño-Southern Oscillation and Southern Annular Mode variability, *J. Geophys. Res.*, *113*, C03S90, doi:10.1029/2007JC004269.

Steele, M. (1992), Sea ice melting and floe geometry in a simple ice-ocean model, *J. Geophys. Res.*, *97*(C11), 17,729–17,738, doi:10.1029/92JC01755.

Steig, E., Q. Ding, D. Battisti, and A. Jenkins (2012), Tropical forcing of Circumpolar Deep Water inflow and outlet glacier thinning in the Amundsen Sea Embayment, West Antarctica, *Annals of Glaciology*, *53*(60), 19–28, doi:10.3189/2012AoG60A110.

Steig, E. J., D. P. Schneider, S. D. Rutherford, M. E. Mann, J. C. Comiso, and D. T. Shindell (2009), Warming of the Antarctic ice-sheet surface since the 1957 International Geophysical Year, *Nature*, *457*(7228), 459–462, doi:10.1038/nature07669.

Stroeve, J. C., V. Kattsov, A. Barrett, M. Serreze, T. Pavlova, M. Holland, and W. N. Meier (2012), Trends in arctic sea ice extent from CMIP5, CMIP3 and observations, *Geophys. Res. Lett.*, *39*(16), L16502, doi:10.1029/2012GL052676.

Swart, N. C., and J. C. Fyfe (2013), The influence of recent Antarctic ice sheet retreat on simulated sea ice area trends, *Geophys. Res. Lett.*, *40*(16), 4328–4332, doi:10.1002/grl.50820.

Takahashi, T., et al. (2009), Climatological mean and decadal change in surface ocean pCO_2, and net sea-air CO_2 flux over the global oceans, *Deep Sea Research Part II: Topical Studies in Oceanography*, *56*(8-10), 554–577, doi:10.1016/j.dsr2.2008.12.009.

Talbot, M. H. (1988), Oceanic environment of George VI Ice Shelf, Antarctic Peninsula, *Annals of glaciology*, *11*, 161–164.

Talley, L. D. (2013), Closure of the global overturning circulation through the Indian, Pacific, and Southern oceans: Schematics and transports, *Oceanography*, *26*, 80–97, doi:10.5670/oceanog.2013.07.

Tamura, T., K. I. Ohshima, and S. Nihashi (2008), Mapping of sea ice production for Antarctic coastal polynyas, *Geophys. Res. Lett.*, *35*, L07606, doi:10.1029/2007GL032903.

Tamura, T., K. I. Ohshima, S. Nihashi, and H. Hasumi (2011), Estimation of surface heat/salt fluxes associated with sea ice growth/melt in the southern ocean:, *SOLA*, *7*, 17–20, doi:10.2151/sola.2011-005.

Tang, C. L. (1991), A two-dimensional thermodynamic model for sea ice advance and retreat in the Newfoundland marginal ice zone, *J. Geophys. Res.*, *96*(C3), 4723–4737, doi:10.1029/90JC02579.

Tang, C. L., and B. M. DeTracey (1998), Space-time variation of mixed-layer properties, heat and salt fluxes, and ice melt in the Newfoundland marginal ice zone, *J. Geophys. Res.*, *103*(C1), 1177–1191, doi:10.1029/97JC02788.

Taylor, P. D., and D. L. Feltham (2004), A model of melt pond evolution on sea ice, *J. Geophys. Res.*, *109*, C12007, doi:10.1029/2004JC002361.

Thoma, M., A. Jenkins, D. Holland, and S. Jacobs (2008), Modelling Circumpolar Deep Water intrusions on the Amundsen sea continental shelf, Antarctica, *Geophys. Res. Lett.*, *35*(18), L18602, doi:10.1029/2008GL034939.

Thomas, D. N., and G. S. Dieckmann (2002), Antarctic sea ice–a habitat for Extremophiles, *Science*, *295*(5555), 641–644, doi:10.1126/science.1063391.

Thompson, D. W. J., and S. Solomon (2002), Interpretation of recent Southern Hemisphere climate changes, *Science*, *296*(5569), 895–899, doi:10.1126/science.1069270.

Thompson, D. W. J., and J. M. Wallace (2000), Annular modes in the extratropical circulation. Part I: Month-to-month variability*, *J. Climate*, *13*(5), 1000–1016, doi:10.1175/1520-0442(2000)013⟨1000:AMITEC⟩2.0.CO;2.

Thompson, D. W. J., S. Solomon, P. J. Kushner, M. H. England, K. M. Grise, and D. J. Karoly (2011), Signatures of the Antarctic ozone hole in Southern Hemisphere surface climate changes, *Nature Geosci*, *4*(11), 741–749, doi:10.1038/ngeo1296.

Thomson, A., et al. (2011), RCP4.5: a pathway for stabilization of radiative forcing by 2100, *Climatic Change*, *109*(1-2), 77–94, doi:10.1007/s10584-011-0151-4.

Timmermann, R., and A. Beckmann (2004), Parameterization of vertical mixing in the Weddell Sea, *Ocean modelling*, *6*(1), 83–100, doi:10.1016/S1463-5003(02)00061-6.

Timmermann, R., and H. Hellmer (2013), Southern Ocean warming and increased ice shelf basal melting in the twenty-first and twenty-second centuries based on coupled ice-ocean finite-element modelling, *Ocean Dynamics*, pp. 1–16, doi:10.1007/s10236-013-0642-0.

Timmermann, R., and M. Losch (2005), Erratum: Using the Mellor-Yamada mixing scheme in seasonally ice-covered seas - Corrigendum to: Parameterization of vertical mixing in the Weddell Sea [Ocean Modelling 6 (2004) 83-100 10.1016/S1463-5003(02)00061-6], *Ocean Modelling*, *10*(3-4), 369–372, doi:10.1016/j.ocemod.2004.11.001.

Timmermann, R., A. Beckmann, and H. H. Hellmer (2002), Simulations of ice-ocean dynamics in the Weddell Sea 1. Model configuration and validation, *J. Geophys. Res.*, *107*(C3), doi:10.1029/2000JC000741.

Timmermann, R., et al. (2010), A consistent dataset of Antarctic ice sheet topography, cavity geometry, and global bathymetry, *Earth Syst. Sci. Data Discuss.*, *3*(2), 231–257, doi:10.5194/essdd-3-231-2010.

Toggweiler, J. R., and B. Samuels (1995), Effect of sea ice on the salinity of Antarctic bottom waters, *J. Phys. Oceanogr.*, *25*(9), 1980–1997, doi:10.1175/1520-0485(1995)025⟨1980:EOSIOT⟩2.0.CO;2.

Trenberth, K. E. (1997), The definition of El Niño, *Bull. Amer. Meteor. Soc.*, *78*(12), 2771–2777, doi:10.1175/1520-0477(1997)078⟨2771:TDOENO⟩2.0.CO;2.

Tsamados, M., D. L. Feltham, and A. V. Wilchinsky (2013), Impact of a new anisotropic rheology on simulations of Arctic sea ice, *J. Geophys. Res. Oceans*, *118*(1), 91–107, doi:10.1029/2012JC007990.

Tsamados, M., D. Feltham, D. Schroeder, D. Flocco, S. Farrell, N. Kurtz, S. Laxon, and S. Bacon (submitted), Impact of variable atmospheric and oceanic form drag on simulations of Arctic sea ice, *J. Phys. Oceanogr.*

Turner, A. K., E. C. Hunke, and C. M. Bitz (2013a), Two modes of sea-ice gravity drainage: A parameterization for large-scale modeling, *J. Geophys. Res. Oceans*, *118*(5), 2279–2294, doi:10.1002/jgrc.20171.

Turner, J. (2004), The El Niño-Southern Oscillation and Antarctica, *Int. J. Climatol.*, *24*(1), 1–31, doi:10.1002/joc.965.

Turner, J., S. R. Colwell, G. J. Marshall, T. A. Lachlan-Cope, A. M. Carleton, P. D. Jones, V. Lagun, P. A. Reid, and S. Iagovkina (2005), Antarctic climate change during the last 50 years, *Int. J. Climatol.*, *25*(3), 279–294, doi:10.1002/joc.1130.

Turner, J., J. C. Comiso, G. J. Marshall, T. A. Lachlan-Cope, T. Bracegirdle, T. Maksym, M. P. Meredith, Z. Wang, and A. Orr (2009), Non-annular atmospheric circulation change induced by stratospheric ozone depletion and its role in the recent increase of Antarctic sea ice extents, *Geophys. Res. Lett.*, *36*, L08502, doi:10.1029/2009GL037524.

Turner, J., T. J. Bracegirdle, T. Phillips, G. J. Marshall, and J. S. Hosking (2013b), An initial assessment of Antarctic sea ice extent in the CMIP5 models, *J. Climate*, *26*(5), 1473–1484, doi:10.1175/JCLI-D-12-00068.1.

UNESCO (1981), Background papers supporting data on the international equation of state of seawater 1980, *UNESCO Technical Papers in Marine Science*, *No. 38*, 192.

Untersteiner, N. (1964), Calculations of temperature regime and heat budget of sea ice in the central Arctic, *J. Geophys. Res.*, *69*(22), 4755–4766, doi:10.1029/JZ069i022p04755.

Untersteiner, N. (1968), Natural desalination and equilibrium salinity profile of perennial sea ice, *J. Geophys. Res.*, *73*(4), 1251–1257, doi:10.1029/JB073i004p01251.

van den Broeke, M., W. J. van de Berg, and E. van Meijgaard (2006), Snowfall in coastal West Antarctica much greater than previously assumed, *Geophys. Res. Lett.*, *33*, L02505, doi:10.1029/2005GL025239.

van Lipzig, N. P. M., J. Turner, S. R. Colwell, and M. R. van Den Broeke (2004), The near-surface wind field over the Antarctic continent, *Int. J. Climatol.*, *24*(15), 1973–1982, doi:10.1002/joc.1090.

Vancoppenolle, M., T. Fichefet, and H. Goosse (2009), Simulating the mass balance and salinity of Arctic and Antarctic sea ice. 2. importance of sea ice salinity variations, *Ocean Modelling*, *27*(12), 54–69, doi:10.1016/j.ocemod.2008.11.003.

Vaughan, D. G., G. J. Marshall, W. M. Connolley, C. Parkinson, R. Mulvaney, D. A. Hodgson, J. C. King, C. J. Pudsey, and J. Turner (2003), Recent rapid regional climate warming on the Antarctic Peninsula, *Climatic Change*, *60*(3), 243–274, doi:10.1023/A:1026021217991.

Wadhams, P. (2000), *Ice in the Ocean*, 351 pp., Gordon & Breach Science Publishers, Amsterdam.

Wåhlin, A. K., X. Yuan, G. Björk, and C. Nohr (2010), Inflow of warm Circumpolar Deep Water in the central Amundsen shelf, *J. Phys. Oceanogr.*, *40*(6), 1427–1434, doi:10.1175/2010JPO4431.1.

Walker, D. P., M. A. Brandon, A. Jenkins, J. T. Allen, J. A. Dowdeswell, and J. Evans (2007), Oceanic heat transport onto the Amundsen sea shelf through a submarine glacial trough, *Geophys. Res. Lett.*, *34*(2), L02602, doi:10.1029/2006GL028154.

Whitworth, T., and W. D. Nowlin (1987), Water masses and currents of the Southern Ocean at the Greenwich Meridian, *J. Geophys. Res.*, *92*(C6), 6462–6476, doi:10.1029/JC092iC06p06462.

Whitworth, T., W. D. Nowlin, and S. J. Worley (1982), The net transport of the Antarctic Circumpolar Current through Drake Passage, *J. Phys. Oceanogr.*, *12*(9), 960–971, doi:10.1175/1520-0485(1982)012⟨0960:TNTOTA⟩2.0.CO;2.

Whitworth, T., A. H. Orsi, S.-J. Kim, W. D. Nowlin, and R. A. Locarnini (1998), Water masses and mixing near the Antarctic Slope Front, in *Ocean, Ice, and Atmosphere: Interactions at the Antarctic Continental Margin*, pp. 1–27, American Geophysical Union, doi:10.1029/AR075p0001.

Wilchinsky, A. V., and D. L. Feltham (2009), Numerical simulation of the Filchner overflow, *J. Geophys. Res.*, *114*, C12012, doi:10.1029/2008JC005013.

Williams, G. D., S. Aoki, S. S. Jacobs, S. R. Rintoul, T. Tamura, and N. L. Bindoff (2010), Antarctic Bottom Water from the Adélie and George V Land coast, East Antarctica (140–149°E), *J. Geophys. Res.*, *115*, C04027, doi:10.1029/2009JC005812.

Wingham, D. J., D. W. Wallis, and A. Shepherd (2009), Spatial and temporal evolution of Pine Island Glacier thinning, 1995-2006, *Geophys. Res. Lett.*, *36*, L17501, doi:10.1029/2009GL039126.

WMO (World Meteorological Organization) (2011), Scientific assessment of ozone depletion: 2010, in *Global Ozone Research and Monitoring Project*, 52, p. 516, Geneva, Switzerland, 2011.

Worby, A. P. (1999), Observing Antarctic sea ice: A practical guide for conducting sea ice observations from vessels operating in the antarctic pack ice., CD-ROM produced for the ASPeCt program of the SCAR Global Change and the Antarctic Program.

Worby, A. P., C. A. Geiger, M. J. Paget, M. L. Van Woert, S. F. Ackley, and T. L. DeLiberty (2008), Thickness distribution of Antarctic sea ice, *J. Geophys. Res.*, *113*, C05S92, doi:10.1029/2007JC004254.

Yi, D., H. J. Zwally, and J. W. Robbins (2011), ICESat observations of seasonal and interannual variations of sea-ice freeboard and estimated thickness in the Weddell Sea, Antarctica (2003-2009), *Annals of Glaciology*, *52*, 43–51, doi:10.3189/172756411795931480.

Yuan, X., and C. Li (2008), Climate modes in southern high latitudes and their impacts on Antarctic sea ice, *J. Geophys. Res.*, *113*, C06S91, doi:10.1029/2006JC004067.

Zhang, J. (2007), Increasing antarctic sea ice under warming atmospheric and oceanic conditions, *J. Climate*, *20*(11), 2515–2529, doi:10.1175/JCLI4136.1.

Zunz, V., H. Goosse, and F. Massonnet (2013), How does internal variability influence the ability of CMIP5 models to reproduce the recent trend in Southern Ocean sea ice extent?, *The Cryosphere*, *7*(2), 451–468, doi:10.5194/tc-7-451-2013.

Zwally, H. J., J. C. Comiso, C. L. Parkinson, D. J. Cavalieri, and P. Gloersen (2002), Variability of Antarctic sea ice 1979-1998, *J. Geophys. Res.*, *107*(C5), doi:10.1029/2000JC000733.